

Quantitative Susceptibility Mapping in the Human Brain

THÈSE N° 7050 (2016)

PRÉSENTÉE LE 7 OCTOBRE 2016

À LA FACULTÉ DES SCIENCES DE BASE

LABORATOIRE LEENAARDS-JEANTET D'IMAGERIE FONCTIONNELLE ET MÉTABOLIQUE

PROGRAMME DOCTORAL EN PHYSIQUE

ÉCOLE POLYTECHNIQUE FÉDÉRALE DE LAUSANNE

POUR L'OBTENTION DU GRADE DE DOCTEUR ÈS SCIENCES

PAR

Diana KHABIPOVA

acceptée sur proposition du jury:

Prof. C. Hébert, présidente du jury

Prof. R. Gruetter, Dr J. P. Rebelo Ferreira Marques, directeurs de thèse

Prof. Y. Wiaux, rapporteur

Prof. C. Langkammer, rapporteur

Prof. J.-Ph. Thiran, rapporteur



ÉCOLE POLYTECHNIQUE
FÉDÉRALE DE LAUSANNE

Suisse
2016

Acknowledgement

Many, many people affected me during my PhD thesis. In order to not go beyond the scope of this section I would like to shortly mention the main contributors.

First of all I would like to thank my thesis advisor Rolf Gruetter for providing such a great atmosphere and the research facility, which is the backbone of the research. Without your commitment and response I would not have been able to finish my PhD.

José, my direct supervisor, thank you sooooo much! During the last years you provided me not only with many great ideas, but you also made sure I do well at conferences and lab meetings. I'll never forget how you improved almost all of my images (starting with size, alignment and position) few days before my very first ESMRMB presentation. You also took care of my drafts, so my confusingly long sentences became more understandable for the research community. Thank you a lot for being the supervisor you are!

I was blessed with a co-supervisor, Yves Wiaux. You and your BASP group (Gilles, Rafael, Anna) took care of me during my first project not only by providing me your optimization knowledge, but also by explaining me the theoretical background. Also you introduced me to the delicious Belgian Beer for drinks in the Satellite and snowshoeing in Les Diablerets.

David Norris I would like to thank for giving me the opportunity to be a researcher in your MR group in the Donders Institutes during my SNF Doc.Mobility year. You made me feel great by showing interest in my research and you gave me excellent ideas and feedback not only during our weekly meetings, which resulted in three ISMRM abstracts.

To my colleagues from the CIBM (Dan, Emine, Andrea, Joao, Masoumeh, Jessica, Benoit, Bernard, Martin, Chems, Joao the great, Francisca, Dan, Lali, Florent, Mayur, Lijing, Jessica, Martin, Bernard, Rajika, Natalie, Hongxia, Nathalie, Mor, Christina): I spend so many lunch breaks with you, trying to decide which cafeteria has the best food of the day (taking the weather into account). We discussed not only work relevant problems but had also a great time beside it. With you I learned how to snowboard, although my back was hurting the next week and stairs were a torture. Also the snow fight during our 7km sledging run in Les Diablerets will always be a nice memory in the winter time and the nice barbecues in the summer time.

Another huge thank goes to the Donders people (Rita, Zahra the small, Zahra the tall, Jenny, Irati, Tim, Bart, Daniel, Marcel and so many more). It was a pleasure to spend the SNF Mobility year with you. You made me feel a part

of the group from the very beginning. Our lunch breaks were a special part of the day, sitting in the cafeteria or later in the black room . Also our group drinks were always great, not to forget our dinners and sleepovers. A special thank to Rita, my Master student, to supervise you was just a pleasure!!! I would also like to thank both Zahras for everything, your very delicious dishes, your soul, your kindness, your “being you”!

Not to forget all my friends, who accompanied me on my road of the thesis: Special thanks to my “worst movie” companions Konstantin and Dimitri with whom we watched the worst, but also a few surprisingly nice movies together with the pimped up pizzas and in the winter time the tasty raclettes evenings.

I would like to thank my Russian friends (Natalia, Alexandra, Katharina, Valeria, Alexander, Sergey) for all the uncountable coffee breaks und support.

I will always remember the tango midi for the nice break during lunch-time on Tuesdays which made the week very pleasant and also the Sunday evening Milongas on the BH-terrace with the incredible view over the lake Lemán and the mountains. And especially my Tango friends, here only very few but I would like to thank all of them; Lilia with whom I was a pleasure to dance, Pablo for the great Tango moves, especially when Nuevo Tango was played and who took me to so many Milongas, you showed me the real Spanish paella and improved my snowboard skills. Also a huge thanks to my dancing partner Andres, my dear friend. With you I had the most interesting adventures and seen Lausanne from a completely different view. Thank you for the many crazy moments with you!!!

My starting doc girls, Christina and Nancy, who make me realize I like the problems of my own PhD the most. The nice lunch breaks and picnics by the lake. The coffee breaks in the evening. The nice cooking dinners together. Nancy, you with your wisdom made me realize that in some years I will look back at my problems and smile how serious I took them. Christina, you showed me so many things I have never heard about and opened my mind. Our talks and meetings meant a lot to me, especially your sympathy!

I would also like to thank the many house mates I met while living in the nice house in Ecublens. Each and every one contributed to my life in its special way! The nice meals we cooked together and the different dishes I never heard of and were able to try out! Specially to Patric, my best friend. Having you as my room- and later on housemate enlightened my life!

Zum Schluss ein ganz besonders großes Dankeschön an meine Familie! Die Berliner Familie (Heikki, Manfred, Michi, Marko, Nicole, Leon, Dennis, Sophia, Janik, Renate, Edith, Gerd), die mich so unterstützt hat und mir so oft in den Hintern getreten hat, ich solle mal gefälligst bald fertig machen.

Danke besonders an Heikki für die seelische Unterstützung und die unzähligen Mittagessen, die ich bekommen habe, du bist wie eine zweite Mama für mich.

Und natürlich ein riesengroßes Danke meiner Familie! Papa, der mich immer unterstützt hat, komme was wolle. Dein unglaubliches Wissen und deine unendliche Geduld, auf meine nicht enden wollenden Fragen zu antworten, haben zu meiner Liebe zum Wissen, der Wissenschaft und wohl auch der Physik geführt. Mama, ich kann dir gar nicht genug danken. Du warst immer für mich da, hattest immer ein Ohr offen für mich und hast mich motiviert nicht aufzugeben. Meinen Kleinen danke ich dafür, dass ich immer die schlaue, kluge große Schwester bin, wie hätte ich da nicht fertig schreiben können?

And the most my husband without whom this work would have never been finished. You motivated and encouraged me to stay on track and not to give up. Thanks for the morning skype calls, you're the reason I was early at work and you not being around was also the reason I worked late. I don't want to know how much money we spent flying to each other, at the end we almost knew the Berlin-Geneva crew from easyjet. You always supported and encouraged me and dried my tears, you motivated me to stick to this PhD, to not change and not to give up. Ich danke dir für deine Liebe und Geduld, einfach für alles mein Liebster!

Summary

Magnetic resonance imaging (MRI) offers a good tissue contrast and the ability to visualize many disease related morphologies. The work presented in this thesis investigates the study of underlying structure of the brain using quantitative methods with a special emphasis on quantitative susceptibility mapping (QSM). Magnetic susceptibility reflects the interaction of a material to the magnetic field and measures in biological tissues the magnetic susceptibility of inclusions. The properties of paramagnetic and diamagnetic entities (iron and myelin) have opposing effects allowing QSM to distinguish the origin of the resulting dephasing.

The reconstruction of QSM requires further processing steps as the magnetic field produced by the sources needs to be disentangled from the orders of magnitude bigger background field. The produced field also depends not only on the shape and the orientation, but also on the anisotropy of susceptibility and the microstructural compartmentalization of the biological source. For this reason, reconstruction methods need to be capable to calculate accurate values for different brain regions as well as applicable in the everyday clinical diagnosis.

Within the framework of the thesis a data acquisition protocol based on a multiple-echo gradient echo sequence as well as a post-processing protocol was implemented. One of the processing steps, the background removal method, was applied to preserve the brain regions close to the cerebrospinal fluid (CSF). This method outperforms state of the art methods in this regions but is computationally intensive.

Different brain regions were studied using quantitative methods with special emphasis on the QSM. A new method, the modulated closed form solution, with extremely fast computational time is proposed. The comparison with other single orientation methods revealed similar results and the highest correlation to the state-of-the-art method (COSMOS) in the deep gray matter. The R_2^* maps calculated from the same dataset are also able to distinguish the deep gray matter structures with a similar quality. However, QSM shows a higher sensitivity in early stage multiple sclerosis lesions as well as white matter-gray matter structures.

In the human cortex the obtained cortical maps show enhancement of the primary sensory cortex, which is known to be highly myelinated, on three evaluated quantitative contrasts R_1 , R_2^* and susceptibility. The contrasts based on the relaxation rates, R_1 and R_2^* , show a monotonically decrease from the white matter to the CSF imitating the decrease in iron and myelin. The susceptibility behaviour is more complex as iron and myelin content introduce an opposing sensitivity, allowing to study iron and myelin content

when combining the three contrasts.

The microstructural organization of white matter influences the R_2^* , R_2 as well as field map from which QSM is calculated. This structure leads to an orientation dependence of the studied contrasts and for QSM the spherical assumption is not valid anymore. Therefore a new QSM method is introduced, which includes the Lorentzian correction in white matter. Main fibres such as forceps major and minor and the cortical spinal tract were analysed for the three different quantitative contrasts. The anisotropic component associated with susceptibility is similar for the relaxation rates whereas the isotropic component of R_2^* shows a higher variability. The resulting deep gray matter structure of the new QSM method remained similar to the state-of-the-art method when comparing the isotropic component but calculates physically meaningful susceptibility maps with improved contrast between known fibre bundles.

Zusammenfassung

Die Magnetresonanztomographie (MRT) bietet nicht nur einen guten Gewebekontrast, sondern auch die Möglichkeit, viele Krankheitsbilder zu visualisieren. Die Arbeit, die in dieser Dissertation vorgestellt wird, untersucht die zugrunde liegende Struktur des Gehirns mit Hilfe quantitativer Methoden mit einem besonderen Schwerpunkt auf dem so genannten „quantitative susceptibility mapping“ (QSM). Die Magnetische Suszeptibilität reflektiert die Wechselwirkung zwischen einem Material und dem anliegenden Magnetfeld und stellt in biologischen Geweben die magnetische Suszeptibilität von Einschlüssen dar. Paramagnetische und diamagnetische Objekte (wie Eisen und Myelin) haben entgegengesetzte Wirkungen und ermöglichen mittels QSM den Ursprung der Dephasierung zu unterscheiden.

Die Rekonstruktion von QSM erfordert weitere Verarbeitungsschritte wie die Differenzierung des Magnetfeld der gesuchten Objekte von dem um Größenordnungen größeren Hintergrundmagnetfeld. Das erzeugte Feld hängt zudem nicht nur von der Form und Ausrichtung, sondern auch von der Anisotropie der Suszeptibilität und der mikrostrukturellen Kompartimentierung der biologischen Quelle ab. Aus diesem Grund muss bei der QSM-Berechnung nicht nur die verschiedenen Hirnregionen berücksichtigt werden, sondern diese muss auch in der täglichen klinischen Diagnose anwendbar sein.

Im Rahmen dieser Dissertation wurde die Datenakquise auf Basis einer Multi-Echo-Gradientenechosequenz implementiert sowie ein Protokoll zu deren Nachbearbeitung entwickelt. Einer der Verarbeitungsschritte ist das Verfahren zur Entfernung des Hintergrundmagnetfeldes, welches speziell im Hinblick auf das Erhalten der Hirnregionen in der Nähe des Liquor cerebrospinalis (CSF) angewendet wurde. Dieses Verfahren übertrifft den Stand der Technik in diesen Regionen, ist jedoch rechenintensiv.

Verschiedene Gehirnregionen wurden mit quantitativen Methoden mit besonderem Schwerpunkt auf der QSM untersucht. Ein neues Verfahren wurde entwickelt, die Modulated Closed Form Solution, mit extrem schneller Rechenzeit. Der Vergleich mit anderen auf einer Orientierung des Kopfes basierenden Verfahren erzielte ähnliche Ergebnisse, wobei die höchste Korrelation mit dem Stand der Technik (COSMOS-Methode) in der tiefen grauen Substanz erreicht wurde. Die aus dem gleichen Datenbestand berechneten R_2^* -Werte unterscheiden auch die tiefen grauen Substanz-Strukturen mit ähnlicher Qualität. Allerdings zeigt QSM eine höhere Empfindlichkeit in einem frühen Stadium der durch Multiple Sklerose hervorgerufenen Läsionen sowie bezüglich der weißen Substanz-graue Substanz Strukturen.

Im menschlichen Kortex zeigen die erhaltenen kortikalen Karten der drei untersuchten quantitative Kontraste R_1 , R_2^* sowie der Suszeptibilität erhöhte

Werte des primären sensorischen Kortex, der eine verstärkte Myelinisierung aufweist. Die auf der Relaxationsgeschwindigkeit basierenden Kontraste, R_1 und R_2^* , zeigen ein monoton abfallendes Verhalten von der weißen Substanz zu der CSF, was auf einer Abnahme der Eisenkonzentration und der Myelinisierung zurückzuführen ist. Das Verhalten der Suszeptibilität ist komplexer, da Eisen und Myelingeht eine entgegengesetzte Wirkung ausüben. Daher kann durch das Kombinieren dieser drei quantitativen Methoden der Eisen- und Myelingeht untersucht werden.

Die mikrostrukturelle Organisation der weißen Substanz beeinflusst die R_2^* und R_2 -Werte sowie das induzierte Magnetfeld, aus dem QSM berechnet wird. Diese organisierte Struktur führt zu einer Orientierungsabhängigkeit der untersuchten Kontraste, so dass für QSM die Annahme einer sphärischen Quelle nicht mehr gültig ist. Daher wurde im Rahmen der Dissertation eine neue QSM-Methode vorgestellt, welche die Lorentz-Korrektur in der weißen Substanz enthält. Hauptfasern wie der Forceps minor und major als auch corpus callosum wurden für die drei verschiedenen quantitativen Kontraste analysiert. Die anisotrope Komponente der Relaxationsraten, die auf die Suszeptibilität zurückzuführen ist, zeigte sich ähnlich, während die isotrope Komponente von R_2^* eine höhere Variabilität zeigte. Die isotrope Komponente der tiefen grauen Substanz der neuen QSM-Methode blieb ähnlich dem Stand der Technik und es konnten physikalisch sinnvolle QSM-Karten mit verbessertem Kontrast zwischen bekannten Faserbündel berechnet werden.

Contents

Acknowledgements	i
Summary(English/Deutsch)	iv
List of Figures	xiii
Abbreviations	xvi
1 Introduction	1
1.1 Historical background and MRI in a nutshell	2
1.2 Motivation and Thesis Outline	5
2 Basics of MRI	9
2.1 Magnetic Resonance Physics	10
2.1.1 Nuclear spin in an applied magnetic field	10
2.1.2 Spin statistics	12
2.1.3 Relaxation times	14
2.1.4 Bloch equations	16
2.2 Image generation	20
2.2.1 Magnetic field and shimming	20
2.2.2 Gradients	22
2.2.3 Image encoding	23
2.2.3.1 Slice selection	23
2.2.3.2 Frequency and phase encoding	24
2.2.4 Fourier Transform	25
2.2.4.1 Specific characteristics in data acquisition	27
2.2.5 Parallel acquisition technique	29
2.3 Image contrast	31
2.3.1 GRE - gradient recalled echo	31
2.3.2 SE - spin echo	36
2.3.3 DTI - Diffusion tensor imaging	39

2.3.4	SWI - susceptibility weighted imaging	42
3	Susceptibility	47
3.1	Theory	48
3.2	Susceptibility in biological tissues	52
3.2.1	Iron	53
3.2.2	Myelin sheath	54
3.2.3	Microstructure	56
3.2.4	Further influences	57
3.3	Advanced descriptions of the susceptibility	59
3.3.1	Generalized Lorentzian Approach: account for anisotropic structure	59
3.3.2	Susceptibility tensor: account for anisotropic magnetic susceptibility	60
3.3.3	Generalized Lorentzian Tensor Approach: account for anisotropic structure and magnetic susceptibility	61
4	QSM step-by-step	65
4.1	Phase combination and unwrapping	66
4.1.1	Phase difference methods	66
4.1.2	Phase imaging methods	68
4.2	Background removal	69
4.3	Reconstruction of QSM	70
4.3.1	k-space based reconstruction	72
4.3.2	Image space based reconstruction	73
4.3.3	Direct reconstruction	74
5	Modulated Closed Form	75
5.1	Introduction	77
5.2	Theory	78
5.2.1	Multiple orientation method - COSMOS	79
5.2.2	l_2 regularized single-orientation method	79
5.2.3	l_1 total variation denoising method	80
5.2.4	Modulated Closed Form solution	81
5.3	Methods	81
5.3.1	Numerical Simulation Phantom	81
5.3.2	In vivo Data	82
5.3.2.1	Data Acquisition	82
5.3.2.2	Data processing	82
5.3.2.3	Field and R_2^* Map calculation	83
5.3.2.4	Background field removal	83

	5.3.2.5	Gradient Mask calculation	84
	5.3.2.6	Susceptibility mapping and evaluation	84
5.4	Results		85
	5.4.1	Numerical simulation phantom	85
	5.4.2	In vivo Data	87
	5.4.2.1	Qualitative comparison of multiple orientation susceptibility and R_2^* maps	87
	5.4.2.2	Single orientation susceptibility mapping methods	88
	5.4.2.3	Quantitative comparison of susceptibility and R_2^* mapping	94
	5.4.2.4	Multiple sclerosis lesion detection	95
5.5	Discussion		96
	5.5.0.5	Comparison of Susceptibility and R_2^* mapping	96
	5.5.0.6	Single orientation susceptibility mapping methods	96
	5.5.0.7	Multiple sclerosis lesions	97
5.6	Conclusion		98
5.7	Appendix		99
6	Quantitative imaging in the cortex		103
6.1	Introduction		105
6.2	Methods		108
	6.2.1	Data acquisition	108
	6.2.1.1	R_1 maps	108
	6.2.1.2	R_2^* and susceptibility maps	108
	6.2.2	Data processing	109
	6.2.2.1	R_1 calculation	109
	6.2.2.2	R_2^* and susceptibility calculation	109
	6.2.3	Cortical maps	110
	6.2.4	Iron and Myelin	112
6.3	Results		113
	6.3.1	Data and segmentation quality	113
	6.3.2	Cortical surfaces and ROI	114
	6.3.3	Through cortex analysis	116
	6.3.4	Myelin and Fe information through quantitative contrasts combination	117
6.4	Discussion		118
6.5	Conclusion		122
6.6	Acknowledgements		122
6.7	Appendix		122

7	(apparent) relaxation rate in white matter	127
7.1	Introduction	129
7.2	Methods	130
7.2.1	Theory	130
7.2.2	Data Acquisition	131
7.2.3	Data processing	132
7.2.3.1	R_2^* and R_2 calculation	132
7.2.3.2	Co-registration	133
7.2.3.3	DTI data processing	133
7.2.3.4	Angle map calculation	134
7.2.3.5	Fiber mask calculation	135
7.2.3.6	Computation of (an)isotropic components of (apparent) transverse relaxation rates	136
7.3	Results	136
7.3.1	Data and co-registration quality	136
7.3.2	Isotropic and anisotropic evaluation	137
7.4	Discussion	141
7.5	Conclusion	145
7.6	Acknowledement	145
8	QSM in white matter, Lorentzian correction	147
8.1	Introduction	149
8.2	Methods	150
8.2.1	Data Acquisition	150
8.2.1.1	DTI	150
8.2.1.2	QSM	151
8.2.2	Data processing	151
8.2.2.1	DTI data processing	151
8.2.2.2	Co-registration	151
8.2.2.3	Angle map calculation	152
8.2.2.4	ROI mask calculation	152
8.2.2.5	QSM calculation	153
8.3	Results	154
8.4	Discussion	157
8.5	Conclusion	158
8.6	Acknowledement	159
9	Conclusion and Outlook	161
9.1	Conclusion	161
9.2	Future Work	163

<i>CONTENTS</i>	xiii
Bibliography	165
List of Publications	191

List of Figures

2.1	precession of the magnetic spin	13
2.2	statistics of the spins	14
2.3	T_1 , T_2 and T_2^* relaxation	15
2.4	magnetization vector in presence of RF-pulse	19
2.5	application of gradient magnetic field	22
2.6	slice encoding	24
2.7	spatial frequencies and the k-space	26
2.8	k-space and wave representation on image space	28
2.9	k-space and corresponding image space	29
2.10	gradient recalled echo	32
2.11	frequency and phase encoding	33
2.12	weighting of contrasts	35
2.13	magnitude and phase for multiple GRE	36
2.14	spin echo	37
2.15	multiple spin echo	38
2.16	iterative reconstruction algorithm of T_2	39
2.17	diffusion tensor imaging	41
2.18	gradient directions and fractional anisotropy map	42
2.19	tractography	43
2.20	susceptibility weighted imaging	44
2.21	lesions in different contrasts	45
3.1	magnetic dipole and dipole kernel	51
3.2	sources of susceptibility in human brain	52
3.3	iron in ferritin and blood	53
3.4	susceptibility in deep gray matter	54
3.5	white matter structure	55
3.6	microstructure in white matter	57
3.7	Susceptibility Tensor Imaging	61
4.1	background removal methods	70

4.2	COSMOS method	71
4.3	regularization method for quantitative susceptibility mapping	73
5.1	Numerical Evaluation of single orientation methods	86
5.2	Quality of analyted contrasts	88
5.3	Performance evaluation on in vivo data	89
5.4	regularization parameter influence on χ maps	90
5.5	additional information influence on χ maps	92
5.6	optimal χ reconstructions for different methods	93
5.7	correlation between single/multiple χ and R_2^*	94
5.8	multiple sclerosis lesion detection	95
5.9	coil combination methodologies comparison	101
6.1	processing pipeline	111
6.2	inter subject	114
6.3	average subject	116
6.4	SVD	117
6.5	Iron and myelin maps	119
6.6	background removal comparison for χ	124
6.7	background removal comparison for cortex	125
7.1	co-registration procedure	134
7.2	data quality	137
7.3	orientation dependance of R_2^*	138
7.4	orientation (in)dependent R_2 and R_2^* maps	138
7.5	fitting quality	139
7.6	specific white matter fibre values	140
7.7	R_2^* map aquired at 7T	143
8.1	susceptibility maps with proposed methods	155
8.2	deep gray matter correlation	156
8.3	white matter fibre values	156

List of Abbreviations

BW	Band Width
COSMOS	Calculation Of Susceptibility through Multiple Orientation Sampling
CSF	CerebroSpinal Fluid
CT	Computed Tomography
DTI	Diffusion Tensor Imaging
FA	Flip Angle
FA	Fractional Anisotropy
FID	Free Induction Decay
FLIRT	FMRIBs Linear Image Registration Tool
FOV	Field Of View
GM	Gray Matter
GRAPPA	Generalized Autocalibrating Partially Parallel Acquisitions
HP	High Pass filtering
ISMRM	International Society of Magnetic Resonance in Medicine
MEDI	Morphology Enabled Dipole Inversion
MD	Mean Diffusivity
MIP	Minimum Intensity Projection
MRI	Magnetic Resonance Imaging
NMR	Nuclear Magnetic Resonance
PDF	Projection onto Dipole Fields
QSM	Quantitative Susceptibility Mapping
RF	Radio Frequency
ROI	Region Of Interest
SNR	Signal-to-Noise Ratio
SWI	Susceptibility Weighted Imaging
TE	Echo Time
TR	Repetition Time
WM	White Matter

Chapter 1

Introduction

From the past to the future: historical background, motivation and thesis outline

1.1 Historical background and MRI in a nutshell

This chapter contains a short summary of the history of the magnetic resonance imaging (MRI) and the inventions which lead to the MRI concept followed by the motivation of this thesis and its outline.

In the beginning of the 20th century the model of the atoms was thought to be a plum pudding model proposed 1904 by Thomson [1]. In this model the atom is composed of negatively charged “raisins” (electrons) surrounded by a positively charged “pudding”, a cloud of positive charge. This model was overturned 1911 by Rutherford’s interpretation of the unexpected result of his well-known experiment of alpha particle scattering on a gold foil [2]. The Rutherford model described the atom as a central positive charge concentrated into a very small volume in the centre containing the majority of the atomic mass, the nucleus, surrounded by orbiting electrons. However, this planetary like model predicts that the electrons emit radiation during their circulation which leads to an unstable atom. Also the resulting continuous frequency contradicts the experimentally shown light emission of atoms at discrete frequencies. In order to overcome these discrepancies Bohr proposed 1913 his model in which the electrons orbit stable without radiation in certain discrete energy levels and are only able to emit or absorb electromagnetic radiation which frequency is determined by the energy difference of the levels [3]. The discrete spectral emission lines of the hydrogen atom which were empirically described by the Rydberg formula, are theoretically explained by the Bohr model including fundamental constants of nature like the electron charge and the Planck constant.

Although the first measurement of the electron spin was performed already 1922 with silver atoms by Stern and Gerlach, their actual intention was to test the quantization of the angular momentum in the Bohr and Sommerfeld hypothesis [4]. Later it turned out, that due to the specific electron distribution of silver only the electron spin contributed to the angular momentum. The electron spin itself was theoretically introduced by Uhlenbeck and Goudsmit [5]. After the discovery of the hyperfine structure of the atomic spectrum of hydrogen Pauli postulated the existence of the nuclear spin 1924 [6] and received the Nobel price in 1945 similar to the previously suggested electron spin. Rabi and colleagues used an extended version of the Stern-Gerlach measurement by applying a varying magnetic field to modify the quantized magnetic moment [7]. The transitions from one quantum state to another were induced using a radio frequency field (RF field) first in 1937 [8], this work was granted the Nobel price in 1944. Independently, Felix

Bloch [9] and Edward M. Purcell [10] found a way to study the magnetic nuclear spin in liquids and solids instead of individual atoms and molecules. They shared 1952 the Nobel price for the discovery of the nuclear magnetic resonance (NMR). With this method the material properties like the chemical structure can be determined, which is the basis for MRI.

The origin of this method is the magnetic spin of the hydrogen atom. The magnetic spin can be described as an angular momentum with a magnetic moment. In a magnetic field this magnetic moment with a given spin quantum number of $1/2$ orients parallel or antiparallel with respect to the applied field. This alignment results in an energy difference of these two states with the parallel orientation being the favourable condition, due to the lower energy state. Because of the favourable energy state more spins are aligned parallel to the field than antiparallel which leads to a formation of a longitudinal nuclear magnetization. A distortion from the parallel alignment leads to a precession of the nuclear magnetization with the so called Larmor frequency. When the longitudinal nuclear magnetization is flipped to the transverse plane it takes time until the excited state relax into the ground state limiting the transversal component of the magnetization, which also decays exponentially. This induces a current to the receiver coil, due to the Faraday-Lenz-Law, this signal is called the free induction decay (FID). The relaxation time was called by Bloch the longitudinal T_1 relaxation time and the transverse magnetization decays with the transversal T_2 relaxation time. The tissue specific relaxation rates were measured in NMR studies on living cells and animal tissues. The discovery of different relaxation times in healthy and cancerous tissues by Damadian offered a good framework for cancer diagnosis [11], although no application to in-vivo measurements was possible at that time. In 1973 Lauterbur suggested to superimpose the static magnetic field with a magnetic gradient field in order to retrieve spatial information [12]. As the above mentioned resonance frequency is a function of the field strength, the gradually varying magnetic field results in the resonance frequency being a function of the location and thus can be used to collect spatial information. This method was applied to measure 1973 the first nuclear spin slice images by Paul C. Lauterbur with a projection reconstruction method similar to the computed tomography (CT) image reconstruction, where the gradients were rotated around the object. This imaging technique, dubbed magnetic resonance zeugmatoraphy [13], moved the single dimension NMR to the second dimension of spatial orientation creating an in-vivo cross-sectional mouse image, the basis of MRI . The back projection was replaced by Ernst in 1975 [14] who was granted the Nobel prize in 1991 for his contribution to NMR spectroscopy. The reconstruction of the final image was performed using the two dimensional Fourier transfor-

mation in a rectangular (cartesian) grid. Mansfield proposed at the same time a method to study the spatial structures in solids [15] and a slice selection technique [16]. 1977 he suggested a special technique, the echo-planar imaging (EPI), [17] for MRI to be reconstructed rapidly, which theoretically would decrease the scanning time from hours down to a fraction of seconds. It took another decade to implement his suggestion due to gradient and computation requirements. He shared the Nobel price in 2003 with Lauterbur for their discoveries concerning the MRI. After this period of basic research for MRI the clinical application developed very fast from the mid 80s with the MRI performance still improving in terms of scanning time as well as its capability up to this days.

1.2 Motivation and Thesis Outline

Magnetic resonance imaging (MRI) has become a workhorse in the medical diagnostics due to the good tissue contrast and the ability to visualize many disease related morphologies. Qualitative contrasts are able to diagnose e.g. vascular malformations (arteriovenous or cerebral cavernous malformations), strokes (ischemic and haemorrhagic) and tumors (active and necrotic), but the reproducibility of these contrasts is not provided. Quantitative contrasts are independent on the facility as they depend on the underlying structures which are the origin to these contrasts. However, the specific effect of the structures to the contrasts are the topic of various research studies.

The R_1 contrast measures the longitudinal relaxation rate and has been shown to directly correlate with the myelin content, yet also the impact of the iron content should not be neglected. The apparent relaxation rate R_2^* has a linear relationship with the iron content in deep gray matter, but is also increased by the myelin content when white matter is studied. This increase of R_2^* is caused by para- or diamagnetic inclusions (like iron and myelin), which lead to a dephasing of the protons close to the perturbers. Quantitative susceptibility mapping (QSM) measures the magnetic susceptibility of the inclusions and therefore paramagnetic and diamagnetic entities (iron and myelin) have opposing effects, enabling to disentangle the origin of the dephasing. Susceptibility is a magnetic property which reflects the interaction between the source and magnetic field and induces an additional local magnetic field with a long range spatially varying dipole distribution. The reconstruction of QSM from the measured MRI data is therefore not trivial and some processing steps are need to be done. In a first step, the small magnetic field produced by the sources needs to be disentangled from the orders of magnitude bigger background field. This large field is caused by imperfect shimming as well as the surrounding air-tissue interfaces. In order to preserve the relevant information as much of as possible while obtaining reliable values, an appropriate background removal method is needed, especially when studying the human cortex.

After the background removal the actual susceptibility can be reconstructed. However, the magnetic field produced by the susceptibility does not fundamentally describe the underlying source. The field depends not only on the shape and the orientation, but also on the anisotropy of susceptibility and the microstructural compartmentalization of the biological source. Therefore methods to reconstruct the susceptibility from the measured field are needed that are applicable in the everyday clinical diagnosis and are capable to calculate accurate values for different brain regions.

The first two chapters of this thesis provide a short overview of the basics of

MRI and quantitative susceptibility mapping. The following chapters present work produced in this thesis:

1. **Step by step processing pipeline for multi-channel multi-echo acquisition**

Chapter 3 presents a short description of the different steps needed to be taken in order to obtain quantitative susceptibility maps when multi-channel, multi-echo data is acquired; i) coil combination and phase unwrapping of 2π phase aliasing, ii) background removal to disentangle the desired susceptibility effect from other phase variations based on e.g. imperfect shimming of external field or air-tissue boundary susceptibility effects, iii) quantitative susceptibility reconstruction methods to solve the ill-posed problem.

2. **Modulated closed form solution (MCF), comparison of different QSM methods and R_2^***

Chapter 4 proposes a new method to calculate QSM and performs a thorough comparison of the newly presented method with three state-of-the-art QSM techniques: over-determined multiple orientation method (COSMOS) and two single orientation minimization methodologies based on the l_2 and l_1 TV norm of prior knowledge. For all four QSM methods the relevant parameters were evaluated to determine the optimal reconstruction in dependence of the relevant regularization and prior-knowledge parameters which were systematically changed. Additionally, R_2^* maps obtained from the same gradient recalled echo (GRE) dataset were compared to the QSM contrast.

3. **Quantitative mapping in the human cortex**

Chapter 5 deals with the ability of three quantitative contrasts to study cyto- and myelo-architecture of the human cortex; i) longitudinal relaxation rate (R_1), ii) apparent transverse relaxation rate (R_2^*), iii) quantitative susceptibility mapping (QSM). The different quantitative methods were compared based on their contrast of the main primary Brodmann regions and remaining cortex. Furthermore, the transition from the inner to the outer layers (white matter to cerebrospinal fluid), which varies its cyto- and myelo-architecture, was evaluated. As in the process of susceptibility mapping the background removal traditionally removes the cortex, various methods were systematically compared in order to preserve cortical regions close to the brain surface.

4. **(An)isotropy of white matter for relaxation rates: R_2 and R_2^***

Chapter 6 presents the combination of two methodologies: diffusion tensor imaging (DTI) and quantitative contrasts (R_2^* and R_2). Hereby the fibre orientation information retrieved from the DTI acquisition was used as prior information for the fitting problem of R_2^* and R_2 . The different retrieved myelin related parameters were evaluated throughout the brain with a particular focus on major white matter fibre bundles.

5. Introduction of Lorentzian correction in the white matter for QSM

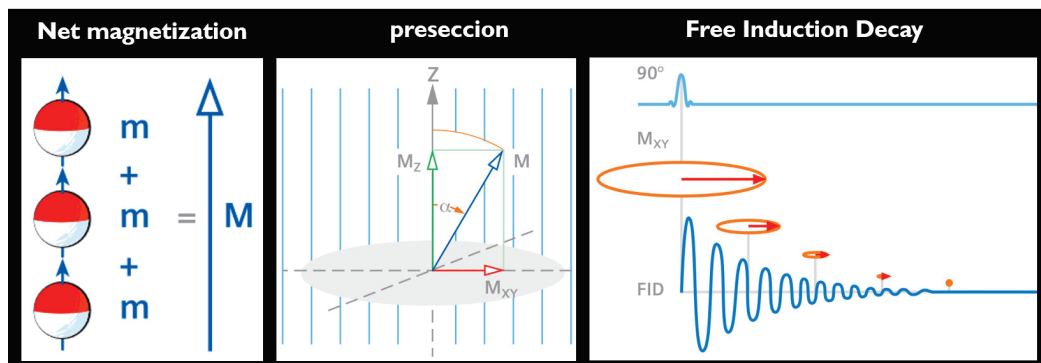
Chapter 7 proposes a new QSM method, which implements the Lorentzian correction in a COSMOS like reconstruction. The white matter fibre orientation was retrieved from DTI acquisition and the effect of implementation of only the primary and additionally the secondary diffusion orientation was evaluated. The Lorentzian correction impact on the susceptibility maps was analyzed in the deep gray matter as well as main white matter fibres.

The final conclusion chapter summarises the obtained results during the thesis and presents future directions.

Chapter 2

Basics of MRI

The basics of MRI: from quantum mechanics to image reconstruction



2.1 Magnetic Resonance Physics

The spin is a quantum mechanical property which has no classical (macroscopic) analogy. Generally, atomic nuclei with an odd number of nucleons have a spin. When an external magnetic field is applied the spins will orient parallel to the magnetic field producing a net magnetization (2.1.2) and precess with the Larmor frequency (2.1.1). Considered classically, it can be compared to an object rotating around its own axis, \underline{r} , like a spinning top, which precesses once it's tilted, 2.1b. Because every system tends to be in its minimum energy state, the net magnetization will relax with a given relaxation rate to its equilibrium state along the magnetic field (2.1.3). The time dependent behaviour of the net magnetization is characterized by the Bloch equations (2.1.4).

2.1.1 Nuclear spin in an applied magnetic field

Generally, the total angular momentum I of a charged particle is proportional to its magnetic moment, μ

$$\mu = \gamma \cdot I \quad (2.1.1)$$

where the proportional factor γ is described by the gyromagnetic ratio:

$$\gamma = g \cdot \mu_N / \hbar \quad (2.1.2)$$

with g being the g-factor and $\mu_N (= e\hbar/2m_p)$ the so called nuclear magneton. The latter is the natural unit for expressing magnetic dipole moments of Dirac particles (heavy particles such as nucleons and atomic nuclei), with m_p being proton rest mass, e the elementary electron charge and \hbar the reduced Planck constant.

The g-Factor or Landé-Factor of an atom, nucleus or a fundamental particle describes the ratio between the measured magnetic moment and the expected theoretical magnetic moment taking into account the angular momentum from the classical physics. As the measured magnetic moment depends on the total angular momentum, I which consists of the orbital angular momentum L and the spin angular momentum S , the g-factor depends on the particle. When only the orbital angular momentum is involved in the total angular momentum the resulting angular momentum of the measured and classical physics is the same and the g-factor $g = g_l = 1$. The total angular moment of the spin angular momentum has characteristic values for each particle, e.g. electron $g_e \approx -2$, proton $g_p \approx 5.6$, neutron $g_n \approx -3.8$ [18]. When the total angular momentum of the system consists of both the orbital and spin angular momentum, the g-factor is a combination of g_l and g_s using the

Landé-equation. By placing a particle with a magnetic moment in a magnetic field the resulting effect is described by the Hamiltonian and is given by:

$$H = -\mu B = -\gamma I B, \quad (2.1.3)$$

and in the case of the magnetic field being in the z-direction ($\vec{B} = B\hat{e}_z$):

$$H = -\gamma I_z B_z. \quad (2.1.4)$$

As the system is usually non-static, the time-dependent probability of the eigenstates is of great interest. The time evolution operator is

$$\hat{U} = e^{(-i/\hbar\hat{H}t)} = e^{-i/\hbar\alpha I_z} \quad (2.1.5)$$

with the time dependent angle

$$\alpha = -\gamma B_z t = \omega_L t,$$

with ω_L is the Larmor frequency given by

$$\omega_L = -\gamma B_z. \quad (2.1.6)$$

Magnetic resonance imaging is based mainly on hydrogen nuclei (charged protons) of water molecules. Therefore the total angular momentum is reduced to the proton spin $I_z = S_z$ and the g-Factor is $g = g_s \approx 5.6$. Moreover, the important ratio between the magnetic field and the Larmor frequency reduces to the value:

$$\gamma = g_s e / 2m_p \approx 267.513 \cdot 10^6 [s^{-1}T^{-1}] \quad (2.1.7)$$

or, more practically $42MHzT^{-1}$. The dynamic of such magnetic moments in external magnetic fields can be described using quantum mechanics. The starting state can be assumed as a linear combination of two spin states; spin-up and spin-down, at start time $t=0$

$$|\psi(t=0)\rangle = \frac{1}{\sqrt{2}} \left(\begin{pmatrix} 1 \\ 0 \end{pmatrix} + \begin{pmatrix} 0 \\ 1 \end{pmatrix} \right) = \frac{1}{\sqrt{2}} \begin{pmatrix} 1 \\ 1 \end{pmatrix}, \quad (2.1.8)$$

the time dependent behaviour is expressed with the time evolution operator

$$\hat{U} = e^{(-i/\hbar\alpha I_z)} I_z = \pm \hbar/2 e^{(-i/2\omega_L t)}, \quad (2.1.9)$$

Applying the spin operator

$$S_{x,y,z} = \hbar/2\sigma_{x,y,z}$$

with $\sigma_{x,y,z}$ being the Pauli-Spin matrices the time dependant expectation value becomes

$$\begin{aligned}
\langle S_x(t) \rangle &= \langle \psi(0) | \hat{U}^\dagger S_x \hat{U} | \psi(0) \rangle \\
&= \frac{\hbar}{2} \cdot \frac{1}{2} \left(e^{+i1/2\omega_L t} e^{-i1/2\omega_L t} \right) \begin{pmatrix} 0 & 1 \\ 1 & 0 \end{pmatrix} \begin{pmatrix} e^{+i1/2\omega_L t} \\ e^{-i1/2\omega_L t} \end{pmatrix} \\
&= \frac{\hbar}{2} \cdot \frac{1}{2} \left(e^{+i\omega_L t} + e^{-i\omega_L t} \right) \\
&= \frac{\hbar}{2} \cdot \cos \omega_L t
\end{aligned} \tag{2.1.10}$$

$$\begin{aligned}
\langle S_y(t) \rangle &= \langle \psi(0) | \hat{U}^\dagger S_y \hat{U} | \psi(0) \rangle \\
&= \frac{\hbar}{2} \cdot \frac{1}{2} \left(e^{+i1/2\omega_L t} e^{-i1/2\omega_L t} \right) \begin{pmatrix} 0 & -i \\ i & 0 \end{pmatrix} \begin{pmatrix} e^{+i1/2\omega_L t} \\ e^{-i1/2\omega_L t} \end{pmatrix} \\
&= \frac{\hbar}{2} \cdot \frac{1}{2} i \left(-e^{+i\omega_L t} + e^{-i\omega_L t} \right) \\
&= \frac{\hbar}{2} \cdot \sin \omega_L t
\end{aligned} \tag{2.1.11}$$

$$\begin{aligned}
\langle S_z(t) \rangle &= \langle \psi(0) | \hat{U}^\dagger S_z \hat{U} | \psi(0) \rangle \\
&= \frac{\hbar}{2} \cdot \frac{1}{2} \left(e^{+i1/2\omega_L t} e^{-i1/2\omega_L t} \right) \begin{pmatrix} 1 & 0 \\ 0 & -1 \end{pmatrix} \begin{pmatrix} e^{+i1/2\omega_L t} \\ e^{-i1/2\omega_L t} \end{pmatrix} \\
&= \frac{\hbar}{2} \cdot \frac{1}{2} \left(e^{+i\omega_L t} - e^{-i\omega_L t} \right) \\
&= 0
\end{aligned} \tag{2.1.12}$$

The expectation value of the starting state can be interpreted as a vector rotating in the x-y plane at the Larmor frequency ω_L , see figure 2.1a.

2.1.2 Spin statistics

In the quantum mechanics formalism for a particle with the spin 1/2 only two different energy states exist in the presence of an external magnetic field B . The spins are oriented parallel or antiparallel to the field leading to two different energy levels

$$E_{\pm} = \pm \frac{1}{2} \hbar \omega_L. \tag{2.1.13}$$

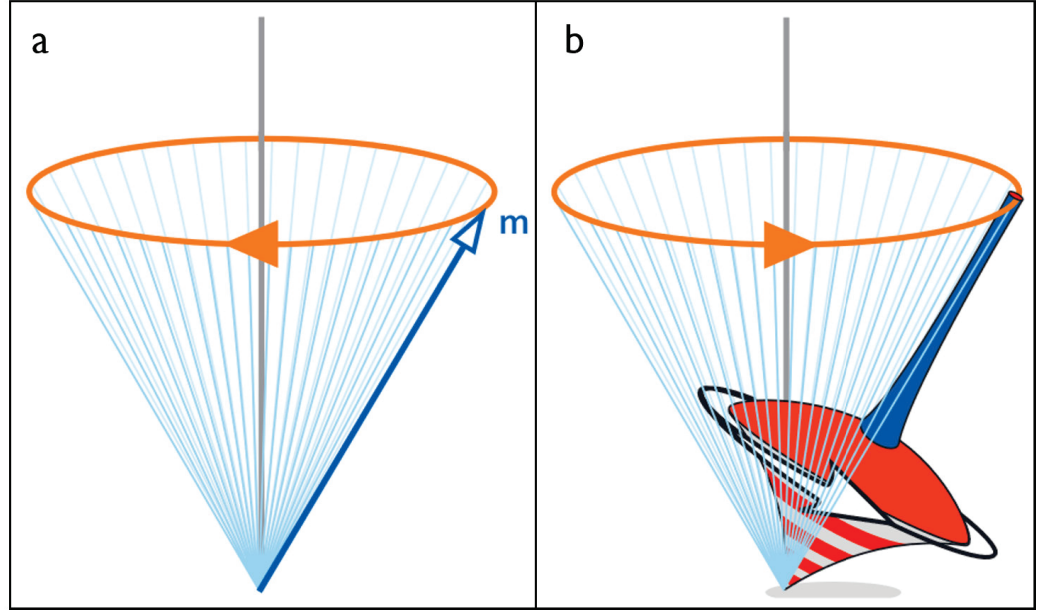


Figure 2.1: a) precession of magnetic spin in presence of an applied magnetic field, b) mechanical analogon of tilted spinning top in presence of gravity, [19].

The probability p for such an energy level can be described by the Boltzmann equation:

$$p_{\pm} \sim e^{-\beta E_{\pm}}. \quad (2.1.14)$$

Assuming the temperature being the normal room temperature and the magnetic field strength being few Tesla we notice that the thermal influence is much bigger than the magnetic energy difference $\beta^{-1} = k_B T \gg E$, with k_B being the Boltzmann constant. Therefore the Boltzmann factor can be assumed as $p_{\pm} (1 - \beta E_{\pm})$. The calculation of the net magnetization, the difference between the spins oriented along and opposite to the magnetic field direction is given by:

$$\begin{aligned} \frac{p_- - p_+}{p_- + p_+} &= \frac{(1 + \beta E) - (1 - \beta E)}{(1 + \beta E) + (1 - \beta E)} \\ &= \beta E = \frac{\hbar g \mu_B}{2 k_B T} B \\ &\approx 6.6 \cdot 10^{-6} B \end{aligned} \quad (2.1.15)$$

It means that by applying an external magnetic field of 1 Tesla, among the 1 million spins the two energy levels are almost equally distributed and only 7 spins out of this million are unpaired. These spins are in the lower energy state and are the origin of the net magnetization, see figure 2.2. This is

the reason for the low signal to noise ratio (SNR) of MRI. Moreover, the net magnetization is proportional to the applied magnetic field and anti-proportional to the temperature. This suggests some methods to improve the signal like: to apply higher magnetic fields (known as Ultra High fields) or to use lower temperature.

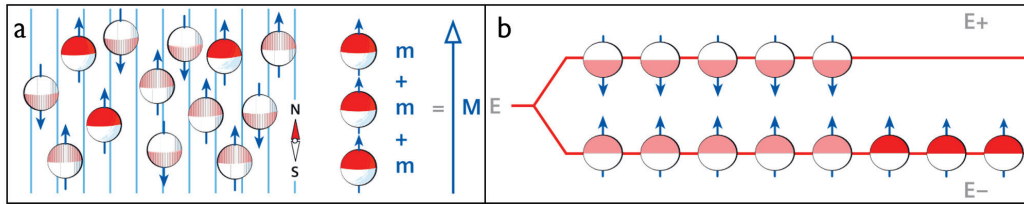


Figure 2.2: a) bulk magnetization in the presence of an applied magnetic field and resulting net magnetization, b) 2 energy states for spin 1/2 system, [19].

2.1.3 Relaxation times

The relaxation times describe the return to equilibrium of the net magnetization in the presence of a strong magnetic field.

The protons within a tissue are in constant translational, vibrational and rotational motion. Therefore, many interaction possibilities are available between a spin and its surrounding e.g. either through direct interaction, Raman or Orbach processes. When the spin population interacts with the surrounding, it releases the energy obtained from the RF pulse and relaxes to the equilibrium. This process is called spin-lattice relaxation because of its origin in the solid state physics and is described with the longitudinal time T_1 or longitudinal rate $R_1 (= 1/T_1)$. It means T_1 characterizes the rate at which the longitudinal magnetization vector M_z of the spins recovers exponentially towards the equilibrium. In dense tissues the complex lattice consists of more contributors, offering more interaction partners and therefore leading to a fast recovering of the longitudinal component M_z of the magnetization. Because of this relationship, denser tissues, like fat, have a shorter T_1 compared to the cerebrospinal fluid (CSF) that has longer T_1 , see figure 2.3a.

Another effect is the so called transversal relaxation. In this process no energy is transferred, it is an entropic process. Instead, its origin lies in the interaction between the spins themselves. Every spin can be seen as a small magnet which creates a small magnetic field. When taking into account all spins they generate fluctuation fields which are interacting with a certain single spin. Therefore some of the spins speed up due to higher local field

strength and some slow down due to lower local field strength. Because of this fluctuation the phase of the translational component $M_{x,y}$ of the rotating spins varies and the spins dephase. This process is called spin-spin relaxation and is described by the transversal relaxation time T_2 or transversal rate $R_2 (= 1/T_2)$, see figure 2.3b.

Besides the spin-spin interaction from the same particles, an additional ef-

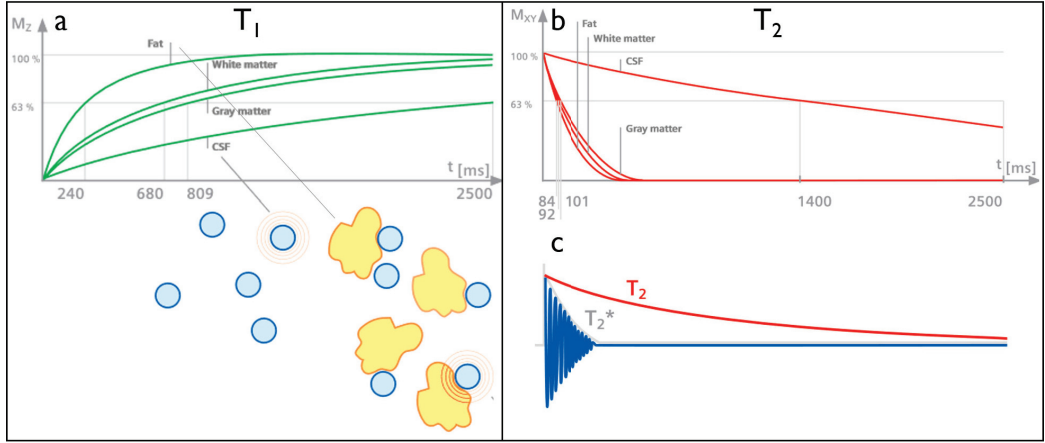


Figure 2.3: relaxation of different brain tissues over time for a) longitudinal relaxation T_1 and b) transversal relaxation T_2 , c) shortening of T_2 leads to apparent transversal relaxation T_2^* due to inhomogeneous fields, [19].

fect which leads to the dephasing is caused by any inhomogeneous field δB . This inhomogeneity can be created by the non-perfect external magnetic field as by the substances with different magnetic susceptibility. This additional process leads to a faster decay of the transversal magnetization and is referred to by T_2' . The final dephasing consists of the dephasing caused by spin-spin interaction and the additional field inhomogeneities. The final transversal relaxation time is therefore called the apparent transversal relaxation time, which is shorter, see figure 2.3c and is denoted as:

$$\begin{aligned} \frac{1}{T_2^*} &= \frac{1}{T_2} + \delta B \\ &= \frac{1}{T_2} + \frac{1}{T_2'} \end{aligned} \quad (2.1.16)$$

Its notation as apparent transversal relaxation rate is given by

$$R_2^* = R_2 + R_2'$$

The presence of many interaction partners as in dense tissues leads to a faster dephasing compared to tissues with lower molecular density. Therefore fluids

have the longest transversal relaxation time while tissues with paramagnetic impurities have a much faster decay.

2.1.4 Bloch equations

The magnetization M of a system is composed of the sum of all magnetic moments of each component μ_n of the system

$$M = \sum_n \mu_n.$$

The equilibrium magnetization is parallel to the magnetic field in z-direction and can be written as

$$M = \begin{pmatrix} 0 \\ 0 \\ M_0 \end{pmatrix}. \quad (2.1.17)$$

A magnetization vector which is not in its equilibrium will relax in order to return to equilibrium. These relaxations can be termed using a common approach with differential equations as:

$$\frac{d}{dt}M_z = \frac{M_0 - M_z}{T_1} \quad (2.1.18)$$

$$\frac{d}{dt}M_{x,y} = \frac{M_{x,y}}{T_2} \quad (2.1.19)$$

The equation 2.1.18 describes the relaxation of the whole system, the “spin-lattice” or “longitudinal” relaxation where T_1 refers to the mean time for the spin ensemble to return to 63% of the steady state. The equation 2.1.19 describes the “spin-spin” or “transversal” relaxation where T_2 refers to the mean time for the transverse magnetization to be attenuated by 63%. The relaxation rates depend on the tissue and are thoroughly discussed in subsection 2.1.3.

An applied external field, B , leads to a torque moment, T , acting on the magnetization

$$T = M \times B,$$

which interlinks with a change of the total angular momentum I :

$$T = \frac{d}{dt}I$$

The magnetic moment itself also depends on the total angular momentum

$$M = \sum \mu_n = \gamma \sum I_n = \gamma I,$$

which leads to the resulting equation

$$\frac{d}{dt}M = \gamma(M \times B) = \omega \times M$$

of a rotation of the magnetization with the angular speed $\omega = -\gamma B$. This is the same result as the microscopic quantum mechanical expectation value. Taking into account rotation as well as the relaxation rates the differential equations for the magnetization become:

$$\begin{aligned} \frac{d}{dt}M_z &= \gamma(M \times B)_z + \frac{M_0 - M_z}{T_1} \\ \frac{d}{dt}M_{x,y} &= \gamma(M \times B)_{x,y} - \frac{M_{x,y}}{T_2} \end{aligned} \quad (2.1.20)$$

In the case of a circular polarized radiofrequency (RF) field in the xy-plane with frequency ω_L and amplitude B_1 is applied for the excitation with the resulting magnetic field being

$$B(t) = \begin{pmatrix} B_1 \cos(\omega_L t) \\ B_1 \sin(\omega_L t) \\ B_0 \end{pmatrix}. \quad (2.1.21)$$

In order to simplify the equations a transformation to a rotating frame can be done.

For the transformation of a general vector V into a rotating frame with the angular speed ω_{rot} circulating around the origin the following expression is used:

$$\left(\frac{d}{dt}V\right)_{rot} = \left(\frac{d}{dt}V\right)_{stable} - (\omega_{rot} \times V).$$

The new rotating coordinate system has hence the same frequency as the RF pulse:

$$\omega = \begin{pmatrix} 0 \\ 0 \\ \omega_L \end{pmatrix} \quad (2.1.22)$$

The Bloch-equation in the rotating frame denoted with \tilde{V} , with

$$\omega_{L,0} = -\gamma B_0, \omega_{L,l} = -\gamma B_l (\neq \omega_l)$$

can be written as

$$\begin{aligned}
\frac{d}{dt}\tilde{M}_x &= (\omega_l - \omega_{L,0})\tilde{M}_y - \frac{\tilde{M}_x}{T_2} \\
\frac{d}{dt}\tilde{M}_y &= -(\omega_l - \omega_{L,0})\tilde{M}_x - \omega_{L,1}M_z - \frac{\tilde{M}_y}{T_2} \\
\frac{d}{dt}\tilde{M}_z &= \omega_{L,1}\tilde{M}_y + \frac{\tilde{M}_0 - \tilde{M}_z}{T_1}
\end{aligned} \tag{2.1.23}$$

The natural rotating frame frequency is the same as the precessional frequency or Larmor frequency $\omega_l = \omega_{L,0}$ and the equation system simplifies to

$$\begin{aligned}
\frac{d}{dt}\tilde{M}_x &= \frac{\tilde{M}_x}{T_2} \\
\frac{d}{dt}\tilde{M}_y &= -\omega_{L,1}M_z - \frac{\tilde{M}_y}{T_2} \\
\frac{d}{dt}\tilde{M}_z &= \omega_{L,1}\tilde{M}_y + \frac{\tilde{M}_0 - \tilde{M}_z}{T_1}
\end{aligned} \tag{2.1.24}$$

When the amplitude of the applied pulse is much bigger than the relaxation $\omega_{L,1} \gg 1/T_1$ and $\omega_{L,1} \gg 1/T_2$ the influence of the relaxation towards the steady state can be neglected and the Bloch equation can be further simplified to

$$\frac{d}{dt}\tilde{M}_x = 0 \tag{2.1.25}$$

$$\frac{d}{dt}\tilde{M}_y = -\omega_{L,1}M_z$$

$$\frac{d}{dt}\tilde{M}_z = \omega_{L,1}\tilde{M}_y \tag{2.1.26}$$

These Bloch equation can be interpreted as a rotation around the x-axis in the rotating frame. In the non-rotating frame the magnetization vector is tilted away from the z-axis towards the xy-plane during its precession.

By regulating the amplitude and the duration of the applied RF-pulse, the final magnetization vector can be adjusted. The angle between the original steady state magnetization and the final flipped magnetization, is called flip angle α , see figure 2.4a. Two specific cases are the application of 90° pulse flipping the magnetization to the xy-plane and 180° causing the magnetization vector to be in the -z-axis as shown in figure 2.4b.

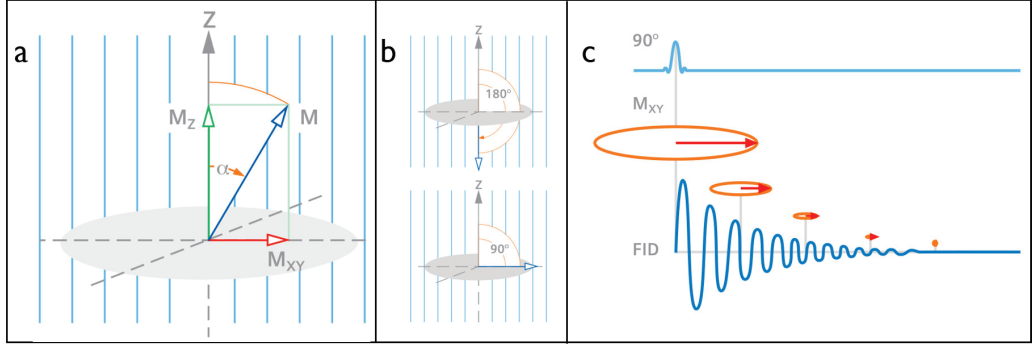


Figure 2.4: a) flipping movement of magnetization vector in case of applied RF-pulse, where M_z is the projection to z-axis, longitudinal magnetization, M_{xy} is the projection to xy-plane, transversal magnetization and α is the flip angle, b) resulting flipping of the magnetization vector for two RF-pulses $\alpha = 180^\circ$ and $\alpha = 90^\circ$, c) generation of free induction decay (FID) signal, [19].

After the application of the 90° RF-pulse, the magnetization is flipped to the xy-plane. At the end of the RF-pulse ($\omega_{L,l} = 0$), the magnetization driven by the relaxation rates can be written as:

$$\begin{aligned} \frac{d}{dt} \tilde{M}_x &= \frac{\tilde{M}_x}{T_2} \\ \frac{d}{dt} \tilde{M}_y &= \frac{\tilde{M}_y}{T_2} \\ \frac{d}{dt} \tilde{M}_z &= \frac{\tilde{M}_0 - \tilde{M}_z}{T_1} \end{aligned} \quad (2.1.27)$$

This leads to the very simple solution in the rotating frame of the differential equation being the exponential decay.

$$\begin{aligned} \tilde{M}_x(t) &= M_x(0) \cdot e^{\frac{-t}{T_2}} \\ \tilde{M}_y(t) &= M_y(0) \cdot e^{\frac{-t}{T_2}} \\ \tilde{M}_z(t) &= M_z(0) \cdot e^{\frac{-t}{T_1}} + (1 - M_0) \cdot e^{\frac{-t}{T_1}} \end{aligned} \quad (2.1.28)$$

This leads to the generation of the FID signal. The transverse magnetization can be measured with the receiver coil via Faraday induction. Because of the spin-spin interactions this signal decays dependant of the T_2 time of the measured object, as shown in figure 2.4. To take into account the additional dephasing caused by field inhomogeneities, the T_2 relaxation time needs to be substituted and the FID decays with the T_2^* relaxation time.

2.2 Image generation

After having presented the fundamental basics of MRI this section will focus on what is needed to create a MR image. In order to achieve a MR signal an external homogeneous magnetic field is applied (subsection 2.2.1). The magnetization is brought to the x-y plane by application of a rotating field emitted by a RF coil. The precessing magnetization in this plane induce a voltage difference in the RF coil which is used for signal detection. In order to retrieve the spatial distribution of this signal gradient fields are used (subsection 2.2.2). Finally the measured information needs to be transformed to the spatial domain to create an anatomical image subsection (2.2.3). Hereby a short overview of the used Fourier Transform is given in subsection 2.2.4.

2.2.1 Magnetic field and shimming

The main properties of a magnetic field are described by the Maxwell equations. As there are no single magnetic field sources, the following equation is valid:

$$\nabla B = 0$$

In the absence of a static magnetic field, which means no current floss exists and no magnetic eddy currents are available, the second Maxwell equation becomes:

$$\nabla \times B = 0.$$

The application of $(\nabla \times)$ to the equation $\nabla \times (\nabla \times B) = \nabla(\nabla B) - (\nabla \nabla)B$ and taking into account $\nabla \nabla = \Delta$ results in the Laplacian differential equation

$$\Delta B = 0.$$

The direction of the static main magnetic field in MR imaging is usually defined to be along the z-axis. Thus, the Laplacian can be simplified to

$$\Delta B_z = 0.$$

Functions which solve the Laplacian equations are called harmonic and can be written as spherical functions that are by themselves solutions of the laplacian equation. To solve this equation usually spherical coordinates (r, φ, θ) are used instead of the Cartesian coordinates (x, y, z) . The spherical coordinate r is the radial distance to the origin, ϕ the azimuthal angle and θ the polar angle. While using the spherical coordinates the Laplacian equation becomes:

$$\Delta B_z = \frac{1}{r^2} \frac{\partial}{\partial r} \left(r^2 \frac{\partial B_z}{\partial r} \right) + \frac{1}{r^2 \sin(\theta)} \frac{\partial}{\partial \theta} \left(\sin^2(\theta) \frac{\partial B_z}{\partial \theta} \right) + \frac{1}{r^2 \sin^2(\theta)} \frac{\partial^2 B_z}{\partial \phi^2} \quad (2.2.1)$$

To find the spherical functions, the variables separation method is used first to untangle the radial from the angular dependencies and then to separate the polar from the azimuthal. Taking into account boundary conditions and changing some variables leads to the Legendre equation, whose solution are the multiples of the Legendre Polynomials $P_l^m(\cos(\theta))$. Therefore, the solution of the Laplacian equation is the description of B_z as a linear combination of spherical harmonic functions as follows:

$$B_z = \sum_{l=0}^{\infty} \sum_{m=0}^l P_l^m(\cos(\vartheta)) \cdot r^l \cdot (a_{l,m} \cos(m\varphi) + b_{l,m} \sin(m\varphi)) \quad (2.2.2)$$

For each value of l there are $2l + 1$ sums and P_l^m are the associated legendre polynomials which can be expressed as

$$P_l^m(z) = \frac{(z^2 - 1)^m / 2d^{l+m}}{2^l l} \frac{d^l(l + m)}{z dl + m} (z^2 - 1)^l. \quad (2.2.3)$$

Similar to other concepts of representing a function as an infinite sum, like the Taylor series, the most important terms are the very first ones and its expression and interpretation can be written as:

l	m	P_l^m	term	interpretation
0	0	$P_0^0(\cos(\vartheta)) = 1$	$a_{0,0}$	= const = B_0
1	0	$P_1^0(\cos(\vartheta)) = \cos(\vartheta)$	$a_{1,0}r \cos(\vartheta)$	= $a_{1,0}z$
1	1	$P_1^1(\cos(\vartheta)) = \sin(\vartheta)$	$a_{1,1}r \sin(\vartheta) \cos(\varphi) +$ $b_{1,1}r \sin(\vartheta) \sin(\varphi)$	= $a_{1,1}x + b_{1,1}y$

The constant term describes the constant main magnetic field, the first order terms ($l = 1$) represent the linear gradients and the coefficients $a_{1,0}$, $a_{1,1}$ and $b_{1,1}$ of the gradients z-gradient, x-gradient and y-gradient, respectively. This concept of decomposing a function into a subset of known functions is used for shimming, to produce a homogeneous magnetic field in a certain volume. This volume is a theoretical sphere in the centre of the magnetic field, the isocenter inside the MR scanner. The diameter of this sphere denotes the theoretical maximal distortion free field of view (FOV) for the image acquisition. As the Laplacian equation forbids extrema (minima and/or maxima) inside the sphere, the main deviations from homogeneity occur on the edge of the sphere. The magnetic field on the surface of this sphere can be measured and deviations from the harmonic behaviour can be corrected by usage of active shimming coils. These produce field corrections, for several first order terms of the spherical harmonics, which replicate the inhomogeneities with the opposite effect and thus compensate the inhomogeneities. However, once

an object is placed inside the MR scanner the main magnetic field is distorted by the objects susceptibility effects. For humans the distortion caused by the susceptibility is particularly noticeable at air-tissue boundaries like the sinuses as the oxygen in the air is paramagnetic. This leads to image artefacts especially in the frontal lobe. By shimming, currents in the shim coils are adjusted such that the homogeneity is restored.

2.2.2 Gradients

The spatial encoding of the object is achieved by the use of so called magnetic gradient fields in the z-direction. The main magnetic field is highly homogeneous along the z-direction and weak on x and y. Therefore the field along z-direction is reported as B_z and the gradient field is meant as gradient of the scalar field

$$B_z = \left(\frac{\partial B_z}{\partial x} \frac{\partial B_z}{\partial y} \frac{\partial B_z}{\partial z} \right) = (G_x G_y G_z). \quad (2.2.4)$$

The MR-scanner contains gradient coils with which such modifications of the main magnetic field can be created. To create a gradient along each cartesian direction a separate gradient coils exist. The main property of such generated field changes is its linearity. With the homogeneous main magnetic field B_0 and its linear change the resulting magnetic field, as in figure 2.5 can be described as

$$B = B_0 + G \cdot r$$

Therefore, by combination of the three gradient coils a field gradient along any direction can be generated. 2.5.

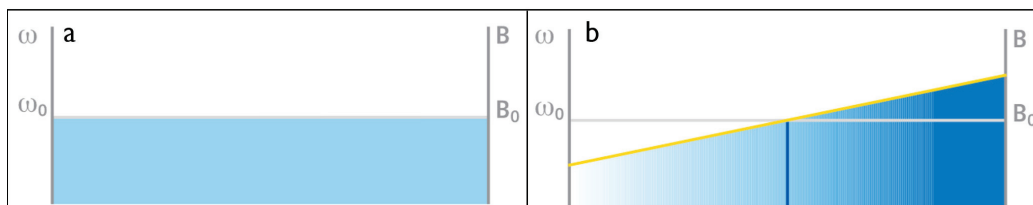


Figure 2.5: magnetic field and the resulting Larmor frequency when a) no and b) an gradient field is applied, [19].

The gradient field is physically not possible, as the Maxwell equation forbids a non-zero gradient of the magnetic field. Therefore, such gradient coils produce also other magnetic field components as required by the Maxwell

equation

$$\nabla B = \frac{\partial}{\partial x} B_x + \frac{\partial}{\partial y} B_y + \frac{\partial}{\partial z} B_z = 0$$

therefore

$$\frac{\partial}{\partial z} B_z \neq 0 \Rightarrow \frac{\partial}{\partial x} B_x + \frac{\partial}{\partial y} B_y \neq 0$$

Which means a non-zero component of z-Gradient leads to non-zero x- and y-Gradients. The difference to the strong main magnetic field B_0 is therefore as follows:

$$\delta B = B_{new} - B_0 = \sqrt{B_{x,y}^2 + B_0^2} - B_0$$

Because B_0 (\sim T) is much bigger than $B_{x,y}$ (\sim mT) the relative change of the B_z component approximates to

$$\frac{\delta B}{B_0} = \frac{1}{B_0} (\sqrt{B_{x,y}^2 + B_0^2} - B_0) \approx \frac{B_{x,y}^2}{2B_0^2}.$$

The field distortions from the x- and y-Gradient are therefore negligible.

2.2.3 Image encoding

2.2.3.1 Slice selection

The main magnetic field leads to a precession of the spins around the z-axis with a certain frequency ω . When an additional field gradient along z-direction G_z is added to the main magnetic field B_0 , the precession frequency depends on the localization of the spins within the MR scanner. When a radio frequency is applied, only the spins which have a Larmor frequency (produced by this magnetic field) that matches the radio frequency, are excited. Thus a specific xy-plane is excited whose plane thickness depends on the bandwidth of the excitation pulse and the strength of the gradient field, see figure 2.6a. The relationship between the excitation slice thickness Δz , the gradient field G_z and the bandwidth of the excitation pulse leads to:

$$\omega = -\gamma \cdot B = -\gamma \cdot (B_0 + G_z \Delta z)$$

And thus to

$$\Rightarrow \Delta\omega = -\gamma \cdot G_z \cdot \Delta z.$$

For thinner slice profiles steeper gradient fields are needed, as shown in figure 2.6b. The slice profile should be as sharp as possible to avoid signal from the surrounding spins of other slices. Hence, the frequency spectrum of the excitation pulse should have rectangle function characteristics as it can be achieved by the sinc-function, $\text{sinc}(x) = \frac{\sin(x)}{x}$. The slice selection reduces the image encoding problem to a two dimensional problem.

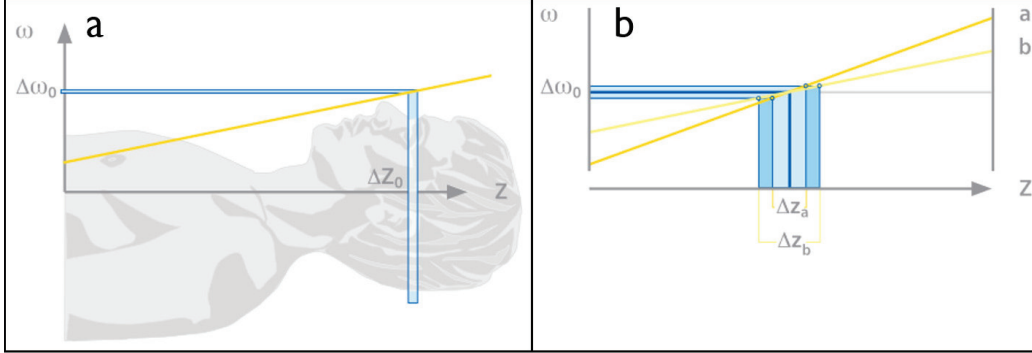


Figure 2.6: a) slice selection with thickness Δz_0 using frequency $\Delta\omega_0$ in the xy plane, b) steeper gradient field **a** produces thinner slice Δz_a compared to gradient **b**, [19].

2.2.3.2 Frequency and phase encoding

The slice selection was achieved by the application of a gradient field in the z -direction and an excitation pulse with a slice specific frequency. The resulting signal from the selected slice now needs to be further spatially encoded to get a three dimensional image.

This is achieved by using the effect of the gradient fields along the other directions G_y and G_x on the phase of the slice selected spins. The resonance frequency ω inside a magnetic field with the presence of a gradient field is

$$\omega = -\gamma \cdot B = -\gamma(B_0 + \vec{G} \cdot \vec{r})\Delta\omega = -\vec{G} \cdot \vec{r}, \quad (2.2.5)$$

with $\Delta\omega$ being the spatially dependent Larmor frequency. The application of a gradient during a certain time T leads to a phase difference $\Delta\Phi$ of the spin orientation which depends on its localization.

$$\Delta\Phi = \Delta\omega T = -\gamma G r T.$$

The resulting emitted signal is now further encoded by the phase difference of the spins of the excited x-y plane. This phase encoding depends on the localization of the spins in respect to the gradient field strength at a certain line along the selected plane. Therefore, this phase difference leads to a spatially dependent complex phase factor

$$e^{-i\gamma G r T}$$

The explicit application of the gradients is explained for several contrasts in section 2.3.

When detecting with a RF coil the spatially dependent signal density with its phase factors is integrated over the excited slice A :

$$S = \int_A dx dy \sigma(x, y) \cdot e^{-i\gamma G_x x T_x + G_y y T_y}.$$

Defining $k_x = \gamma G_x T_x$ and $k_y = \gamma G_y T_y$ the equations simplifies to

$$S = \int dx dy \sigma(x, y) \cdot e^{-ik_x x + k_y y} = S(k_x, k_y)$$

This describes the Fourier transformation of the function $\sigma(x, y)$ itself. It means for each slice the k-space needs to be sampled at all k_x and k_y coordinates and by applying a Fourier transformation the final MR image can be retrieved.

2.2.4 Fourier Transform

The Fourier Transform is not unique to MRI, however this mathematical formulation is essential for the understanding of MR and its artefacts. The formal connection between the measured spatially dependent signal density and the Fourier Transformation is crucial. The data acquired with MR is localized in the k-space and can be converted into the image space by the application of the inverse Fourier transformation [20] [21] [22]. The Fourier Transform is a complex integral transformation of arbitrary number of dimensions, n , and is given by the following expression:

$$F(k) = \frac{1}{(\sqrt{2\pi})^n} \int_{-\infty}^{\infty} d^n x e^{-ikx} f(x) \quad (2.2.6)$$

Where x is the coordinate in the image space and k is the reciprocal variable wavenumber in frequency space, k-space. Under similar conditions its inverse transformation is given by:

$$f(x) = \frac{1}{(\sqrt{2\pi})^n} \int_{-\infty}^{\infty} d^n k e^{+ikx} F(k) \quad (2.2.7)$$

The Fourier Transform describes the transition of the data from the image space (spatial domain) to the k-space, which contains the information of the spatial frequencies of the object.

The complex exponential e^{ikx} in equation 2.2.6 can be interpreted as a complex wave in the direction of k with the spatial frequency $\|k\|$ and the complex values of $F(k)$ describe its amplitude and phase. The sum of all those waves

retrieves the MR image. A point $k = k_x$ far away from $(0,0)$ represents a wave along the x-direction with a high frequency, whereas $k = k_y$ describes a wave with longer wavelength in y-direction. Any $k = (k_x, k_y)$ in k-space is a wave superposition in the image-space as shown in figure 2.7.

On the image space each (x, y) point contains the intensity on a certain

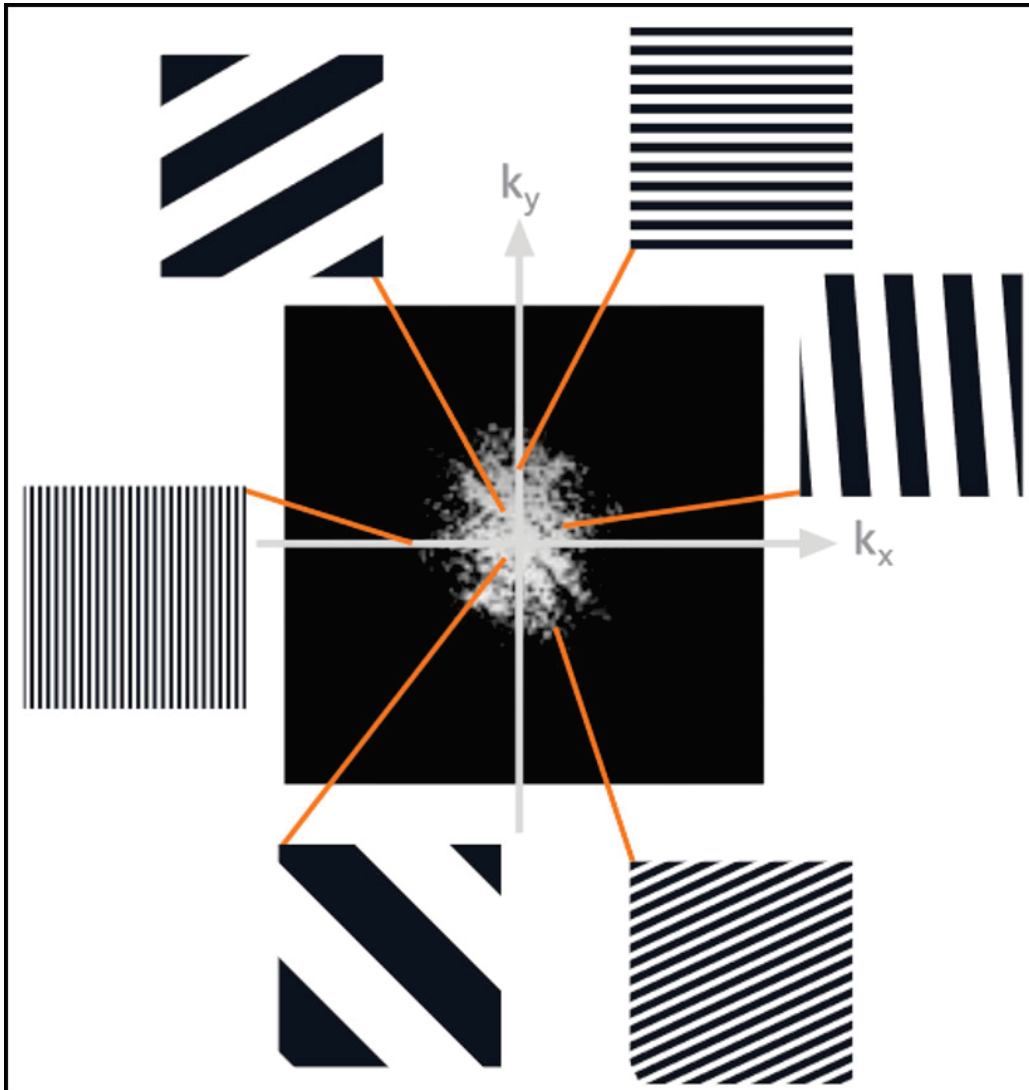


Figure 2.7: points in the k-space and their corresponding image space wave representation, [19].

position whereas in the k-space (k_x, k_y) point represents the amplitude and phase of the spatial frequency. These two representations can be converted to each other by using the Fourier Transformation, see figure 2.8a and d.

The (x, y) and (k_x, k_y) points are not corresponding to each other in a bijective, meaning one-to-one, way. In the image space every single (x, y) point maps to every (k_x, k_y) point and contrariwise, every point in the k-space contains spatial frequency and also phase information about every point in the image space. Manipulations in the k-space result in a non-local effect on the image space. Despite the absence of a direct correspondence between the location of a point in k-space and the location in the image, different parts of k-space correspond topologically to spatial frequencies in the MR image. Data near the centre of the k-space ($k = (0, 0)$) corresponds to low spatial frequencies. Therefore the reduction of the non-zero values to the centre of k-space leads to loss of details but preservation of the contrast and general shapes and corresponds to an application of a low-pass filter, see figure 2.8b and e. On the contrary, data from the periphery relates to high-spatial frequencies. When the centre of k-space is eliminated but the remaining periphery preserved it results in a loss of contrast but preserved details on the image like edges, comparable to high-pass filter, see figure 2.8c and f.

2.2.4.1 Specific characteristics in data acquisition

The continuous and infinite number of frequency components of the k-space as in 2.2.6 can clearly not be met in the MR imaging due to limited computer memory and acquisition time. Moreover, the number of samples of the signal is limited by the digitizing rate.

The Fourier series describes any signal, in given interval, as a sum of an infinite number of waves with discrete different frequencies. The series in the interval of the length L can be written as:

$$F(x) = \sum_{n=-\infty}^{\infty} c_n e^{i2\pi(n/L)x} = \sum_{n=-\infty}^{\infty} f_L(k) e^{ikx}, \quad (2.2.8)$$

where the n^{th} coefficient of the Fourier series is given by:

$$C_n = \frac{1}{L} \int_{-\frac{1}{L}}^{\frac{1}{L}} f(x) e^{-i(2\pi \cdot n/L)r}. \quad (2.2.9)$$

The Fourier series is also limited to a finite number of frequencies and the measured interval defines the field of view (FOV). The periodicity of the Fourier transform results in an artefact called “phase wrap-around”. Analysing the coefficient of a point located outside the FOV at the position $x_L = x + L$ leads to a phase shift of 2π which is exactly $1(e^{i2\pi n/L \cdot L} = 1)$. Thus

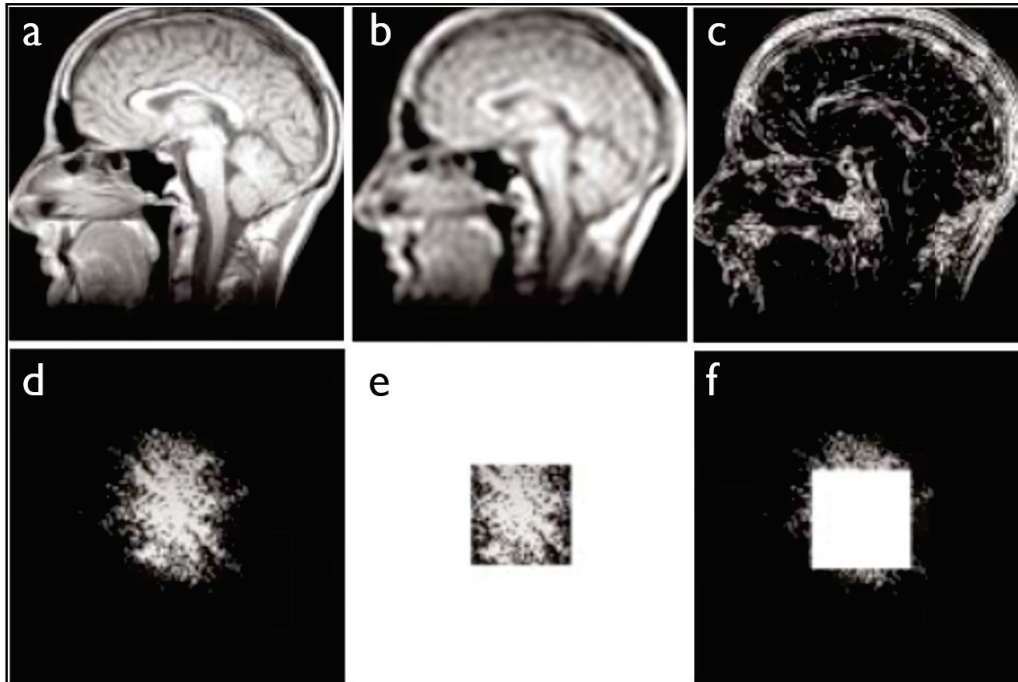


Figure 2.8: shows the data representation in the k-space and the corresponding image space with the whole k-space (a and d), when non-zero k-space points are restricted to the centre (b and e) and the centre of the k-space is removed (c and f), [19].

points outside the FOV, which are shifted by L , contribute to the Fourier coefficient as if they were inside the FOV. Therefore, anatomical parts outside the FOV are folded into the area of interest. As an example, the nose of the patient's head will therefore be wrapped around and spatially mismatched to the opposite side of the image, the back of the head and vice versa, see figure 2.9b.

As the Fourier series representation of an MR image is not unlimited at some point it must be cut short (truncated) which leads to characteristic errors in its reconstruction. The exclusion of the higher order summands is equivalent to only low frequency sampling in the k-space and a rectangular window sampling in the frequency domain. As the inverse Fourier Transform of a rectangular window corresponds to the sinc function it results in its convolution in the image space. Therefore the undershoot and overshoot oscillations of the sinc function appear as multiple fine parallel lines especially in high contrast interfaces like the dura and brain surface. The physicist Gibbs studied the Fourier series behaviour at discontinuities and described

ripples arising at sharp edges, therefore this artefact is called “Gibbs” or “truncation” artefact, see figure 2.9a. To reduce this problem a smoothly decreasing window like the Hamming window can be applied to the k-space prior to further processing or higher resolution data can be acquired.

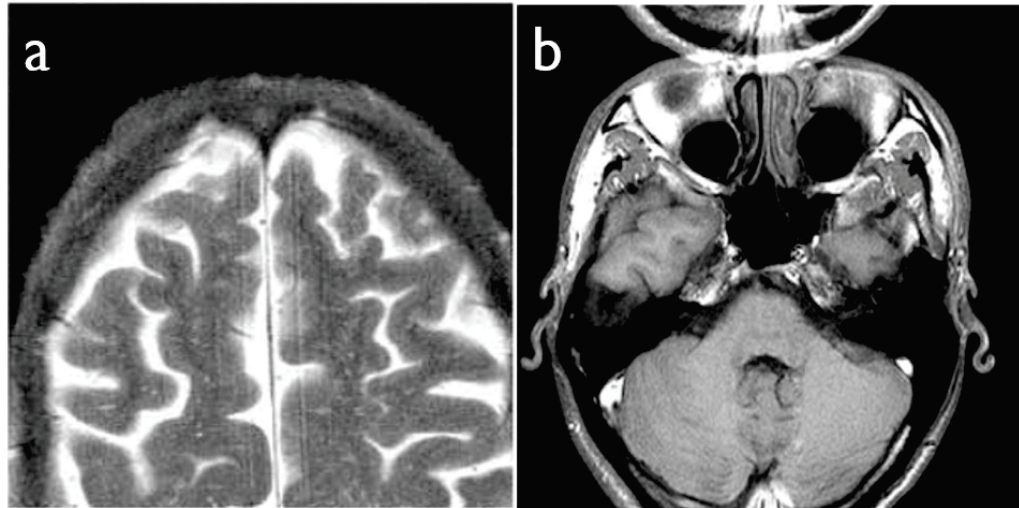


Figure 2.9: a) shows the Gibbs artefact on the border between dura and cortex shows, b) shows the wrap-around artefact in the human brain, [19].

2.2.5 Parallel acquisition technique

The parallel data acquisition aims at using information from signal acquired with different, simultaneously acquired, coils to fulfill the Nyquist criteria, while reduce the number of measurements. This is done by sampling only a limited number of k-space lines, which means phase encoding steps. This phase undersampling reduces the scanning time but also results in aliasing of the signal. This aliasing occurs when an insufficient number of k-space components have been sampled, which results in a wrap-around of the image. One option for untangling of the image is the measurement with different receiver coils. Each coil has its own coil sensitivity and therefore the measured signal is weighted and depends on the location of the coil as well as the signal origin. The correction of the aliasing artefacts can be performed either on the k-space or in the image-space.

The method performing the correction in the k-space is called GRAPPA (GeneRalized Autocalibrating Partial Parallel Acquisition) [23]. In this approach the lines through the centre of k-space (reference lines) are fully sam-

pled, but k-space lines away from the center are missing because multiple phase-encoding steps have been skipped, which defines the acceleration factor. The estimation of the missing points is the critical step in the GRAPPA method. The missing k-space points are estimated using the known acquired reference lines. Using a kernel weights can be calculated for each coil (using all coils) on how to interpolate the missing k-space points. When each coil the k-space is fully sampled, the Fourier transformation of the k-space of each coil results in an individual image with no aliasing artefacts. Finally, the individual coil images are combined to obtain the final image.

An alternative method which performs the correction for the aliasing after the fourier transformation is called SENSE (SENSitivity Encoding) [24]. From the undersampled k-space the image is reconstructed, which contains the aliasing artefacts. The crucial and important step is to calculate the sensitivity of each coil. Once this processing step is performed a matrix inversion is used to combine and unfold the aliased images acquired for each coil, resulting in one unaliased image.

2.3 Image contrast

Right after the pulse excitation the signal response of the spins reflects its density distribution, the proton density. However, this signal decays with the tissue specific relaxation times.

This tissue dependant signal decay can be used to enhance the signal contrast and retrieve information of the underlying structure. Many parameters influence the signal behaviour, application of gradient pulses, the time points and strength of RF pulses or the time point of signal measurement. For this reason many different sets of parameters are available which define different sequences. Some of these sequences used in the thesis are described in the following subsections.

2.3.1 GRE - gradient recalled echo

In order to illustrate an MR imaging sequence, a pulse diagram is used as shown in figure 2.10

In this diagram the application of the RF pulse, the different gradient amplitude as well as the resulting signal acquisition are shown (y-axis) as a function of time (x-axis). This diagram can be interpreted as follows:

First the gradient field along z , G_S is switched on to create a position dependent frequency offset. To excite a slice, slice selective excitation RF pulse is applied with the frequency of the desired slice. By adjusting its time duration and amplitude the flip angle is chosen. The dephasing from the slice selective gradient field, G_z , is rephased by the refocusing gradient, shown as opposite sign, with half its area.

After the slice selection the gradient field in y -direction G_P is applied and leads to a phase difference of the rotating spins in y -direction (phase encoding gradient), see the y -axis in figure 2.11. During the signal measurement the gradient in x -direction G_F is applied, causing different frequencies of the spins in x -direction (frequency encoding gradient), as in figure 2.11. First, this gradient is applied in the opposite direction in order to induce spin dephasing and signal suppression. When this gradient is reversed, the spins that are precessing at different frequencies will refocus, which leads to a signal rephasing, a gradient recalled echo (GRE). The echo time denotes the time between the excitation and the signal maximum.

The signal measurement of a selected slice is $S = \int dx dy \sigma(x, y) \cdot e^{-ik_x x + k_y y} = S(k_x, k_y)$ as shown in section 2.2.3. Therefore the whole k -space needs to be sampled if the inverse Fourier Transform is to be used to create an image free of artefacts. This can be achieved by varying the amplitude and duration of the gradient fields, because the position in k -space is given by

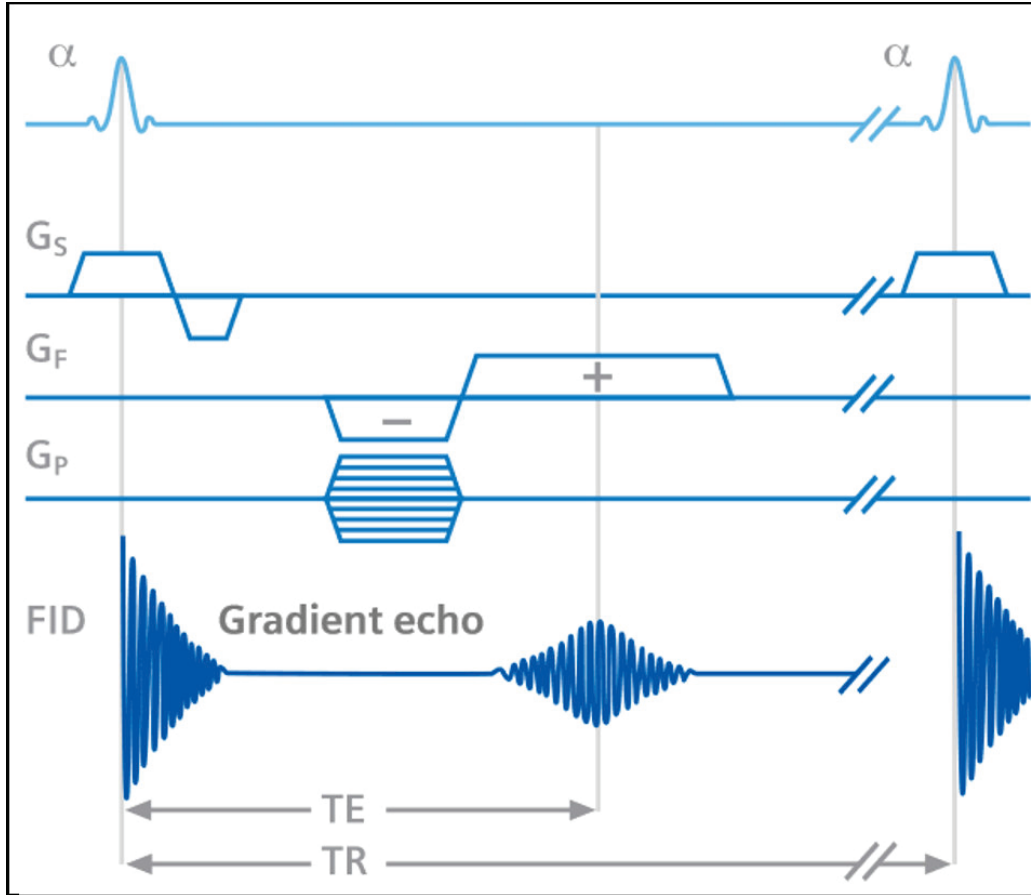


Figure 2.10: Puls diagram for gradient recalled echo sequence (GRE): from the top to the bottom: applied excitation pulse with flip angle α , slice selection gradient field G_S along z-direction, frequency encoding gradient field G_F in x-direction and phase encoding gradient field G_P in y-direction. TE denotes the time between excitation and signal measurement, echo time, and TR the time of two successive excitations, repetition time, [19].

$k_i = \gamma \int_T G_i(t) dt$. When applying the G_y gradient a certain point in y-direction of the k-space is set and by then acquiring the signal during the application of G_x , the k_x line is read. To summarize the gradient field effects:

1. slice selection with slice selective gradient field G_z (slice encoding direction, G_S)
2. phase difference with phase encoding gradient field G_y (phase encoding direction, G_P)
3. frequency difference with read out gradient G_x (frequency encoding

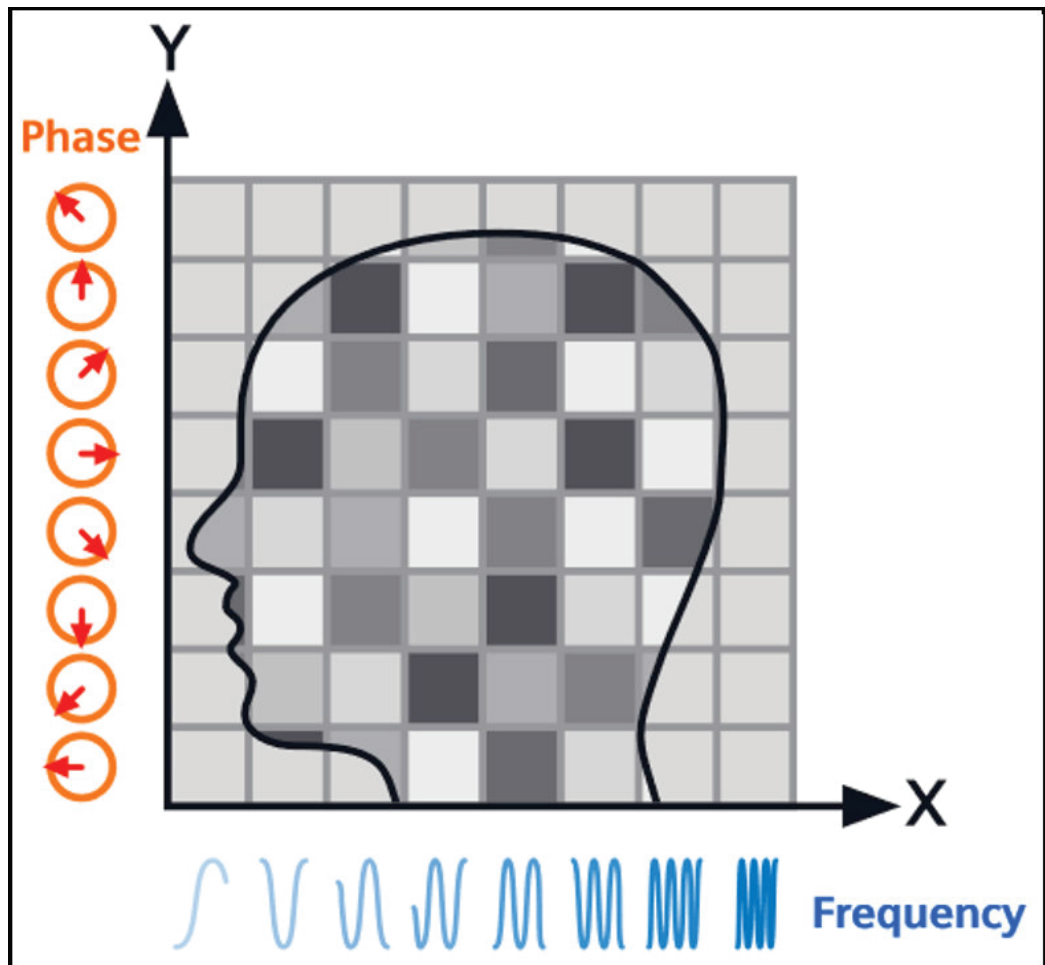


Figure 2.11: Application of gradient along y and x results in location dependent phase and frequency differences, [19].

direction, G_F)

With this process only one k_x line at a certain k_y coordinate is acquired. The magnetization then recovers towards its equilibrium and this excitation and encoding procedure needs to be repeated to fill the whole k -space. In the case of multiple slice imaging, the multiple slices are acquired in an interleaved fashion (remaining slices are excited in between two successive excitations of a given slice) taking advantage of the recovery time needed. The time between two successive RF pulse of the same frequency (excitation of the same slice) is named repetition time, TR.

Three additional parameters can be adjusted:

1. duration and/or amplitude of the RF pulse tunes the angle of the spins

in respect to the main magnetic field B_0 , called the flip angle α

2. time between the applied RF pulse and the signal measurement, called the echo time TE
3. time between two successive RF pulses, called repetition time TR .

The measured signal intensity is proportional to the transversal magnetization M_{xy} after flipping the z-magnetization with a certain angle α using the RF pulse, $\sim M_z \cdot \sin(\alpha)$. The decay of the signal, due to the dephasing of spins (T_2 relaxation) during the measurement with echo time TE , is considered with the term

$$e^{-\frac{TE}{T_2^*}}.$$

Another term proportional to the signal intensity is the proton density ρ . Moreover, the exponential recovery of the longitudinal magnetization M_z towards the equilibrium during two successive RF pulses (TR):

$$M_0(1 - e^{-\frac{TR}{T_1}}).$$

Finally, the signal intensity after the application of multiple RF pulses is given by:

$$S_s s \sim \rho \frac{1 - e^{-\frac{TR}{T_1}}}{1 - \cos(\alpha) \cdot e^{-\frac{TR}{T_1}}} \cdot \sin(\alpha) \cdot e^{-\frac{TE}{T_2^*}}.$$

In the clinical environment the acquisition of a MR image is preferable as fast as possible in order to minimize motion artefacts and maximize patient comfort, therefore a short TR is selected. In order to retrieve the highest signal intensity for a given TR the optimal flip angle has to be calculated. This is based on the computation of the maximum of the signal intensity. Therefore the first derivative of the signal intensity in respect to the variable flip angle needs to be zero. The solution is given by

$$\alpha_E = \arccos(e^{-\frac{TR}{T_1}})$$

and is known as the Ernst-angle [25].

The different parameters α , TE and TR are influencing the signal behaviour and the signal intensity depends on tissue specific properties T_1 , T_2^* , as described in figure 2.12.

When using T_1 -weighted contrast the signal response for the white matter (*shorter* T_1) is brighter than gray matter. The T_1 - weighting is suitable for the morphological assessment of normal anatomy.

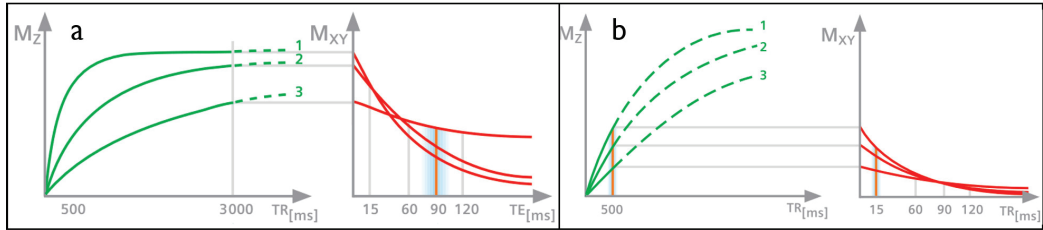


Figure 2.12: For the illustration of weighting contrast two tissues are chosen: fatty tissue and the CSF. The fatty tissue has a higher density and therefore a short longitudinal as well as short apparent transversal relaxation time T_1 and T_2^* (line 1). On the other hand the CSF, which is a fluid, has a long longitudinal and transversal relaxation time T_1 and T_2^* (line 3). Tissues like white or gray matter have relaxation times in between, [19].

When applying the RF pulse, the spins of fatty tissue and CSF are flipped to the xy-plane. The net magnetization of fat tissue along z , M_z , relaxes very fast to its equilibrium reaching a steady state $M_{z,ss}$. By applying the next RF pulse shortly after, so that the repetition time TR is smaller than the T_1 , the spins are flipped again towards the xy-plane. Within this time M_z of fat tissue is almost recovered, leading to a high transversal signal M_{xy} , whereas CSF shows only small M_z . In T_1 -weighting the echo time TE is selected to be short. For this reason the dephasing of the transversal magnetization for both tissues is rather small. After the image acquisition, fatty tissue appears bright and the CSF dark.

For T_2 -weighting the influence of the signal recovery after the excitation is avoided. For this reason the TR is kept long, which implies that the longitudinal net magnetization of both tissues reaches $M_{z,ss}$. The spin flipping by the next RF pulse results in a similar transversal magnetization. The T_2 -weighting reveals differences in the T_2 time, which influences the dephasing of the spins and therefore also the decay of the M_{xy} . By selecting a long echo time, TE , the transversal magnetization of the fatty tissue is decreased due to the fast dephasing property of dense tissues. While the CSF transversal magnetization is almost persistent. For this reason the CSF appears in this contrast bright and fatty tissues dark.

The T_2^* -weighted contrast enhances fluids which makes it useful in the detection of abnormal fluids like bruises or cerebral hemorrhage after stroke. Hence this contrast is helpful when analysing pathologies. The gradient reversal process used to create a single gradient echo can be repeated multiple times in order to produce additional GRE signals after a single RF-pulse. This sequence is called multi-echo GRE.

The gradient reversal rephases only those spins which have been dephased by the gradient itself (magnetic field inhomogeneities or tissue related artefacts like susceptibility are not affected by the gradient switches). The image contrast is therefore still influenced by the T_2^* time unlike its cancellation when applying a spin echo (SE) sequence, see 2.3.2.

The multiple GRE signal decreases exponentially as a function of T_2^* time, see figure 2.13. Hence, the generation of multiple GREs is possible as long as the complete loss of the transverse magnetization due to the T_2^* relaxation has not yet occurred. The corresponding echo times to each measured GRE are commonly denoted as TE_1, \dots, TE_{END} .

Not only the apparent transversal relaxation rate can be measured with the multiple echo GRE but also the phase, see figure 2.13.

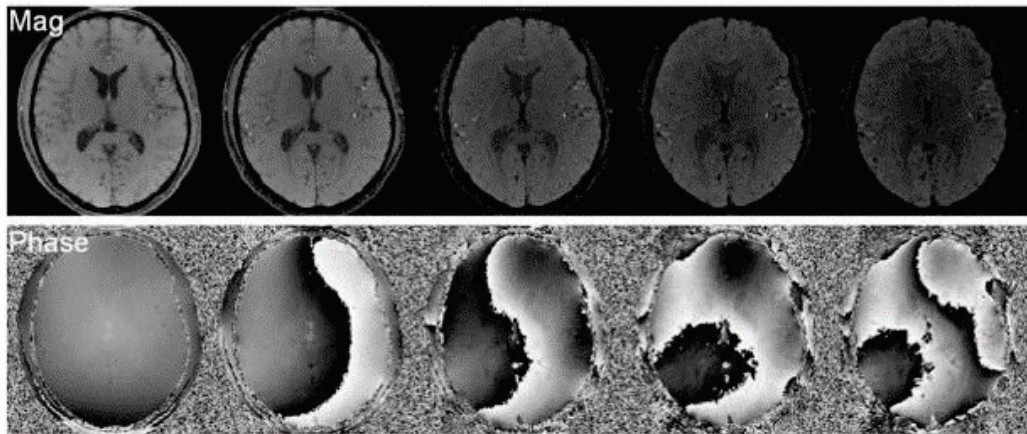


Figure 2.13: magnitude and phase maps acquired with multiple GRE for different echo times show a decrease on magnitude contrast and increase in phase shift and phase wraps on phase contrast, [26].

2.3.2 SE - spin echo

In gradient echo the signal evolution is not only due to transversal relaxation time T_2 from the spin-spin interaction but also to the dephasing arising from magnetic field inhomogeneities. This can be caused either from the system or tissue components. In order to retrieve the spin-spin interaction the spin echo (SE) sequence should be used.

SE sequence takes the advantage of the effect, that the static inhomogeneities that create the transversal net magnetization dephasing are reversible. On the contrary, the dephasing due to the spin-spin interaction cannot be reversed.

First the precessing spins are flipped to the xy-plane with a 90° RF pulse,

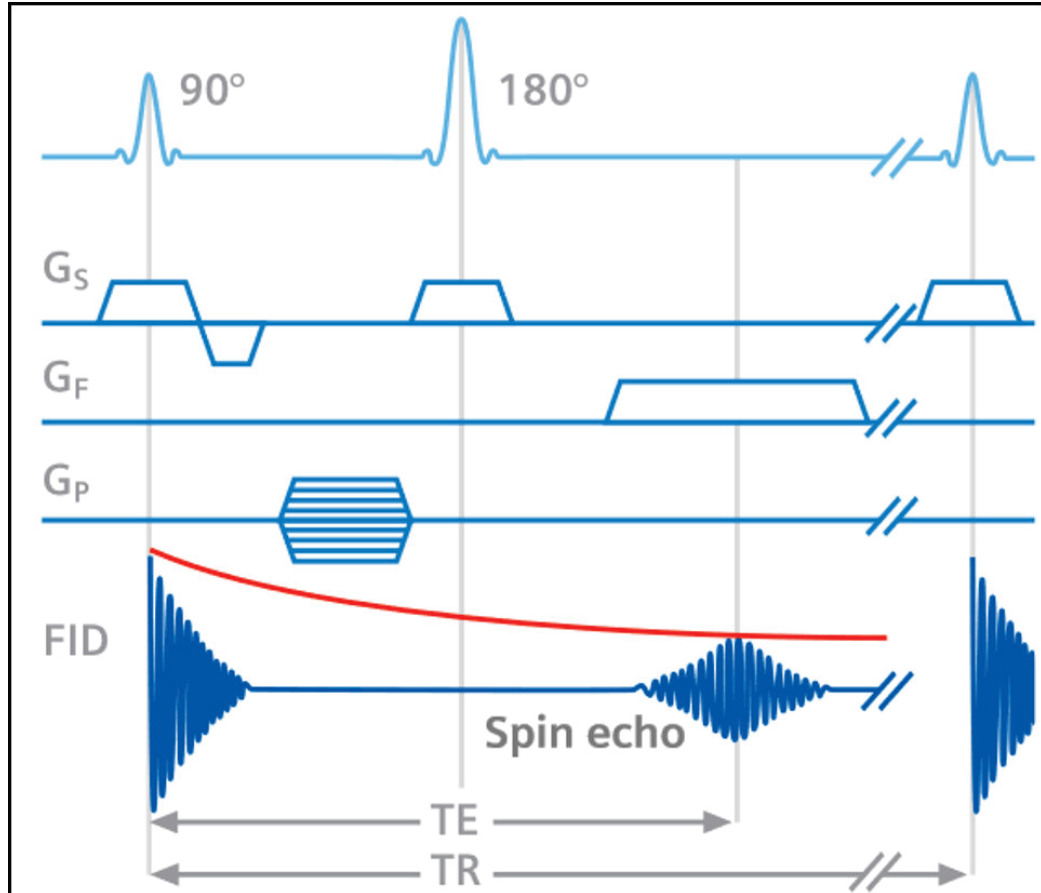


Figure 2.14: Puls diagram for spin echo sequence (SE): from the top to the bottom: applied 90° excitation pulse, slice selection gradient field G_S along z-direction, frequency encoding gradient field G_F in x-direction and phase encoding gradient field G_P in y-direction. TE denotes the time between excitation and signal measurement, echo time, and TR the time of two successive excitations, repetition time, [19].

see figure 2.14. Due to local inhomogeneities as well as spin-spin interaction the spins dephase and the transversal magnetisation M_{xy} decays. The application of an additional π RF pulse at time $TE/2$ rotates the spins by 180° and brings them to the xy-plane with a reversed phase. This leads to a full rephasing of the spins and hence the recovery of the signal after an additional time TE . The π RF pulses enables the disentanglement of the dephasing based on spin-spin interaction from the dephasing caused by local static field inhomogeneities.

Analogous to the steady state signal intensity for the gradient echo, the equation assuming explicitly a 90° RF pulse is as follows:

$$S_{ss} \approx \rho(1 - e^{-TR/T_1}) \cdot e^{-\frac{TE}{T_2^*}}.$$

This allows different contrast weighting depending on the used parameter set.

The successive application of these π pulses and measurement of the M_{xy}

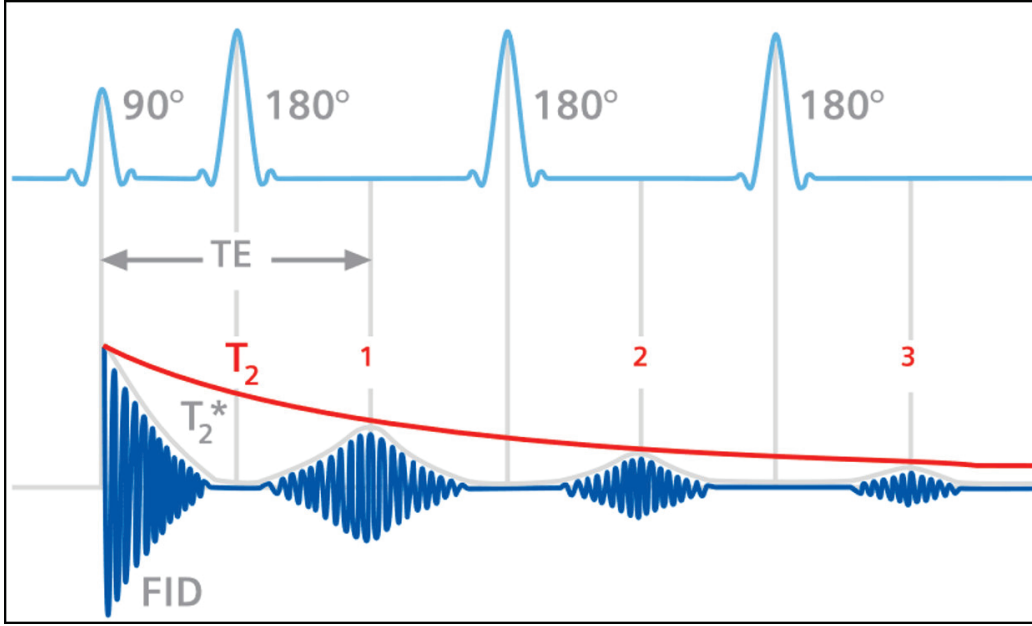


Figure 2.15: Application of successive 180° pulses enables the calculation of the T_2 relaxation time, [19].

generates a signal decay due to the spin-spin interaction. The acquisition of the transversal magnetization at different echo times TE_i provides the opportunity to measure the tissue dependent T_2 time as in figure 2.15 when fitting a mono-exponential signal decay:

$$S(r, t) = \rho(r) \cdot e^{-\frac{TE_i}{T_2(r)}}.$$

In order to accelerate the acquisition time, a method dubbed GRAPPATINI can be used [27]. Hereby, the parallel acquisition method GRAPPA [23] is combined with the model-based reconstruction MARTINI [28] allowing high acceleration rates when using multiple receiver coils. The T_2 time is retrieved with an iterative reconstruction method minimizing the l_2 norm of the simulated and measured undersampled data in the k-space, see figure 2.16.

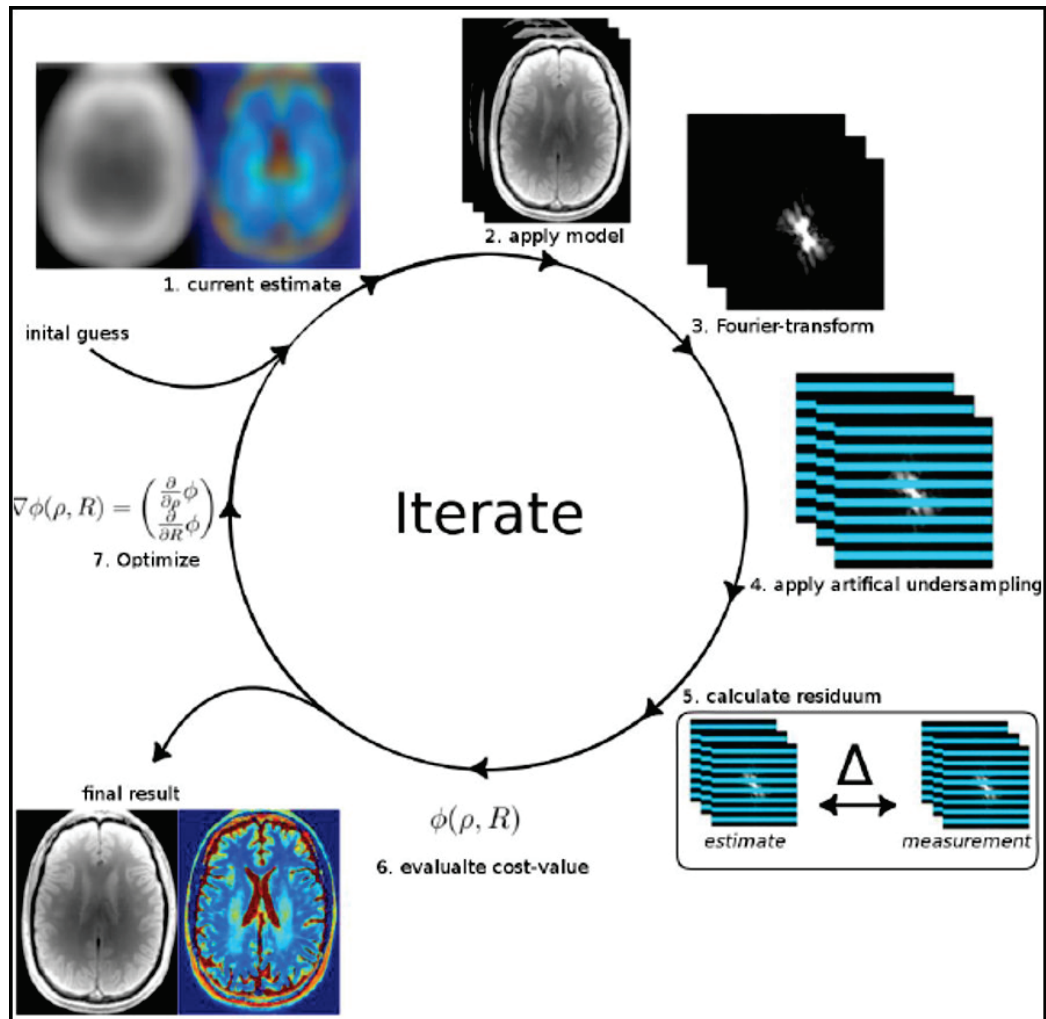


Figure 2.16: GRAPPATINI: First guess of the contrasts is made (1) and with the signal model the T_2 is calculated for each TE_i (2). Their k-space representation (3) is artificially undersampled (4) and by minimizing the l_2 norm of the measured and estimated T_2 (4,5) the final T_2 contrast is iteratively improved (7), [29].

2.3.3 DTI - Diffusion tensor imaging

So far the water spins have been assumed to be static and not moving during the acquisition time. However, each molecule has thermal energy and interacts with its environment and therefore diffuses randomly, performing a random walk. The mean diffusion distance is given by:

$$S = \sqrt{\langle x^2 \rangle} = \sqrt{2 \cdot D_0 \cdot t}$$

With the walking time t and diffusion constant D_0 . In order to describe the diffusion of a free, randomly moving molecule the probability density function of the normal distribution is:

$$P = \frac{1}{\sqrt{4\pi D_0 t}} e^{-\frac{x^2}{4D_0 t}}$$

This equation defines the probability of a free molecule to move within the given time t a certain distance x . Analysing this function reveals that for small times the distribution is very sharp and small distances are more likely than larger ones. When setting a longer diffusion time the Gaussian distribution becomes broader and shallower. The molecule has likely moved further away from the initial positions with a diffusion distance around 1-15 μm during 50-100ms [30].

However, the movement in some biological tissues is restricted as it is the case in the neuronal axon fibers, whose diameter is of the same range as the free diffusion distance. Therefore the diffusivity model needs to be corrected for this restriction with a time dependent diffusion:

$$D(t) = \frac{\langle x_{tissue}^2 \rangle}{2t}.$$

The cell restrictions imply a smaller diffusivity whereas in the case of small restriction the diffusivity is approximately that of free water.

Diffusion imaging measures the amount of the water diffusivity and enables to measure the orientation dependence of this diffusion constraint. Thus, it enables to retrieve microstructural tissue information.

The diffusion weighted sequence (DWI) first flips the net magnetization to the xy-plane. In order to retrieve the diffusion information first a dephasing gradient field is applied. The spins lose their coherence and their phase is spatially encoded. When applying the reversal gradient the dephasing is withdrawn. However, in case of diffusion the spins are displaced and the reverse gradient doesn't lead to their total rephasing. Therefore the measured signal is reduced in respect to the static case and is proportional not only to the strength and duration of the gradient pulse but also to the diffusion coefficient and diffusion time.

This model assumes a Gaussian distribution of the diffusion. However, the diffusion in the myelinated neuronal axons is less restricted along the fiber than in the directions perpendicular to it. Therefore a more complex model is used which takes into account the non-uniform diffusion inside a voxel, mathematically estimated as a tensor. With this method, called diffusion tensor imaging (DTI), for each voxel the orientation dependent tensor is measured. The tensor consists of 9 different parameters, but as the model is

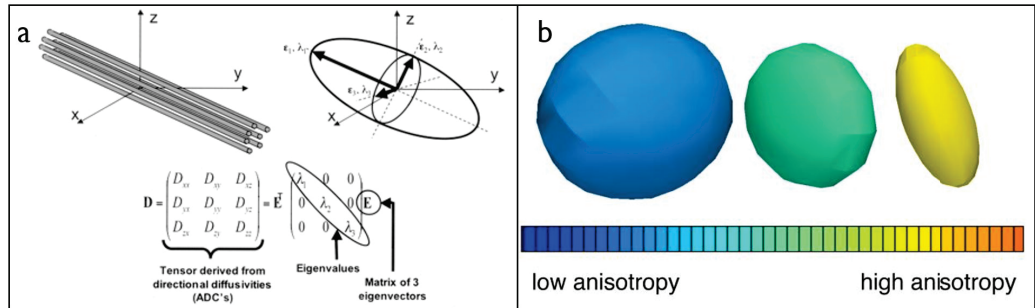


Figure 2.17: a) In presence of restrictions the diffusion is non-uniform and modeled as a tensor, b) transition of spherical shape (isotropic diffusion) to narrow ellipsoid (diffusion in one direction) when the anisotropy increases, [31] and [30].

symmetrical the tensor contains only 6 independent components. The tensor can be interpreted as an ellipsoid, which is oriented along the main diffusion direction, see figure 2.17a. This ellipsoid takes a spherical shape in case of low anisotropy (isotropic diffusion), see figure 2.17b. In order to calculate the tensor, at least 6 measurements with the gradients in different directions need to be acquired additional to one measurement without any gradients, resulting in different contrasts, see figure 2.18a-c and e-g. From the tensor, its eigenvalues and eigenvectors, quantities can be measured, the two most popular properties being:

the mean diffusivity (trace of the tensor)

$$MD = \frac{\lambda_1 + \lambda_2 + \lambda_3}{3},$$

the fractional anisotropy

$$FA = \frac{\sqrt{3}}{\sqrt{2}} \cdot \sqrt{\frac{(\lambda_1 - MD)^2 + (\lambda_2 - MD)^2 + (\lambda_3 - MD)^2}{\lambda_1^2 + \lambda_2^2 + \lambda_3^2}}.$$

The mean diffusivity is the mean of all of the three eigenvalues and therefore the orientation independent mean of the diffusivity for each voxel. The fractional anisotropy on the other hand is a measure for the variation of the diffusion along different orientations and is maximal in case of diffusivity in only one direction as present in white matter fibres, see figure 2.18d. Moreover, the main direction of the fibres can be visualized using the color-coded FA maps, see the green-red-green transition of the forceps minor in figure 2.18. Regions with isotropic diffusion like gray matter or cortex remain dark on the FA maps.

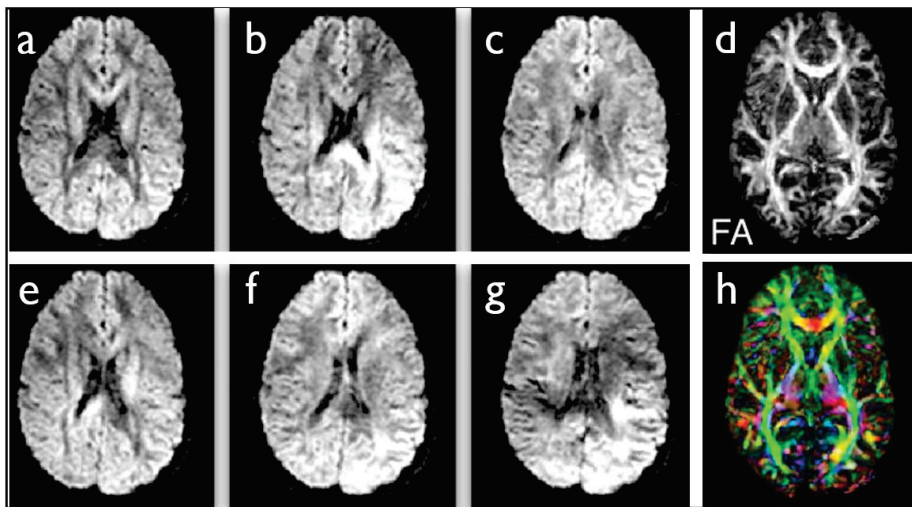


Figure 2.18: a)-c) and e)-g) signal acquired with different gradient directions, d) fractional anisotropy (FA) map highlighting regions with high directional diffusivity, h) color-coded FA map reflects the diffusion direction, [30].

DTI enables the usage of the orientation information for tractography, where the neuronal fiber bundle connections can be calculated using the orientation information of the neighbouring tensors, see figure 2.19. However, DTI allows only a simplified reconstruction of the tissue structure as only average fiber orientation in this voxel is computed. Therefore crossing fibers can't be disentangled. To have a better tissue estimation more sophisticated methods need to be used like the Q-ball imaging which allows more complex diffusion orientation models. This technique requires the measurement with the gradients at many directions (64 and more) and high b-values.

Tractography allows to make assumptions about the connectivity of the brain and is a topic of research. The loss of axons or restrictions, like demyelination, induce a decrease in the fractional anisotropy. Therefore, the knowledge of the fractional anisotropy gives the opportunity to study, e.g. degenerative diseases like multiple sclerosis or Alzheimer disease, or other effects on the fractional anisotropy like brain tumor.

2.3.4 SWI - susceptibility weighted imaging

The magnitude of the GRE image contains the signal decay information, which is affected by the signal inhomogeneity inside the voxel. The phase of the GRE image has the information of the field shift of the voxel due to the local field inhomogeneities.



Figure 2.19: diffusion tensor imaging tractography: streamlines of fiber bundle connections of a human brain, [30].

One method which includes the information present in the phase image is susceptibility weighted imaging (SWI).

In order to increase susceptibility effects, the magnitude image can be combined with the phase image, as was first suggested by [32]. This combination can be used to increase the contrast from the paramagnetic haemoglobin present in small vessels [33]. In SWI, see figure 2.20, the phase image is first highpass-filtered and a mask is created from the phase image such as: all radians above 0 are set to 1 and the values from $-\pi$ to 0 are mapped linearly from 0 to 1 [34]. This mask is multiplied multiple times to the magnitude image (often set to four). Therefore the contrast is increased in respect to the magnitude image in tissues with a negative phase such as iron rich regions, veins and hemorrhages.

SWI has become an important imaging method for diagnostics, especially in the field of clinical neuro imaging. The application of this method enhances

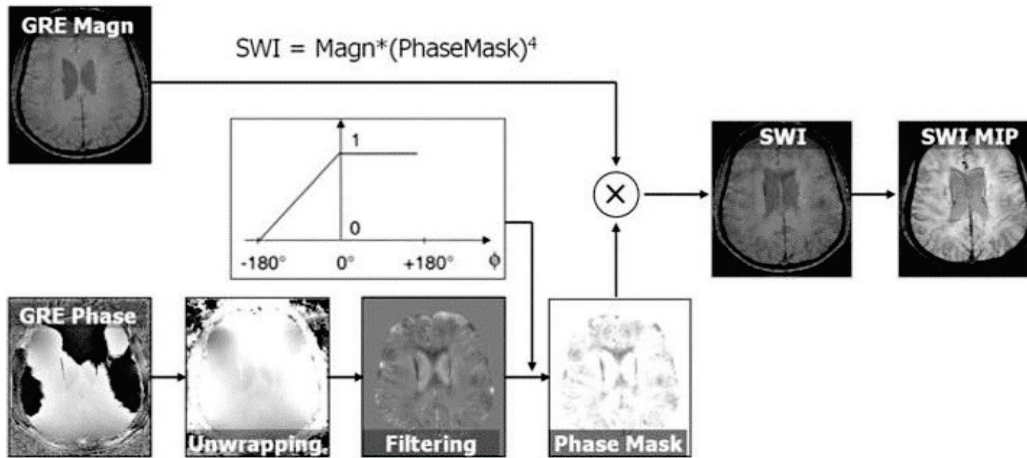


Figure 2.20: Processing steps of susceptibility weighted imaging (SWI). After unwrapping and high-pass filtering of the phase image a specific function is applied to retrieve the phase mask. The combination of the magnitude image and phase mask results in SWI image. To highlight the veins minimum intensity projection (MIP) is applied, [26].

contrasts due to strong susceptibility changes in respect to its surrounding and pathologic mechanisms in the brain which exhibit those variations. As the magnetic properties of oxygenated and deoxygenated haemoglobin changes, SWI is used to image small vessels in the brain [33]. Generally, diseases which include a cerebral vascular pathology can be diagnosed with SWI. For vascular malformations like arteriovenous or cerebral cavernous malformations SWI is used for diagnosis and for some special cases even outperforms imaging techniques like the CT angiography, T_2 fast spin echo or T_2^* GRE [35] [36]. Also restrictions in the blood flow like the developmental venous anomaly are well detected on SWI contrast [37]. SWI is also able to distinguish the two main types of stroke, due to lack of blood flow (ischemic) and due to bleeding haemorrhagic stroke with having the advantage of being more sensitive than CT [38] [39]. Not only stroke but also other kinds of haemorrhages can be visualized using SWI such as caused by cerebral amyloid angiopathy or traumatic brain injury [40] [41] [42]. As the tissue magnetic properties differs between normal and pathologized tissues, this method is also applied in the visualization of tumors, and can be used to characterize active or necrotic tumors and to monitor treatment effects [43] [44] [45]. However, the SWI fails to provide information of the contrast origin. Although the sources producing the inhomogeneities are highlighted in SWI, no information can be gained about its magnetic susceptibility (diamagnetic

or paramagnetic), as shown for active and calcified lesions in figure 2.21. In order to gain quantitative information of the magnetic susceptibility of the source quantitative susceptibility mapping, QSM, is used. The origin of this contrast as well as its calculation and application is the main content of this thesis and the following chapters.

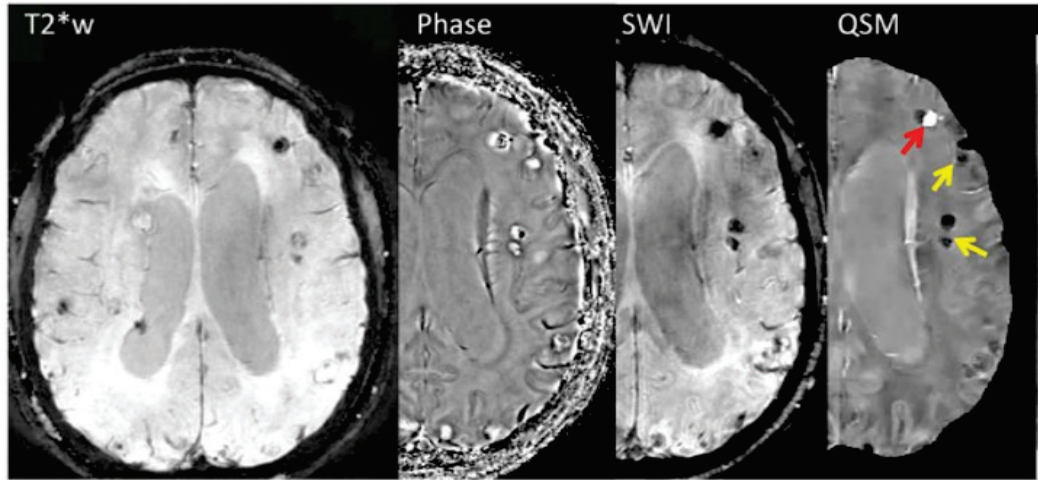
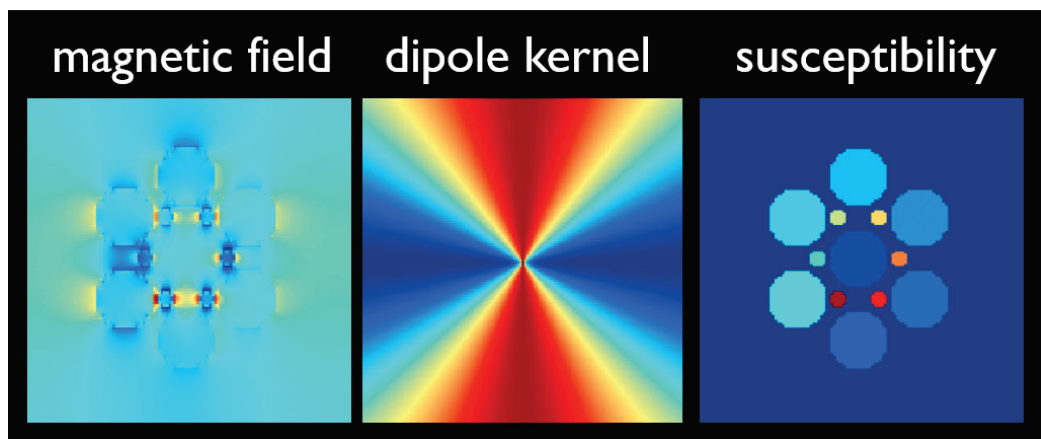


Figure 2.21: Four contrasts are shown for a patient with neurocysticercosis; T_2^* weighted, phase, SWI and QSM. Calcified lesions with negative susceptibility (yellow arrows) are visible on all contrasts with better performance on phase and QSM contrast, whereas active lesion with positive susceptibility is delineated only on QSM, [46].

Chapter 3

Susceptibility

Magnetic susceptibility of tissue and its quantitative mapping in MRI



3.1 Theory

Magnetic susceptibility, χ , describes the reaction of a material to the presence of an external magnetic field H . Generally, the magnetic susceptibility is a tensor that describes the change of magnetization of the material, M , when the magnetic field strength, H , varies and can be written as:

$$\chi_{ij} = \frac{\partial M_i}{\partial H_j}. \quad (3.1.1)$$

This is the general case, when the induced magnetisation and the magnetic field are not necessarily aligned. However, for most liquid and biological tissues the magnetic susceptibility can be described as a scalar. Therefore, the induced magnetization of most materials, which includes biological tissues, is proportional to the applied external magnetic field. Hence, an applied magnetization induces a magnetic induction, B , which depends on the scalar susceptibility. Based in the response to an external magnetic field, materials can be separated in two main material groups:

i. Diamagnetic materials, $\chi < 0$,

have no net intrinsic magnetic moment, in the absence of an external magnetic field. Due to the Lenz's law circulating charged particles generate a magnetic moment with an orientation aligned opposite to that of the applied field. The material is repelled by the external magnetic field and expels the magnetic field from its inside. The diamagnetic materials generate opposing field which leads to a resulting weaker magnetic field. This magnetization disappears once the external magnetic field is removed.

ii. Paramagnetic materials, $\chi > 0$,

have an independent intrinsic magnetic moment, which originates from spins of unpaired charged particles. These moments are randomly distributed in all directions, hence their summed magnetic moment is zero. In the presence of the applied external magnetic field the magnetic moments align themselves along this field, which results in the field amplification. The material is attracted by the external applied field. However, this property is not maintained when the external field is removed. The paramagnetic materials amplify the magnetic field.

Special cases are these of superconductors ($\chi = -1$) which are perfect diamagnets, who expel all fields, or the ferromagnetic materials ($\chi \gg 0$) with a non-linear and much stronger interaction with the external field compared to paramagnetic materials that persists even in the absence of this field.

A distribution of magnetic susceptibility generates, under a constant external magnetic field, a magnetic field perturbation ΔB . This induced magnetic field fluctuations cause not only the transversal magnetization decay but also phase changes. For a homogeneous medium, so there is no surrounding medium, this phase difference in respect to the surrounding tissue is given by:

$$\Delta\varphi = -\gamma \cdot \Delta B \cdot T_E \quad (3.1.2)$$

with ΔB being the difference between the induced magnetic field, B_{int} , from the susceptibility effect and the external magnetic field, B_{ext} . The relationship between the tissue specific induced magnetic field and the resulting measured phase difference is linear. In order to connect the measured phase with the underlying tissue a relationship between the susceptibility and the induced magnetic field needs to be provided.

In the case of a spatially varying distribution of magnetic susceptibility this relationship becomes more complex and the magnetic Maxwell equations need to be analyzed when assuming magneto-statics, [47]

$$\begin{aligned} \nabla \times H &= j \\ \nabla B &= 0 \end{aligned} \quad (3.1.3)$$

A magnetic potential, Φ , exists with the given equation, as no whirls are present

$$H = -\nabla\Phi \quad (3.1.4)$$

This potential is associated with the susceptibility through equation 3.1.4:

$$\begin{aligned} \nabla B &= \nabla(\mu_0\mu_r H) = \mu_0\nabla[(1 + \chi)H] \\ &= \mu_0\nabla[(1 + \chi)(-\nabla\Phi)] = 0 \end{aligned} \quad (3.1.5)$$

Here μ_r is the relative magnetic permeability and μ_0 the permeability of free space (magnetic constant). The magnetic constant is considered 1 in the following calculations for convenience.

$$(1 + \chi)\nabla^2\Phi + (\nabla\chi)\nabla\Phi = 0. \quad (3.1.6)$$

This equation should be valid in the biological tissue where the susceptibility is very small and therefore, $1 + \chi \approx 1$:

$$\nabla^2\Phi = -\nabla\chi\nabla\Phi \quad (3.1.7)$$

The main magnetic field is assumed to be oriented along the z-axis, thus only this component is non-zero for the potential ($\partial_z\Phi = H_0$) and the equation simplifies to

$$\nabla^2\Phi = H_0 \cdot \frac{\partial\chi}{\partial z} \quad (3.1.8)$$

The Fourier Transform, FT , has the property that a spatial derivative in the image space is represented by a multiplication with the k vector in the k -space. Applying the FT to both sides of this equation leads to:

$$\begin{aligned} FT(\nabla^2\Phi) &= FT(H_0 \cdot \frac{\partial\chi}{\partial z}) \\ i^2k^2 \cdot FT(\Phi) &= ik_z H_0 \cdot FT(\chi) \\ FT(\Phi) &= -i\frac{k_z}{k^2} H_0 \cdot FT(\chi) \end{aligned} \quad (3.1.9)$$

The projection on the z -axis of the magnetic field is the searched static component of the magnetic field as this is the only that will affect signal evolution. Introducing the Inverse Fourier Transform, IFT of the equality obtained in 3.1.4 and inserting 3.1.9 leads to:

$$\begin{aligned} H_z &= -\partial_z\Phi \\ &= -IFT[ik_z FT(\Phi)] \\ &= -IFT[ik_z \cdot -i\frac{k_z}{k^2} H_0 \cdot FT(\chi)] \\ &= -H_0 \cdot IFT[\frac{k_z^2}{k^2} FT(\chi)] \end{aligned} \quad (3.1.10)$$

Hence, the induced magnetic field at a certain position depends on both the spatial distribution of the bulk susceptibility and on the applied external magnetic field. The field experienced by any given spin is considered by including a Lorentz sphere correction where the water spins are expected to freely move around this perturbation and are assumed to be point-like sources.

$$\begin{aligned} B_{source} &= (1 - \frac{2}{3}\chi)B \\ &= (1 - \frac{2}{3}\chi)(1 + \chi)H_0 \\ &\approx (1 + \frac{1}{3}\chi)H \end{aligned} \quad (3.1.11)$$

Finally, combining equation 3.1.10 and 3.1.11 results in an expression for the induced magnetic field experienced by the spins

$$\begin{aligned} B_{source} &= (1 + \frac{1}{3}\chi)H \\ &= (1 + \frac{1}{3}\chi) \cdot (-H_0) \cdot IFT[\frac{k_z^2}{k^2} FT(\chi)] \\ &= H_0 + H_0 \cdot IFT[(\frac{1}{3} - \frac{k_z^2}{k^2}) FT(\chi)] \end{aligned} \quad (3.1.12)$$

The magnetic field perturbation induced by the susceptibility distribution is therefore given by

$$\delta B = \frac{B_{source} - B_0}{B_0} = IFT\left[\left(\frac{1}{3} - \frac{k_z^2}{k^2}\right) FT(\chi)\right] \quad (3.1.13)$$

By defining the magnetic dipole kernel in k-space $D(k) = \left(\frac{1}{3} - \frac{k_z^2}{k^2}\right)$ the equation simplifies to

$$\delta B = IFT[D \cdot FT(\chi)]. \quad (3.1.14)$$

The induced magnetic field is given by a convolution of χ with the projection of the dipole field along the z-direction.

During the derivation of this equation the applied external magnetic field

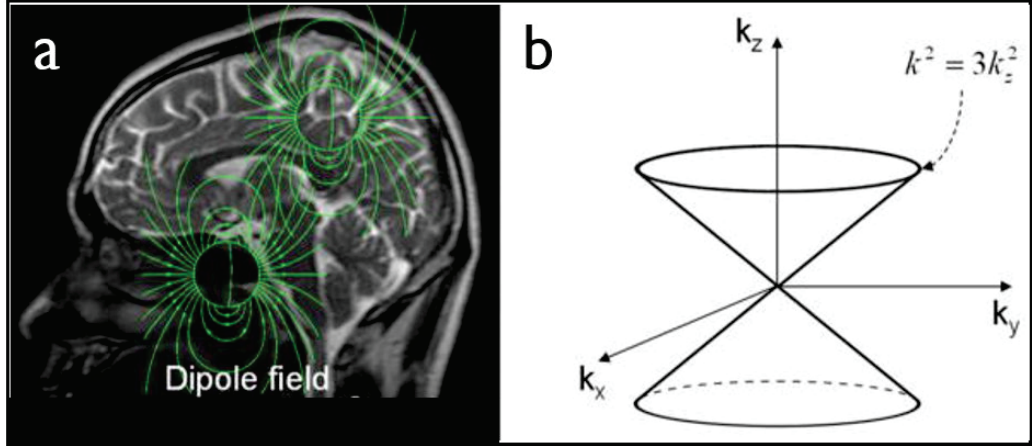


Figure 3.1: a) the magnetic dipole field as produced by magnetic susceptibility (green), b) dipole kernel in the k-space and its cone of zero values for $k^2 = 3k_z^2$, [26].

was considered to be along the z-axis of the susceptibility distribution. For the more general case assuming the magnetic field located at an arbitrary direction the magnetic dipole kernel can be written in k-space as

$$D(k) = \frac{-k_x \sin(\theta) - k_y \cos(\theta) \sin(\varphi) - k_z \cos(\theta) \cos(\varphi)}{\|k\|} + 1/3 \quad (3.1.15)$$

Where θ and φ are the angles that characterize the orientation of the externally applied magnetic field to the reference frame and $k = (k_x, k_y, k_z)$ are the k-space coordinates.

The calculation of such susceptibility from the measured frequency difference is called quantitative susceptibility mapping (QSM) and the different processing steps are further explained in chapter 4

3.2 Susceptibility in biological tissues

The effect of the biological tissue susceptibility on the MR GRE image is complex. The atomic magnetization properties are based on unpaired electrons for the paramagnetic susceptibility and absence of an intrinsic magnetic moment for the diamagnetic susceptibility. However, analysing the biological tissue, the atoms are bond to larger complexes. In molecules, the unpaired electrons are interacting with these of other atoms generating electron clouds with a certain distribution. Moreover the opposite nature of the unpaired electrons and the induced currents that counteract the external field appear together in the molecules. All these effects contribute to the final magnetic susceptibility of the molecule. Not only the molecule's susceptibility but also its spatial orientation and distribution determines the final magnetic field change. Despite this complexity, when analysing the phase or susceptibility maps, some properties of the tissue in the healthy human brain can be accessed.

Most of the human brain tissue is diamagnetic and has values around

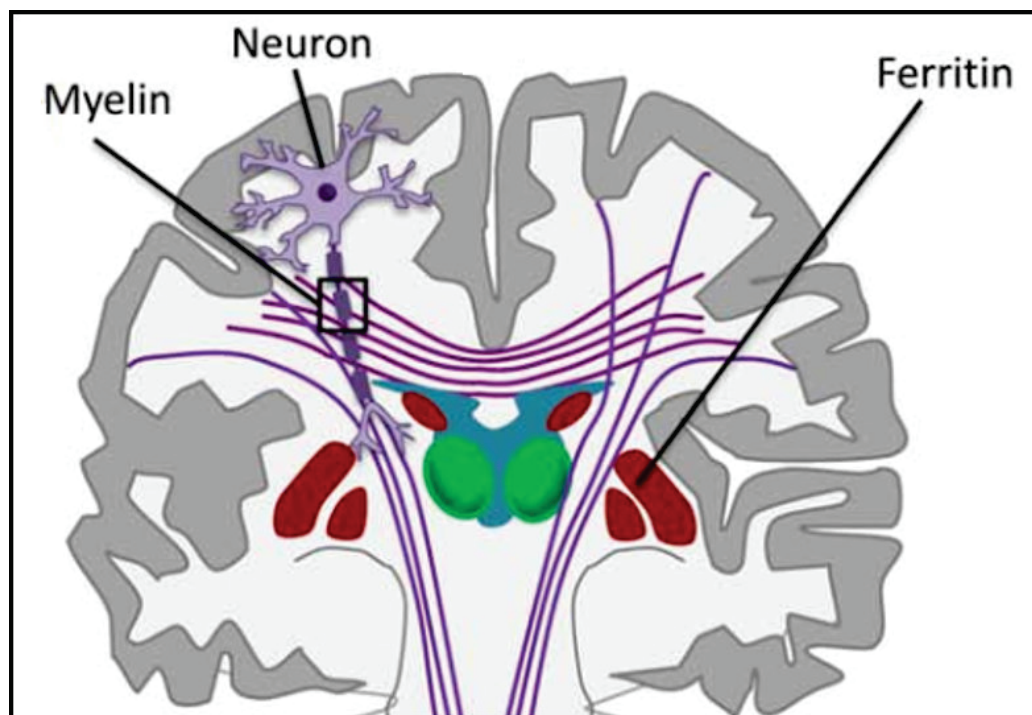


Figure 3.2: sources of susceptibility in the human brain: diamagnetic myelin as insulator of neurons (violet) in white matter (white), iron bound as complex in ferritin in deep gray matter (red), [46].

10^{-6} [48] [49]. Myelin, which is wrapped around the axons and forms nerve fibres is a main diamagnetic origin, see violet white matter fibers in figure 3.2. For the paramagnetic component iron is the main contributor. The iron concentration in the human brain varies between different regions, as e.g. ferritin in red deep gray matter in figure 3.2. In the human cortex (gray in figure 3.2) the concentration amounts varies from $30 \mu\text{g}$ per gram of tissue up to $210 \mu\text{g}$ in the deep gray matter (Substantia nigra, Globus pallidus, Putamen, Nucleus Caudatus) [50] [51].

The susceptibility values as measured by QSM range from -0.1ppm for the diamagnetic white matter, WM, up to 0.1ppm for the deep gray matter, GM, regions [52] [53] [54] [55] [56] [57].

3.2.1 Iron

The iron in the human brain is bound as a complex in hemosiderin and ferritin [51] [48], see figure 3.3. Although the haemoglobin in the blood is the main iron source, it has diamagnetic properties in the oxygenated state but paramagnetic in the deoxygenated state [58]. The iron in the blood is located in the haemoglobin, the oxygen transporter, more specific as Fe^{2+} in the heme molecule. The deoxyhemoglobin has four unpaired electrons and therefore is paramagnetic, whereas for the oxyhemoglobin the oxygen atoms binds to the heme leading to no unpaired electrons left [58] [59], see 3.3b. Hence, only the protein shell contributes to the susceptibility of the oxyhemoglobin and results in its diamagnetic nature [60] [58]. This change of magnetic property allows the visualization of veins and vessels in susceptibility weighted imaging (SWI) [33] as described in section 2.3.4 and is the basis of the BOLD contrast used in functional MRI.

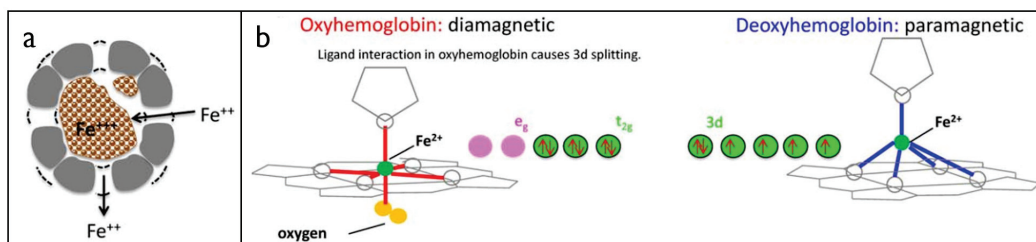


Figure 3.3: a) iron stored as Fe^{3+} in ferritin complex, released as Fe^{2+} , b) diamagnetic oxyhemoglobin (left) and paramagnetic deoxyhemoglobin (right). The bounded, paired electrons of Fe become unpaired, once the oxygen, O_2 is released, [46].

Many QSM studies show that the paramagnetic susceptibility contrast in

deep gray matter is associated with iron depositions and a linear relationship exists between susceptibility and iron quantification, see figure 3.4, as has been demonstrated using x-ray based methods or mass spectrometry in post mortem samples [61] [53] [62] [55] [63] [64].

Moreover, an iron concentration increase during the lifespan in humans was shown in QSM studies [52] [65].

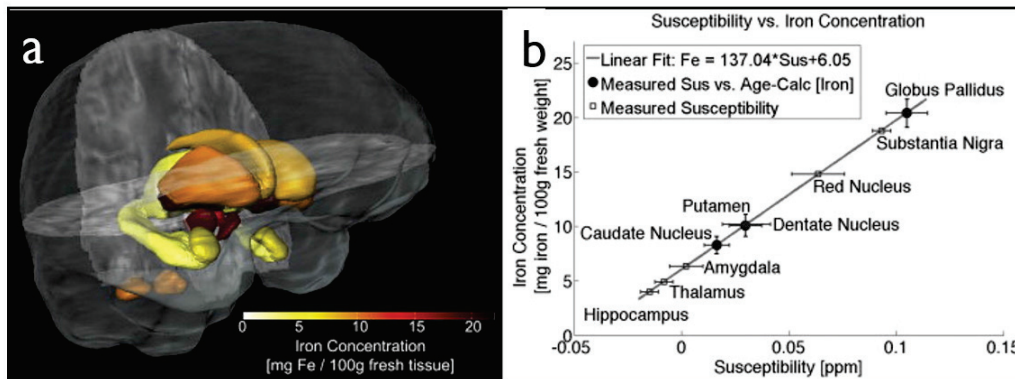


Figure 3.4: a) iron concentration in deep gray matter structures, b) linear relationship between measured quantitative susceptibility and iron concentration in deep gray matter structures, [53].

3.2.2 Myelin sheath

Although a paramagnetic phase shift can be seen in the human cortex, which was often attributed to iron [66], an extraction of iron in post-mortem tissues did not affect the present strong gray and white matter contrast [67]. Also haemoglobin is not able to generate such strong contrast [68].

This leads to the conclusion, that in white matter the origin of the susceptibility effect is myelin.

In order to form an electrically insulating layer for the axons of the nervous system a myelin sheath is wrapped around them, see 3.5a and b. It covers the axons in white matter and consists of cylindrically aligned lipid molecules, see figure 3.5c. Most lipids and proteins have diamagnetic susceptibility, myelin due to its high volume fraction is expected to be the origin of the diamagnetic susceptibility of white matter. The contrast between gray and white matter was shown to disappear in the shiverer mice which was genetically modified to not develop properly the myelin sheath [69] [70]. In another experiment a mice on cuprizone diet resulted not only on the demyelination of the axons but also of the decreased phase contrast between

gray and white matter [71]. The myelination of the brain increases with

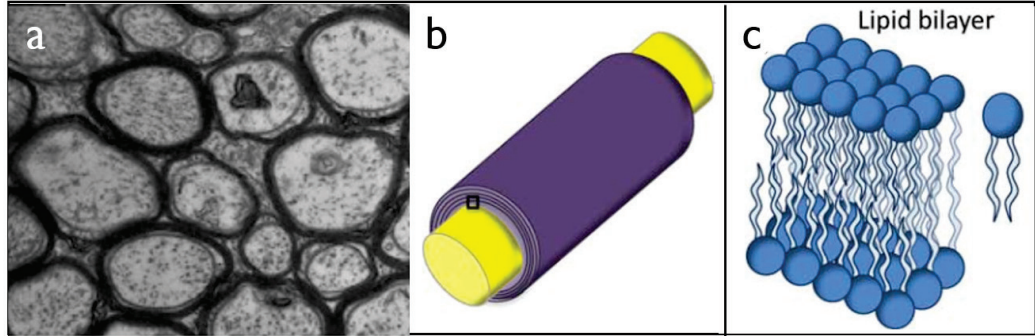


Figure 3.5: a) white matter structure, b) axon (yellow) is wrapped by myelin sheath (purple) zoom-in of black square shows in c) proteins form a lipid bilayer, [72] and [46].

the age, persists into adolescence and follows a continuous demyelination as the brain ages [73]. The phase contrast between gray and white matter has been shown to correlate myelin content, assessed by myelin stained histological tissues during mouse brain development [70], whereas iron extraction lead to an unchanged contrast. Also in human neonates, whose brains are known to be not well myelinated, a reduced phase contrast compared to the adults was shown [74]. In white matter, the susceptibility first became more diamagnetic with the brain development during childhood and adolescence, followed by a continuous decrease in the diamagnetic properties as the brain ages, as shown by [65]. In mouse a high correlation was found between the diamagnetic susceptibility and the intensity of the myelin stain as well as an increased anisotropy of the susceptibility with age [75].

Particularly interesting is the case of the evolution of white matter lesions in Multiple Sclerosis, MS, which leads to the loss of macromolecules and therefore also to the loss of the myelin sheaths wrapped around the white matter axons. This decrease results in a reduction of the R_2^* relaxation rate [76]. The changes on the phase however depend on the underlying structural change. Damage on the myelination leads to a susceptibility which is less diamagnetic and results in hyper-intensities on the susceptibility contrast, whereas the axonal damage leads to hypo-intensities [76]. This competing effects of R_2^* reduction due to demyelination and R_2^* increase due to iron deposition results in the better sensitivity of QSM when analysing the basal ganglia in MS patients [77]. Lesions with damage of the myelin sheet, without loss of the tissue, are visible in the phase contrast map without being visible neither on the R_2^* nor on the magnitude [76]. In the presence of demyelination the

susceptibility of myelin in white matter can be similar to that of gray matter [71] [69]. As theoretically suggested [76] the evaluation of the magnetic susceptibility of some MS lesion reveals a gradual change from enhanced to nonenhanced contrast compared to the normal-appearing white matter. During the initial few years the lesion shows a high susceptibility value, whereas as the lesion ages further gradually dissipates to values similar to that of normal white matter [78]. Therefore, QSM has been suggested as a method for myelin loss measurement in white matter in the brain [75] [70] [71] [69]. The evaluation of the subtle myelination changes induced by prenatal alcohol exposure in mice have shown significant reduction of the susceptibility contrast and susceptibility anisotropy of white matter. QSM was suggested to be more sensitive than DTI for detecting these subtle myelination changes [79].

3.2.3 Microstructure

The tissue structure on the cellular and subcellular level as well as its geometrical arrangement within the tissue also affects its susceptibility, see figure 3.6a and b. The axons are covered by the myelin sheath in the white matter. The susceptibility from all the separated compartments contributes to the resulting phase and T_2^* behaviour [80] [81] [82] [83] [84]. When analysing white matter two main effects should be separated; the structural anisotropy and the anisotropy of the magnetic susceptibility.

The *structural anisotropy* refers to the fact that the magnetic field generated by elongated structures depends on the orientation in respect to the applied magnetic field. This orientation dependent phase change occurs also when isotropic susceptibility of the tissue is present due to the elongated geometric shape of this tissue. This effect was shown for the angular dependence of vessels [85] as well as axons [86]. Its description is discussed in section 3.3.1. The *anisotropic susceptibility* takes into account the response of the susceptibility itself which changes with the magnetic field orientation [87] [88] in which case the susceptibility needs to be described as a tensor. The susceptibility calculation modeling this property is called susceptibility tensor imaging (STI) [88] and is discussed in section 3.3.2.

The *compartmentalization* of white matter describing the origin of the protons from three components; axonal space, myelin space, and extracellular space, see figure 3.6c. Each compartment contributes to the MR signal [86] [89] [90] [91] and cause a nonlinear dependence of the phase as shown experimentally by [89] [91]. As a results a multicompartment model of the tissue properties was established [83] [84] and is further explained in section 3.3.3.

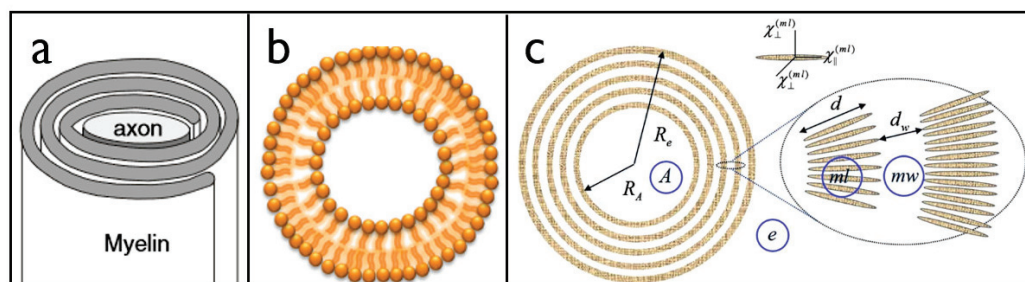


Figure 3.6: a) myelin sheath wrapped around the axon, b) lipid bilayer forms restrictive structures, c) myelin consists of several layers of lipid bilayer resulting in the compartment model for white matter including the axonal space (A), myelin space (myelin layer and myelin water) and extracellular space (e), [72] and [84].

3.2.4 Further influences

Calcifications in the brain tissue have the opposite effect on the phase compared to iron depositions. Pathologic tissues like tumors are diamagnetic and this property is used to distinguish the calcified lesions from iron loaded tissue. This delineation of lesions was confirmed with a computed tomography, CT [92]. As calcifications are diamagnetic they can be differentiated from microbleeds and iron deposition [92].

In patients with glioblastoma more accurate differentiation of calcification from haemorrhage was achieved with QSM having the benefit of radiation absence in the case of CT imaging [93].

Also copper accumulation due to abnormal copper metabolism in Wilson's disease has been demonstrated to result in significantly increased susceptibility values in the basal ganglia compared to healthy controls [94].

The human brain is more complex and consists not only of many different components but also the interaction between them contributes to the susceptibility contrast. The chemical exchange of macromolecules with mobile protons contributes to the gray and white matter contrast on the phase image and decreases the susceptibility contrast [95] [96] [97].

The ability to measure quantitative values of susceptibility with QSM enables the direct comparison of different clinical conditions. Patients with a blood disorder leading to a reduced haemoglobin production had higher susceptibility values than controls in red nucleus and choroid plexus suggesting iron loading [98] on the other hand in the globus pallidus and substantia nigra lower susceptibility values were reported in respect to normal controls. Hence potentially making QSM a valuable method for brain iron assessment

and offering the study of iron related disease such as sickle cell disease and Parkinson's disease [99].

3.3 Advanced descriptions of the susceptibility

In a first approximation the susceptibility sources can be assumed to be point-like spheres with the measured molecule water able to freely move around those structures. In that formulation, the Lorentz Sphere correction is used to correctly estimate the field shift δB_z experienced by the protons. These assumptions are valid only for some brain tissues and more specific susceptibility calculations are required when describing the myelin content and microstructure. This is discussed in the following subsections.

3.3.1 Generalized Lorentzian Approach: account for anisotropic structure

As the cellular structure is expected to be close to isotropic throughout the gray matter and the water molecules are able to diffuse randomly in the cerebro-spinal fluid (CSF) the Lorentz sphere correction is valid in these brain tissues. However, considering the susceptibility origin in proteins aligned along the axon in the white matter, better descriptions are needed. White matter is a bundle like structure, in which water does not have access to myelin compartment. In this case the angle of the axon to the applied magnetic field should be taken into account. The Lorentz correction for some tissues within the brain, namely white matter (WM), gray matter (GM) and the cerebro-spinal fluid (CSF) was proposed to be given by [86]

$$\begin{aligned}\Delta B_{GM} &= 1/3B_0 \cdot \chi_{GM} \\ \Delta B_{CSF} &= 1/3B_0 \cdot \chi_{CSF} \\ \Delta B_{WM} &= 1/3B_0 \cdot \chi_{WM} - 1/2\chi_a(\cos^2(\varphi)-1/3)\end{aligned}\quad (3.3.1)$$

with χ_a being the susceptibility within the bundles/axons and χ_{WM} is the average susceptibility in the WM including the bundles. The additional part $1/2\chi_a(\cos^2(\varphi)-1/3)$ denotes the orientation dependency.

However, this model includes only the assumption of the bundle wise structure of the WM and its divergence from the point-like nature. This model accounts for the structural anisotropy in the generalized Lorentzian approach (GLA) and the resulting frequency shift is given by [100]

$$\frac{\delta f}{f_0} = \left(\frac{1}{3}\chi_{sphere} + \frac{1}{2}\chi_{long}\right) \cdot \sin^2(\varphi)\quad (3.3.2)$$

With χ_{sphere} and χ_{long} being the susceptibility from uniformly distributed sources which are spherical or oriented longitudinally, respectively. This

description can be interpreted as a first order correction.

3.3.2 Susceptibility tensor: account for anisotropic magnetic susceptibility

The myelin sheath, which covers the WM axons consists of cylindrically aligned lipid molecules. This structure leads to an anisotropic susceptibility. Hence, the induced magnetization and magnetic field generated by the magnetic susceptibility depends on its orientation in respect to the applied external magnetic field [68] [88], see figure 3.7a and c.

In order to measure the anisotropic susceptibility the susceptibility tensor imaging (STI) is used, see 3.7b and d. This method describes the orientation dependent susceptibility as a second order tensor with six independent entries due to the symmetry of the problem and in the case of isotropic susceptibility only the diagonal entries of this tensor are non-zero [88]. The magnetic field perturbation generated by the anisotropic susceptibility can be expressed as

$$\delta B = IFT\left(\frac{1}{3}FT(\chi) \cdot H - k \frac{k^T \cdot FT(\chi) \cdot H}{k^2}\right) \quad (3.3.3)$$

with k being the spatial frequency vector, H the applied magnetic field vector.

As the susceptibility tensor consists of six independent variables at least six different measurements are necessary for the reconstruction of the anisotropic susceptibility. The independent measurements can be achieved by acquiring the susceptibility response to magnetic fields at different rotations. In case of the brain, the head of the subject needs to be rotated to different positions in respect to the main magnetic field, e.g tilting. When the number of measurements is less than the number of the independent variables to determine, the problem is ill-posed and further information is needed. Using the prior knowledge fiber orientation of the white matter, as estimated by DTI, allows to reduce the number of unknowns and the susceptibility tensor can be reconstructed with fewer than six different orientations [101] [102]. Another approach applies a regularization with a morphology constrain on the mean magnetic susceptibility and improves the susceptibility tensor estimation in WM [103].

The STI enables to reconstruct fiber tractography based on the susceptibility tensor similar to DTI. This fiber tracking method was demonstrated on mouse brains [104].

Moreover, this technique can also be applied to other tissues outside the brain as long as an anisotropic susceptibility is present. One example is the

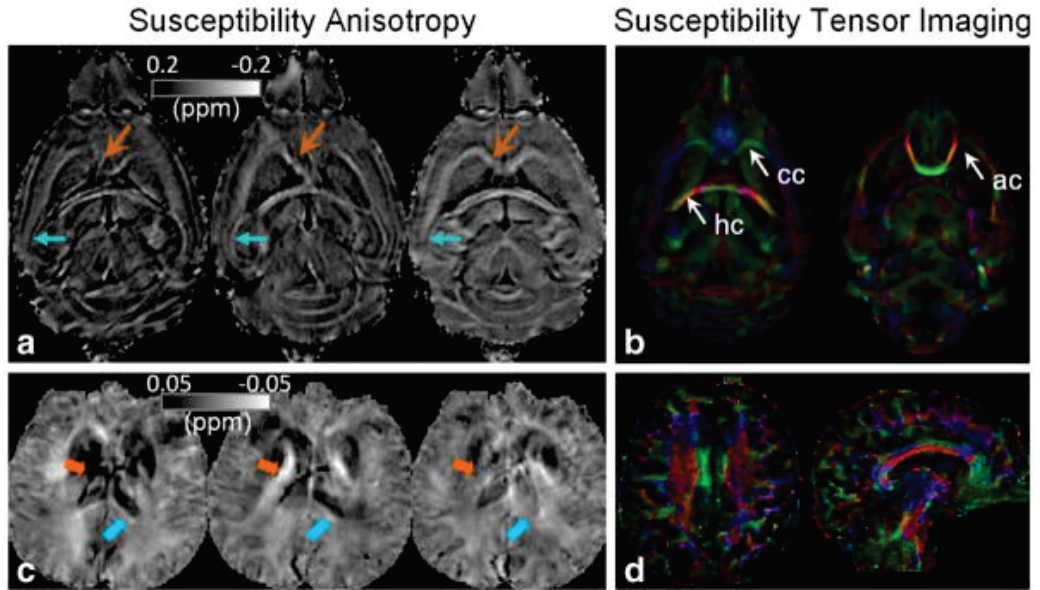


Figure 3.7: susceptibility maps for three different orientations and color-coded eigenvector maps calculated by STI for mouse brain at 9.4T(a,b) and human brain at 3T. For QSM the intensity scale is flipped (diamagnetic susceptibility-bright), [26].

tracing of renal tubules was possible throughout the mouse kidney using the STI, whereas the DTI was limited to the inner medulla [105].

3.3.3 Generalized Lorentzian Tensor Approach: account for anisotropic structure and magnetic susceptibility

The generalized Lorentzian shows that the magnetic field is created by the bulk magnetic susceptibility, which is assumed to result from inclusions outside the cavity with a homogeneous distribution, whereas inclusions inside this certain cavity are not contributing to it. The inclusions are considered as any kind of biological structures, whose susceptibility value differs in comparison to water, i.e. iron compartments, myelin layers, cell membranes, but have reduced or no water content.

To further specify the problem three different magnetic fields are differentiated: the static magnetic field, H ; the magnetic field outside of the inclusion, H_e , when the inclusion does not contain any water; and the magnetic field H_i , when averaging inside the inclusion. The occupied volume fraction

within the measured voxel connects these magnetic fields. The inclusion is influenced, additionally to the externally applied magnetic field, also by the induced magnetic field from other inclusions as well as the magnetic field created by itself. The shape of the inclusion affects the resulting magnetic field with the so called demagnetization tensor (which assumes an ellipsoid shape). Therefore not only the common induced magnetic field contributes to the frequency shift, but there are also anisotropic effects dependant on the shape of the inclusion. The structural anisotropy is accounted for by the demagnetization tensor and the magnetic susceptibility anisotropy is described by the susceptibility tensor. The final field perturbation can be expressed as [84]

$$\delta B = IFT[n^T \cdot L_k \cdot n(n \cdot k) \frac{(k^T \cdot \chi_k \cdot n)}{k^2}] \quad (3.3.4)$$

With n being the vector along the magnetic field. Assuming isotropic and longitudinal inclusions in the WM the susceptibility tensor in the referencing system of the axon is given by

$$\underline{\chi} = \chi_{iso} \cdot \begin{pmatrix} 1 & 0 & 0 \\ 0 & 1 & 0 \\ 0 & 0 & 1 \end{pmatrix} + \begin{pmatrix} \chi_r & 0 & 0 \\ 0 & \chi_r & 0 \\ 0 & 0 & \chi_a \end{pmatrix} \quad (3.3.5)$$

and the Lorentzian tensor is described as

$$\underline{L} = \frac{1}{3} \chi_{iso} \cdot \begin{pmatrix} 1 & 0 & 0 \\ 0 & 1 & 0 \\ 0 & 0 & 1 \end{pmatrix} + \frac{1}{2} \cdot \begin{pmatrix} \chi_r & 0 & 0 \\ 0 & \chi_r & 0 \\ 0 & 0 & 0 \end{pmatrix} \quad (3.3.6)$$

In the Generalized Lorentzian Approach it was assumed, that no water molecules were present inside the inclusions and the MR signal resulted from water molecules located only outside the susceptibility sources. Analysing the biological structure of the WM fibers results in a more complex description of the water molecule localization.

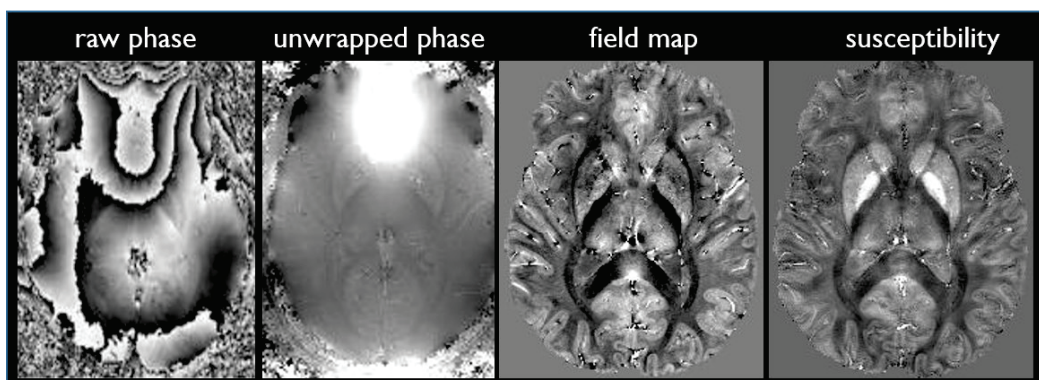
As axons are covered by several layers of the myelin sheath, water is present in the intra- and extracellular space as well as inbetween the myelin layers and restricted in its movement. These different water components contribute to the MR signal [86] [89] [90] [91] and cause a nonlinear echo time dependence of the phase of WM as shown experimentally by [89] [91]. Therefore an even more general frequency shift expression can be derived which includes the apparent component in the Lorentzian tensor. These apparent components take into account the original susceptibility components but also the multicompartment tissue properties as well as sequence parameters as defined

in [84]. Some of the susceptibility components calculated with the generalized Lorentzian approach using the data published by [106], are similar to the ones calculated by [83].

Chapter 4

QSM step-by-step

Magnetic susceptibility of tissue in MRI and its resulting quantitative mapping



The first step to compute QSM data is the acquisition of gradient recalled multi-echo datasets and keeping both, the magnitude and phase information. After the data acquisition further processing steps need to be taken in order to retrieve the final QSM image. The first processing step is the unwrapping of the 2π phase aliasing, see section 4.1. The next step is the disentanglement of phase variation due to the desired susceptibility effects from phase variations due to imperfect shimming and field inhomogeneities from air-tissue boundary susceptibility effects. Some of the background removal methods are explained in section 4.2. Finally, the field map represents only the induced field variations due to the magnetic susceptibility of the tissue, the QSM images can be reconstructed. However, this problem is ill-posed and many methods have been developed to overcome this limitation, which are further referred to in section 4.3.

4.1 Phase combination and unwrapping

When studying phase images acquired with a multi-channel multi-echo acquisition a proper channel combination is required. The reconstruction of phase images suffers from two main artefacts.

The first effect originates from the intrinsic spatial phase variation of each coil, which have its own spatially varying phase offset.

The second artefact, phase wraps, is due to phase 2π periodicity (phase = $\theta = 2\pi \cdot n + \theta$). The phase values can only be attributed in the range $[-\pi, \pi]$. These phase wraps occur in the images as isocontours.

When these artefacts are not taken into account, the combined phase images will show signal cancellation and (open-ended) fringe lines.

”When phase data is acquired at multiple echo times, the temporal evolution of the signal over the echoes can be used to retrieve the phase offset. Methods found in literature to compute phase images can be classified into two groups: those which reconstruct *phase difference images* and those which reconstruct *phase images* for each echo.

4.1.1 Phase difference methods

One approach is to eliminate the channel dependent phase offsets, $\varphi_j^0(\vec{r})$, is to calculate a phase difference for each coil using the phase from one or more pairs of echoes [107] [108] [109] acquired at two different echo times TE_n and TE_m . These can be combined over channels in the Hermitian inner product $\Theta^d(\vec{r}, n, m)$ using the complex images for a given coil $I_j(\vec{r}, TE_n) =$

$m_j \cdot e^{-i\varphi_j(\vec{r}, TE_n)}$. To consider the SNR of the individual coil-dependent noise factors, σ_j^2 , the phase difference is magnitude squared weighted according to

$$\begin{aligned}\Theta^d(\vec{r}, n, m) &= \angle \left[\sum_j \sigma_j^{-2} \cdot I_j(\vec{r}, TE_n) \cdot I_j^+(\vec{r}, TE_n) \right] \\ &= \angle \left[\sum_j \sigma_j^{-2} \cdot |m_j(\vec{r}, TE_n)| \cdot |m_j(\vec{r}, TE_m)| \cdot e^{-i(\varphi_j(\vec{r}, TE_n) - \varphi_j(\vec{r}, TE_m))} \right]\end{aligned}\tag{4.1.1}$$

This method can be performed without the requirement of unwrapping the phase image for each channel, but the SNR is reduced as the optimal combination is not obtained because the individual weights are retrieved from the images themselves and contain noise. When applying a low-pass filter and therefore smoothing the weights, the noise can be decreased as long as the coil sensitivities are not corrupted [110].

When data is acquired with multiple echoes, the singular value decomposition (SVD) method can be applied to the data from all echoes to calculate the coil sensitivities, resulting in an optimum SNR both for the magnitude and phase [111]. This approach has been shown to be effective for spectroscopy data [112]. The pixel by pixel SVD factorization of the channel vs. echo time matrix combines the data from the different coils. Hereby, the first singular value is the maximal coherently constructed signal from all channels and echoes, S^1 , and the eigenvectors contain the coil sensitivity estimations as well as the complex signal, SE , of the acquired echoes. The phase of the complex data has an arbitrary offset due to the pixel by pixel nature of the method, but not the phase differences, ΔSE , between the first echo and each subsequent echo. The complex signal evolution difference is given by $\Delta SE^d = abs(SE) \cdot e^{-i(\vartheta_n - \vartheta_i)}$ and the phase difference and magnitude are calculated as $\Theta^d(\vec{r}, n) = \angle[\Delta SE^d]$ and $M^d(\vec{r}, n) = abs[\Delta SE^d]$, respectively. The field map is calculated using the unwrapped phase difference between each different echo acquired at TE_n and the first echo TE_1 . The final field map is obtained by a weighting

$$W^d(r, n) = \frac{M^d(r, n)^2}{M^d(r, n)^2 + M^d(r, 1)^2}\tag{4.1.2}$$

as in [113], where M^d is the absolute value of the signal evolution between echo 1 and echo k. This results in the field map:

$$\Delta B = \frac{1}{2\pi\gamma} \frac{\sum_n \Theta^d(r, n) \cdot (TE_n - TE_1) \cdot W^d(r, n)}{\sum_n (TE_n - TE_1)^2 \cdot W^d(r, n)}\tag{4.1.3}$$

4.1.2 Phase imaging methods

Instead of cancelling the phase offsets, $\varphi_j^0(\vec{r})$, by using the phase difference, an alternative method calculates them, for each channel using a dual echo scan [114]. This has the advantage of the HiP approach that $\varphi_j^0(\vec{r})$ can be smoothed before it is subtracted from the phase at each echo time, leading to a higher SNR result. This method is computationally intensive as the phase data from all echoes and channels needs to be unwrapped to retrieve the phase offset. This can be mitigated either by using a low resolution multi-echo scan to calculate the phase offsets (applying MCPC-3D-II to the multi-echo data) or by downsampling the high resolution data for the phase offset calculation step, but it is nonetheless subject to the shortcomings of spatial phase unwrapping.

In the MAGPI approach (Maximum AmbiGuity distance for Phase Imaging) [115] the measured phase $\varphi_j(\vec{r}, TE_k) = \varphi_j^0(\vec{r}) + 2\pi\gamma TE_k \Delta B_0$ is extended to

$$\varphi_j(\vec{r}, TE_k) = \varphi_j^0(\vec{r}) + 2\pi\gamma TE_k \Delta B_0 + \varphi_{jk}^{noise} + \varphi_{jk}^{wrap} \quad (4.1.4)$$

where φ_j^0 denotes the phase offset for each coil j , φ_{jk}^{noise} the additive noise for each coil j and echo time TE_k and φ_{jk}^{wrap} attributes to the 2π phase wraps. This method uses the likelihood function resulting in an increase of the SNR in case of a three echo measurement. The reconstruction of the corrected phase image is performed in three steps. In the first step an estimation of the most likely tissue based frequency, which describes the phase difference between echoes, is calculated and removed from the original data. The angle difference is assumed to be: $\Theta^d(r, n, m) = 2\pi\Delta B(TE_2 - TE_1) + (\varphi_j^2 - \varphi_j^1) + 2\pi R$, where the phase wrapping is attributed by the integer R , which forces the angle difference to be in the range $(-\pi, \pi]$. The remaining data is associated with random noise, φ_{jk}^{noise} , as well as the phase offset $\varphi_j^0(\vec{r})$, which are separated in the second step. Finally the most likely tissue frequency that explains the three echoes is calculated. This method estimates the underlying phase without phase unwrapping or denoising and outperforms previous methods especially for measurements with low SNR, with the drawback of being computationally intensive.

In summary, the phase difference method using the HiP approach can be used to combine the phase images from multiple channels. This can be performed very fast without the need of phase unwrapping, although the SNR of the combined phase image is reduced by the voxel-by-voxel subtraction. Using the 3D correction of the coil sensitivities improves the reconstructed phase image at the cost of computationally intensive phase unwrapping for each channel and the two echoes. The whole dataset is used for the calculation of the complex signal evaluation for the SVD method resulting in

optimal SNR. Both phase unwrapping and phase offset are incorporated in the maximal likelihood (MAGPI) calculation, which performs better at low SNR measurements.” (own contribution of the NMR in Biomedicine review paper from Robinson and Schweser [116]).

Many phase unwrapping algorithms are available and can be separated regarding their operating domain in two groups: the spatial and temporal domain. As examples of phase unwrapping methods in the spatial domain are the 3D best path phase unwrapping image [117], the quality guided phase unwrapping [118] and phase unwrapping based on optimization [119] or Laplacian algorithms [120]. The phase difference of successive echos is used for temporal domain algorithms which allow a fast pixel-wise unwrapping with the drawback of failure in regions with steep phase gradients [121]. When selecting the phase unwrapping method a compromise between running time and robustness needs to be taken into account.

4.2 Background removal

The small magnetic field variations generated by the magnetic susceptibility of the tissue sources are overlaid by the strong background fields due to surrounding tissue-air interfaces as well as imperfect shimming.

A simple approach to remove the background is the application of high-pass filtering like the homodyne filtering successfully applied in SWI [34]. However, its performance depends on the selected parameters. A small filter size can fail to remove the entire background field, especially close to the sinuses. On the other hand, a large filter size performs well in the background removal, but results in the removal of low-frequency components of the phase induced by the local tissue leading to an underestimation of the susceptibility quantification. This underestimation depends, among other parameters, on the size of the tissue structure of interest.

While high pass filtering is purely phenomenological, more complex methods rely on the identification of region of interest (ROI). They remove only the field that can be physically expected to be generated from sources outside this ROI. There are two main types of methods: the sophisticated harmonic artefact reduction for phase data (SHARP) [55] and its further improvements [122] [123]; projection onto dipole fields (PDF) [124].

SHARP methods are based on the mean value property of harmonic functions. They exploit the non-harmonic property of the field generated by the local susceptibility distribution, whereas sources outside the ROI are harmonic and satisfy the Laplace equation.

PDF uses the orthogonality of the dipole magnetic field generated by sources inside and outside of the ROI. This method fits the background field inside the ROI generated by sources outside of the ROI. Although these methods perform well in the centre of the brain, they give unreliable values close to the borders or erode the ROI.

Various methods have been proposed which preserve the data near the boundary such as the efficient and automated harmonic field pre-filtering (EAHF) [125] and the Laplacian boundary value (LBV) method [126].

All these methods are based on the Maxwell equations and similar assumptions are made. Therefore the background removal techniques provide a similar performance far from the boundary and their impact on the quantification of the susceptibility of deep gray matter structures is minimal, see figure 4.1. The performance in regions close to the boundary of some of these methods, based on SHARP, PDF and EAHF, is compared in section 6.

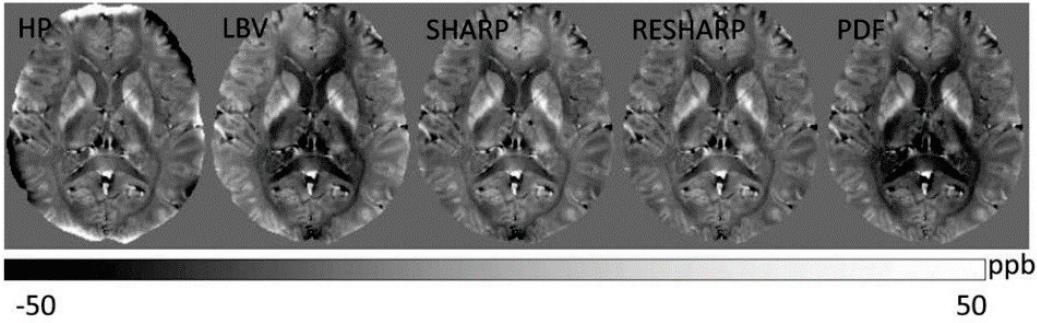


Figure 4.1: Five methods for background removal; HPF-high-pass filtering, LBV-Laplacian boundary value, SHARP-sophisticated harmonic artifact reduction on phase data, RESHARP-regularization enabled SHARP, PDF-projection onto dipole fields, [46].

4.3 Reconstruction of QSM

After the phase unwrapping and the background field removal, the resulting field map δB is assumed to originate from the susceptibility distribution χ in the tissue. The correlation between the measured field map δB and susceptibility is given in the k-space as a simple multiplication [127] [47]:

$$\delta B(k) = D(k) \cdot \chi(k) \quad (4.3.1)$$

with $D(k)$ being the general dipole kernel in k-space

$$D(k) = \frac{(-k_x \sin(\theta) - k_y \cos(\theta) \sin(\varphi) - k_z \cos(\theta) \cos(\varphi))^2}{\|k\|^2} + 1/3 \quad (4.3.2)$$

The angles θ and φ denote the orientation of the externally applied magnetic field in respect to the measured reference frame. The dipole kernel becomes zero on a cone surface in k-space ($k^2 = 3k_z^2$ for $\theta = 0$), hence the same field perturbation can be generated by a large number of different susceptibility distributions. As a consequence, the inversion of equation 4.3.1 being $\chi(k) = 1/D(k) \cdot \delta B(k)$ is problematic in regions close to this cone surface. Noise in the measured field is significantly amplified resulting in streaking artefacts in the reconstructed susceptibility maps. Many techniques have been suggested in order to overcome this ill-posed problem.

One method to eliminate the undetermined points covers the whole k-space

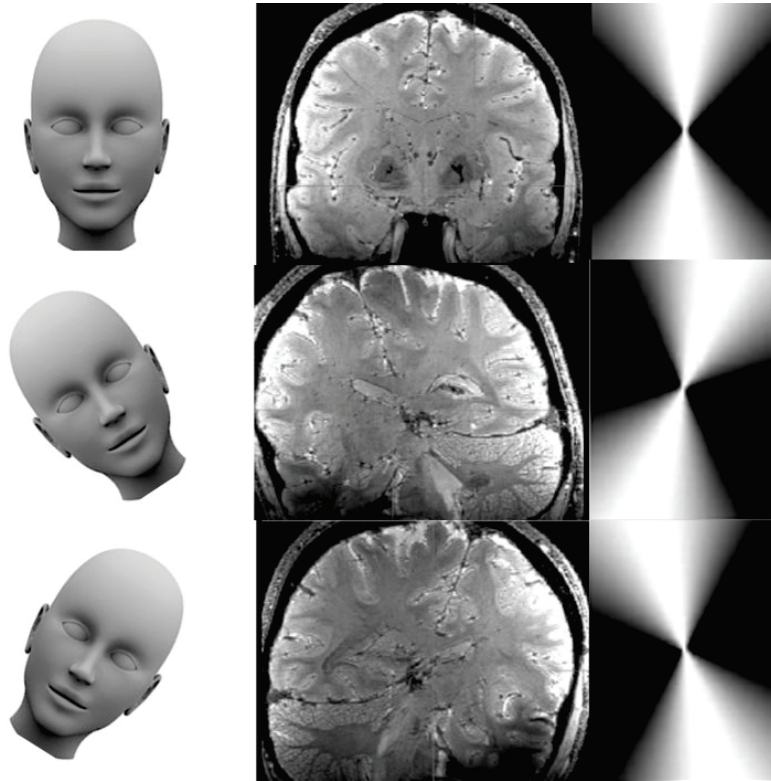


Figure 4.2: shows the head orientation (first column), the acquired signal (second column) and resulting dipole kernel after co-registration (third column).

by measuring the field distribution within the object at several orientations in respect to the main magnetic field and hence providing an over-determination

of the ill-posed problem [128] [54]. Hereby the χ map is calculated iteratively minimizing distance between the measured, δB and the estimated field $F^H D_i(k) F \chi(r)$ for all orientations,

$$\min_{\chi} \sum_{i=1}^N \|M(F^H D_i(k) F \chi(r) - \delta B_i(r))\|_2^2 \quad (4.3.3)$$

Where D_i and $\delta B_i(r)$ are the dipole kernel and measured field perturbation for a specific object position, F denotes the Fourier Transform and M represents the ROI (e.g. brain). The number of measured orientations is indexed by i . The head position, acquired magnitude data and resulting dipole kernel are shown for three different orientations in figure 4.2. A measurement at three orientations was shown to be sufficient for the k-space coverage [54]. Although this procedure is the current state of the art method, it is not practical for clinical studies due to the increased scanning time as well as the limited mobility of some patient populations.

For these reasons many methods were proposed using additional regularization. Generally, the susceptibility reconstruction techniques can be separated into two groups relating to their operating space. One group exploits the prior knowledge in *k-space* (either with direct or iterative methods), while the other group applies the prior knowledge in the *image space*, see figure 4.3.

4.3.1 k-space based reconstruction

The noise amplification artefacts can be reduced by application of a fixed threshold on the k-space positions, which are responsible for the ill-conditioned nature of QSM [129] [130] [131] [132]. The susceptibility distribution is calculated as

$$\chi = IFT\left(\frac{FT(\delta B)}{D(k)}\right) \quad (4.3.4)$$

where the dipole kernel $D(k)$ is set to a constant value when $D(k)$ is below a chosen threshold. However, these methods tend to underestimate the susceptibility.

Iterative k-space methods improve on this by the application of an additional regularization on the region of the ill-conditioned points. One method uses the structural information from a masked approximation of QSM to iteratively replace the ill-conditioned k-space points [133]. Another approach deals with the ill-conditioned cone surface as missing points and iterative compressed sensing is used to retrieve them. In these methods a first approximation QSM is calculated and its k-space points far from the cone sur-

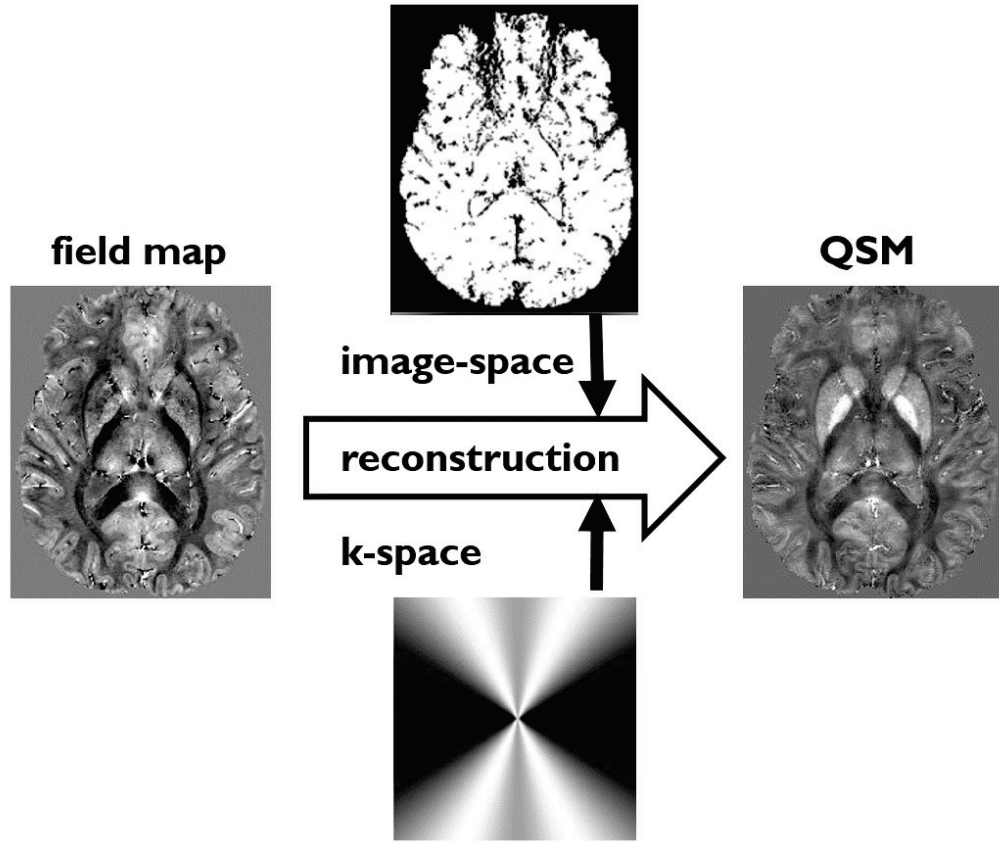


Figure 4.3: prior knowledge applied either on the image space (top) or k-space (bottom) in order to solve the inverse problem.

face are assumed to be well-conditioned. In a second step the l_1 TV norm minimization is performed on the ill-conditioned points while preserving the well-behaved [122] or well-behaved and transitional k-space points [134].

4.3.2 Image space based reconstruction

Methods acting on the image space use iterative regularization. The distance between the measured field and the estimated field caused by the underlying susceptibility is minimized using the l_2 norm while using additional prior knowledge.

$$\min_{\chi} \underbrace{\|M(F^H D_i(k) F \chi(r) - \delta B_i(r))\|_2^2}_{\text{data consistency}} + \alpha \underbrace{\|M M_{\nabla} \nabla \chi(r)\|_{1,2}^2}_{\text{regularization}} \quad (4.3.5)$$

Hence, susceptibility reconstruction is regularized by minimizing the error on the data consistency and an additional regularization term that enforces prior knowledge with either the l_2 norm [135] or the l_1 norm [136] [137]. Here, the prior information is extracted from the phase and/or magnitude maps that one expect to have similar anatomical edges of the underlying brain structure. Another minimization method, in order to account for unreliable phase changes, assumes the data constraint to be complex exponential functions consisting of susceptibility and field while prior knowledge regularization is performed with l_1 TV norm [138].

4.3.3 Direct reconstruction

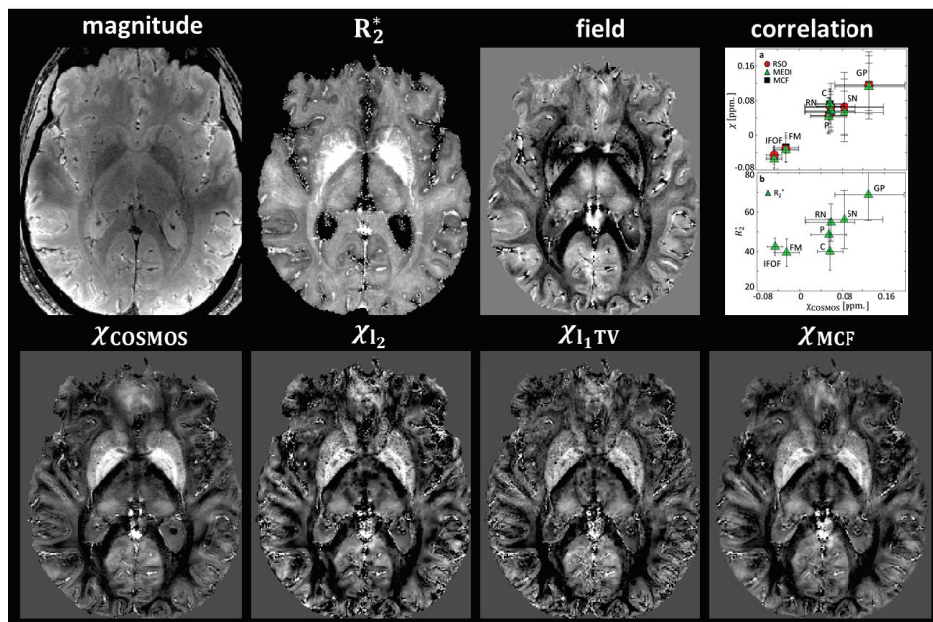
Analytically, a direct inversion formulation for the susceptibility map in the k-space can be used assuming smoothness of the susceptibility map. This formulation relies on l_2 norm minimization of the data consistency and an additional non-iterative regularization based on l_2 norm of the susceptibility gradient [139]. The efficient computation of the closed-form was used to propose a fast l_1 TV iterative regularized QSM [140]. To counterbalance the smoothness of the susceptibility maps induced by the closed-form a weighting in the k-space was introduced [111].

Some of the mentioned methods are evaluated and the performance of QSM reconstructions is more thoroughly analysed in the next chapter.

Chapter 5

Modulated Closed Form

A Modulated Closed Form solution for Quantitative Susceptibility Mapping - a thorough evaluation and comparison to iterative methods based on edge prior knowledge



Abstract

The aim of this study is to perform a thorough comparison of quantitative susceptibility mapping (QSM) techniques and their dependence on the assumptions made. The compared methodologies were: two iterative single orientation methodologies minimizing the l_2 , l_1 TV norm of the prior knowledge of the edges of the object, one over-determined multiple orientation method (COSMOS) and a newly proposed modulated closed-form solution (MCF).

The performance of these methods was compared using a numerical phantom and in-vivo high resolution (0.65mm isotropic) brain data acquired at 7T using a new coil combination method. For all QSM methods, the relevant regularization and prior-knowledge parameters were systematically changed in order to evaluate the optimal reconstruction in the presence and absence of a ground truth. Additionally, the QSM contrast was compared to conventional gradient recalled echo (GRE) magnitude and R_2^* maps obtained from the same dataset.

The QSM reconstruction results of the single orientation methods show comparable performance. The MCF method has the highest correlation ($corr_{MCF} = 0.95$, $r_{MCF}^2 = 0.97$) with the state of the art method (COSMOS) with additional advantage of extreme fast computation time. The l-curve method gave the visually most satisfactory balance between reduction of streaking artifacts and over-regularization with the latter being overemphasized when using the COSMOS susceptibility maps as ground-truth. R_2^* and susceptibility maps, when calculated from the same datasets, although based on distinct features of the data, have a comparable ability to distinguish deep gray matter structures.

5.1 Introduction

Phase imaging has shown over the last decade to offer a good contrast, both between and within brain tissues in respect to the conventional magnitude signal [66] [141] as well as veins and iron rich regions [50]. The effect observed in the phase is known to be non-local, it reflects the magnetic field induced by the tissues' magnetic susceptibility [127], which scales linearly with the increase of the fields strength (making it suitable at high field strengths).

Several studies have been performed on the origin of the susceptibility contrast with the main modulators being iron and myelin. Iron contributes to tissue contrast especially in the deep gray matter (globus pallidus, putamen and caudate) which has histologically derived high iron concentration showing good correlation with phase and susceptibility contrast [52] [55] [54]. The other proposed contributor to the phase contrast, particularly between white and grey matter, is myelin where pathological demyelination has shown a decreased phase contrast between gray and white matter [69] [70] and good correlation was found between myelination and phase contrast during development [70].

In addition to the non-local effects associated with magnetic susceptibility, the chemical shift of water affected by macromolecules has been proposed to influence the measured phase [95] [96] [97]. More recently it was proposed [86] and demonstrated [142] [143] [76] that the microstructural compartmentalization in the organization of lipids on the cellular and subcellular level (e.g. lipids, proteins) has a dominant effect on the contrast observed between white and grey matter in phase imaging.

Nevertheless, despite the last two effects being ignored when doing quantitative susceptibility mapping (QSM), this technique has demonstrated remarkable robustness in the ability to map iron deposition in deep grey matter structures [61] [55] [143]. However, this problem is known to be ill-posed, and many methodologies have been suggested in order to better condition this problem. To make the problem over-determined, field maps of the object have to be measured with the object positioned in different orientations in respect to the magnetic field [128]. This method is not practical for clinical studies, due to the increased measurement time and not applicable to subjects with reduced mobility. For these reasons many methods have been proposed using single orientation field maps together with additional regularization which can be broadly fitted in two classes: (i) correction of the k-space regions responsible by the artifact; (ii) prior-knowledge based on assumptions of smoothness and boundaries of the resulting QSM in the real space. In the first class can be found direct methods that modify the kernel in a certain region which are responsible for the ill-conditioned nature of

QSM [129] [130] [131] [132], and the iterative methods that only use prior knowledge or sparsity constraints (l_1 or TV norm) to reconstruct the ill-conditioned points while trusting the remaining k-space with [134] or without different weighting in the transition regions [122]. Alternatively, in the second approach (ii), the whole k-space is affected by the introduced prior knowledge. The susceptibility calculation can be done by minimizing the l_2 norm in real space field generated by the susceptibility map and the measured field maps together with additional regularization based on prior knowledge with either the l_2 norm [135] (see section 5.2.2) or the l_1 norm [136] [137] (see section 5.2.3). The prior information is extracted from the phase and magnitude maps assuming them to have similar edges of the underlying brain structure or simply assuming that natural images are sparse in some basis set. Recently, it was noted that this could be performed as a direct inversion when assuming smoothness of the susceptibility map [139] (see section 5.2.4). The aim of the present study was to perform a thorough comparison of some of these methods [135] [128] [137] and a newly proposed methodology dubbed modulated closed form (MCF) both in simulations and in in-vivo data. Particularly we accurately evaluate the impact of the prior information and of the regularization parameters and how their optimality can be evaluated in the absence of ground truth. Additionally, the susceptibility results were compared to R_2^* contrast in both the contrast between gray and white matter, deep gray matter and ability to detect multiple sclerosis lesions.

5.2 Theory

The magnetic susceptibility, χ , describes the reaction of a material to the presence of an external magnetic field. The magnetic field perturbation δB generated by a distribution of small magnetic susceptibility under a constant external magnetic field aligned to the z-direction, B_0 , is given by a convolution of χ with the projection of the dipole field along the z-direction, D [127] [47]. In the Fourier domain this can be simplified into a simple local expression:

$$\delta B(k) = D(k) \cdot \chi(k) \quad (5.2.1)$$

Where k are the k-space coordinates and the magnetic dipole kernel can be written in k-space as

$$D(k) = \frac{-k_x \sin(\theta) - k_y \cos(\theta) \sin(\varphi) - k_z \cos(\theta) \cos(\varphi)}{\|k\|} + 1/3 \quad (5.2.2)$$

Where θ describes the angle of rotation around the x-axis and φ the angle of rotation around the y-axis. These angles characterize the orientation of

the externally applied magnetic field, B_0 , in respect to the z-direction of the object.

The dipole kernel in k-space has zero elements located in two conical surfaces. These surfaces lie at the magic angle direction in respect to the main magnetic field orientation. This means that the same field perturbation can be generated by a large number of different susceptibility distributions. As a consequence the direct inversion of (5.2.1) is an ill posed problem and noise in the measured field, $\delta B(r)$, gets significantly amplified in k-space regions close to the two surfaces, leading to streaking artifacts in the reconstructed susceptibility maps. In the following subsections a detailed description of the methods evaluated to overcome the ill posed nature of QSM will be given.

5.2.1 Multiple orientation method - COSMOS

Calculation Of Susceptibility through Multiple Orientation Sampling (COSMOS) takes advantage from the observation that the zero surface of the dipole kernel rotates with the magnetic field orientation B_0 [128] [127]. Hence the straightforward methodology to overcome the ill posed nature of QSM implies the measurement of the field perturbation with the object oriented in various directions in respect to B_0 [128] [127]. The χ map can then be calculated iteratively using a least squares conjugate gradient algorithm that minimizes,

$$\min_{\chi} \sum_{i=1}^N \|M(F^H D_i(k)F\chi(r) - \delta B_i(r))\|_2^2 \quad (5.2.3)$$

Where D_i and $\delta B_i(r)$ denote the dipole kernel and field perturbation for a specific object position, i indexes the multiple object orientations, F represents the Fourier Transform. M is a spatial mask that represents the regions inside the brain and is further modulated by a weighting term that guarantees that the noise throughout the field is equalized.

5.2.2 l_2 regularized single-orientation method

In the case where it is only possible to measure the field perturbation with the object positioned along one single orientation, extra information has to be introduced in the process of calculating the χ map. It is fair to assume that (i) the χ maps vary smoothly within anatomical boundaries/different tissue regions and (ii) that the artifacts, which are caused by the missing information around the magic angles, have structured sharp edges which cannot be found in the corresponding magnitude image. Consequently, regularization based on the l_2 norm of the gradient has been widely promoted to tackle this

problem [135]. As both the magnitude and the phase image images [134] are expected to have similar edges as the underlying susceptibility distribution, they can be used as additional information to avoid the smoothing of the χ distribution close to tissue boundaries.

The Regularized Single-Orientation (RSO) method incorporates prior knowledge of the expected edges by solving the following minimization problem using a least-squares conjugate gradient algorithm

$$\min_{\chi} \|M(F^H D_i(k)F\chi(r) - \delta B_i(r))\|_2^2 + \beta \|MM_{\nabla}\nabla\chi(r)\|_2^2 \quad (5.2.4)$$

Where the first term minimizes the distance between the estimated and measured field and the second term is the regularization prior tuned by a parameter *beta*. The regularization term is a pixel by pixel multiplication of gradient of the susceptibility by a mask, M_{∇} , containing prior information regarding the regions where the gradients along a Cartesian direction are expected ($M_{\nabla} = 0$) or not ($M_{\nabla} = 1$). Both the regularization parameter and the gradient mask definition have a strong impact on the calculated χ map, the calculation of the latter will be discussed in the methods sections.

5.2.3 l_1 total variation denoising method

Alternatively, because the χ maps, as many other natural images, have well defined sharp contours surrounding areas of constant signal, total variation priors l_1 methods have been proposed in literature [52] [136]. l_1 norm minimization boosts sparse solutions with a small number of non-zero elements and represents a useful convex relaxation of the l_0 norm, which simply counts the number of signal coefficients [144] [145]. To facilitate the convergence, similarly to what has been suggested in the previous section for the l_2 method, a prior information mask including the edge information, can also be applied [137] [146]. The susceptibility map is reconstructed from the field map by solving a so-called total variation denoising, TVDN [147], problem consisting of minimizing the TV norm of χ (the l_1 norm of the gradient) which is subject to the same data constraint as for the l_2 regularization:

$$\min_{\chi} \|MM_{\nabla}\nabla\chi(r)\|_1^2 \quad s.t. \quad \|M(F^H D_i(k)F\chi(r) - \delta B_i(r))\|_2^2 < \varepsilon \quad (5.2.5)$$

In this constrained minimization, it is assumed that the data consistency term follows a χ^2 distribution. The value of the bound ε is thus driven by the noise statistics and should be simply set to a high percentile, of about 99%, of this distribution.

5.2.4 Modulated Closed Form solution

The closed-form (CF) solution described in [139] relies on the Tikhonov problem $\min_{\chi} \|(F^H D_i(k) F \chi(r) - \delta B_i(r))\|_2^2 + \beta \|\nabla \chi(r)\|_2^2$, which can be evaluated in closed form as $\chi(r) = \|(F^H D^2(k) F + \beta \nabla^H \nabla)\|^{-1} F^H D(k) F \delta B_0(r)$. The gradient operator along a direction i can be described as $\partial_i = F^H E_i F$, where F is Fourier Transform, E_i is given by $E_i = 1 - e^{(-2\pi j k_i / N_i)}$, and k_i is the k-space coordinate along i direction. Using the k-space representation of the gradient operator the closed form can be analytically formulated as $\chi(k) = \frac{D(k)}{D(k)^2 + \lambda^2 \sum_{i=1}^{n=3} E_i^2} \delta B(k)$. This method is extremely fast but, when compared to the previously described iterative methods, the application of the gradient regularization in the whole image (and k-space), gives rise to smoother χ maps. To overcome these limitations, a weighting in the k-space of the regularization term was introduced to ensure that the regularization is only applied on the ill-conditioned k-space points, where the dipole kernel is smaller than a given threshold n_{th} . The final expression of the modulated closed-form (MCF) solution can be written as

$$\chi(k) = \frac{D(k)}{D(k)^2 + \lambda^2 \Lambda(k)^2 \sum_{i=1}^{n=3} E_i^2} \delta B(k) \quad (5.2.6)$$

where $D(k)$ is the k-space representation of the dipole kernel, λ is a regularization parameter, and $\Lambda(k)$ is a weighting matrix defined as

$$\Lambda(k) = \begin{cases} \cos\left(\frac{\pi/2 D(k)}{n_{th}}\right), & D(k) < n_{th} \\ 0, & D(k) > n_{th} \end{cases}$$

5.3 Methods

5.3.1 Numerical Simulation Phantom

A 3-dimensional numerical simulation phantom consisting of 64x16x64 pixels containing 7 cylinders with different magnetic susceptibilities (between 2-14 a.u.) was used to evaluate the reconstruction performance of the different quantitative susceptibility mapping methods. The field map was calculated by using (5.2.1) assuming a magnetic field aligned along the z-direction. Zero mean Gaussian noise was added to the numerical phantom and the field map with the resulting SNR was defined in dB as $SNR_{dB} = 10 \log_{10} \frac{\sigma_{noise}^2}{\sigma_{image}^2}$ with σ_{image}^2 being the variance of the image without noise and σ_{noise}^2 being the noise variance of the background. This scaling was used to match the definition of noise in 5.2.5. For the numerical simulations a metric that was

initially suggested in [135] was used to create a continuous gradient mask (if $abs(\nabla Magn) < n_{th}\sigma_{Magn}$, $M_{nabla} = 1$, else $M_{\nabla} = n_{th}\sigma_{Magn}/\nabla_{Magn}M$) and a binary mask (if $abs(\nabla Magn) < n_{th}\sigma_{Magn}$, $M_{nabla} = 1$, else $M_{\nabla} = 0$).

5.3.2 In vivo Data

5.3.2.1 Data Acquisition

Three healthy volunteers (2 male and 1 female, mean age of 30 ± 6 years) and one multiple sclerosis patient were scanned according to a protocol approved by the local ethics committee. Scans were performed on a 7T MR scanner (Siemens, Erlangen, Germany) using a 32 channel receive coil (Nova Medical). The protocol consisted of a standard T_1 -w MP2RAGE contrast [148] and T_2^* -w imaging using 3D gradient echo multi echo sequence. The 5 acquired echoes were equally spaced and acquired with the same polarity gradients, the rewinding waveform was kept equal to the readout gradient waveform to ensure flow compensation between successive echoes. The following parameters: TR/TE1/TE5= 42/4.97/37.77 ms; bandwidth (BW)=260 Hz/Px; FA=10°, FOV=256×192×137mm, spatial image resolution $660\mu\text{m} \times 660\mu\text{m} \times 660\mu\text{m}$; iPAT=2×2; Tacq=11min. This protocol was performed only once for the MS patient while for the healthy volunteers the 3D-GRE sequence was repeated 4 times with different head positions: normal; head tilted around medio-lateral axis(left–right axis, pitch) in head-to-neck direction (up to 14°) position; tilted around anterior-posterior (nose-neck axis, roll) in head-to-left-shoulder direction (up to 25°) and head-to-right-shoulder direction (up to 25°). For the co-registration protocol to cope with the large head rotations that resulted in large variations of the image intensity, a bias field correction was applied to all magnitude images using FSL-FAST. Subsequently, a first co-registration in was conducted prior to brain extraction in order to achieve a rough alignment of the structural images. Brain extraction was then performed to the co-registered head positions. On the resulting brain extracted images an additional FSL-FLIRT co-registration was calculated to get a more accurate registration. The movement matrices of the first and second stage co-registration were combined and the resulting movement matrix was applied to the original head positions to minimize the effect of double smoothing from FSL-FLIRT.

5.3.2.2 Data processing

All data processing was performed in MATLAB (version 2010b, The MathWorks, Natick, MA, USA) on a workstation (2x Intel Xeon X5650) with 96

GB RAM. The multi-channel GRE data from the different coils was combined using a pixel by pixel SVD factorization of the channel vs. echo time matrix. The first singular value of the diagonal matrix is the maximum signal that can be coherently constructed from the 32 channels and the 5 echoes acquired, the corresponding eigenvectors correspond to the 32 complex coil sensitivity estimations that produce the desired image and the complex signal evolution along the 5 echoes. Because the analysis is done on a pixel by pixel basis, the phase is somewhat arbitrary but the phase differences between successive echoes are not. This methodology gives the optimum SNR both for the magnitude and phase evolution as the coil sensitivities are constructed using the whole dataset and not only the first echo.

5.3.2.3 Field and R_2^* Map calculation

The GRE phase differences between successive echoes were then unwrapped with a 3D phase unwrapping algorithm [117] in order to put the least demand in terms of number of wraps the algorithm had to cope with (also, by using phase differences between successive echoes, the data is devoid of phase singularities). Four field maps were computed by integrating the phase differences from the first to echo n ($n=2:5$) and the final field map was calculated using the phase differences between each phase image and that of TE1, weighted as in [113] using a pixel by pixel R_2^* estimation. Because the magnitude images for each echo were computed by complex coil combination followed by taking the absolute part of the complex signal (Im_{ec}), and not by simple sum of squares of the separate coils, the magnitude evolution is not biased by Rician noise to the same extent (see Appendix for a discussion). Hence, the R_2^* maps can be robustly calculated by integration of the magnitude decay:

$$R_2^* = \frac{\sum_{echo=1}^{N-1} (abs(Im_{echo}) + abs(Im_{echo+1}))/2}{abs(Im_1) - abs(Im_N)} \quad (5.3.1)$$

5.3.2.4 Background field removal

The measured field, δB , inside the brain consists of the sum of internal variations, δB_{in} , the mean brain susceptibility, B_{mean} , and variations induced by external sources, δB_{out} , such as air tissue interfaces and imperfect shimming. This background field (δB_{out}) was removed from the calculated field map using the recently proposed Efficient and Automated Harmonic Field Pre-Filtering [125]. As it is known that the Laplacians (Δ) of δB_{out} and δB_{mean} are equal to 0, δB_{in} was calculated by solving the following minimization

problem

$$\min_{\delta B_{in}} \|W_{\Delta}(\Delta\delta B - \Delta\delta B_{in})\| \quad (5.3.2)$$

with W_{Δ} being a shrunked brain mask modulated by the SNR of the measured field map. This methodology has the advantage of reducing the erosion around the brain introduced by methods such as SHARP [55] and is less prone to introducing artifacts due to phase errors in regions of low SNR.

5.3.2.5 Gradient Mask calculation

The results obtained with the simulations suggested there was no added value from introducing the continuous gradient mask, therefore with the in vivo data only the binary mask was used. The in vivo gradient mask integrated information from the R_2^* and δB_{in} as suggested in recent studies [134]. Because the two data sets have different noise characteristics, the images were first wavelet denoised and the gradients of each image were calculated. The final mask was defined as (if $(abs(\nabla R_2^*) < P_{abs(\nabla R_2^*),nth})$ AND $abs(\nabla\delta B_{in} < P_{abs(\nabla\delta B_{in}),nth})$, $M_{\nabla} = 1$, else $M_{\nabla} = 0$), where P_{nth} represents the gradient corresponding to a percentile n_{th} . Although the two methodologies are not equivalent, they both reflect a variation of the number of points used to define the mask, so there should be a simple monotonic relationship between the two.

5.3.2.6 Susceptibility mapping and evaluation

Four different reconstruction algorithms were evaluated both for the numerical simulations and the in vivo data: l_2 minimization (section 5.2.2), l_1 TV minimization (section 5.2.3) and modulated closed form solution (section 5.2.4). The COSMOS method (section 5.2.1) was used to calculate the in vivo ground truth susceptibility map.

For all methods their reconstruction parameters were varied systematically over a wide range (β for the l_2 , ε for l_1 TV minimization, and λ for closed-form solution) as well as the masking defining parameter, n_{th} . The reconstruction performance of the methods in respect to the ground truth was computed as $\|\chi_{recon} - \chi_{GroundTruth}\|_2 / \|\chi_{GroundTruth}\|_2$. The heuristic L-curve method [149] was also evaluated as a possible mean to estimate the optimal reconstruction. This method consisted in the assessment of the data consistency term, $\|M(F^H D(k)F\chi(r) - \delta B_0(r))\|_2^2$, as a function of the regularization term of each method while varying values of the respective regularization parameters. The optimal reconstruction was considered as the parameter set of largest curvature on the L-curve (maximum of second derivative) as done by [52].

To evaluate the impact of the regularization used on the various single orientation methods on the measured susceptibility, regions of interest were defined using fslview (www.fmrib.ox.ac.uk) on the following brain regions: GP -globus pallidus; SN - substantia nigra; C – caudate; RN - red nucleus; P – putamen; FM - forceps major; IFOF - inferior fronto-occipital fasciculus. Various regions of interest with changing susceptibility values were defined and masking of these regions was manually performed. The mean value is derived from first averaging voxels for each ROI within individual subjects and then averaging over three subjects. The error was calculated as the mean value over the different subjects of the standard deviation in each ROI.

5.4 Results

5.4.1 Numerical simulation phantom

To determine the influence of different parameters on the reconstruction quality of the susceptibility maps we compared the performance of the different algorithms on the simulated data set. When using a continuous prior for the l_2 algorithm, the range of the regularization parameter β was restricted to values in the range of one order of magnitude (figure 5.1a). When using a binary mask prior for the l_2 algorithm, the range of acceptable regularization increased by a factor ~ 10 , (figure 5.1b). Generally, the reconstruction quality of the susceptibility maps was higher using the binary mask as the prior information and the optimum β value increases with the reduction of the threshold.

These observations were similar when using the l_1 denoising algorithm similar for the continuous and binary mask reconstructions (fig.5.1c and 5.1d), however, an increased independence on the parameter ε was noted, provided the optimal threshold was achieved (marginally higher than for the l_2 method) and lower deviation from the ground truth was observed. This reconstruction quality was for both, l_1 TV and l_2 , algorithms less parameter dependent when using the binary mask, hence only this mask was used in the in vivo applications.

When setting the prior information to a high threshold (regularization was applied virtually on all pixels) lead only to a blurred reconstruction of the susceptibility in areas where the edges were not identified if the regularization parameter was not “correctly” defined (compare 1f and g for l_2 method and 1i and 1j for l_1 method). When using a low threshold lead to noise propagation in the reconstructed susceptibility maps (see fig. 5.1h and 5.1k), implying that a priori information is required to ensure a good reconstruction quality

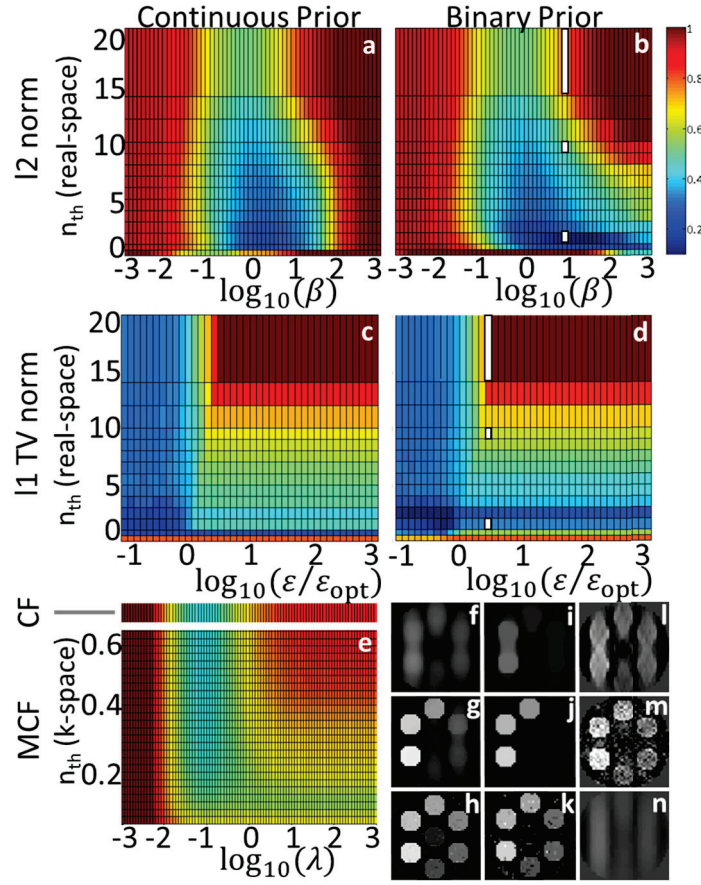


Figure 5.1: First, second and third rows show the reconstruction error for l_2 norm (a,b), l_1 TV norm (c,d) and modulated closed form and closed form solution (e) of the numerical simulated data (zero being the lowest reconstruction error). The reconstruction error maps have as x-axis their dependence on the regularization parameters: β for l_2 norm (a, b), ε for l_1 TV norm (c, d) and λ for modulated closed form (e). The reconstruction error maps have as y-axis their dependence on the threshold value n_{th} : for prior information using the continuous mask (a, c), the binary mask (b, d) and threshold in the k-space modulation mask (e). The white squares are pointing the parameter-set out for the reconstructed susceptibility maps using the binary mask calculated with; l_2 norm (f-h), l_1 TV norm (i-k) minimization and modulated closed form (l-n) for different thresholds having; many points excluded (h, k, n), little points excluded (g, j, m) and almost no points excluded (f, i, l) (low, high and very high threshold).

as well as independence of the reconstruction from regularization parameter. The modulated closed form method has reconstruction errors smaller than those obtained both with similar direct methods proposed by other groups [139] [130]. Not surprisingly, the optimum results (and independence on the regularization parameters) are found when the regularization is limited to a region tightly positioned around the magic angle cones ($n_{th} = 0.1-0.2$) as done in other k-space modulated iterative methods [134] [122].

5.4.2 In vivo Data

5.4.2.1 Qualitative comparison of multiple orientation susceptibility and R_2^* maps

Following the evaluation of the algorithms on simulated data, we evaluated their performance on 3D-GRE data obtained as described in the methods section. The magnitude data obtained was computed after estimating the coil sensitivities that explain the maximum power of the signal over all echo times. As expected, the magnitude signal has high intensity variations associated with the use of the surface coil reception (the transmit coil effect is less clear). This methodology allows the calculation of very robust R_2^* maps over the whole brain which show both good vein delineation and deep grey matter contrast (thanks to the strong magnetic susceptibility of de-oxygenated blood and iron) but also contrast between different white matter bundles (optic chiasm and the internal capsule amongst others are very clearly distinguishable) and grey white matter contrast (increased contrast is perceived on the frontal white matter in respect to the occipital and parietal). The background field removal quality from the complex data can be seen from the absence of large fields close to the boundaries together with the Laplacian of B_{out} having no visible brain structure information. Note that this method allows most of the brain to be kept after background removal (including cortical regions parallel to the brain surface).

The resulting high spatial resolution susceptibility maps obtained with COSMOS show the expected features described in other reports at 7T [150]. In addition to deep grey matter regions, and the thalamic nuclei, white matter and significant variations of the contrast in different cortical regions were noted: e.g. the rim of increased para-magnetism of the frontal cortex noticeable at its white matter surface; increased para-magnetism of the occipital cortex in respect to the frontal cortex was evident from increased contrast. The latter is in agreement with previous reports increased transverse relaxation rates (decreased T_2) in the occipital contrast in respect to both white matter and frontal cortex [151].

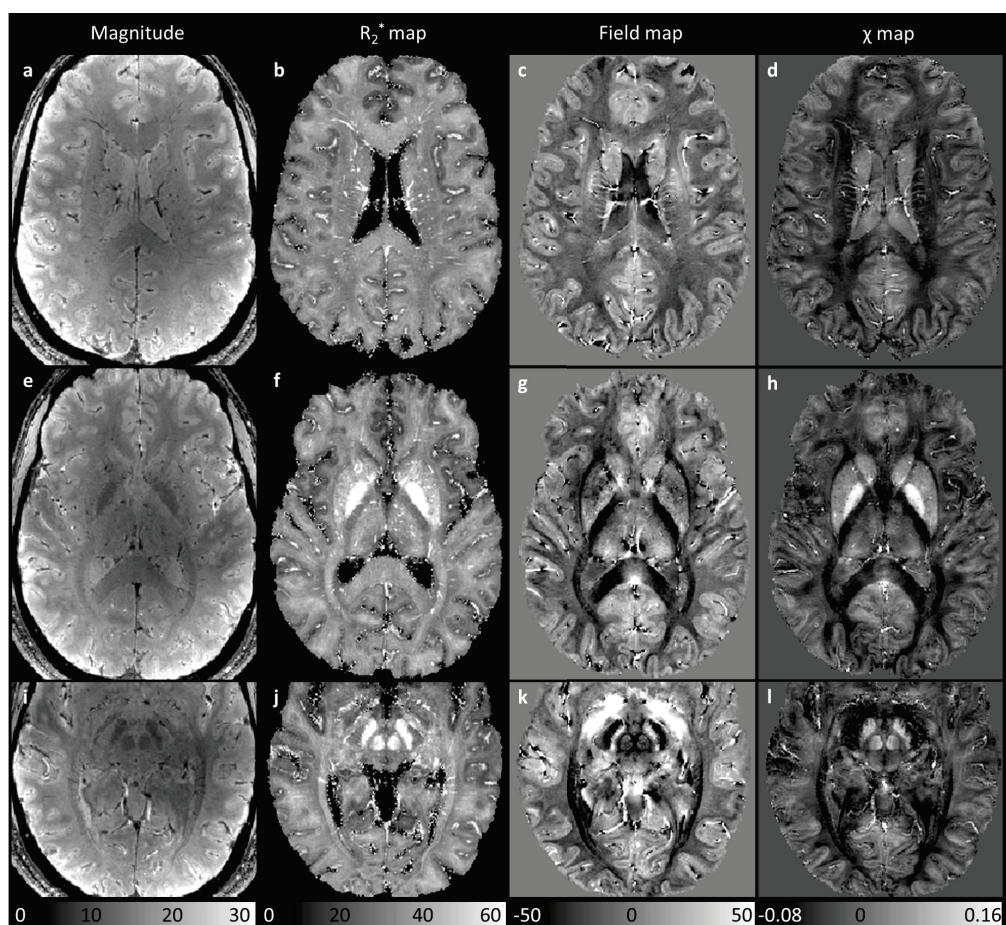


Figure 5.2: First, second, third and fourth rows show: magnitude, R_2^* , field and susceptibility map reconstructed with the COSMOS method. Different rows show axial slices covering cortex (a-d); basal ganglia (e-h); substantia nigra (i-l).

5.4.2.2 Single orientation susceptibility mapping methods

To evaluate the reconstruction quality of the single orientation methods for a given regularization and threshold the power of the difference to the susceptibility maps was calculated with the COSMOS method, which was considered as the reference method, similarly to what was done for the numerical simulations.

When using the l_2 norm algorithm the optimum β value increased with the reduction of the non-zero points (points where the regularization is effectively applied) present in the binary mask similar the numerical simulations.

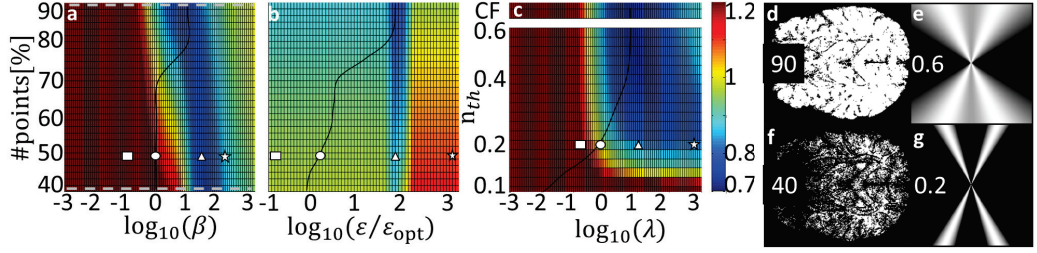


Figure 5.3: First, second, third column show the mean reconstruction error of all in-vivo data (zero being the lowest reconstruction error) dependence on regularization parameters β for l_2 norm (a), ε for l_1 TV norm (b) minimization with binary prior and λ for modulated closed form solution (c). The white squares, circles, triangle and star are pointing the parameter-set out for the reconstructed susceptibility maps used in figure 5.4 as examples of under regularization, optimal regularization based on L-curve heuristic, optimal regularization based on power of difference to the ground truth (reconstruction with COSMOS method) and over regularized reconstruction respectively. An example of the; binary prior M_{∇} along the left-right direction where 90 and 40 percent of the pixels are non-zero is shown on panels (d) and (f), and weighting mask $\Lambda(k)$ in the k-space for thresholds 0.2 and 0.6 is shown on panels (e) and (g) respectively.

The reconstruction quality using the l_1 algorithm shows good reconstruction using an optimal regularization parameter, although “better” results seem to be achieved using a binary mask with a high percentage of non-zero points unlike in numerical simulations. When using modulated closed form method optimal results were achieved when regularizing a relatively high region around the magic angle ($n_{th}=0.3$), as judged from the used weighting matrix in (figure 5.3 for e) broad and g) tight region around the magic angle). To verify the quality of the suggested optimal parameter set, susceptibility reconstructions for different parameter sets were compared (figure 5.4). After this initial evaluation all the remaining calculations of susceptibility maps shown throughout this manuscript were based on the following choice of parameters: the gradient weighting mask was defined with a $n_{th}=50\%$; the modified closed form solution was obtained with $n_{th}=0.2$. Therefore, the modified closed form solution was selected due to its ability to provide results that are largely independent from the regularization parameter.

Figure 5.4 shows a small section of a coronal slice where the striking artifacts from the ill conditioned nature of susceptibility mapping originating

from a large vein are clearly visible. The original phase measurement in those voxels is expected to have the largest errors, either due the low SNR of those voxels or due to incomplete flow compensation (only first order flow compensation was used). The impact of the regularization parameters for the different single orientation magnetic susceptibility methodologies can be observed both in the reduction of the striking artifacts and the intensity and separation between the different deep grey matter structures (and their intensities). When largely under-regularized solution was used, all methods exhibited large striking artifacts with the largest, unsurprisingly, being those associated with the CF and MCF methodology (left column of figure 5.4). Iterative methods are intrinsically regularized by the limited number of iterations. The QSM maps that suffers the most from over-regularization method are the l_2 based methodology (l_2 norm and CF) in which the values of all brain structures had reduced intensity due to the smoothness constraint as shown on the right column of figure 5.4. The l_1 based method suffered less in the over-regularized regime in terms of intensity attenuation, with the over-regularization manifesting itself in the piece-wise smoothness of different white matter regions (right column of figure 5.4). The MCF method

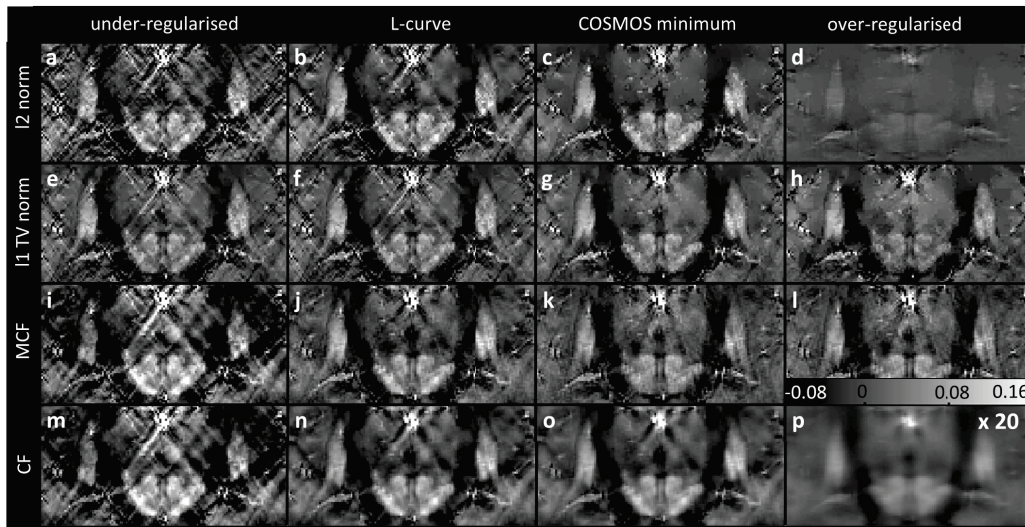


Figure 5.4: First, second, third and fourth columns show the reconstructed susceptibility maps in case of an under-regularization (a, e, i, m), optimal regularization based on L-curve heuristic (b, f, j, n), optimal regularization based on the power of difference to the COSMOS method (c, g, k, o) and over regularization (d, h, l, p). Different rows show susceptibility maps reconstructed with: l_2 norm (a-d); l_1 TV norm minimization (e-h), modulated closed-form solution (i-l) and closed-form solution (m-p).

had the lowest impact of the over-regularization, although most striking artifacts have clearly disappeared. This was attributed to the use of a mask with a k-space smoothness term applied ($n_{th}=0.2$) means that large sections of the k-space suffer no regularization, in contrast to the CF method where the whole k-space is regularized. For example, in the image space it can be seen that the red nucleus has a sharper edge on its vertical orientation than on the oblique ones. Surprisingly, many of these over-regularized features can still be observed for regularization parameters that corresponded to a minimum deviation from the solution using the over-determined COSMOS method (solutions corresponding to colder colors in Figure 5.2 a-c). Using the heuristic L-curve point (represented in Figure 5.2 a-c by the black line) indicated solutions with reduced striking features where the intensity of the all deep grey matter structures was better preserved. For example, in the MCF image with the L-curve derived regularization (Fig. 5.4j) it can be seen that the red nucleus has a sharper edge on its vertical orientation than on the oblique ones while in the CF solution (Fig. 5.4n) the all the boundaries appear smoother.

Figure 5.5 shows the impact of different prior information mask, M_{∇} , for l_2 norm and l_1 TV norm minimization and weighting mask, $\Lambda(k)$, for modulated closed form solution. Applying M_{∇} , with a small number of non-zero points (40%) on the single orientation methods (l_2 norm and l_1 TV norm), leads to a regularization performed only on a limited number of pixels causing noise amplification (red arrows in fig. 5.5). When the percentage of non-zero points is high (70%), the regularization is performed everywhere, only excluding points with the strongest edge information, causing a blurred susceptibility map (fig. 5.5c, f). In the case of the MCF method, a very tight weighting mask ($n_{th}=0.1$), only a small number part of ill-conditioned points close to the magic angle cones were included in the regularization, causing noise related amplification artifacts (blue arrows in fig. 5.5g). Green arrows point out the border between the substantia nigra and the red nucleus and the lamina pallidi, which can be easily distinguished using an optimal cone around the magic angle ($n_{th}=0.2$), but not when applying the regularization on almost the whole k-space as done by the regular closed form solution (fig 5.5h, i).

High quality whole brain images could be obtained with the three single orientation methods using a regularization parameter obtained from the L curve analysis, although the best separation between the red nucleus and substantia nigra on the coronal slices was obtained with the COSMOS method (see Fig. 5.6). The COSMOS reconstruction also showed previously reported [150] differentiable grey white matter contrast throughout the brain with a thin paramagnetic layer being observed in the frontal cortex in the

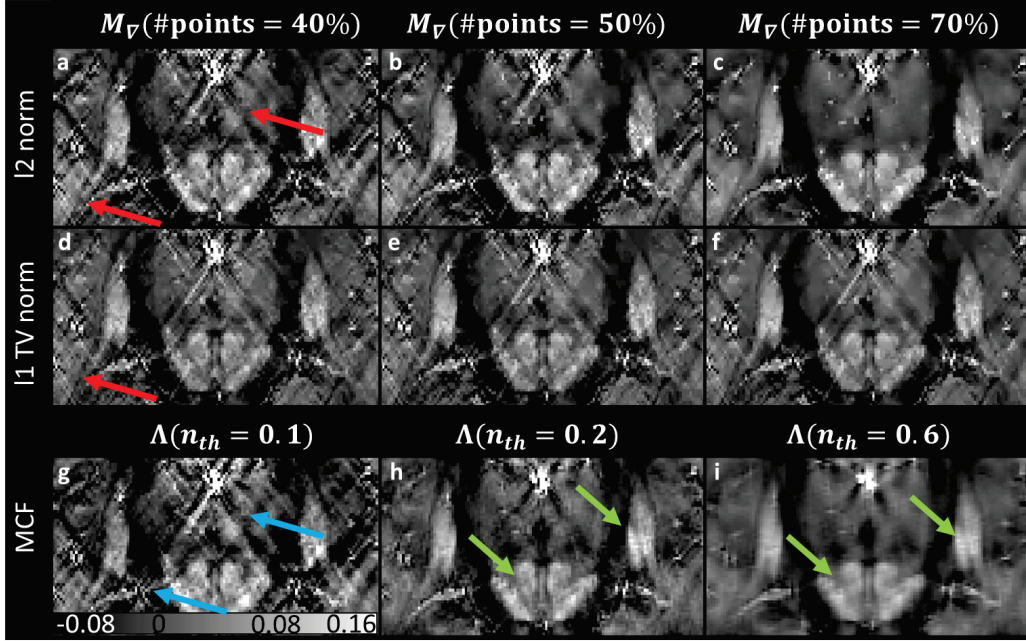


Figure 5.5: First, second and third columns show the reconstructed susceptibility maps with optimal regularization based on L-curve heuristic in the case of different prior information mask M_{∇} (a-f) for l_2 norm and l_1 TV norm minimization and weighting mask $\Lambda(k)$ for modulated closed form solution (g-i). The M_{∇} was varied from low to high percentage of non-zero points; 40% (a, d), 50% (b, e) and 70% (c, f) and $\Lambda(k)$ from tight to broad region around the magic angle with n_{th} ; 0.1 (g), 0.2 (h), 0.6 (i). Different rows show susceptibility maps reconstructed with: l_2 norm (a-c); l_1 TV norm minimization (d-f) and modulated closed-form solution (g-i).

GM – WM interface (highlighted with a yellow arrow). This layer is not so clearly observable on any of the single orientation methods χ maps. The red arrows show regions where the iterative single orientation methods (l_2 norm and l_1 TV norm minimization) have noise amplification problems associated with regions where, due to the high gradients observed on the field map and R_2^* maps, the gradient weighting terms, M_{∇} , had many contiguous points equal to zero, and hence no regularization was effectively applied. In this case the degree of prior knowledge of the susceptibility information effectively deteriorates the images reconstructed with these methods. The blue arrows highlight the white matter (optic radiation bundle) contrast observed throughout all the χ mapping methodologies. The green arrow shows the strong contrast and geometrical delineation of the cerebellum dentate nu-

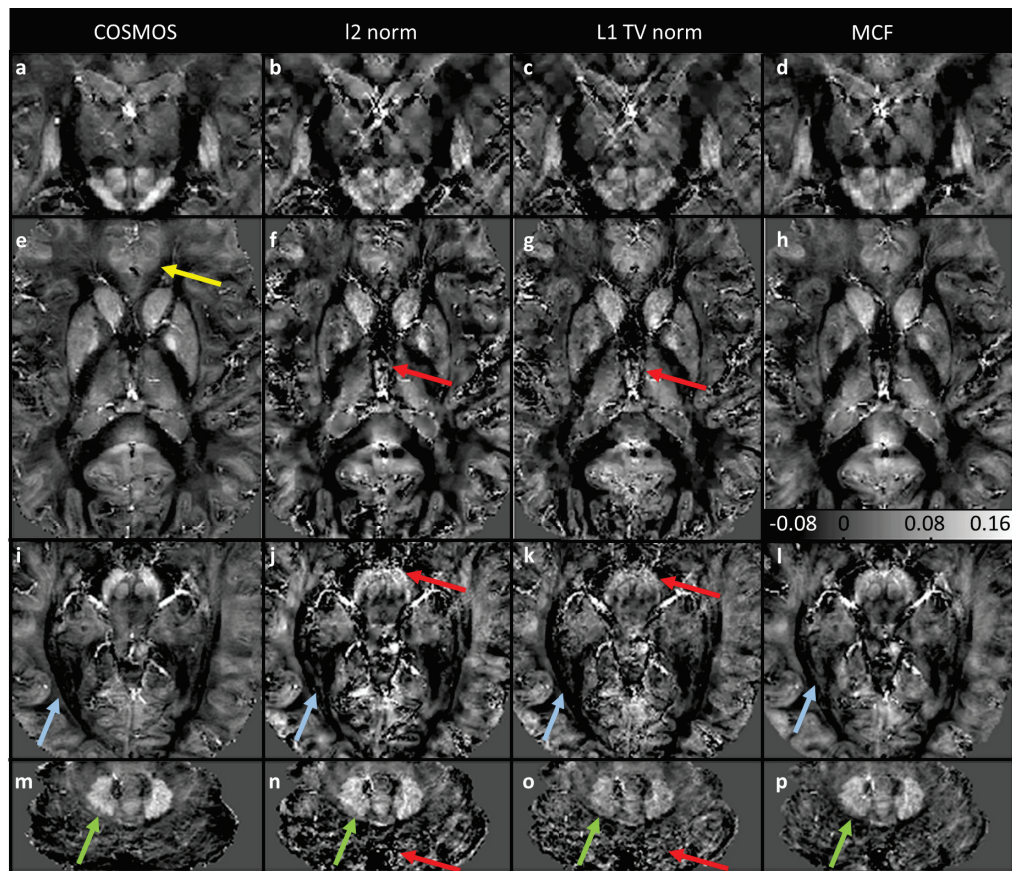


Figure 5.6: First, second third and fourth columns show susceptibility maps reconstructed with: COSMOS method (a, e, i, m); l_2 norm minimization (b, f, j, n); l_1 TV norm minimization (c, g, k, o) and modulated closed-form solution (d, h, l, p). Reconstructions were obtained with optimal regularization parameters as defined by L curve heuristic (see circles on Figure 5.3). Different rows show: coronal slice cutting the substantia nigra and the red nucleus (a-d); axial slice through basal ganglia (e-h); axial slice through substantia nigra (i-l), axial slice through the nucleus dentatus in the cerebellum (m-p). Colored arrows highlight: red - regions where prior knowledge introduced artifacts on iterative methods; blue - white matter contrast; yellow - frontal grey matter structures with enhanced subcortical contrast; green - structure of the nucleus dentatus.

cleus that appears with lower intensity on the l_1 TV norm minimization χ map but is otherwise successfully reconstructed.

5.4.2.3 Quantitative comparison of susceptibility and R_2^* mapping

To compare the performance of the different χ reconstruction methods and R_2^* maps the correlation was evaluated in ROI in deep GM and WM. All single orientation methods (l_2 norm (red circle), l_1 TV norm (green triangle) and MCF method (black square)) showed a linear correlation of the ROI with respect to the multiple-angle COSMOS method (see Fig. 5.7a) ($corr_{l_1}=0.94$, $r_{l_1}^2=0.94$, $corr_{l_2}=0.93$, $r_{l_2}^2=0.96$, $corr_{MCF}=0.95$, $r_{MCF}^2=0.97$). The regions

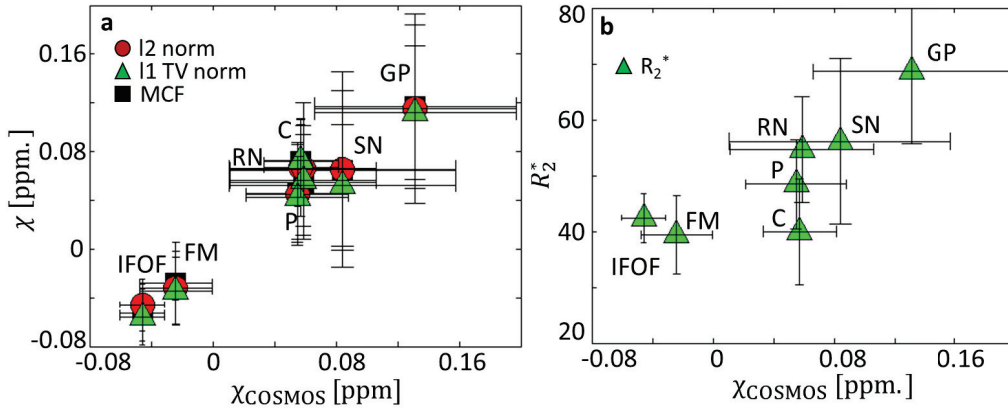


Figure 5.7: Shows the correlation between the average susceptibility values calculated with single orientation methods; l_2 norm (red circle), l_1 TV norm (green triangle) and MCF method (black square) (a), R_2^* map (b) and the COSMOS method on various manually defined regions of interest ($corr_{l_1}=0.94$, $r_{l_1}^2=0.94$, $corr_{l_2}=0.93$, $r_{l_2}^2=0.96$, $corr_{MCF}=0.95$, $r_{MCF}^2=0.97$, $corr_{R_2^*}=0.304$, $r_{R_2^*}^2=0.77$). Error bars represent the standard deviations of the mean value in each ROI over the different subjects. The labels represent: RN-red nucleus, SN-substantia nigra, GP-globus pallidus, P-putamen, C-caudate, FM-Forceps major, IFOF-Inferior fronto-occipital fasciculus.

with the highest standard deviation (substantia nigra and globus pallidus) show also the highest difference within the single orientation methods. When performing the same analysis as done in Fig. 5.7a using the single orientation methods of the remaining head positions, the substantia nigra had a tendency to be underestimated, yet the underestimation was always smaller than the variability observed in the ROI of the different subjects. Although a correlation could be found between R_2^* and χ values for the deep gray matter structures, it should be noted that for some of the deep gray matter structure significant R_2^* variations were observed without a corresponding variations on susceptibility (Figure 5.7b). The standard deviation found within each deep

gray matter ROI in the R_2^* maps was of the order of magnitude of the difference between their mean values while for the susceptibility this ratio was increased. As reported in order studies, the difference between white matter and deep gray matter was significantly increased for the susceptibility [150] which is to be expected given that the individual contributions of iron and myelin both tend to increase relaxation, whereas for susceptibility they have opposite behavior.

5.4.2.4 Multiple sclerosis lesion detection

The ability of χ maps to detect multiple sclerosis lesions was compared to conventional GRE acquisition contrasts (magnitude, R_2^* , field) and MP2RAGE T_1 -weighted images. Figure 5.8 shows a dataset from a multiple sclerosis patient where only one head orientation was acquired, and hence the COSMOS susceptibility map could not be calculated. The green arrow points

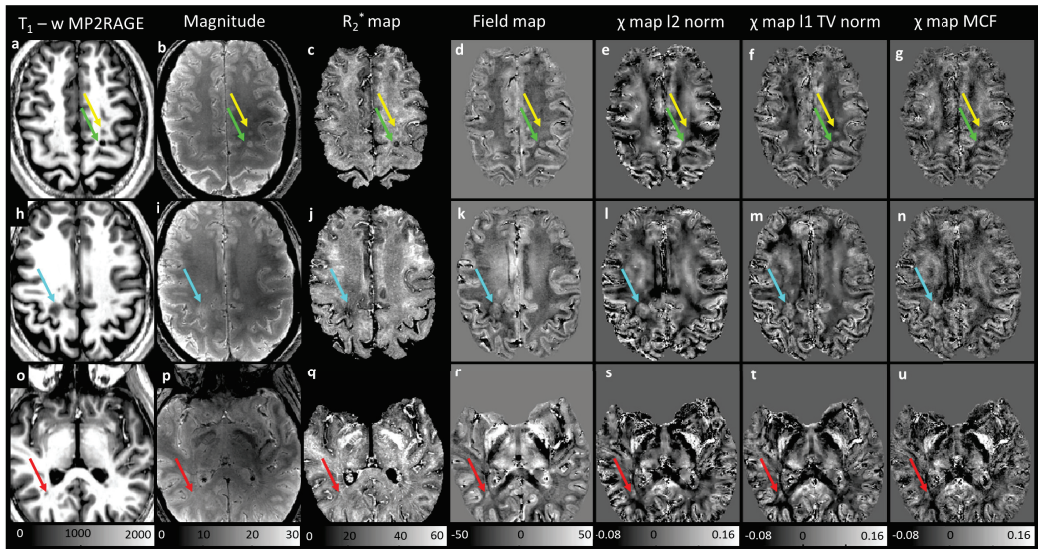


Figure 5.8: First, second third, fourth, fifth sixth and seventh columns show: T_1 -weighted, magnitude, R_2^* , field and susceptibility map reconstructed with single orientation algorithms; l_2 norm minimization, l_1 TV norm minimization and MCF of a patient with multiple sclerosis. Different rows show axial slice through different lesions. The arrows define different lesions; red - visible on all maps but the R_2^* , field and susceptibility maps but has no contrast on the magnitude map. The green arrow point on well-defined lesion with a positive contrast on all maps but for the T_1 w and R_2^* map.

out a well-defined lesion with a positive contrast (increased paramagnetism)

on all χ maps but that on the R_2^* map it shows a decreased relaxation rate while on the T_1 -w MP2RAGE image it appears dark, suggesting a very short longitudinal relaxation rate. The yellow arrow shows a lesion with a positive contrast on the magnitude images and susceptibility maps but on the R_2^* map it shows bright ring surrounding the lesion and the phase image shows a dark ring. The blue arrow highlights a lesion which appears diffuse both on the magnitude and the R_2^* maps (with lower relaxation rate), but appears better confined and with a positive contrast on the susceptibility maps and negative contrast on the T_1 -w images (R_1 values similar to grey matter). The red arrow shows a lesion with well-defined positive contrast susceptibility and field maps but shows no contrast on the magnitude map.

5.5 Discussion

5.5.0.5 Comparison of Susceptibility and R_2^* mapping

For the first time, at 7T, a comparison of the sensitivity of R_2^* and χ maps calculated from exact the same data set was performed, where all different orientations were used to create both the R_2^* and the susceptibility maps while in previous reports two different sequences and repetitions were used to retrieve R_2^* and susceptibility maps [150]. We conclude that using the proposed coil combination protocol, the R_2^* maps showed comparable or superior contrast to that shown by the susceptibility maps between the different deep grey matter regions. The biggest sensitivity of the susceptibility maps in respect to the R_2^* maps was found between white matter fiber bundles and between white and grey matter (even though recent findings suggest the observed contrast seen in white matter in phase images is wrongly attributed to the susceptibility [142]).

5.5.0.6 Single orientation susceptibility mapping methods

We performed first numerical simulations to evaluate the importance of the amount of prior knowledge. All methods benefited from having information from all possible boundaries in which case the result always showed the lowest distance to the ground truth and good results could be met for a large range of regularization parameters. It should be noted that the very piece wise constant nature of the phantom used in this numerical simulations benefited the performance of the iterative methods described that promote pice-wise constant or smooth solutions and are able to effectively denoise the reconstructed susceptibility map. This explains why the optimum modulated closed form solution had a significantly greater distance to the ground truth.

The modified closed form solution was able to reduce the striking artifacts but the level of noise introduced in the field maps is maintained in the χ reconstructions (see fig. 5.1 l-n).

When comparing the difference between multiple orientation and single orientation in vivo data, some small anatomical changes in the subcortical white matter in the frontal lobe (yellow arrow in fig. 5.6) could be attributed both to: (a) the higher SNR associated with the implicit averaging performed by having 4 datasets contributing to the COSMOS reconstruction; (b) or increased artifacts of the single orientation methods; (c) or a forward model inconsistency associate with the microstructure; (d) inconsistent co-registration in the frontal lobe due to air tissue related artifacts. The last two are a plausible hypothesis because the subcortical layer is not clear on any of the individual field map images, and the fact that it gets reconstructed on the COSMOS, where the four datasets have to be physically consistent with one single susceptibility map (χ_{COSMOS}) makes the methodology more sensitive both to the co-registration and the accuracy of the forward model. It was noticeable that the iterative methods exhibited increased noise in regions rich in both anatomical and phase contrast (see red arrow on fig. 5.6). Because these regions were discarded from the mask, M_{∇} , the regularization did not affect them and therefore the ill-posed nature of the problem was emphasized. The discussed noise regions on the single orientation susceptibility maps corrupt the comparison to the COSMOS method. The effect of the noise regions with very high variability and standard deviation have a bigger effect than the over regularization artifacts when comparing single orientation methods to the COSMOS. Therefore the COSMOS method provided a less than optimal estimation and tended to favour over-regularized results. In the in vivo data, a good choice of the regularized information, either the prior information mask or ill-conditioned k-space region, rendered the susceptibility reconstruction methods highly independent of the regularization parameter. Under this scenario it was found that the L-curve heuristic method gave better results. As computing the l-curve is inherently computationally intensive having a fast method to perform the inversion can be an important asset. Throughout this paper the l_1 TV norm seemed to give the sharper anatomical results, yet this was at a cost of very large computation times (1 hour per reconstruction) while the MCF solution could be calculated in a few seconds.

5.5.0.7 Multiple sclerosis lesions

It has been shown that tissue damage due to multiple sclerosis leads to the loss of macromolecules (myelin sheaths of the white matter axons) and

therefore to a R_2^* hypo-intensities (negative contrast), reduction of the R_2^* relaxation rate [76], which were clearly visible (green and blue arrow in Figure 5.8). The phase contrast changes are dependent from the underlying structural change; myelination damage could lead to hyper-intensities (positive contrast) while axonal damage could lead to hypo-intensities (negative contrast) [76], in our study all lesions showed a positive phase and susceptibility contrast. Moreover, in multiple sclerosis lesions where there are changes/damage/injury of the myelin sheet, without loss of the tissue, could make them visible in the phase contrast map without being visible neither on the R_2^* nor on the magnitude [76]. This is the case of the lesion pointed with the red arrow which has been hypothesized to correspond mild or early multiple sclerosis lesions.

Various lesions could be easily detected in the T1-w MP2RAGE data as reported by others [152]. All the detected lesion were visible in all the single orientation susceptibility reconstruction methods. However, some of the lesions are not as clearly defined on the l_2 norm minimization as with the l_1 TV norm minimization, which expects to have an underlying piece wise contrast. The susceptibility reconstructions with the modulated closed form solution have a lower SNR in respect to the iterative susceptibility reconstruction methods, but their SNR is comparable to that of the R_2^* map.

5.6 Conclusion

In this article we have implemented a fully flow compensated protocol for high spatial resolution GRE imaging at 7T based on a multi-echo gradient echo sequence. The introduced combination of the multiple coil data both prevents phase singularities and maximizes the available SNR of the combination - this is done by implicitly using all the echo times to compute the receiving coil sensitivities. The proposed method to compute the field map is, from an error propagation perspective, the one that gives maximum SNR for the given echo times available [113]. We have implemented different state-of-the-art methods to reconstruct susceptibility maps and performed a systematical analysis and comparison of the effects of the different regularization parameters and prior knowledge introduced. From the compared methodologies similar results were obtained with the highest correlation to the state of art methodology (COSMOS) being found for the MCF which has the additional advantage of being of extremely fast computationally.

We conclude that R_2^* and susceptibility have comparable quality to distinguish the deep gray matter structures while the susceptibility maps have a higher sensitivity to myelin related contrast, both in terms of white matter

grey matter structures and early stage multiple sclerosis lesions.

5.7 Appendix

Numerical simulations were performed to evaluate the impact of the singular value decomposition (SVD) coil combination in the obtained quantitative maps. An exponential decay with a $T_2^*=20\text{ms}$ and frequency shift of 0.13 rad/ms was considered as our ground truth signal. The simulations assumed that nechoes =5 were acquired using ncoils=32 (as in the experimental protocol).

The sensitivities of the 32 coils were created using a random complex number generator in order to take into account the different sensitivities of each coil, C_{coil} (which in real data depends to a first order on the distance to the pixel of interest) and also to take into account the unknown receiving phase. Gaussian distributed complex noise was added to each channel and echo time. Resulting on

$$S(\text{echo}, \text{coil}) = C_{coil} \times e^{(i\Delta\omega + 1/T_2^*)t_{echo}} + n \quad (5.7.1)$$

The noise, n , was introduced so that, in the case where the coil sensitivities were known, the mean SNR after combining the 32 channels over the 5 echoes was either 100 or 22. The matrix S (with ncoils columns and nechoes rows) was factorized using singular value decomposition and the vectors corresponding to the first singular value were kept. The left and right eigenvectors correspond to normalized relative coil sensitivities and the normalized time course. Alternatively, the magnitude time course was calculated by sum of squares combination (SOS) of the different coils. The field map calculation was done as described in the methods section (using the SNR weighting associated with a given echo time) but, while for the SVD timecourse it was computed only once, for the SOS methodology the fieldmaps were calculated independently for each channel and these were then combined using the power of each given channel as a weighting. This process was repeated 5000 times.

Figure 5.9 shows on the first row that the SVD time course remains closer to the simulated signal. The reason for this discrepancy is likely due to the presence of channels that are noise dominated (which is also the case when using coil arrays with small loops). This deviation is larger for lower SNRs (see Fig 5.9b) which will contribute to an overestimation of the relaxation time (especially if doing the fit in the logarithmic scale). When fitting the simulated signal to the magnitude data as computed by SVD or by the SOS and plotting the residuals obtained over the 5000 iterations (see Fig 5.9d)

it is possible to observe that: the SVD residuals have a smaller spread than the SOS (although for higher SNR values >150 they converged); the SVD residuals keep their Gaussian shape up to much lower SNRs (see Fig. 5.9d). With the parameters used in the simulation the Gaussian shape of the SVD residuals was kept down to an SNR of 5 although from an SNR <10 deviations from the expected signal decay could be observed (looking at the magnitude images in Fig. 5.1, it can be seen estimated that such low SNR is only present in regions around veins but not in tissue). When looking at the impact of the SVD combination prior to the frequency calculation (see Figs 5.9e and f), it can be seen that such a combination renders the calculation both more precise and accurate. The negative shift observed in the SOS frequency error at SNR=22 (see Fig. 5.9f) results from the fact that in noise dominated channels the calculated frequency shift will be on average the zero. Despite making a weighted combination of the different channels, the underestimation propagates to the final SOS field maps.

It should be noted that some vendors already offer solutions with similar properties for the complex data by using a low resolution coil sensitivity prior scan. Our SVD method has the particularity advantage of creating data driven normalized coil sensitivities that have the feature of generating the maximum signal. Such a method could find applicability in, for example, DTI where, instead of various echoes, various contrasts exist with different degrees of SNR. Reducing the noise propagation in the low SNR measurements would allow a better accuracy of the measured diffusion parameters.

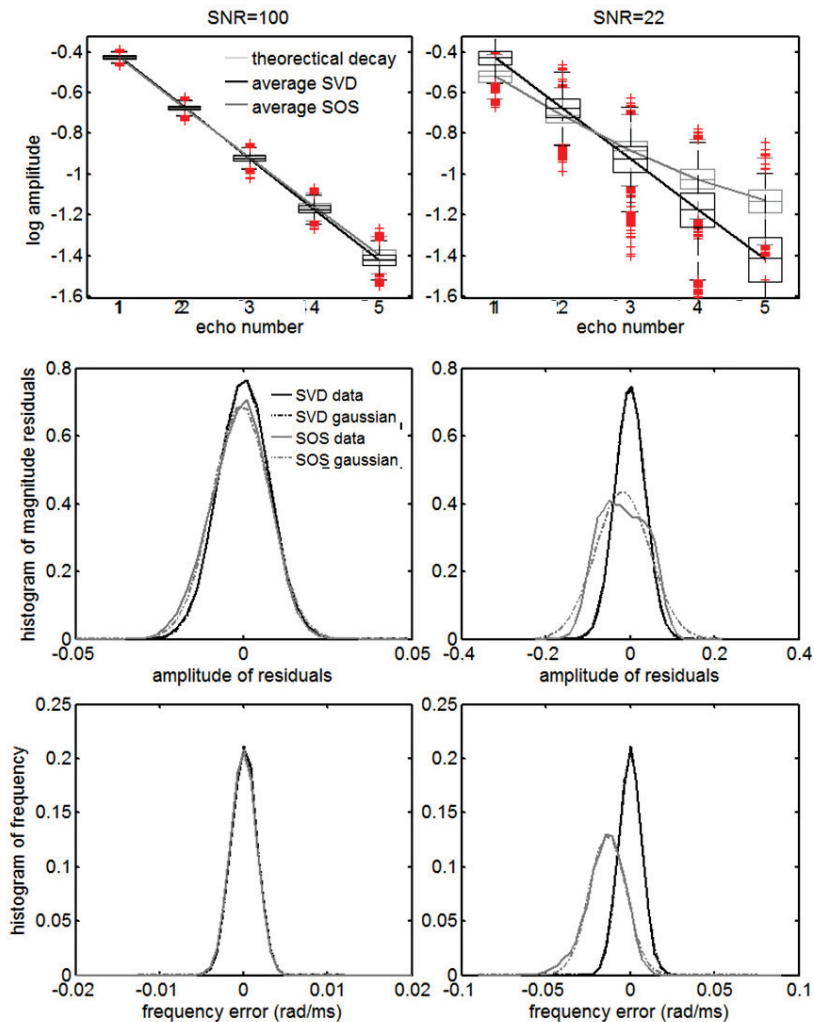
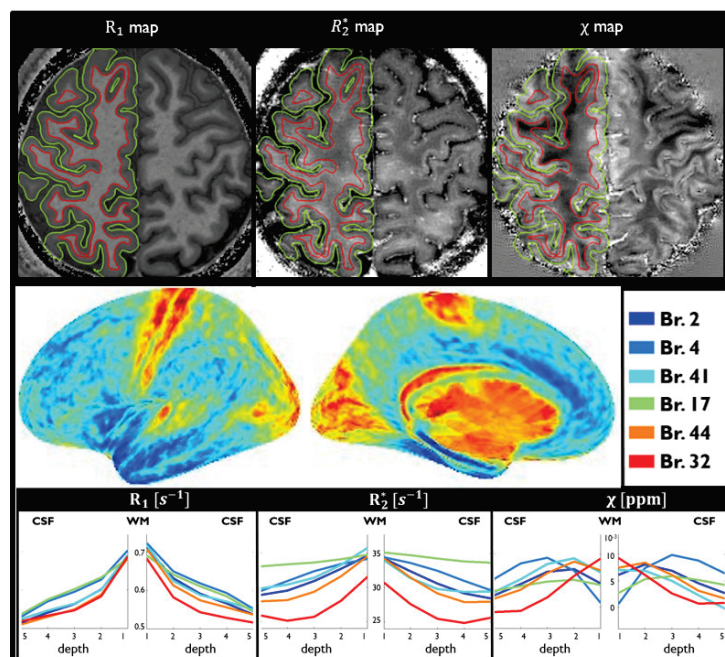


Figure 5.9: Whisker plots of the SVD (black) and SOS (dark gray) signal at each echo over the 5000 simulations and their respective mean curves compared to the simulated signal (light gray) for an SNR of (a) 100 and (b) 22. Histograms (c,d) of the magnitude data residuals (solid black line – SVD and solid grey – SOS) after fitting the timecourses with theoretical signal for an SNR of (c) 100 and (d) 22 respectively. Histograms of the error on the frequency measurement using the SVD (solid black line) and SOS (solid gray line) method for an SNR of (e) 100 and (f) 22 respectively.

Chapter 6

Quantitative imaging in the cortex

Studying cyto and myeloarchitecture of the human cortex at ultra-high field with quantitative imaging:
 R_1 , R_2^* and susceptibility



Abstract

In this manuscript, the use of quantitative imaging at ultra-high field is evaluated as a mean to study cyto and myelo-architecture of the cortex. The quantitative contrasts used are the longitudinal relaxation rate (R_1), apparent transverse relaxation rate (R_2^*) and quantitative susceptibility mapping (QSM).

The quantitative contrasts were acquired using in-vivo high resolution ($0.65mm$ isotropic) brain data acquired at 7T.

Susceptibility mapping is traditionally limited to inner regions of the brain due to the process associated with the removal of background fields. Various methods were systematically evaluated to test which could better preserve cortical regions close to the brain surface. The performance of the different quantitative approaches was evaluated by visualizing the contrast between known highly myelinated primary sensory cortex regions and the remaining cortex. Also the transition from the inner layers to the outer layers (from white matter to the pial surface) of the human cortex, which is known to have varying cyto- and myelo architecture was evaluated.

The across cortex and through depth behaviour observed for the different quantitative maps was in good agreement between the different subjects, clearly allowing the differentiation between different Brodmann regions. While both R_1 and R_2^* maps decrease monotonically from the white matter to the pial surface reflecting the decrease of myelin and iron between these regions, susceptibility has a more complex behaviour reflecting the its opposing sensitivity to myelin and iron concentration.

6.1 Introduction

The study of cortical brain structure has been an important field of research for the last century. In the beginning of the twentieth century, the cytostructure and myelostructure were studied through the Nissl and Weisss stain method, despite the limitations of these methods, various groups did study the cytostructure [153–155] and the myelostructure [156, 157] of the human cortex. Under the assumption that delimited regions with similar cyto- and myeloarchitecture would lead to specific functions, these groups have parcellated the cortex of the human brain into regions, which can be further specified into areas and subareas, with the most well know parcelation being that suggested by Brodmann. The brain cortex consists of many different kinds of neurons and, although neurons are very diverse, a typical neuron can be divided in three parts; the cell body or soma, the dendrites and axon. Signals from other neurons are received by the dendrites and transmitted by the axon, which leads to a huge network system within the brain. The myelinated fibers in the human cortex have two main orientations: tangentially organized bands in respect to the cortical surface and radially arranged bundles.

Modern histology has evolved and new methods have been developed to study the cyto- and myeloarchitecture in a more specific and quantifiable way, e.g. immunohistochemistry and receptor mapping [158–160]. Also many analytical techniques are used to analyse the elementary composition of the tissue such as synchrotron X-ray fluorescence (XRF), proton-induced X-ray emission mapping (PIXE), inductively coupled plasma mass spectrometry (ICPMS) as well as atomic absorption spectrometry measurements [161] [162] [163] [164] [64].

During most of the 20th century, the understanding of human brain function heavily relied on clinical cases of brain injuries [165–167]. This has suffered a dramatic shift with the development of functional brain imaging techniques such as positron emission tomography (PET) in a first instance and later functional magnetic resonance imaging (fMRI) which allowed Neuroscientists to study the brain regions or networks associated with a given task [168] or even during rest. Although functional MRI and diffusion weighted imaging have had a huge role in the study of human brain function and connectivity, both at the group and individual level, there is still interest in being able to, with high spatial resolution, find anatomical landmarks that are associated with cortical structure that go beyond the simple observation of the cortical folding, but measure directly the tissue properties. Using standard weighted imaging MR this is not as straightforward because the hardware used to detect the signal that creates spatial variations of the image intensity

and contrast due to the receive array technology used for reception and the inhomogeneity of the transmit field used for signal excitation at high magnetic fields. Standard weighted imaging has long been shown to be able to visualize locally differences in cortical structure [169] and the first reports showing whole brain cortical maps that showed the differential properties of sensory and motor cortices in respect to surrounding tissue have been obtained over 10 years ago by [170, 171]. Only recently though, has this field had a renovated attention thanks to the first reports suggesting that by combining T1-weighted and T2-weighted images, a measure of myelin could be inferred that revealed many cortical areas boundaries defined in the Brodmann atlas. The ratio T_1w/T_2w improves not only the contrast of heavily and lightly myelinated areas but also removes some MR-related intensity bias fields [172]. However, these ratio based method remains sensitive to the B_1 transmit field inhomogeneity, which contaminates comparisons of different subjects, scanners and facilities with different protocols.

An alternative to this phenomenological ratio is the use of MR quantitative methods which are independent on the facility, reproducible and depend only on the underlying structures which are the origin to the contrast. Various studies have shown a direct relationship between myelin content and R_1 [173–175]. In the human cortex R_1 variations have also been shown to not only iron content but also water mobility [176–178], yet the impact of the iron content to the R_1 tissue contrast is should not be fully neglected [179]. This has now been clearly demonstrated in a recent ex-vivo study showing that it is beneficial to think of R_1 in grey and white matter to have a multivariate dependence on both myelin and iron concentration [63]. In vivo R_1 and R_2^* maps in the cortex show increased relaxivity in the primary Brodmann regions [180, 181]. Other than the ability to distinguish Brodmann areas, the study from Cohen et al also observed that, within each region, there was a small dependence on the orientation of the cortical surface in respect to the magnetic field, suggesting that, in part, this contrast is not only modulated by iron load but also due to the structurally organized myelin bundles running through the cortex. When looking at cortical R_1 maps, it was observed that the boundaries obtained using R_1 maps were in good agreement with those obtained using functional imaging to define on a single subject basis V1, MT [181] and the auditory cortex [182].

Inhomogeneities caused by para- or diamagnetic perturbers, such as iron and myelin, lead to a dephasing of nearby protons [50], increasing their apparent transverse relaxation rate. Such processes are responsible for the clear delineation of veins, hypo intensities in deep gray matter structures and even the contrast between different white matter fibers in standard T_2^* weighted imaging. Instead, in quantitative susceptibility mapping (QSM)

paramagnetic and diamagnetic entities, like iron and myelin, have opposing effects - reflecting the local increase of induced magnetisation. However, to compute susceptibility maps from measured frequency shift maps, many pre-processing steps need to be performed.

One essential step is to remove the background field caused by surrounding tissue-air interfaces as well as imperfect shimming, which is superimposed on the the small magnetic field variations arising from the varying magnetic tissue properties. In order to remove such background field from the measured field, a mask that defines the region of the local effects of interest and the background has to be defined. Many methods presented in the literature will either end up eroding this mask (losing relevant information) or giving values close to the boundary that are unreliable. Many methods have been suggested [55,123,124] and their performance being evaluated mostly regarding their impact on the quantification of the susceptibility of deep gray matter structures. Another essential step is the actual calculation of the QSM from field maps (after background field removal) based on the knowledge of the analytical description of the magnetic dipole field in k-space [47,127]. As this problem is not ill-posed, many methods have been proposed in the past years to overcome this problem both when doing the calculation directly: thresholding the not well-defined values [131,132], redefining the dipole kernel in k-space [130] or using spatial regularization approaches in k-space [111,139]. Alternatively iterative methods can also be used with different regularization factors and prior-knowledge regarding the regions where edges are expected (or not) to appear or using different k-space weightings in region where the problems is more ill-posed [122,134–137]. Despite all these advances the most robust method is still the originally proposed over-determination of the problem by measuring the subjects head at different orientations in respect to the main magnetic field [54,127,128]. Despite the discomfort and the increased scanning time, that is still the ground truth method and will be used in our study to complement the information obtained from R_1 and R_2^* maps.

Iron concentration in deep gray matter structures (globus pallidus, putamen, caudate) have been shown to have a correlation with QSM [52–54,61,183]. When looking at white matter , the picture is less clear, myelin content does contribute to the gray and white matter contrast in phase imaging [69,70] yet, this contribution is driven by the microstructural compartmentalization of lipid organization and its orientation on respect to the static magnetic field [76,86,106,143]. This mechanism is not taken into account in the COSMOS formalism, but it is only a dominating factor in regions of where tissue is highly anisotropic (unlike grey matter).

The aim of this study is to analyse the cortical brain surfaces retrieved from the three presented quantitative contrasts: R_1 , R_2^* and QSM. A qualitative

analysis is done of the reproducibility of the obtained cortical maps as well as the identification of the features and Brodmann areas. The cortex is studied in its transition from the inner (border between gray matter (GM) – white matter (WM)) to the outer surface (border between gray matter (GM) - cerebrospinal fluid (CSF), pial surface). This “through depth behaviour” of the brain cortex is evaluated for all quantitative contrasts in regions of interest based on the Brodmann atlas and the different curve behavior is used to calculate myelin and iron distribution in the human cortex.

6.2 Methods

6.2.1 Data acquisition

Six healthy volunteers (age = 27 ± 4 years) were scanned according to a protocol approved by the local ethics committee. Scans were performed on a 7T MR scanner (Siemens, Erlangen, Germany) using a 32 channel receive coil (Nova Medical).

6.2.1.1 R_1 maps

The R_1 -maps were acquired using the MP2RAGE [148] sequence. The sensitivity of the R_1 map estimation from the measured MP2RAGE to B_1^+ field inhomogeneities increases with the resolution (number of excitations per MP2RAGE repetition time) aimed. To overcome this problem the B_1^+ field was measured separately with the SA2RAGE sequence [184]. Subsequently the two datasets were used to compute high resolution, full brain and bias field free R_1 maps [185].

The SA2RAGE acquisition had the following parameters: $TR/TD_1/TD_2 = 2.4/0.045/1.8$ s; $BW = 1200$ Hz/Px, $FA(\alpha_1/\alpha_1) = 4^\circ/10^\circ$; spatial resolution = $2.2 \times 2.2 \times 2.0$ mm³; $iPAT = 3 \times 1$; $T_{acq} = 1$ min 55sec.

The MP2RAGE parameters were the following: $TR/TI_1/TI_2 = 6/0.8/2.7$ s; $BW = 300$ Hz/Px; $FA(\alpha_1/\alpha_1) = 7^\circ/5^\circ$; spatial resolution = $0.6 \times 0.6 \times 0.6$ mm³; $T_{acq} = 10$ min 25sec.

6.2.1.2 R_2^* and susceptibility maps

To retrieve the quantitative maps of the R_2^* and susceptibility, a standard 3D gradient echo multi echo sequence was used. The five acquired echoes were equally spaced and acquired with the same polarity gradients, the rewinding waveform was kept equal to the readout gradient wave form to ensure flow compensation between successive echoes. The following parameters were

used: $TR/TE_1/TE_5 = 42/4.97/37.77$ ms; bandwidth (BW)=260 Hz/Px; flip angle (FA)=10°, FOV=256×192×137mm, spatial resolution = $0.66 \times 0.66 \times 0.66$ mm³; iPAT=2×2; acquisition time (T_{acq})=11min. The protocol was repeated four times for each volunteer with different head positions: normal; head tilted around medio-lateral axis(left–right axis, pitch) in head-to-neck direction (up to 14°) position; tilted around anterior-posterior (nose-neck axis, roll) in head-to-left-shoulder direction (up to 25°) and head-to-right-shoulder direction (up to 25°). The exact head rotations were determined by using a protocol on FSL (www.fmrib.ox.ac.uk) as explained in [111].

6.2.2 Data processing

All data processing was performed in MATLAB (version 2010b, The Math-Works, Natick, MA, USA) on a workstation (2x Intel Xeon X5650) with 96 GB RAM.

6.2.2.1 R_1 calculation

First, the low resolution SA2RAGE was co-registered to the high resolution mp2rage using FLIRT (www.fmrib.ox.ac.uk/fsl). Lookup tables were used to relate each pixel of the SA2RAGE to their B_1^+ values. Then this B_1^+ value was used to estimate the T_1 value of a certain pixel of the MP2RAGE intensities with a lookup table. This process was repeated with three iterations as the variations were shown to be negligible [185].

6.2.2.2 R_2^* and susceptibility calculation

The multi-echo GRE data from the different coils was combined and processed as described in [111] to obtain the field and R_2^* map.

Additionally, restrictions of the range of R_2^* values were applied for each orientation and subject. These restrictions are based on trustworthy R_2^* value calculation with the used echo times. An assumption was made for the minimal R_2^* value being $1/(3 \cdot \max(TE))$ and the maximal R_2^* value being $1/(3 \cdot \min(TE))$. To achieve an average R_2^* for each subject the co-registration procedure was performed as explained in [111].

Local tissue magnetic sources generate small magnetic field variations which are overlaid by the strong background fields due to surrounding tissue-air interfaces as well as imperfect shimming. In order to retrieve the magnetic field map generated only by the local tissue sources, the EAHF (Efficient and Automatic Harmonic Field Pre-Filtering) background field removal was applied [125]. Although this method is expected to have smaller effects in

the boundary region, an additional mask was applied to erode 2 pixels from the boundary to account for present minor striking artefacts.

A comparison of three different background field removal techniques was performed. The selected methods were the EAHF [125], ReSharp [123], and PDF [124, 135]. These methods were selected because they are potentially the most robust methods in superficial regions of the brain cortex. Their quality was evaluated on their ability to keep cortical specific contrast in the final QSM maps.

Quantitative susceptibility maps were calculated using the COSMOS method [128] using four different head orientations.

6.2.3 Cortical maps

To transform all quantitative contrasts (R_1 , R_2^* and susceptibility) to the same subject-space for each subject first the magnitude contrast of the GRE acquisition was co-registered to the R_1 map using FSL-FLIRT. This registration matrix was applied to the χ and R_2^* maps as shown in Fig.6.1.

In the next step the cortical surfaces of the gray-white matter border and GM-CSF border (pial) were retrieved from the common FreeSurfer software pipeline. These surfaces were used to compute equi-volume cortical surface layers from R_1 maps [186] by sampling the surface vertex in steps of 20% of cortical volume across the entire cortical hemisphere without using any smoothing. These surfaces at different cortical depths were applied to χ and R_2^* maps to obtain the corresponding cortical maps. The pial surface was excluded from the remaining analysis because the quantitative maps of CSF have a large uncertainty and hence the pixels where CSF has a larger partial volume will be less reliable. In the remaining layers, all points whose quantitative maps were outside the range of 3-standard deviation of the mean value of each subject at each depth were excluded from the further analysis (resulting in the exclusion of less than 1% of the cortical data, 0.03% and 0.2%).

For each subject, contrast and surface, spatial smoothing was performed in the inflated space with a Gaussian of 2mm width and a 6mm radius kernel. The smoothing process was integrated with the transition from the individual space to the average subject space from freesurfer and allowed to recover information in regions where the background field removal erosion had removed grey matter pixels of the outer cortical surface in cortical gyrus. Before averaging all the subjects, a single value decomposition (SVD) was applied to each quantitative contrast dataset (163842 vertices x 5 cortical depths). By removing the fifth SVD component the noise was reduced while the data remained almost the same (the data changes are in the order of $< 1\%$ for R_1

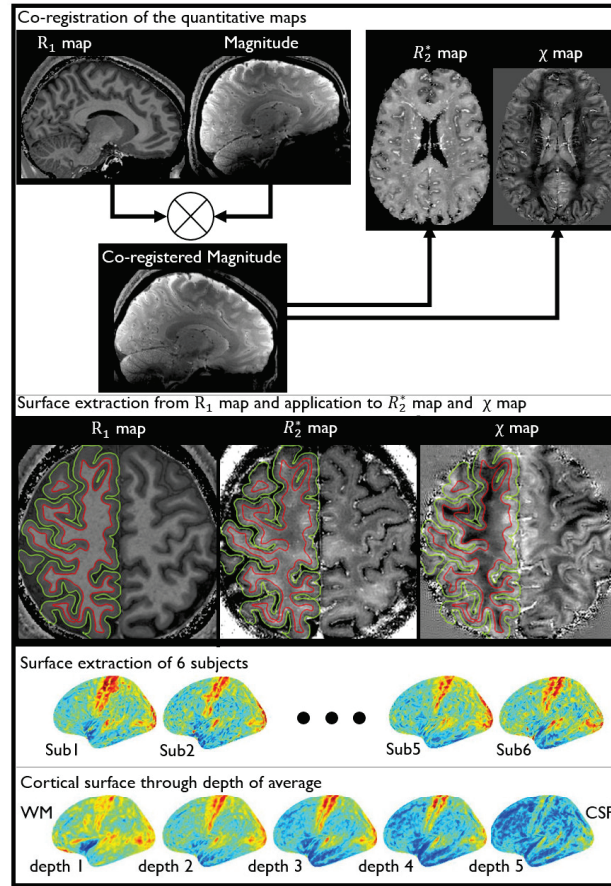


Figure 6.1: shows the co-registration procedure for the three different quantitative contrasts. In the first panel the magnitude image of the GRE sequence is co-registered to the calculated R_1 map. This co-registration is afterwards applied to the R_2^* and QSM map. The second panel describes the surface extraction from R_1 maps and its application to the R_2^* and susceptibility maps overlaid by the calculated cortical surface of red (GM-WM) border and green (GM-CSF) border.. The last panel shows the R_1 cortex map from the middle surfaces for different subjects (top) and the R_1 cortex maps for different depths trough the cortex (bottom).

and R_2^* maps and $< 5\%$ for susceptibility maps).

The reproducibility of the behaviour of the different layers from the inner to the outer part of the cortex was studied for all quantitative contrasts. This “through depth behaviour” in certain regions of interest (ROI) based on the main Brodmann areas as defines in the PALS B12 atlas [187] were analysed. An average subject was calculated in the inflated space for each quantita-

tive contrasts (R_1 , R_2^* and susceptibility) containing different depths. The “through depth behaviour” in the various Brodmann areas across hemispheres was analysed.

6.2.4 Iron and Myelin

If it is assumed that iron (Fe) and myelin (My) concentration are the sole contributors to the measured quantitative maps in grey matter and assuming they have a linear impact on both the relaxation parameters and susceptibility values then, the measured quantitative contrasts can be expected to have the following dependence on the concentrations of [Fe] and [My]:

$$R_1(Fe, My, BA, L) = R_{1,BL} + r_{1,Fe} \cdot [Fe(BA, L)] + r_{1,My} \cdot [My(BA, L)] \quad (6.2.1)$$

$$R_2^*(Fe, My, BA, L) = R_{2,BL}^* + r_{2,Fe}^* \cdot [Fe(BA, L)] + r_{2,My}^* \cdot [My(BA, L)] \quad (6.2.2)$$

$$\chi(Fe, My, BA, L) = \chi_{1,BL} + \chi_{Fe} \cdot [Fe(BA, L)] + \chi_{My} \cdot [My(BA, L)] \quad (6.2.3)$$

Where $R_{1,BL}$, $R_{2,BL}^*$ and $\chi_{1,BL}$ represent baseline values of the quantitative parameters in the absence of those perturbors, $r_{1,Fe}$ and $r_{1,My}$ are the longitudinal relaxivity of iron and myelin respectively and $r_{2,Fe}^*$ and $r_{2,My}^*$ are the apparent transverse relaxivity of iron and myelin. Such model has been successfully demonstrated in ex vivo experiments [63]. If only these two sources of contrast contribute to the three quantitative maps, the number of measurements is greater than the number of unknowns even when the relaxivity and baseline values are unknown provided that the number of measurements is greater than nine.

In Equations 6.2.1-6.2.3 the indexes BA and L correspond to the Brodmann area and depth layer respectively. Hereby, 18 ROIs (based on the Brodmann atlas (Brodmann areas)) at 5 different depths were used in the fitting procedure. The regions of interest were chosen to represent significantly different relaxations behaviour to better condition the problem. In order to increase the reliability of the fitting procedure, the iron coefficients to R_2^* (0.27) and susceptibility (0.84 10⁻³) were assumed as reported in [61, 188] for deep grey matter structures which are in close agreement with those obtained in other studies [52–55]. The use of this parameters implies the calculated iron concentration will be in *mg/Kg*. Although various studies correlate R_1 with myelin concentration we did not find any literature with in vivo data at 7T. The myelin longitudinal relaxivity coefficient was therefore arbitrarily set to 1. Such ad-hoc definition implies an arbitrary unit to the measured myelin

concentration, but is crucial for the stability of the fitting procedure to reduce the search space.

To avoid biasing the fitting procedure by the size of the different quantitative maps ($R_2^* > R_1 \gg \chi$), each of the equations was weighted by the standard deviation across subjects found for the respective quantitative measurement. The fitting procedure was performed using `lsqfit`, a non-linear solver distributed with MATLAB. Once the relaxivity parameters were calculated, Eq. 6.2.1 and 6.2.2 were used to create average iron and myelin maps of the cortex.

6.3 Results

6.3.1 Data and segmentation quality

Figure 6.1 shows an outline of the processing protocol starting from the moment when the magnitude data from the gradient echo sequence has already been coregistered to the R_1 space. Representative slices of the three coregistered quantitative maps are enhancing different features of the human brain and cortex. The R_1 map shows the best separation contrast between the white and gray matter, which enables the best cortical gray-white matter segmentation (and was therefore used in the freesurfer pipeline). The R_2^* map shows good vein delineation and has a grey-white matter contrast which is increased in the frontal lobe (black arrows) in comparison to the parietal (white arrows) and occipital lobe. The susceptibility map obtained with COSMOS shows white matter and significant variations of the contrast in different cortical regions: e.g. the rim of increased para-magnetism of the frontal cortex at its white matter surface (dashed back arrow); increased para-magnetism of the occipital cortex in respect to the frontal cortex is evident from increased contrast, as described in other reports at 7T [150].

The cortical surfaces calculated with the FreeSurfer software (green (GM-pial) and red (GM-WM surface) lines in Fig.6.1) correspond well to the underlying R_1 contrast (from which they were calculated), whereas the R_2^* and χ contrast reveal dissimilarities that are not attributed to poor co-registration. While in the outer layer (the pial surface) the χ contrast is significantly noisier due to the background removal, the mismatches in the grey white-matter contrast between R_2^* (and χ) and R_1 is solely due to the different mechanisms generating the contrast.

6.3.2 Cortical surfaces and ROI

The cortical maps of the left hemisphere extracted from the middle layer for different subjects and quantitative contrasts is shown in Fig.6.2. For all subjects, all the contrasts (but mainly R_1 and R_2^*) show a similar enhanced regions, e.g. the primary motor cortex (dashed black arrow), the auditory cortex (dot-ended dashed arrow), the visual cortex (solid arrow), and the MT region (grey arrow).

Not only are the cortical maps across subjects consistent, (see Figure 6.1 and

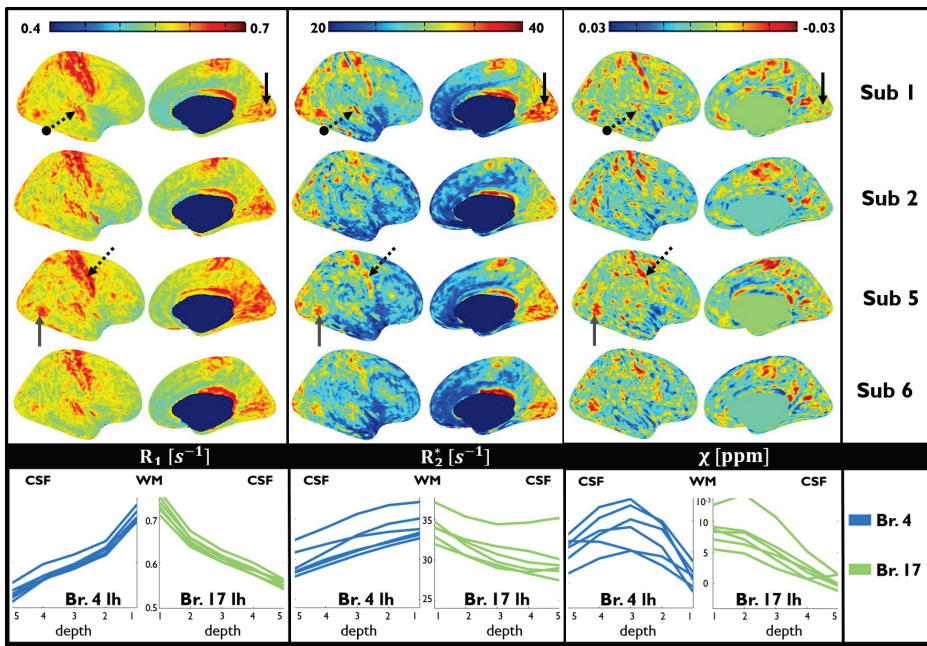


Figure 6.2: first, second, third rows show the cortical map at the middle layer for the three quantitative contrasts (a-d)- R_1 , (e-h)- R_2^* , (i-l)-QSM for different subjects (columns) in the upper panel and plots of the for different quantitative contrasts (R_1 , R_2^* and χ) as a function of the layer number (depth 1 being closest to the GM-WM surface and depth 5 closest to the pial) of the left hemisphere (lh) of Brodmann 4 (left) and right hemisphere (rh) of Brodmann 17 (right) for all 6 subjects on the bottom panel. The black arrows define different primary Brodmann areas; solid – visual cortex, dashed – motor cortex, dot-ended dashed – auditory cortex, and grey - MT region.

Figure 6.2), the high resolution at which the measurements were done allows the extraction at intermediate depths (see last row of Figure 6.1). To evaluate the reproducibility of the through depth behaviour of the relaxation proper-

ties across the different subjects, the mean value of the relaxation parameters in two Brodmann areas (blue: 4-somatosensory and green: 17-primary visual cortex), was evaluated for each depth. The through layer behaviour on the R_1 , R_2^* and χ was in good agreement between the six subjects and varied between different brain regions, as shown for the two Brodmann areas in Figure 6.2. Interestingly, the subject's curve that has the largest deviation on the R_1 values of the somatosensory corresponds to the subject that shows the largest deviation from the mean not only on the visual cortex R_1 values (which could have been attributed to some systematic error in the R_1 quantification or segmentation outcome) but also on the R_2^* and susceptibility. The fact that the differences are also present on the gradient echo related data and that the differences which in R_1 maps could be attributable to a segmentation shift of the different layers could not be used to successfully match the R_2^* and susceptibility curves. Hence this differences should reflect subject specific variability of the tissue properties.

Yet, the similar behaviour of the different subjects qualifies the study of the through depth behaviour on the average of the 6 subjects. While combining the subjects to an average subject, the information through depth of the cortex from the inner to the outer layer was kept.

All three contrasts show a variation through depth as can be seen by the intensity decrease in the R_1 cortical maps in Fig. 6.3. A wider set of ROIs, being the mean within chosen Brodmann areas, is shown on Figure 6.3 as the behaviour of the contrasts when averaged over the subjects. The behaviour differs between different ROI and is coherent between left and right hemisphere.

While the through depth behaviour of the contrasts based on the relaxation rates (R_1 and R_2^*) show a monotonically decay from inner to outer surface, the susceptibility maps show a curvature like behaviour, as pointed out in the visual cortex (solid arrow) and motor cortex (dashed arrow) on the left hemisphere for different depths for all contrasts. These differences are expected to be generated by the origin of the contrasts. The magnetic field inhomogeneities as produced by iron and myelin are dephasing MR signal and as a consequence the apparent relaxation rate increases. On the other hand the susceptibility contrast is sensitive to the average susceptibility value inside the voxel. The decrease of iron (paramagnetic) component results in a decrease of susceptibility while the decrease of myelin leads to an increase of the susceptibility. Thus the initial increase in the susceptibility is dominated by the decrease in iron while the final decrease in susceptibility is dominated by the reduction of myelin.

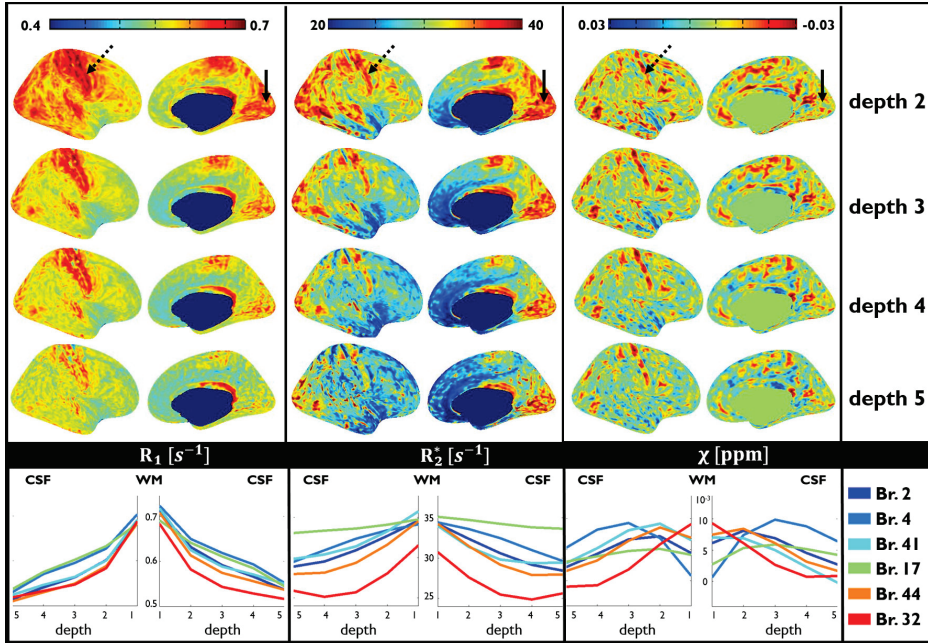


Figure 6.3: first, second, third rows show the cortical map of the average subject for the three quantitative contrasts (a-d)- R_1 , (e-h)- R_2^* , (i-l) QSM for different depths shown in columns (layer 1 being closest to the GM-WM surface and layer 5 closest to the pial) on the top panel and plots of the for different quantitative contrasts (R_1 , R_2^* and χ) as a function of the depth of the average subject where the different colours correspond to different Brodmann regions (Brodmann 2 somatosensory, 4 primary motor cortex, 17 primary visual cortex, 41 auditory cortex, 44 Broca’s area and 32 cingulate region) on the bottom panel. The arrows point to; solid – visual cortex, dashed – motor cortex.

6.3.3 Through cortex analysis

To benefit from this information without the need to rely on segmentation, singular value decomposition (SVD) was performed for each contrast to separate cortical maps with different through layer behaviour. The SVD decomposes a matrix in orthogonal components that explain most of the behaviour in the matrix. The first component explains most of the contrast information (98% for R_1 and R_2^* maps and 93% for the χ maps) whereas the second component points rather minor changes (2% for R_1 and R_2^* maps and 5% for χ maps). Similar to the eigenvalues and eigenvectors from the mathematical linear algebra, the singular vectors show the influence of each cortical layer as shown by the curves within each panel in Figure 6.4. The first component

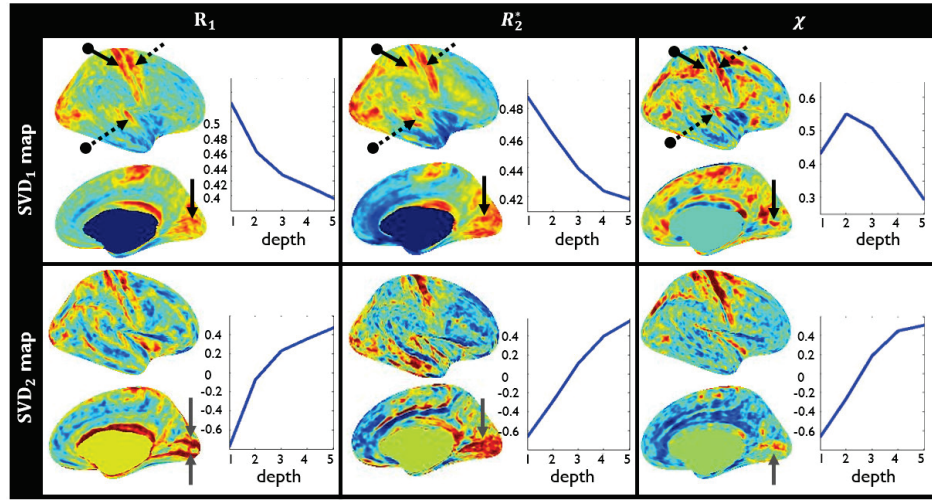


Figure 6.4: shows on first, second and third column the surface maps of the left hemisphere for i) R_1 , ii) R_2^* and iii) χ contrast for the first component (a-c) and the second component (d-f) of the singular value decomposition. The curves inside each panel show the singular vector for the different components for each contrast. Black arrow points to: solid - visual cortex, dashed - motor cortex, dot-ended solid - somatosensory cortex, dot-ended dashed - auditory cortex. The grey arrow shows the separation between primary and supplementary visual cortex.

of the SVD (SVD1) of R_1 , and R_2^* shows similar maps (enhancing all primary sensory regions, see Figure 5, and represents the mean R_1 , and R_2^* decay over the different layers. As already revealed by the ROI through layer behaviour the χ SVD1 has a curvature like behaviour (in Figure. 6.3 and 6.4). While the R_1 contrast shows both the motor and somatosensory cortex, the R_2^* and χ only enhance the motor cortex and show a lower enhancement of the somatosensory cortex (dot-ended arrow in Figure 6.4). The SVD2 map for both R_1 , and R_2^* shows as positive values, brain regions where the decrease of the relaxation rate is not as steep as in the remaining cortex (and negative when it is steeper). The primary visual cortex appears enhance in this SVD component for all 3 quantitative contrasts (gray arrow in Fig. 6.4).

6.3.4 Myelin and Fe information through quantitative contrasts combination

The resulting quantitative contrasts when using the fitted coefficients are in a good agreement with the measured values for the different layers (upper

panel in Fig.6.5) with the final linear equations

$$R_1(Fe, My, BA, L) = 384 + 5 \cdot [Fe(BA, L)] + 1 \cdot [My(BA, L)] \quad (6.3.1)$$

$$R_2^*(Fe, My, BA, L) = 0.34 + 0.27 \cdot [Fe(BA, L)] + 49,85 \cdot [My(BA, L)] \quad (6.3.2)$$

$$\chi(Fe, My, BA, L) = 0.24555 + 0.00084 \cdot [Fe(BA, L)] + 0.51637 \cdot [My(BA, L)] \quad (6.3.3)$$

The coefficients in bold are those that were kept fixed during the fitting procedure. While the apparent transverse relaxivity of iron and its susceptibility were taken from previous studies [61, 188], the longitudinal relaxivity of the diamagnetic component was arbitrarily defined to stabilize the fitting process. It is known that many of these parameters change significantly with fixation processes and temperature, to understand the meaningfulness of the obtained results and how they compare to literature values that are mainly based on ex vivo imaging, the following analysis was performed. The ratio between the R_2^* and χ dependency on iron, $r_{2,Fe}^*/\chi_{Fe} = 321$, is similar to earlier work on correlation of quantitative mapping with proton induced X-ray emission spectroscopy by [63], $r_{2,Fe}^*/\chi_{Fe} = 367$. The iron maps show increased contrast in all primary Brodmann regions as pointed out by the arrows in Fig.6.5. Although on the primary visual Brodmann region V17 (green) the high myelinated Stria of Gennari cannot be detected as a maximum, its influence can be seen by the sudden decrease from layer 4 to 5 in the middle panel in Fig.6.5. The diamagnetic distribution is highly increased in contrast to the B44 with a low myelination.

6.4 Discussion

In this paper we were able to obtain both quantitative R_1 and R_2^* cortical maps, which are in qualitative agreement with those shown by other groups [181, 189] and, for the first time, shown quantitative susceptibility maps that enhance similar features to the relaxivity maps of the cortical surface (i.e. primary sensory regions).

The calculation of susceptibility maps using a multiple angle acquisition methodology (COSMOS) eliminates concerns from the ill posed nature of single orientation methods, yet it suffers from two potential limitations when applied to the study of the human cortex. The forward problem [47, 127] expressed on the COSMOS method assumes the validity of the sphere of Lorentz correction and the isotropic nature of the susceptibility in grey matter. In ex vivo experiments, these assumptions have been shown not to be

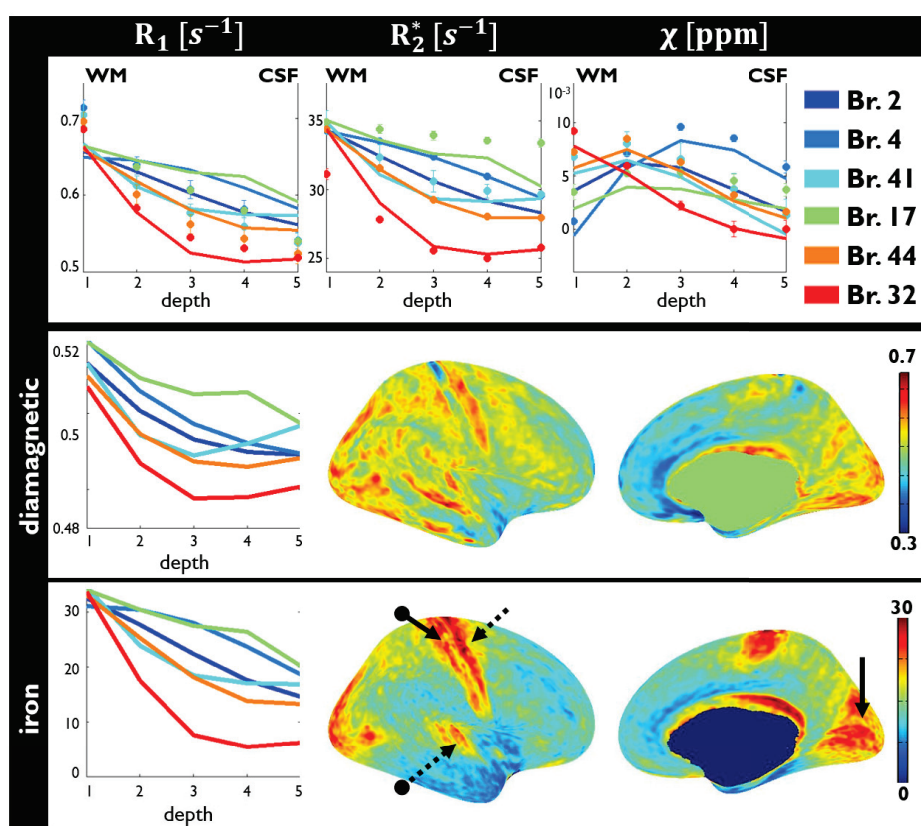


Figure 6.5: shows plots of the measured quantitative contrasts (circles) as well as the fitting result (solid line) on the first row and the reconstructed myelin and iron distributions as a function of the depth on the second and third row where the different colours correspond to different Brodmann regions (Brodmann 2 somatosensory, 4 primary motor cortex, 17 primary visual cortex, 41 auditory cortex, 44 Broca’s area and 32 cingulate region).

valid in white matter [86, 88, 104]. The difference between longitudinal and perpendicular susceptibility of white matter in a perfectly organized optic radiation or spin cord is relatively small, $0.018\text{--}0.03\text{ppm}$ [83, 106, 190], with the dominating anisotropic effect being that associated with its compartmentalization [83]. Although the amount of myelinated axons in the GM is not negligible and has been shown to cause small orientation related relaxation changes in the human cortex [189], the fact that these axons run both parallel and perpendicular to the cortex surface renders this structures quasi-isotropic. Furthermore, by using the multiple head position acquisition these anisotropic effects are further averaged out. The other main concern when using susceptibility mapping to study the brain cortical surface is the

accuracy of the field maps in cortical regions after background field removal. In this manuscript, we took advantage of the high spatial resolution achievable at high field strengths, and have explored a variety of methods found in literature that were expected to have minimal effects in the outer parts of the brain. The example data provided in the appendix shows that the method chosen, EAHF, is able to provide filtered fieldmaps whose susceptibility maps have the expected features found in relaxation based cortical maps.

The high spatial resolution of our data allowed the study not only at the middle layer behaviour across the cortex, but also the “trough depth behaviour”. As a result of the choice of inversion times of the MP2RAGE sequence used to compute R_1 maps and the echo times used to calculate R_2^* maps, the relaxation rate values of CSF are not accurate. Incidentally, this layer was also missing in large parts of the susceptibility cortical maps as a result of the erosion associated with the background field removal. Hence the GM-CSF border was not taken into consideration when mapping the through depth behaviour of both the relaxation parameters and the susceptibility maps. Although similar behaviours were observed across subjects and, to some extent, quantitative maps (see Figures 6.4 and 6.5), for the sake of tractability of the analysis, the quantitative evaluations were performed using regions of interest associated with Brodmann areas defined on the BA12 atlas [187]. This atlas, derived from T_1 -weighted MRI volumes of 12 young adults, is based on the varying cytoarchitecture (rather than the varying iron concentration and the myelin content) it is possible to observe that differences in both mean values and through depth variation of the quantitative maps (see Figure 6.4) persist even after this averaging process.

To better emphasize the differences between different brain regions a myelostucture based atlas could have been more appropriate [191] as it is known that within one Brodmann region, several myelin based regions can exist [192], the use of Broadman areas as ROI will tend to average out such differences. Another segmentation approach is the automatic segmentation of the subject specific clusters for different quantitative contrasts similar to the functional parcellation of the cortex [193]. The richness of the cortical information attained in these maps opens the door to more advanced coregistration procedures between subjects as well as its segmentation [194]. In such approaches the spatial distribution as well as the behaviour through the depth of the parcellated ROIs can be compared and taken into account during the transformation of the subject specific clusters to the average subject space. Figure 6.4 clearly shows that, on a pixel by pixel basis, information exists both on the mean value (SVD1) and the differential through depth behaviour (SVD2) of all the measured maps, and it can help differentiating primary and supplemental visual areas.

The through depth behaviour for each quantitative contrast was in good agreement between the different subjects, with only one subject showing significantly different behaviour for all contrasts and both hemispheres (see the example shown in Fig. 6.2 for Brodmann areas 4 and 17). The greatest variations were found in the R_2^* contrast. The observation of differences in various Brodmann areas excludes the hypothesis that they could originate from local segmentation errors and suggests that there might be variations of the underlying structure that are despicable by these methods at the individual level. When creating the average subject the analysis for the different hemispheres was kept separate. Figure 6.3 thus suggest that the differences seen in through depth behaviour of R_1 , R_2^* and χ are meaningful as the curves of the different BA from the left and right hemisphere resemble in both shape and mean value. The observation that χ , as opposed to R_1 and R_2^* maps does not decrease monotonically from inner surfaces to outer surfaces, suggests that myelin and iron susceptibility contributions are cancelling each other out. Both iron paramagnetism (positive χ) and myelin diamagnetism (negative χ) contribute to an increase of the two relaxation maps. Suggesting that one or both this contrast mechanisms decrease from the inner to the outer layer. On the susceptibility contrast, if only one of the contrast mechanisms was contributing, we would expect a decrease of susceptibility (in the case of a decrease of the paramagnetic iron) or an increase (in the case of a decrease of the diamagnetic myelin). The curvature behaviour suggests an initial faster decrease of myelin and later (in space) decrease of iron concentration.

In this study we have tried to, for the first time, combine the information from different in vivo quantitative maps of the cortex and built iron and myelin maps of the cortex. The model used in Eqs 6.2.1-6.2.3 has shown to hold in ex vivo experiments in one single piece of cortex. This does not necessarily hold for different cortical sites that have different cyto- and myelo-architecture organization. For example, while it is valid to assume that the R_2^* and χ contrast are proportional to the myelin volume this is less clear for R_1 . R_1 reflects spin lattice relaxation and is linked to water mobility and could be modulated by the existing myelin surface fraction (rather than its volume). The fits obtained (see Fig.6.4) are suboptimal, suggesting that either the quality of the susceptibility maps is not sufficient to obtain better parameterization (of $r_{1,My}$, $r_{1,Fe}$, $r_{2,My}^*$, $r_{2,Fe}^*$, χ_{My} , χ_{Fe}) or the model suggested is not valid across the cortex because the baseline susceptibility or relaxivity values might vary throughout the brain (which is something not tested ex vivo). Despite this limitations some of the results are sensible and shed some hope on the obtained results. The ratio of R_2^* and χ for both iron (fixed) and myelin are in good agreement with earlier work of [63]. R_1 is known to be particularly sensitive to temperature [195] and it is important to note that

the ratio $((r_{1,Fe}/r_{2,Fe}^*)/(r_{1,My}/r_{2,My}^*))$ obtained in vivo and ex vivo are of the same magnitude.

6.5 Conclusion

The cortical R_1 , R_2^* and susceptibility maps show similar contrast to that reported by other groups [189] [196] [181] with the cortical maps show an enhancing the primary Brodmann regions. The behaviour through the depth from the inner layer, close to the WM border, to the outer layer, close to the pial surface for each contrast is coherent between the left and right hemisphere, which is a first demonstration of the reproducibility of this results. The through depth behaviour information when using R_1 based data alone could be useful for subject specific cortical parcellation. The combination of information of R_1 with R_2^* cortical maps offers the potential to obtain true myelin cortical maps.

6.6 Acknowledgements

This work was supported by Centre d'Imagerie BioMédicale (CIBM) of the UNIL, UNIGE, HUG, CHUV, EPFL and the Leenaards and Louis-Jeantet Foundations. The authors would like to thank Daniel Gallichan for support on the sequence development and also Tim van Mournik for providing the software to calculate equi-volume depth segmentation of the cortical maps. D.K. and this project were funded by the Swiss National Science Foundation (SNF) grant No 132821.

6.7 Appendix

Prior to the calculation of the QSM cortical maps an important step of the data processing is the removal of the background field caused by surrounding air-tissue interfaces, as well as imperfect shimming, which overlays the small magnetic field variations from the magnetic tissue. The performance and quality of some of the state of art background removal techniques are compared. Especially their performance in the brain cortex regarding the background field removal and the estimated susceptibility.

Three background removal methods were compared that are expected to have smaller effects in the boundary region:

i.EAHF

Efficient and Automatic Harmonic Field Pre-Filtering [125] [111] solves

the Laplacian equation (Laplacian of radius 1) iteratively with boundary conditions; $\min_{\delta B_{in}} \|W_{\Delta}(\Delta\delta B - \Delta\delta B_{in})\|_2^2$, where δB is the measured field, δB_{in} is the sum of internal variations and W_{Δ} is a shrunk brain mask modulated by the SNR of the measured field map.
iteration=3000

ii. ReSharp [123]

based on Sharp [55] method and introduces additionally a Tikhonov regularization to enhance the small norm feature of the residual local field after background field removal;
radius=2;4, parameters as provided by default: alpha=0.01; tolerance=1e-2; iteration=40

iii. PDF

projection onto dipole fields [124,135] uses the fact that the background field inside a ROI is composed by fields generated by dipoles outside the ROI
iteration=3000, parameters as provided by default: tolerance=1e-1

The performance of the background removal methodologies shows a similar behavior on the resulting field maps using the EAHF and ReSharp method with the radius of 4, ReSharp(4), although the ReSharp method removes some of the outer cortical structure (see dashed arrows in Fig.6.6). Applying a radius of 2 reduces the removed cortical brain structure but is still not sufficient to keep the whole cortical surface. The PDF method is benign in terms of erosion but introduces a slowly varying field (see dotted arrows in Fig.6.6).

Comparing the cortical QSM maps the EAHF and ReSharp (other than the erosion of the cortex) show similar performance, while the PDF introduces a bias to the brain cortex which can be seen both in the volume maps (Fig.6.6) and in the cortical surface maps (Fig. 6.7). When looking at inner layers of the cortex (further from the edge of the brain mask) the ReSharp method performs as good as the EAHF method (see solid arrow in Fig.6.7), having the advantage of being computationally fast. When looking at the outer layers of the brain cortex, close to the pial surface, the EAHF method contains the most anatomical valid information. The dashed arrow in Fig.6.7 points out the expected high susceptibility values of primary sensory areas similarly to what has been observed in R_1 , R_2^* and susceptibility cortical maps studies [189] [196] [181].

All the compared background removal methods are based on the Maxwell equations and the separation of the observed field perturbation in the region of interest as a superposition of two complementary regions, the dipole field

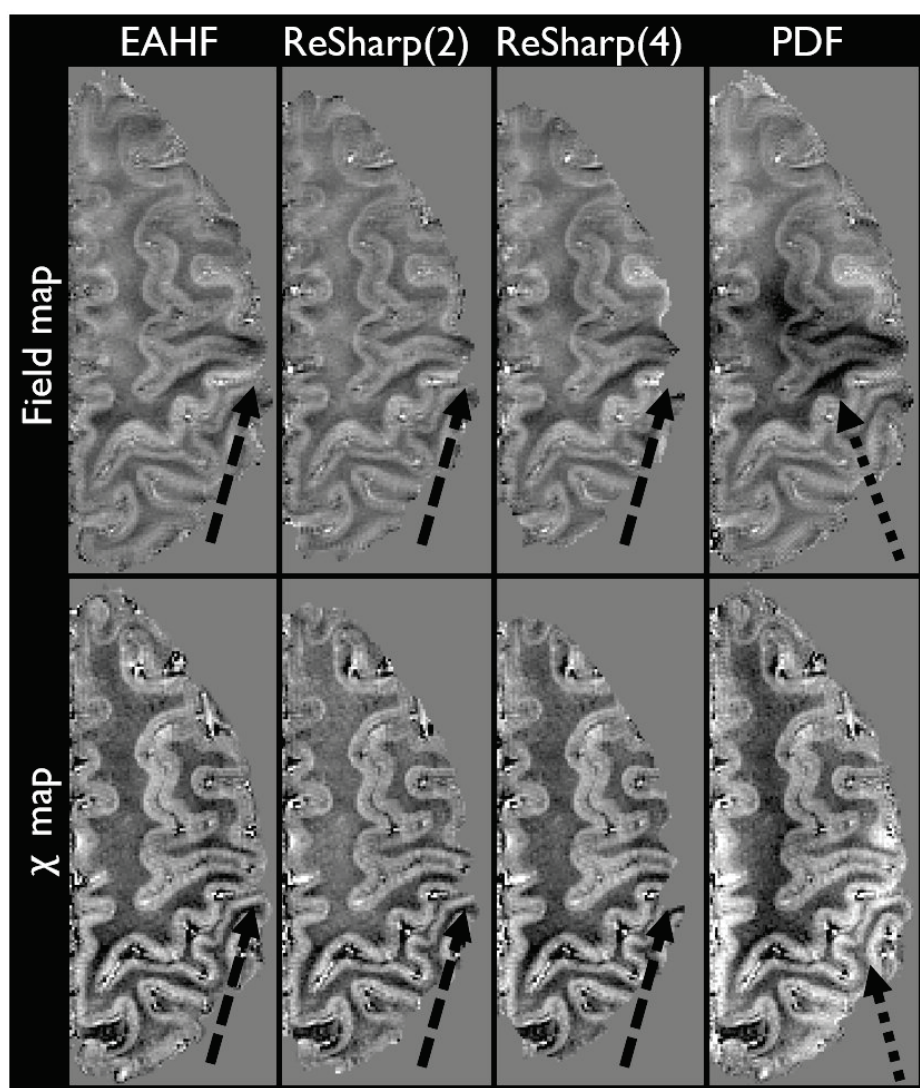


Figure 6.6: shows on first, second, third and fourth column the field map after background removal (first row) and the resulting reconstructed susceptibility maps (second row) using the background field methodologies i) EAHF, ii) ReSharp with radius 2, iii) ReSharp with radius 4 and iv) PDF, dashed arrow points to cortical brain erosion, dotted arrow points to introduced bias field.

generated by susceptibility inside and outside the ROI respectively. Therefore their performance is similar when assuming optimal conditions in the ROI definition and accuracy of the measured dipole field [46].

The PDF method relies on the orthogonality of the field induced by dipoles in-

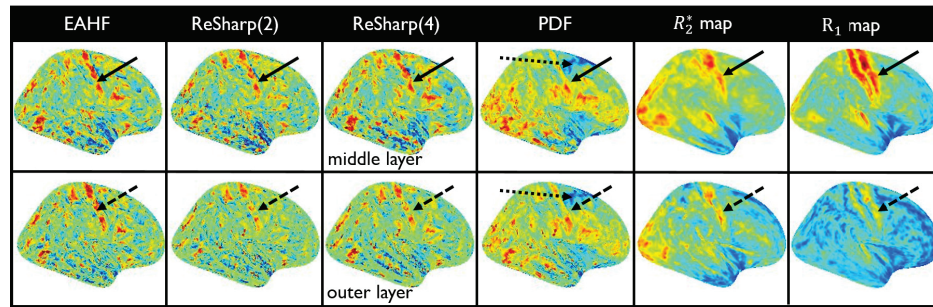


Figure 6.7: shows on the first, second, third and fourth column the QSM inflated cortical surface maps retrieved after using different background removal methodologies: i) EAHF, ii) ReSharp with radius 2, iii) ReSharp with radius 4 and iv) PDF. The first row shows the middle layer between WM and CSF and the second row shows the layer closer to the CSF. Arrows point out: solid and dashed- somatosensory cortex and the middle temporal cortex (as seen in R_1 and R_2^* maps), dotted-introduced bias field. For comparison purposes an R_1 and R_2^* surface maps are shown on the 5th and 6th column.

side and outside of the brain. Close to the boundary, where the orthogonality assumption is violated, the PDF method is prone to over-fitting [124] [126]. Also, the minimization process in the image space can introduce large field variations in the centre part, which has a reduced weight when compared to the outer part of the brain (see also the review article by [46] to observe this effect). As a consequence, in GM and in the extracted cortical layers the resulting field and susceptibility maps contain artefacts.

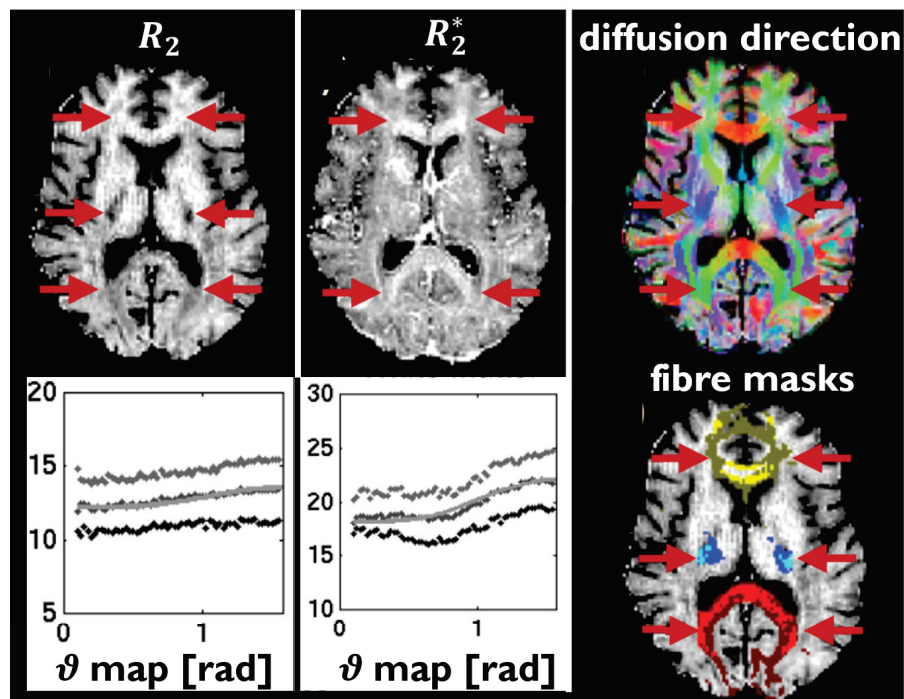
The SHARP method depends on the spherical mean value calculation and therefore the radius as well as the threshold for the k-space truncation has an impact on the resulting background removal. The width of unreliable data on the brain boundaries is decreased by using a Tikhonov regularization at the stage of the deconvolution [123] enabling the study of cortical layers close to the boundary.

The conservation of brain information close to the boundary comes along with the drawback of long computation times using the EAHF method [125]. The resulting background removal in any method depends not only on the assumptions but also on the regularization parameters and their impact propagates to the reconstructed tissue susceptibility.

Chapter 7

(apparent) relaxation rate in white matter

The characterization of the (an)isotropy in quantitative relaxation contrast R_2 and R_2^*



Abstract

Diffusion tensor imaging (DTI) is able to measure fiber orientation and distribution but it fails to provide information about myelin density, fiber concentration or fiber size within each voxel. On the other hand, quantitative contrasts like R_2^* have been demonstrated to offer iron and myelin related contrast and depend on the orientation of the applied magnetic field. The R_2 contrast compared to the R_2^* has the advantage of being robust to large scale field inhomogeneities effects.

The aim of this project was to combine the advantages of these methodologies: the fiber orientation information retrieved from the DTI acquisition and the sensitivity to microstructural information from the quantitative methods. The fiber orientation information was used as prior knowledge for both the fitting problem of R_2^* and R_2 . Using these methodology different myelin related magnetic resonance parameters were extracted from the R_2 and the R_2^* . In a first stage the spatial similarity between these quantities was correlated throughout the brain with a particular focus on the major white matter (WM) fiber bundles such as the corpus callosum (CC), forceps major (FMj), forceps minor (FMn), cingulum (CG) and corticospinal tracts (CST) which have been the subject of various studies in the past.

In a second stage the isotropic and anisotropic components of both R_2 and R_2^* were measured and studied to try and correlate these with axonal and myelination properties of the fibre bundles. With this paper we have for the first time attempted the in-vivo characterization of the orientation dependent and independent components of the transverse relaxation rates and were also able to demonstrate that the orientation of WM fibres influences R_2 and R_2^* contrasts. We also found, for both R_2 and R_2^* contrasts, isotropic and anisotropic values showed coherence between hemispheres.

7.1 Introduction

Assessing WM myelin integrity has always been an intensive field of research since it can have a big impact as potential biomarker of disease helping in early diagnosis and therapeutic methods for neurodegenerative diseases where demyelination of the axons takes place.

Also, during normal aging WM integrity and myelination levels are known to change [197–199]. Since age is the highest risk factor for neurodegenerative diseases, the actual aging society presents a need to study in more detail ways of detecting these early biomarkers.

There are various methodologies that have tried to look into these effects in WM over recent years, from volumetric methods to magnetization transfer [200, 201], relaxometry [197, 202] and even susceptibility mapping [202]. However, one of the main criticisms to many of these methods is their lack of specificity. The same can be said regarding DTI that has been the workhorse to study WM fiber orientation and distribution [203]. While fiber directionality information is very reliable and robust, it has been known that, from the simple measurement of fractional anisotropy, it is not possible to directly infer on the myelin density (and axonal transmission viability) [70] nor on fiber concentration or size within each voxel [204]. Many methodologies have been introduced over recent years to fully model the microstructural properties of WM, which rely on more complex acquisition strategies and processing as NODDI [205] and CHARMED [206] but also on a variety of assumptions. Thus, the interpretation of the fitted parameters is not a straight forward process [207].

The MR signal evolution in WM has been demonstrated [89, 208, 209] to depend on the orientation of its microstructure in respect to the main magnetic field, B_0 . This orientation dependency can be well described using a hollow cylinder model [91] in which free water exists in the intra and extra axonal space and the myelin sheath is modeled as a hollow cylinder with reduced water content with short relaxation times. For the model to be complete, the highly ordered myelin sheaths in the WM have to be assigned an anisotropic susceptibility. The inhomogeneous field around the axons and the frequency shift in the intravascular space induce a signal evolution that can be observed both in the magnitude (increased R_2^* when axons are perpendicular to B_0) and phase (echo time dependent frequency) evolution of the MR signal. This effects have been used for example in ex-vivo samples to create fiber orientation maps [143, 208]. Such susceptibility effects of microstructure are expected to be present also on R_2 maps in the fast diffusion regime which characterizes water diffusion around axons (4-20 μm).

While both R_2^* and R_2 maps are phenomenological MR quantitative param-

eters, R_2 maps have the advantage (compared to R_2^*) of being more robust to large scale field inhomogeneity that are fully refocused in a spin echo sequence. The measured R_2^* values on the other hand can depend on the voxel size used or in the presence of susceptibility inhomogeneities around larger venules and pial veins (diameter $> 100 \mu m$). While large scale B_0 inhomogeneities are discarded, microscopic B_0 field inhomogeneities, of the order of the diffusivity of water in a given time, are not cancelled in R_2 maps. This makes R_2 a strong candidate to look at the effects of myelin χ as a function of WM orientation, while avoiding other possible nuisances associated with vasculature.

While it is well known that relaxation parameters are not very specific measures of one specific biomarker, (as it depends on water mobility, paramagnetic impurities, magnetization and chemical exchange mechanisms), the ability to measure the orientation dependent part of the relaxation rate should be able to isolate mechanisms associated only the axonal and myelin organization.

In this paper we combine the fiber orientation information retrieved from DTI acquisitions (which are the gold standard to study WM orientation) with the sensitivity of R_2^* and R_2 maps to axonal orientation dependent microstructural information. By acquiring various observations of this maps with the subject's head at different positions in respect to the main magnetic field, it is possible to decompose both R_2 and R_2^* values into orientation independent and orientation dependent components. In this way we test in vivo the hypothesis that R_2 maps are also sensitive to WM fiber orientation and try to, for the first time, characterize some of the main WM fibre tracts by their level of anisotropy on the relaxation rates.

7.2 Methods

7.2.1 Theory

In a previous ex vivo study Lee et al [208] characterized the R_2^* anisotropy component due to structured nature of axons. In this work it was observed that, given that the susceptibility of myelin is anisotropic [87, 190], this would imply that the angular dependence would not only have only a $\sin^2(\vartheta)$ dependence (that is proportional to the amplitude of frequency shifts induced by the cylindrical perturber with a different susceptibility) but also a $\sin^4(\vartheta)$. The fitted results, when having a very large number of fiber orientations (18 covering the whole set of polar angles) did support this model.

When taking the hollow cylinder model, Wharton and Bowtell [143] derived

an equation for the R_2^* relaxation dependence assuming that dephasing was in the quadratic regime rather than in the static regime that had a dependence only on $\sin^4(\vartheta)$ (see appendix and equation A10 of the referred publication). This derivation is in agreement with numerical simulations performed in the context of BOLD contrast [210] that show that, at 3T, for cylinder perturber diameters under $15 \mu\text{m}$ both R_2^* and R_2 have a quadratic dependence on the susceptibility.

Wharton et al, [143] further demonstrated that it was possible to obtain fiber orientation maps based multiple acquisitions with the sample rotated. This corresponds to a fit of four parameters: (i+ii) the main fiber orientation in polar coordinates, ϑ and φ ; (iii) one isotropic term, independent of the fiber orientation; (iv) one anisotropic term - changing with ϑ . The fitting of four parameters to a small set of orientations makes the problem sensitive to noise amplification and the non-linearity of the problem makes it's computation less trackable. In our study this was decreased by reducing the number of parameters to two by using prior knowledge on the fiber orientation DWI, which makes the problem simply linear:

$$R_2^{(*)} = R_{2,ISO}^{(*)} + R_{2,ANISO}^{(*)} \cdot \sin^4(\vartheta) \quad (7.2.1)$$

$R_2^{(*)}$ and ϑ are the (apparent) transverse relaxation rate of a given fiber and its angle in respect to the static field when the head is in a certain position. The coefficients $R_{2,ISO}^{(*)}$ and $R_{2,ANISO}^{(*)}$ denote the orientation independent and dependent components of the contrast respectively. For the sake of clarity, it should be noted that the (AN)ISO subscripts in this context do not refer to (an)isotropic susceptibility but to the isotropic or anisotropic nature of the underlying microstructure.

7.2.2 Data Acquisition

Scans were performed on a 3T MR scanner (Siemens, Erlangen, Germany) using a 32 channel receive coil (Nova Medical). Six healthy volunteers (age = 21 ± 3 years) were studied according to a protocol approved by the local ethics committee.

The following protocols were acquired at the start of the session with the subject in the standard supine position:

1. Structural T_1 w imaging and R_1 maps were acquired using the MP2RAGE sequence [148] with the following parameters:
 $TR/TI_1/TI_2/TE = 6000/700/2000/2.34$ msec; $FA_1/FA_2 = 6^\circ/5^\circ$;
 GRAPPA=3; resolution 1mm isotropic; acquisition time $T_{aq}=7$ min 32 sec;

2. Diffusion weighted imaging (DWI) was acquired with a simultaneous multislice diffusion weighted EPI sequence (Human Connectome project) with the following parameters:

MB=3 $TR/TE=3490/74.6$ ms, $FA = 90^\circ$; resolution 1.5mm isotropic; matrix size= 150×150 ; number of slices=90; $BW = 1852$ Hz/Px; slices positioned axially with phase encoding direction AP; GRAPPA=2; b-value = 1000 s/mm²; number of encoding directions=137 (half a sphere); $T_{aq} = 8$ min and 47 sec.

The following protocols were repeated from five up to seven times for each volunteer with different head positions: normal; head tilted around medio-lateral axis (left–right axis, pitch) in head-to-neck direction (up to 14°) position; tilted around anterior-posterior (nose-neck axis, roll) in head-to-left-shoulder direction (up to 25°) and head-to-right-shoulder direction (up to 25°).

3. 3D gradient echo multi echo (GRE) sequence was used to compute R_2^* maps. The following parameters were used:

$TR/TE_1/TE_5 = 63/4.97/37.77$ ms; $BW=200$ Hz/Px; $FA = 10^\circ$; $FOV = 256 \times 192 \times 137$ mm; resolution=1.5mm isotropic; slab positioned axially with phase encoding RL, GRAPPA = 2×2 ; $T_{aq}=2$ min 39 sec.

4. Multi-echo-spin-echo (MESE) prototype sequence provided by Siemens was used to compute R_2 maps. This package uses GRAPPATINI [27], which combines the model-based reconstruction MARTINI [28] with parallel imaging and enables high acceleration factors when using multiple receiver coils. The multi-echo-spin-echo (MESE) sequence with following parameters was used:

$TR/TE_1/TE_{10} = 4080/9.6/96$ ms; $BW = 363$ Hz/Px; resolution 1.5mm isotropic; $FOV_{read} = 213 \times 213$ mm; number of slices = 80; slices positioned axially with phase encoding RL; MARTINI undersampling factor=3; GRAPPA=2, virtual channels=9; $T_{aq} = 2$ min and 53 sec.

7.2.3 Data processing

All data processing was performed in MATLAB (version 2014, The MathWorks, Natick, MA, USA) on a Linux cluster workstation.

7.2.3.1 R_2^* and R_2 calculation

The multi-channel GRE data from the different coils was combined and processed as described in [111] to obtain R_2^* maps and M_0 maps for each head

position.

The R_2 maps were automatically calculated online using a gradient-scaling method which minimizes aliasing artefacts associated with the down sampling while making sure the data is characterized by an exponential decay [27].

Additionally, restrictions of the range of R_2^* and R_2 values were applied for each orientation and subject. These restrictions are based on trustworthy R_2^* and R_2 value calculation with the used echo times: the smallest R_2^* and R_2 value being $1/(3 \cdot \max(TE))$ and the maximal R_2^* and R_2 value being $1/(3 \cdot \min(TE))$. This prevented unwanted large variations of the quantitative parameters in regions with partial volume of CSF and large veins.

7.2.3.2 Co-registration

The co-registration procedure of the normal head orientation to the DTI space was performed using FLIRT tool from FSL software. For the co-registration protocol to cope with the large head rotations that resulted in large variations of the image intensity, a bias field correction was applied to all magnitude images (M_0 maps of both the 3D GRE and 2D MESE) using FSL-FAST. As it can be seen in Figure 7.1, the co-registration of different M_0 maps was divided into three steps. The first step involved a co-registration between the M_0 map in the reference position (brain extracted) and the S_0 map (mean EPI image without diffusion sensitizing gradients) in the diffusion space. In the second step a first co-registration was conducted prior to brain extraction in order to achieve a rough alignment of the structural images. Brain extraction was then performed to the co-registered head positions. The resulting brain extracted images were co-registered with the brain mask from the brain extraction of the M_0 map in the reference position performed in the first step in order to get an alignment of the different head positions to the reference position based on brain tissue alone. The movement matrices from the first and second stage co-registration were combined in the third step and the resulting movement matrix was applied to the original head positions to minimize the smoothing effect from reslicing using FSL-FLIRT. The resulting rotation matrices were applied to the different M_0 maps R_2 and R_2^* maps.

7.2.3.3 DTI data processing

The pre-processing of the DTI data was done using a homemade Matlab toolbox. This tool performed denoising using LPCA, individual volumes were realigned with a mutual information cost function and eddy current artefacts were corrected using SPM. Susceptibility induced distortions were corrected

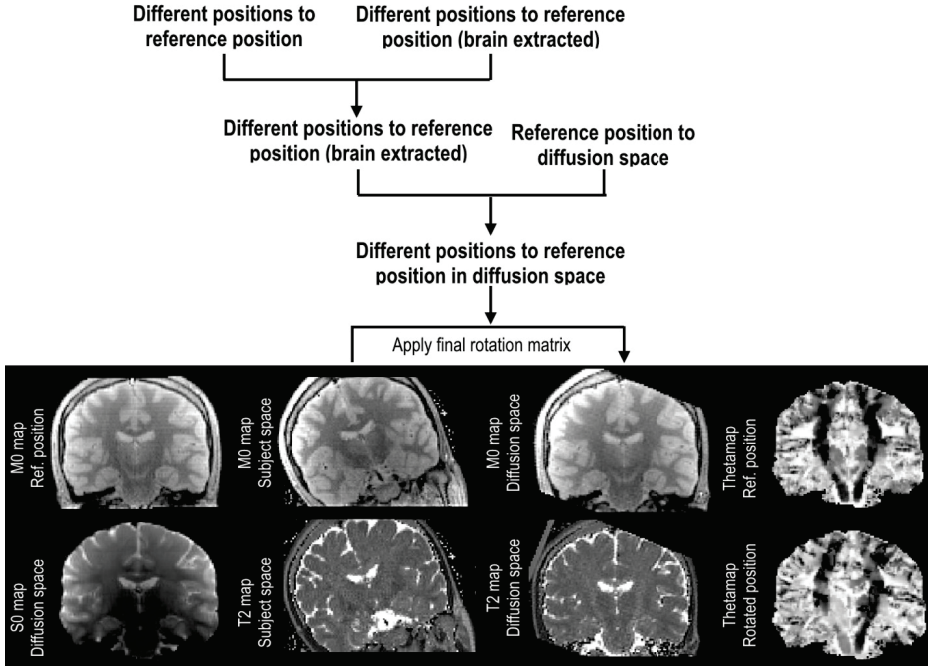


Figure 7.1: Scheme of the co-registration procedure; i) co-registration of the reference position of GRE/MESE data to DTI (first column), ii) rotated head to reference position, iii) combination of rotation matrices and application of final rotation matrix to all rotated head orientations shown on MESE data (second and third row). The calculated angle maps (ϑ maps) are shown for reference and rotated head position (last row).

by co-registration to the T_1 images along the phase encoding direction only using mutual information as the cost function [211]. After pre-processing the diffusion data, the post processing steps included the use of DTIFIT and BEDPOSTX tools from FSL software with the default parameters.

7.2.3.4 Angle map calculation

The post-processed DWI was used to calculate angle maps (ϑ) between the main fibres and B_0 using the following relationship.

$$\vartheta(r) = \arctan\left(\frac{\sqrt{v_x^2(r) + v_y^2(r)}}{|v_z^2(r)|}\right) \quad (7.2.2)$$

where v_x , v_y and v_z represent the fiber orientation in the scanner space being the z direction is along the main static magnetic field. In order to retrieve the fiber orientation maps at the different head positions, the primary diffusion

directions (v_x, v_y, v_z) were transformed with the rotation matrices obtained from the co-registration procedure (as explained in the previous subsection). Equation 7.2.2 was then used to compute new angle maps $\vartheta_i(r)$, which denote the angle between the fiber diffusion direction and the main magnetic field at each head position, i .

The last column of Figure 7.1 shows two angle maps: one in the reference position and another in a rotated position (head to the right). The fact that the two maps have different contrast and that the map in the rotated position has a more asymmetric contrast particularly along the cortico-spinal tract (increase and decrease of the ϑ values of the right and left cortico-spinal tract respectively) than the one in the reference position corroborates the fact that these maps reflect the angle that the fibres would have done with the main magnetic field, had another DWI protocol been acquired.

7.2.3.5 Fiber mask calculation

In order to study fiber specific properties (using the assumption that the main fiber properties remain unchanged through most of its extent), several regions of interest (ROI) based on WM fibers were extracted: CST, CG, inferior long fasciculus (ILF), FMj and FMn. These fiber masks were obtained using the probabilistic tractography PROBTRACX tool from the FSL software.

The masks for the starting point (seed) and passing through (waypoint) of the neural tracts for each fiber were based on the JHU WM Tractography Atlas provided by FSL software. The standard MNI brain image was co-registered to the reference positioned Signal image and the resulting movement matrix was applied to each WM fiber. The co-registered ROI masks were binarized with a low threshold of 1 in order not to exclude any WM fibre portion. To increase the accuracy of the neural tracts, the two masks acted as both the seed and waypoint masks and an additional excluding mask (where no fibers could go through) was applied. The resulting probability map for each WM fiber was binarized with a threshold based on fiber specific percentage (92 percentile). Also, a WM fiber mask from the MNI space, with a higher threshold of 10, was applied to make sure that only fibers from the region of interest were being taken into account. The elimination of gray matter (GM) impact on the fiber masks was achieved by the application of an additional mask based on the thresholded FA map where areas of crossing fibers were also excluded (by using output of the BEDPOSTX tools from FSL software). Finally, five major WM fibres masks were obtained: CST, CG, ILF, FMj and FMn.

7.2.3.6 Computation of (an)isotropic components of (apparent) transverse relaxation rates

On a first instance the computation of the $R_{2,ISO}^{(*)}$ and $R_{2,ANISO}^{(*)}$ was done on a pixel basis by matrix inversion of

$$R_{2,i}^{(*)} = R_{2,ISO}^{(*)}(r) + R_{2,ANISO}^{(*)}(r) \cdot \sin^4(\vartheta_i(r)) \quad (7.2.3)$$

allowing the creation of individual maps of $R_{2,ISO}^{(*)}(r)$ and $R_{2,ANISO}^{(*)}(r)$.

Using the masks described in the previous section it was possible to compute, per subject, fiber specific $R_{2,ISO}^{(*)}(r)$ and $R_{2,ANISO}^{(*)}(r)$. This was done by computing one matrix inversion per fiber, where now all the voxels within a ROI are used for the inversion process increasing the range of angles in each inversion. This makes the inversion process better conditioned by making the two columns of the matrix inversion more independent.

To further improve the inversion, R_2^* outliers that (for each angular bin) had values on the under the 10th and over the 90th percentile were excluded from the fitting procedure because they might reflect poorly mis-assigned pixels containing large fraction of CSF, of venous blood or should be just fitting outliers.

7.3 Results

7.3.1 Data and co-registration quality

From Figure 7.2 it can be seen that both the R_2 (a, e) and R_2^* (b, f) maps show differences in contrast that appear to be well correlated with differences in diffusion direction and different sets of fibers (c, g). In particular it can be seen that for example, the corticospinal tract (parallel to B_0) and the cingulum (perpendicular to B_0) have decreased and increased R_2 rates respectively, when compared to the remaining WM. On the other hand, some of this effects on the specific fibers mentioned earlier, seem to be less dramatic on the R_2^* . By comparing the R_2 and R_2^* maps it is clear that the latter have larger sensitivity to large veins (high values R_2^* in intrahemispheric vessels) and to field inhomogeneities (see arrow highlighting the lower temporal lobe region). Yet, on the R_2^* maps, Figure 7.2 (b, f), some of the fibres that run close to perpendicular to the magnetic field, as the FMj and FMn, have increased relaxation rates that are clearly orientation dependent (as shown on Figure 7.3 a, b) with their values changing as expected with head position and the respective angle of the FMj branch with B_0 (Figures 7.3 c, d). On the last column of Figure 7.2, sections of the calculated WM fibre tracts ROI

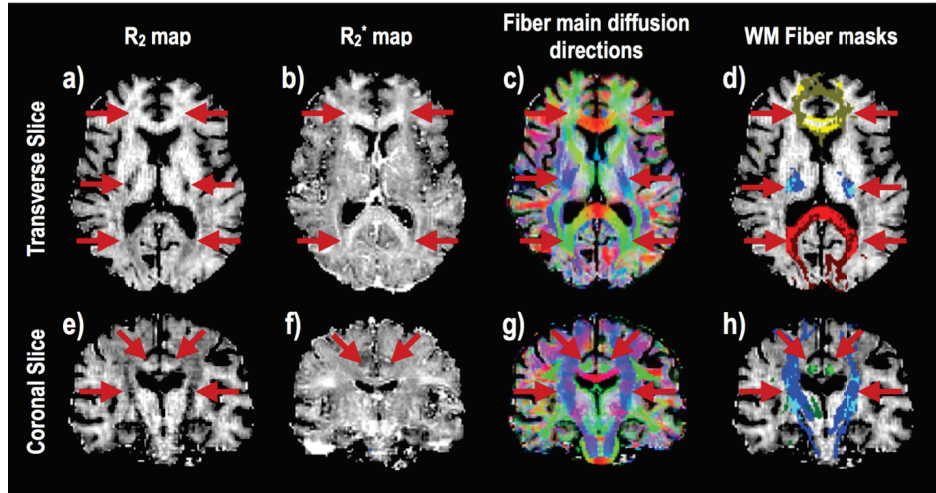


Figure 7.2: First, second, third and fourth columns correspond to a,e) R_2^* map, b,f) R_2 map a,g) diffusion directions and d,h) WM masks on a transverse (top row) and coronal (bottom row) slice. Blue: corticospinal tracts; Red: forceps major; Yellow: forceps minor; Green: cingulum. Masks in light colors come from probtrackX whereas masks in dark colors are the final masks (where an FA mask was applied and areas of crossing fibres were excluded).

that overcame the different criteria (see methods section) appear overlaid on the larger ROI initially derived by PROBTRACX.

7.3.2 Isotropic and anisotropic evaluation

The obtained pixel by pixel maps of $R_{2,ISO}^{(*)}$ and $R_{2,ANISO}^{(*)}$ were generally noisy despite the attempts to smooth the original relaxation rate maps. This can be attributed to only seven positions existing for each measurement and, depending on the orientation of the dominant fiber, a limited range of $\sin^4(\vartheta)$ exists. An example of such instability is the appearance of negative values on the $R_{2,ANISO}^{(*)}$ maps which are not physically plausible. This could additionally be attributed to model inconsistency in case of crossing fibers and registration errors close to regions rich in CSF.

Surprisingly by looking at Figure 7.4, in the R_2 maps the CST presents a low intensity on the isotropic component and comparable properties to surrounding WM on the anisotropic component. The isotropic component on the other hand enhances FMj and FMn when compared to the remaining CC.

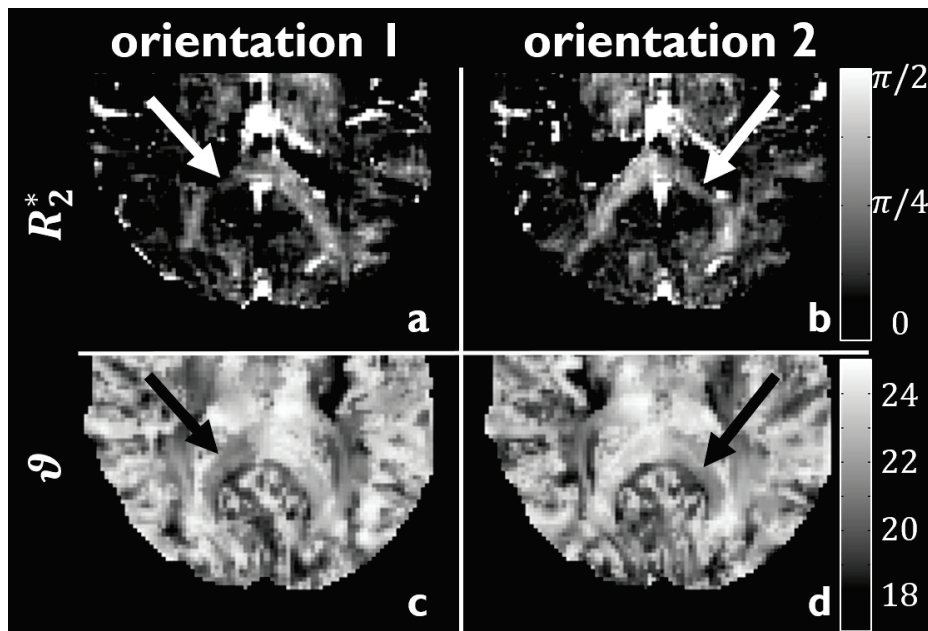


Figure 7.3: Shows R_2^* maps (a,b) and θ maps (c,d) for two different head orientations; head to the right (a,c) and left (b,d) shoulder. The arrows point out the contrast (white) and angle (black) differences in the forceps major fibre bundle.

The maps of the isotropic component of $R_{2,ISO}^*$ maps for one subject (see Fig-

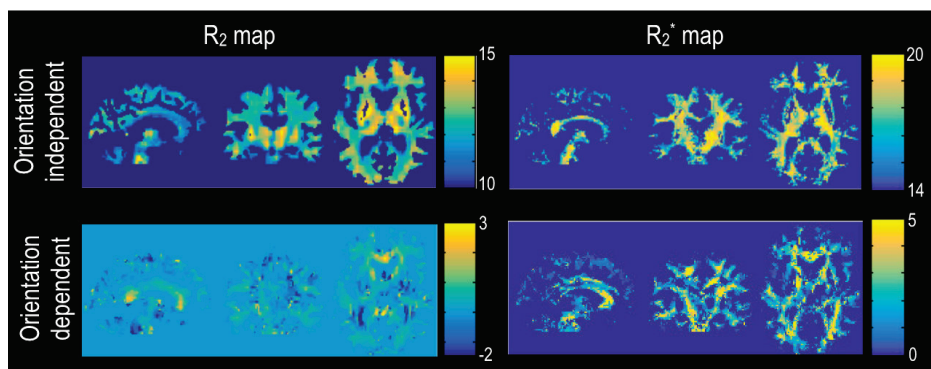


Figure 7.4: Orientation independent (Isotropic) and dependent (anisotropic) maps components of R_2 and R_2^* maps for a three orthogonal slices positioned at the level of the corpus callosum (sagittal slice), posterior thalamic region (coronal slice) and putamen (axial slice). Regions of grey matter and CSF have been masked.

ure 7.4 b,d) show relatively small variations of intensity throughout the brain, with only some variations in the CC/CG region Fig.7.4b. Orientation dependent R_2^* of the same subject are shown in Figure 7.4d demonstrating similar patterns to those observed by bound water pool fraction methods [212] and Vista [209]. These tend to show higher values of myelination of main fibre bundles in the middle of the brain that decay towards the cortex.

Figure 7.5 shows Eq. 7.2.1 model which correctly explains the variation of R_2 and R_2^* of WM fibres as a function of their angle in respect to the main magnetic field for one individual subject. Particularly it can be seen that, for both the total WM inside the masks (in agreement with previous reports [213]) and for each fibre mask, the fitting of the R_2 and R_2^* values closely matches the 50th percentile curve although with different levels of orientation dependence for different fiber bundles. For the sake of completeness a $\sin^2(\vartheta)$ fit was also attempted instead of $\sin^4(\vartheta)$ and it was observed that the fit had a larger deviation from the 50th percentile for all the studied WM fibres (data not shown).

Due to the mobility restrictions inside the head coil ($< 30^\circ$), the whole

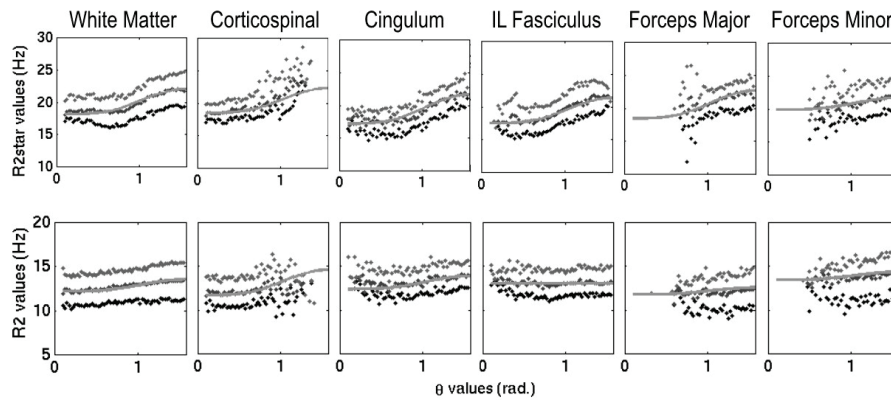


Figure 7.5: Plots of the apparent transverse relaxation rate (top row) and transverse relaxation rate (bottom row) as a function of ϑ (in radians) for one single subject within different WM regions of interest. Light, dark gray and black dots represent the, 10th, 50th and 90th percentile for each angle bin and the grey line represents the fitted model (Eq. 7.2.1) in that ROI.

angle range (0 to 90°) was not obtained for most studied WM fibres, with the CST tract having the smallest range due to its head-foot orientation. This can be seen both on the x-axis of Figure 7.5 where the range of angles available for the fit varies considerably depending on the fiber bundle, but even more dramatically on Figure 7.6f. In fact the robustness of the matrix

inversion depends on the range $\sin^4(\vartheta)$ whose available distribution for each fiber bundle can be seen on Figure 7.6f. From this distribution bars it can be seen that 80% of the relaxation measurements had a $\sin^4(\vartheta)$ range of $\sim 27\%$, 60%, 75%, 50%, and 55% for the CST, CG ILF, FMj and FMn respectively.

From Figure 7.6(a-d) it can be seen that, as expected, both the isotropic

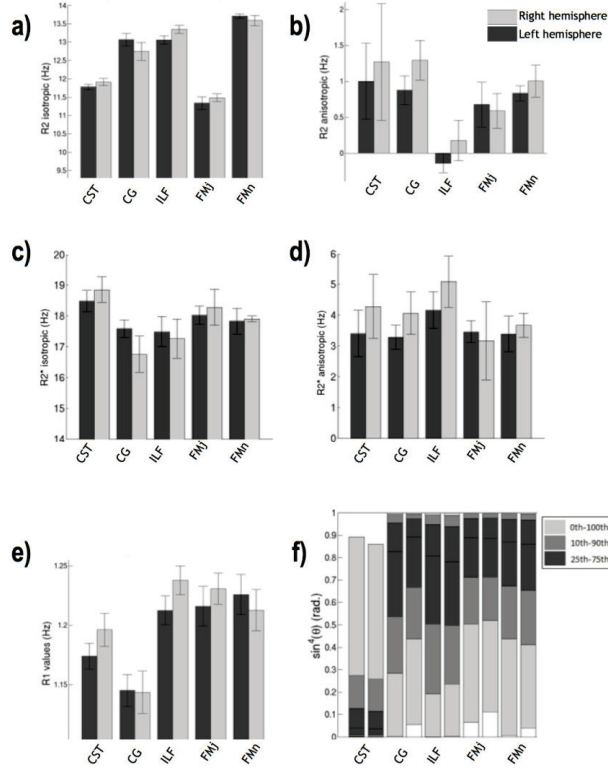


Figure 7.6: Bar plots of the average and standard error of a) R_2 isotropic values; b) R_2 anisotropic values; c) R_2^* isotropic values; d) R_2^* anisotropic values; e) R_1 values for the mean value across subjects and for the different WM masks generated on the left and right hemispheres. Plot f) shows the range of $\sin^4(\vartheta)$ present for each of the fiber masks in a representative subject.

and anisotropic components of R_2^* are always bigger than R_2 . Also, it is encouraging to see that the left and right hemisphere behaviour were very consistent for each fibre and parameter $R_{2,(AN)ISO}^*$ and that all measured anisotropic component (Fig. 7.6b and 7.6c) have physically meaningful values (positive). Yet, the dependence across fibers varied significantly for different parameters with no consistent behaviour. Across the 5 studied fiber bundles, the isotropic component of R_2 (Fig. 7.6a) shows statistically signifi-

cant differences mainly between CST and FMj and the remaining fibers. The reduced $R_{2,ISO}$ of CST and FMj could be attributed to water mobility and axonal size. Yet, this differences disappear (with a tendency to be inverted) when looking at $R_{2,ISO}^*$ (see Fig. 7.6c). Given that $R_{2,ISO}^* = R_{2,ISO} + R'_{2,ISO}$, this could be potentially explained by an increased vascularization of sites with larger axons [214] (that would tend to increase the isotropic component of R'_2 of regions with small R_2).

Fig. 7.6b shows that the CG, FMj and FMn all present significant orientation-dependent R_2 (of similar amplitude on left and right hemispheres and across fibers) of $\sim 1\text{Hz}$, while the ILF shows no significant anisotropic effects, suggesting reduced susceptibility effects and hence myelination compared to the more central set of fibers. This interpretation would be in agreement with more standard methods to measure myelination [209, 212]. The CST fiber bundles have the largest variability of anisotropy which might be related with the smaller range of ϑ values (see Fig. 7.6f) observed even after the 6 head rotations. Although the orientation dependence of R_2^* of all fiber bundles, $\sim 3\text{Hz}$, is bigger than the variability found (see Figure 7.6d), no differences could be found between the different fibers.

R_2 measurements based on multi-echo spin-echo sequences are sensitive to, not only B_1 field inhomogeneities, but also to slice profile imperfections. In the presence such nuisances the measured R_2 values can be artificially lengthened by the longitudinal relaxation, R_1 .

Using the R_1 mapping done with the MP2RAGE, it was possible to see that variations of the mean R_1 between regions (Fig.7.6e) are small (0.05Hz), but reproducible across subjects.

As B_1 profile problems are the same for all acquisitions and pixels, the variations on the anisotropic part of $R_{2,ANISO}$ is independent of the slice profile, while in the case of $R_{2,ISO}$ the variations observed ($>1\text{Hz}$) could not be induced by the 0.05Hz variation in R_1 . The same argument is valid for B_1 inhomogeneities in respect to the computed $R_{2,ANISO}$ as the changes in head position are not expected to create large differences on the measured B_1 maps but could affect the isotropic component. Yet the typical B_1 pattern in the human head is not the dominant feature (bright center) in Figures 7.2 and 7.4.

7.4 Discussion

In this paper we have for the first time attempted the in-vivo characterization of the orientation dependent and independent components of the transverse relaxation rates. We were able to observe this effects in vivo using

a methodology inspired in what has previously been done in ex-vivo samples (using sample rotation) rather than by considering that all WM fibres should have similar properties as it had been done in the past in in vivo experiments [213, 215].

Most studies in the past looking at fiber orientation dependence of contrast have been focused on T_2^* weighted imaging at 7T [91, 208, 216] where the effects are naturally larger (increased susceptibility effect). At high fields though, SAR limitations, B_1 inhomogeneities and shortening of T_2 values in WM pose serious limitations to the acquisition of T_2 maps and high quality diffusion weighted imaging. One of the differences between WM contrast at 3T and 7T is that at higher fields the apparent transverse relaxation rate will have an increased quadratic behaviour for small structures similarly to what has been demonstrated in simulations for BOLD contrast [217]. This could explain the remarkable similarity of the R_2^* map at 7T (see Fig. 7.7, protocol and data acquisition described in [111]) with the R_2 maps at 3T (see Fig. 7.2). In both these maps a low relaxivity rates can be seen for the CST when compared to the FMj, FMn and CG. Other contrasts such as the contrast between the frontal-occipital fasciculus and posterior part of the corona radiata are present across the different maps and magnetic fields.

To achieve this results, various recent technological developments had to be brought together, allowing the acquisition not only of R_2^* maps but also of R_2 maps and fiber orientation at high isotropic spatial resolution (1.5 mm isotropic). Without the use of simultaneous multi-slice diffusion weighted imaging there would be a 3-fold increase in the acquisition time with limited benefit in terms of SNR (given the relatively long TR used) or limited angular resolution. Particularly, the latter plays an important role for the calculations of the orientation dependent components as 70% of the variation expected on the relaxation parameters happens in an angular range of 45 degrees. To achieve whole brain 1.5mm isotropic R_2 maps in a short amount of time (that allowed the acquisition of 7 orientations per subject) this study took the advantage of the combination of parallel imaging techniques with model based reconstruction [27].

Previous measurements of the orientation dependent R_2^* component in ex-vivo WM tissue at 7T have reported ~ 6 Hz [208]. In ex-vivo samples, due to their lower temperature and fixation processes, water is expected to have a reduced diffusion rate and hence relaxation would be constrained to the static dephasing regime. The values obtained in this study at 3T of ~ 3 Hz (see Fig. 7.6) are in the same range if a linear dependence of on the magnetic field is assumed for the apparent relaxation rate.

Furthermore, we have shown that differences exist between sets of fibers both in its orientation dependent and independent components which we hypoth-

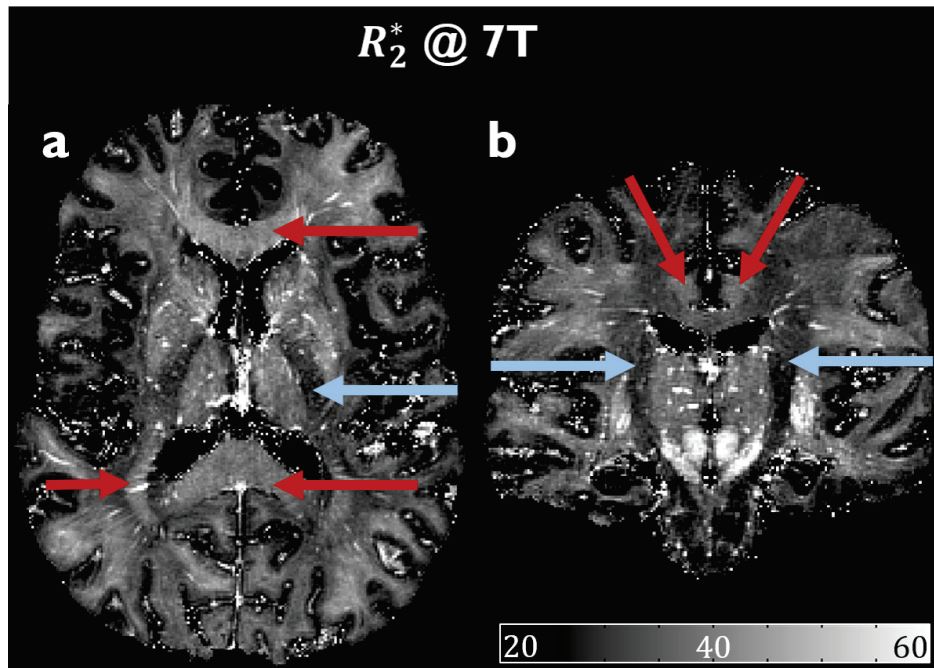


Figure 7.7: Shows R_2^* map with increased and decreased contrast (red, blue arrows) in respect to the remaining white matter, acquired on a 7T MR scanner (Siemens, Erlangen, Germany) using a 32 channel receive coil (Nova Medical), for details see [111].

size could be either related with the axonal size and myelination levels and will be the focus of future research. The orientation independent R_2 values mapped had similar values between most WM bundles (see Figs. 7.4 and 7.6) and lowest rates were found for the CST and FMj. This could potentially be associated with their increased axonal diameter [212,218] that would ensure better water mobility particularly in the intra-axonal compartment. On the other hand, the orientation independent R_2^* values showed a higher variability between the fibre bundles studied, with CST having the highest value (followed by the FMj), and CG and ILF having the lowest values. This corresponds to a quasi inversion of the dependence that is surprising given that the effects of R_2 are included on the R_2^* measurements with the difference being those attributed to static dephasing. One potential source of this increased static dephasing in regions of larger axonal diameter could be attributed to their increased vascularisation [214]. As for the orientation dependent components of R_2 and R_2^* , that should be attributed to susceptibility effects arising from the diamagnetic myelin. The lowest effects on R_2 (0Hz were observed in the ILF) again corresponded to the highest ef-

fect R_2^* although in the latter this difference was not significant (see Figure 7.6). A bigger differentiation was seen between fibers in R_2 than R_2^* despite their reduced amplitude. Another alternative explanation to these different behaviours could be attributed to magnetization transfer effects that are increased on the multi-slice spin-echo experiment in respect to the volumetric gradient echo experiment, making the R_2 and R_2^* maps weighted towards different compartments.

One observation that can be made from the obtained data is that while the within subject variability of the R_2 and R_2^* estimations was comparable (see Fig. 7.5), the reproducibility across subjects was increased on the R_2 maps (see Figure 7.6). Note for example that the orientation dependent transverse relaxation rate, $R_{2,ANISO}$, differences are of the order of $\sim 1\text{Hz}$ which is the size of the standard error of the orientation dependent R_2^* across subjects (Figure 7.6). This observation suggests that some further developments should be envisaged on the gradient echo acquisition methods. Both the R_2 and R_2^* mapping acquisitions could be improved by introducing prospective or retrospective motion tracking to the acquisitions [219, 220]. Despite the relative low resolution (1.5mm isotropic) when compared to the structural data to which many of these motion tracking methods have been developed for, it should be taken into account that some of the positions held by the subjects are far from comfortable and could lead to additional subject movement even on the relatively short acquisition times used throughout. The robustness of the R_2^* measurements is further affected by background field homogeneity which significantly varies for the different head positions. Various methods have been proposed in literature to deal with these artifacts to, a posteriori, use field map estimations to estimate the voxel decay associated with through slice dephasing [221]. In the current implementation, R_2^* were calculated using a sinc modulation correction of the signal evolution [222] which should suffice due to the isotropic nature of our data (no low resolution dimension) and the fact that the WM ROIS were located away from the main air-tissue interfaces. One aspect that could play an important role and should be investigated in future implementation is the use prospective or retrospective compensation of respiration induced frequency offset either by dynamic shimming methodologies [223] or the use of navigation data [224]. One aspect that affects the accurateness of the R_2 maps (using a multiple spin echo sequence) is the varying relative B_1 field across the brain. Higher deviations from the nominal B_1 value result in decreased R_2 estimations (due stimulated echo contamination). This effects could be overcome by adding B_1 map measurement for each orientation that could be used a posteriori (together with the acquired R_1 map) to correct the estimated R_2 [225].

7.5 Conclusion

In this manuscript we have demonstrated in vivo that the orientation of WM fibres influences both R_2 and R_2^* contrasts. Furthermore, we have shown that different fiber bundles have both different orientation dependent and independent components. For all these quantitative measures a high degree of coherence was found between hemispheres. This implies that both when measuring R_2 and R_2^* in WM at 3T it should be taken into account that $1 \sim 3$ Hz are associated with the orientation of the underlying axons and this range might be fiber dependent.

At this stage, the methodology used does not have the sensitivity to characterize the myelin properties such as myelin volume fraction, axonal diameter or axonal g-ratio in vivo. Other than developments that could improve the SNR of the measured maps, the big limitation of this framework is to obtain large enough rotations of the axons in respect to the magnetic field while using a multiple channel RF coil.

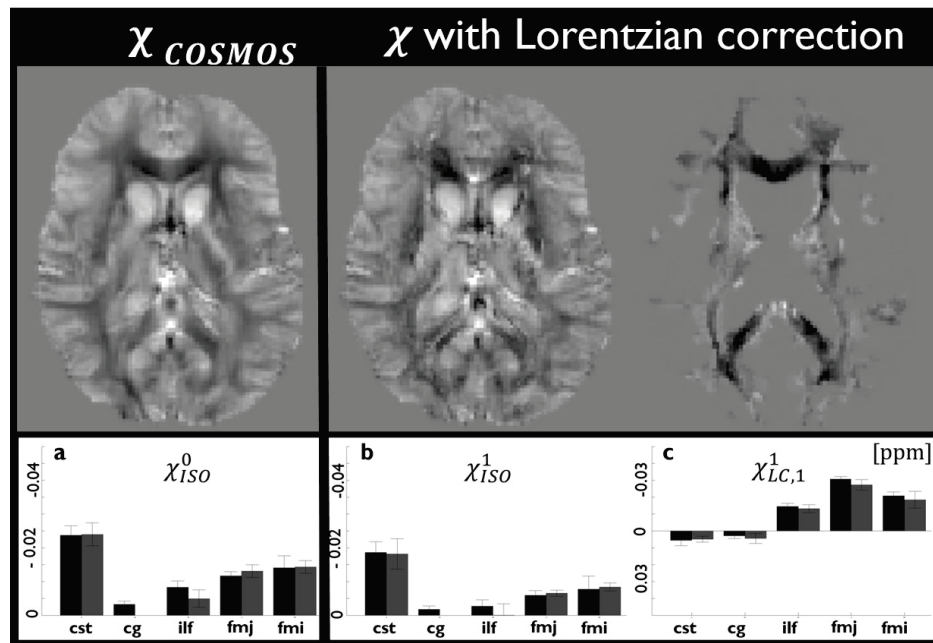
7.6 Acknowledement

This work was supported by the Donders Institutes in the Netherlands. D.K. and this project were funded by the Swiss National Science Foundation (SNF) Mobility grant No 132821.

Chapter 8

QSM in white matter, Lorentzian correction

Quantitative susceptibility mapping including a white matter Lorentzian correction



Abstract

Quantitative susceptibility mapping (QSM) has been shown to provide quantitative measures of iron concentration in deep gray matter structures. In white matter, QSM is affected not only by the local susceptibility but also by the local organized microstructure of axons and its myelin coating where reduced water signal exists. Recently, the anisotropic effect of myelin susceptibility was shown to be minor compared to the effect of its compartmentalization.

In this work, the Lorentzian correction was, for the first time, implemented in a COSMOS like QSM reconstruction. Hereby, the orientation of the white matter fiber was retrieved from the diffusion tensor imaging (DTI) acquisition. The effect of the Lorentzian correction on the computed susceptibility values was analyzed in white matter. Moreover, the impact of including only the main fiber diffusion orientation and additionally also the second fiber orientation was studied.

The correction does not affect the deep gray matter structure values, but creates QSM maps of isotropic susceptibility and maps of the susceptibility of cylindrically organized inclusion spaces.

8.1 Introduction

With the proliferation of high field systems ($> 3T$) in the last decade the contrast of susceptibility origin that can be observed in standard gradient echo images both in magnitude and phase, has gained increased interest. Because of the large RF field inhomogeneities observed at high field, many researchers have put significant efforts on extracting quantitative information from multi-echo gradient echo, GRE, data.

From GRE data it is also possible to extract quantitative information regarding the apparent transverse relaxation rate, R_2^* , of the magnitude data and the local magnetic field inhomogeneity from the phase data. Particularly, the contrast observed in the phase part of the signal has shown to reveal very strong and interesting tissue contrast despite its non-local nature, not only in deep gray matter structures but also within white matter. The signal observed in phase contrast is known to be proportional to the projection along the z direction (direction of the main static field) of the local magnetic field, which is supposed to be a convolution of the local magnetic susceptibility distribution, χ , with that of a magnetic field dipole [127] [47].

In order to reveal the non-local and quantitative contrast of magnetic susceptibility, the quantitative susceptibility map (QSM), many reconstruction methods have been proposed [131] [128] [135] [57] [139] [111].

Subsequently, careful bench work has demonstrated that phase images of WM fibers acquired with a GRE sequence were microstructure orientation dependent [87], suggesting that an anisotropy of the magnetic χ was being observed, which has more recently been demonstrated in non-MRI based experiments [190]. At the same time, another group proposed a formalism that takes the χ anisotropy of the underlying microstructure into account when performing χ mapping, this method was dubbed susceptibility tensor imaging (STI) and has been shown to obtain fiber orientation which are in a good agreement with the conventional DTI fiber tracking method [88] [104] [72].

Alternative physical mechanisms were put forward to explain the strong contrast between white and grey matter (and within white matter) in phase imaging, in which, rather than emphasizing on the role of the anisotropy of χ , it was suggested the compartmentalization of χ in regions with low water concentration and/or very short water T_2^* could play an important role in the measured static field by MRI making the sphere of Lorentz approximation used on the standard forward model [127] invalid in the context of white matter [86] and the need to introduce the generalized Lorentzian correction [84]. Various theoretical models validated both ex-vivo and in-vivo have brought the role of water compartmentalization and anisotropic susceptibility of myelin to be able to completely explain the magnitude and phase

signal evolution of MR signal in white matter [91] [84]. Yet, in a recent post-mortem and simulation study [83], it was shown that, to be able to reproduce the phase images typically observed in vivo, taking account of the microstructure orientation via Lorentzian correction (LC) had a dominant role over the anisotropy of the susceptibility of myelin. Furthermore, the presence of Lorentzian correction on the forward model had a strong impact on the calculated susceptibility measures of white matter using STI.

The aim of this study is to combine the fiber orientation information retrieved from conventional DTI acquisitions to compute susceptibility maps with a Lorentzian correction (LC). The impact of the Lorentzian correction on the susceptibility values of major WM fiber bundles was studied. A particular focus was given to the study of major white matter fiber bundles such as the corpus callosum (CC), forceps major (FMj), forceps minor (FMn), cingulum (CG) and corticospinal tracts (CST) which have been the subject of various studies in the past. The LC was performed when using only the first fiber orientations as well as including both the first and second fiber orientation to the correction.

8.2 Methods

8.2.1 Data Acquisition

Six healthy volunteers (age = 23 ± 3 years) were scanned on a 3T MR scanner (Siemens, Erlangen, Germany) using a 32 channel receive coil (Nova Medical). This study was performed according to a protocol approved by the local ethics committee.

8.2.1.1 DTI

A simultaneous multislice DWI-EPI [226] sequence was used to obtain DWIs with the following scanning parameters: $TR/TE=3490/74.6$ ms, $FA = 90^\circ$; spatial image resolution= $1.5 \times 1.5 \times 1.5$ mm; matrix size= 150×150 ; number of slices=90; $BW = 1852$ Hz/Px; iPat=2; MB=3; b-value = 1000 s/mm²; diffusion encoding directions=137; acquisition time (T_{acq}) = 8min and 47 sec.

Structural T_1w imaging and R_1 maps were acquired using the MP2RAGE sequence [148] with the following parameters: $TR/TI_1/TI_2/TE = 6000/700/2000/2.34$ msec; $FA_1/FA_2 = 6^\circ/5^\circ$; GRAPPA=3; resolution 1mm isotropic; acquisition time $T_{acq}=7$ min 32 sec;

The post-processed DWI was used to calculate angle maps (ϑ) between the main fibers in respect to the applied magnetic field B_0 .

8.2.1.2 QSM

A standard 3D gradient echo multi echo (GRE) sequence was used to retrieve field maps which are used to compute QSM. To ensure flow compensation for all echo times in addition to standard flow compensation provided the manufacturer, the rewinding waveform between successive echoes was kept of equal amplitude and duration to the readout gradient (echoes were always acquired with the same gradient polarity). The following parameters were used: $TR/TE_1/TE_5 = 63/4.97/37.77$ ms; bandwidth (BW)=200 Hz/Px; flip angle (FA)=10°, FOV=256 × 192 × 137mm, isotropic spatial image resolution=1.5 × 1.5 × 1.5 mm; iPAT=2 × 2; T_{acq} =2min39sec. For each volunteer this protocol was repeated five to seven times with different head positions: normal; head tilted around medio-lateral axis(left–right axis, pitch) in head-to-neck direction (up to 14°) position; tilted around anterior-posterior (nose-neck axis, roll) in head-to-left-shoulder direction (up to 25°) and head-to-right-shoulder direction (up to 25°). The exact head rotations were determined by using a protocol on FSL (www.fmrib.ox.ac.uk) as explained in [111].

8.2.2 Data processing

All data processing was performed in MATLAB (version 2014, The MathWorks, Natick, MA, USA) on a Linux cluster.

8.2.2.1 DTI data processing

An in-house Matlab tool was used for the DTI data pre-processing. The different pre-processing steps consisted of denoising using LPCA, realignment with a mutual information cost function and correction for eddy current artefacts with SPM. Cardiac and head motion were corrected with a robust tensor estimation [227]. Susceptibility induced distortions were corrected by co-registration to the T1 images along the phase encoding direction only using mutual information as the cost function [211]. After pre-processing the diffusion data, the post processing steps included the use of DTIFIT and BEDPOSTX tools from FSL software with the default parameters.

8.2.2.2 Co-registration

In order to co-register the different contrasts and orientations the FLIRT tool from the FSL software was used. The co-registration procedure consisted of two main steps which contained further stages; i) the co-registration of the rotated head position to the normal head position of the GRE data as in [111]

(two step process, first co-registration of whole head images followed by co-registration of brain extracted images); ii) the co-registration of the normal head position of the GRE space to the DTI space; iii) To minimize the effect of double smoothing the movement matrices from the three co-registrations were combined and the resulting transformation matrix was applied to the pre-aligned GRE data based contrasts (magnitude and field maps).

8.2.2.3 Angle map calculation

Final rotation matrices from the previous co-registration were combined with the post-processed DWI information to calculate angle maps ($\vartheta_i(r)$). These maps denote the orientation of fibre diffusion direction (primary and secondary) in respect to the static magnetic field B0 for each of the different measured head position. For each subject and head position two angle maps were calculated for the primary and secondary diffusion direction with the following equation:

$$\vartheta_{i,primary}(r) = \arctan\left(\frac{\sqrt{x_{i,primary}^2(r) + y_{i,primary}^2(r)}}{|z_{i,primary}^2(r)|}\right) \quad (8.2.1)$$

where x_i , y_i and z_i represent the orientation of the primary (or secondary) diffusion vector when taking into account the rotation matrix associated with the head position i .

8.2.2.4 ROI mask calculation

In order to evaluate measured susceptibility of different white matter tracts, several regions of interest (ROI) based on WM fibers were extracted: CST, CG, inferior long fasciculus (ILF), FMj and FMn. These fiber masks were obtained using the probabilistic tractography PROBTRACX tool from the FSL software.

The masks for the starting point (seed) and passing through (waypoint) of the neural tracts for each fibers described above were based on the JHU WM Tractography Atlas provided by FSL software. The standard MNI brain image was co-registered to the reference magnitude image and the resulting movement matrix was applied to each WM fiber mask. To increase the symmetry of the neural tracts, for each fiber the two masks acted as both the seed and waypoint masks and an additional excluding mask (where no fibers can go through) was added. The resulting probability map for each WM fiber was binarized with a threshold based on fiber specific percentage (92 percentile). The elimination of gray matter (GM) impact on the fiber

masks was achieved by the application of an additional mask based on the thresholded FA map where areas of crossing fibers were also excluded (by using the output of the BEDPOSTX tools from FSL software). Finally, five major WM fibers masks were obtained: CST, CG, ILF, FMj and FMn.

8.2.2.5 QSM calculation

The multi-channel GRE data from the different coils was combined and processed as described in [111] to obtain the field and R_2^* map.

Local tissue magnetic sources generate small magnetic field variations which are overlaid by the strong background fields due to surrounding tissue-air interfaces as well as imperfect shimming. In order to retrieve the magnetic field map generated only by the local tissue sources, the EAHF (Efficient and Automatic Harmonic Field Pre-Filtering, [125]) background field removal was applied to the field map as denoted in [111].

Reference QSM maps were calculated using the COSMOS methodology [128]

$$\min_{\chi} \sum_{i=1}^R \|M(\delta B_i(r) - F^H(D_i(k)F\chi(r)))\|_2^2 \quad (8.2.2)$$

where R is the number of acquired orientations, δB_i the measured field map after the background removal and $D_i(k)$ the dipole kernel for a specific head orientation i . F and F^H denotes the Fourier and inverse Fourier transform, respectively.

While various groups have tried to perform susceptibility tensor imaging and a general approach was introduced, up to now no other group has introduced the generalized Lorentzian ellipsoid as in [83] [84] in a COSMOS like formalism [128] in which the following minimization problem is attempted experimentally

$$\min_{\chi} \sum_{i=1}^R \|F_{ISO}(\chi_{ISO}^f) - F_{LC}(\chi_{LC,f}^f, \vartheta_{i,f})\|_2^2, \quad (8.2.3)$$

where $F_{ISO} = \delta B_i(r) - F^H(D_i(k)F\chi(r))$ is equivalent to the QSM COSMOS formulation and $F_{LC}(\chi_{LC,f}^f, \vartheta_{i,f}) = M_{WM} \sum_{f=0}^F \chi_{LC,f}^F \cdot (3 \cdot \sin^2(\vartheta_{i,f}) - 2)$ accounts for the phase correction in presence of microstructural compartmentalization susceptibility in WM.

Hereby, M_{WM} , denotes the white matter mask obtained using FSL-FAST on the MP2RAGE data, which was further refined by excluding deep grey matter regions based on QSM, χ_{COSMOS} , and R_2^* maps. Deep gray matter is known to have increased magnetic susceptibility and apparent transverse

relaxation rate (Deitsung et al, and others) and thus a threshold of 40 and 0.05 was used to these two parameters for its segmentation. $\vartheta_{i,f}$ is the angle of fibre direction in respect to the static magnetic field for a given orientation i . The index f refers to the number of WM fibre populations within each pixel. When the Lorentzian correction was applied to the primary fibre orientation only, $F=1$, the method outputs an isotropic susceptibility χ_{ISO}^1 and a susceptibility of the inclusions associated with the primary fibre orientation, PF, $\chi_{LC,1}^1$. When a secondary fibre orientation was used, $F=2$, additionally to $\chi_{LC,1}^2$ (associated with the PF orientation) a third susceptibility map is reconstructed associated with the secondary fibre orientation $\chi_{LC,2}^2$.

8.3 Results

The isotropic susceptibility components as well as the components from the Lorentzian correction are shown for the COSMOS method in Fig. 8.1 (a), for LC with only the primary fiber orientation ($F=1$) in Fig. 8.1 (b, c) and for LC with both the primary and secondary fiber orientation ($F=2$) in Fig. 8.1 (d, e, f). In the cortical gray matter as well as the caudate nucleus the isotropic susceptibility for the three methods were similar. The visible contrast in the χ_{ISO} maps of white matter tracts, like fmj, on the COSMOS method was decreased when correction of the PF was applied.

It is important to note that $\chi_{LC,1}^1$ has the same polarity throughout most white matter regions. This is to be expected given that it should represent the diamagnetic magnetic susceptibility associated with myelin while, when more than one Lorentzian correction is used, does not happen particularly for $\chi_{LC,2}^2$ (which is less physically meaningful and should be attributed to inversion instability).

While introducing the Lorentzian correction reduced the WM contrast present on the isotropic susceptibility component (note for example the contrast between the optic radiation and neighbouring fibres as pointed out by the white arrow in Figure 8.1c,e) and in the process the residual maps associated with these different head positions, given by $\|F_{ISO}(\chi_{ISO}^f) - F_{LC}(\chi_{LC,f}^f, \vartheta_{i,f})\|_2^2$, is also less structured as L is increased from 0 to 2. While the magnetic susceptibility in white matter changes with the introduction of the Lorentzian corrections, the correlation of the measured QSM inside deep GM regions remains high after 1 LC ($corr_{f=0,f=1} = 0.97, r_{f=0,f=1}^2 = 0.91$) and decreases when the second LC correction is applied ($corr_{f=0,f=2} = 0.91, r_{f=0,f=2}^2 = 0.80$) as shown in Fig. 8.2 a and b, respectively.

When looking at mean properties of different white matter fibre bundles across subjects it is interesting to note that there is a systematic decrease

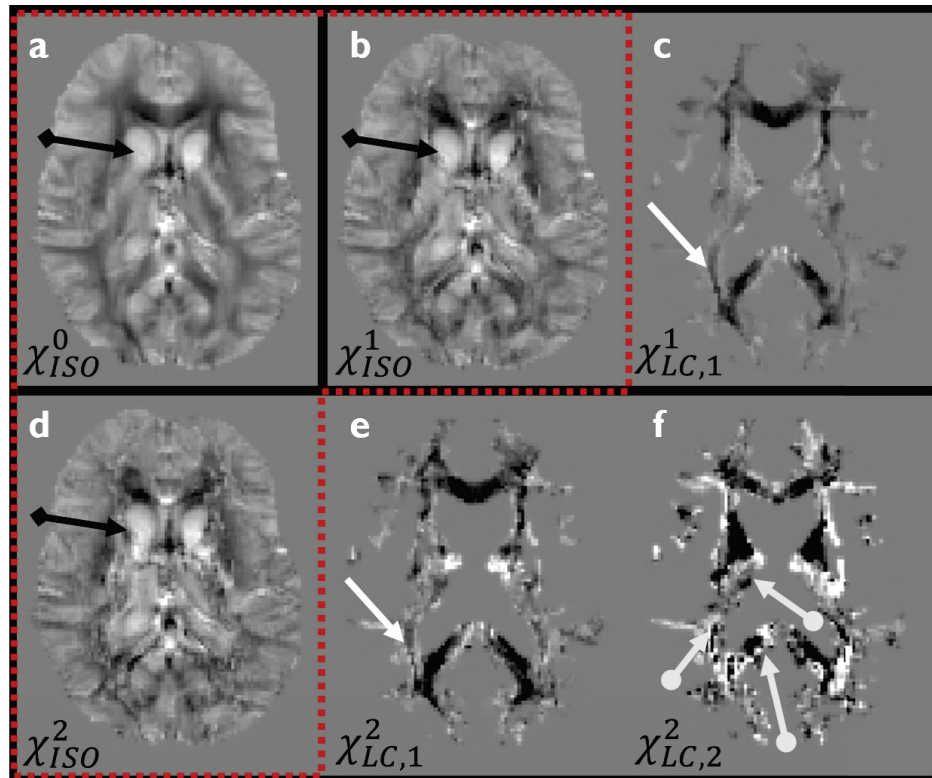


Figure 8.1: Representative susceptibility maps calculated for one subject using the three proposed methods. Isotropic susceptibility components are highlighted by red dotted frame, all reconstructed susceptibility components from each method are black framed. Methods: (a) COSMOS, (b,c) COSMOS with one Lorentzian Correction and (d-f) COSMOS with 2 Lorentzian corrections. A diamond ended black arrow in (a,b,d) highlights the caudate and the white arrow (c,e,f) highlights the contrast between optic radiation and surrounding white matter.

of χ_{ISO} for all WM fibres with the increase degree of Lorentzian correction, Figure 8.3 (a,b,d). Results were systematically reproducible between left and right hemisphere (dark and light gray bars). As for the primary fibre components, the introduction of the Lorentzian correction significantly differentiated the cortico-spinal tract and cingulum from the forceps major and minor. The attempt to characterize a secondary fibre orientation in this major fibre tracts had little effect on the estimated primary components created estimations of strong paramagnetic values for the susceptibility of myelin in, for example, the cortical spinal tract.

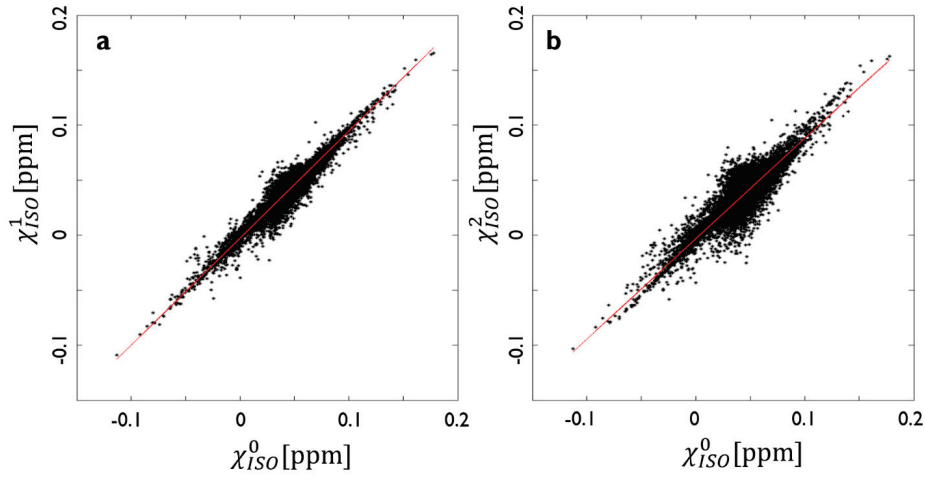


Figure 8.2: Shows the correlation in the deep GM between the isotropic component when no correction is applied χ_{ISO}^0 (similar to COSMOS) and applied to (a) χ_{ISO}^1 , only primary fibre: $corr_{f=0,f=1} = 0.97$, $r_{f=0,f=1}^2 = 0.91$ and (b) χ_{ISO}^2 , primary and secondary fibre $corr_{f=0,f=2} = 0.91$, $r_{f=0,f=2}^2 = 0.80$.

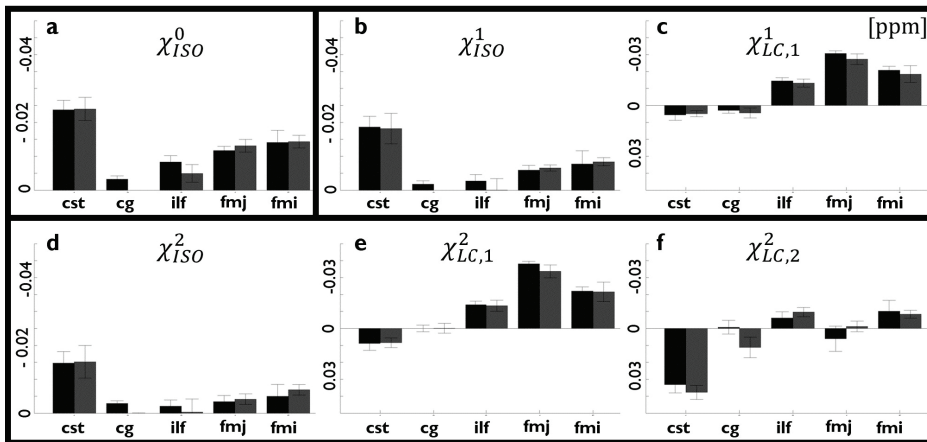


Figure 8.3: Shows mean value across all subjects inside selected WM fibers for both hemispheres (dark gray - right, light gray - left) of reconstructed susceptibility components (black framed) when (a) no, (b,c) only on primary and (d-f) on primary and secondary fibre orientation the Lorentzian corrections were used. The WM fibers are (cst - corticospinal tract, cg - cingulum, ilf - inferior longitudinal fasciculus, fmj - forceps major, fmi - forceps minor).

8.4 Discussion

In regions where highly structured and strong compartmentalization of water exists, the standard Lorentzian sphere assumption used when measuring local magnetic fields with NMR does not hold. In such cases (such as white matter) a Lorentzian correction which takes into account the angular dependence of microstructural compartmentalization in respect to the main static magnetic field has to be used [86]. While that has been long proposed, this is, to the best of our knowledge, its first implementation in the context of susceptibility mapping.

The use of one Lorentzian correction did not impact on the susceptibility values of deep gray matter structures, meaning that in studies where susceptibility maps are used to estimate iron deposition in such brain regions, the use of this correction is unnecessary. Yet, if using susceptibility maps to characterize the evolution of magnetic susceptibility in white matter [202], it is important to take the interpretation of the obtained values with care as they will be dependent both on the orientation of the local and neighbouring white matter [83]. Furthermore, adding the Lorentzian correction term, potentially allows separating the problem from susceptibility of the myelinated axons (χ_{LC}) from the un-compartmentalized and isotropic susceptibility (χ_{ISO}) which could be a new biomarker.

While method proved to be robust to noise when considering the (unrealistic) assumption of only one fibre population per voxel, the addition of a secondary fibre population create less meaningful maps of white matter susceptibility (with large changes of the polarity of its susceptibility) suggesting that the problem is then ill-posed. It is interesting to note that some of the largest susceptibility for the secondary fibre population were found in a region where one fibre orientation is clearly dominant (cortico spinal tract, optic radiation and forceps major) and secondary fibres are either in low percentage or have similar orientation. The induced noise artefacts when the secondary diffusion orientation is applied, could be improved by creating a different white matter mask for each of the Lorentzian Corrections. The white matter mask for the second fibre orientation would only allow the second term if this population is significant and its orientation is different from the primary population by more than a given threshold.

There are three main potential sources of errors in this methodology: the calculation of the angle maps, the number of measurements achievable within one scanning session and the amplitude of the rotation the subjects can achieve within a 32 channel coil setup. The estimation of the angle maps is crucial for calculation of the two susceptibility components; the component associated with isotropic susceptibility and the component related to

the compartmentalization of susceptibility. In order to retrieve the angular distribution of white matter fibres fitting models are applied to the measured diffusion signal. To ensure the high accuracy we have used a large number of orientations (138) positioned along one single hemisphere. In the framework of the “HARDI reconstruction challenge 2012” [228] compared 20 algorithms (including the DTI method from FSL toolbox) for local intra-voxel fibre structure recovery from diffusion data. The analysed reconstruction quality involved among others the angular accuracy as well the number of fibre populations present in each voxel. None of the analysed methods has been found to outperform the others in every studied experimental conditions. However, the selection of a method with the highest angular accuracy, like the ones based on the SPARSE-like approach could improve the calculated angle maps (see [228] for detailed list of available methods)).

The acquisition protocol used was based on the scanner manufacturer gradient echo sequence in which the parallel imaging acceleration without significant losses of SNR due to g-factor noise was limited to 4. Recent sequence developments exploiting the use of more SNR efficient segmented 3D EPI or the Wave Caipi [229] allow significant acceleration of these measurements which would allow the acquisition of more orientations per subject. Also, it has been shown that dynamic shimming compensating respiration frequency offsets can significantly improve the quality of the data used for QSM. Yet, the biggest limitation of the Lorentzian correction methodology was the angular range existing for each fibre. Despite the use of young, flexible subjects with preferably small heads, was the relatively small rotations could be achieved while lying inside a scanner, which meant that the achieved angle distribution of the fibres, depending on their initial orientation was restricted to $< 30^\circ$. This limitation might only be truly overcome in ex-vivo studies of small samples where the whole orientation range can be tested.

8.5 Conclusion

Although the isotropic susceptibility component changed with the number of applied corrections in white matter, the correlation between the original method and the Lorentzian correction in deep gray matter structures remained high. By introducing the Lorentzian correction for the main fibre orientation, physically meaningful susceptibility maps were obtained with improved contrast between known fibre bundles. The susceptibility values showed a good coherence in the studied white matter fibres between the left and right hemisphere. While it is known that various fibre populations exist in each pixel, trying to fit more than one population on our data and with

the current methodology gave results with increased artefacts.

8.6 Acknowledement

This work was supported by the Donders Centre for Cognitive Neuroimaging in the Netherlands. D.K. was funded by the Swiss National Science Foundation (SNSF) Mobility grant No 132821.

Chapter 9

Conclusion and Outlook

9.1 Conclusion

The work presented in this theses investigates the study of underlying structure of the brain using quantitative methods with a special emphasis on quantitative susceptibility mapping. Different brain structures have different microstructural properties and therefore different quantitative methods are compared and combined.

In order to use quantitative susceptibility mapping (QSM) a data acquisition and processing procedure is implemented based on a multi-echo gradient echo sequence. The multiple coil data using all echoes was merged to achieve a maximal available signal to noise ratio of the combination while preventing phase singularities. At the 7T MRI scanner high spatial resolution protocols were designed to look at anatomical information. At 3T a fast acquisition under 3 minutes scan time was designed to ensure a maximisation of the number of angles used and also matched to the acquired diffusion weighted acquisition. The standard processes used to remove the background field generated from air tissue interfaces from the local field induced by susceptibility sources limits the QSM to inner brain regions and hence deletes cortex regions close to the cerebrospinal fluid (CSF). Therefore a background removal method is implemented which preserves these brain regions and contains the most anatomically valid information.

Within the framework of the thesis a new QSM method is presented, the modulated closed form (MCF), with extremely fast computational time. The effects of the different regularization parameters and introduced prior knowledge was systematically analysed in different methods. Comparable results for deep gray matter and the highest correlation to the state-of-the-art method (COSMOS) was found for the proposed MCF method. Furthermore,

this method provides good reconstruction results for a wide range of chosen parameters.

QSM and R_2^* calculated from the same dataset are able to distinguish the deep gray matter structures with a similar quality. When analysing myelin related contrast the susceptibility maps show a higher sensitivity in the white matter - gray matter structures as well as early stage multiple sclerosis lesions.

Deeper insights into the human cortex are tried to be taken by the combination of three different quantitative contrasts: R_1 , R_2^* and susceptibility. The obtained cortical maps show an enhancement in the primary sensory cortex which is known to be highly myelinated. The contrasts based on the relaxation rates, R_1 and R_2^* , show a monotonically decrease from the white matter to the CSF reflecting the underlying iron and myelin decrease. The behaviour of the susceptibility is more complex because the iron and myelin content introduce an opposing sensitivity. The combination of the three quantitative contrasts enabled the calculation of myelin content and iron maps.

The white matter consists of myelin sheath wrapped around the axons and due to their microstructural lipid organization influences to R_2^* , R_2 and field maps. The orientation dependent and independent components are studied in main fibres such as forceps major and minor and cortical spinal tract for the R_2^* , R_2 . The anisotropic component associated with susceptibility is similar for the relaxation rates whereas the isotropic component of R_2^* shows a higher variability. For the QSM the anisotropy of myelin susceptibility is minor compared to its compartmentalization effect. As the assumptions made are not true in white matter, a new QSM method is proposed which includes the Lorentzian correction. The resulting deep gray matter structure remained similar to the state-of-the-art method when comparing the isotropic component but calculates physically meaningful susceptibility maps with improved contrast between known fibre bundles.

9.2 Future Work

Algorithmic improvements

The implemented background removal method preserves brain regions in the human cortex close to the CSF. This perpetuation of anatomical information comes at the expense of long computation times compared to other background removal methods. To speed up the minimization, an initial guess of the resulting field map could be implemented. This information could be based on the background removal method ReSharp, as it provides similar results for regions inside the brain.

The newly presented modulated closed form solution is extremely fast and offers good QSM reconstruction with similar quality for a wide range of parameters. An implementation of an iterative search algorithm of the optimal susceptibility reconstruction based on the L-curve minimum could further improve the results of this method. The best parameter set is considered on the L-curve point with the largest curvature. This would enable the optimal regularization parameter implementation. The extremely fast computational time, of few seconds, allows an iterative minimization implementation without significant time loss.

Verification

QSM has been shown to linearly correlate with the iron deposition in the deep gray matter structures. However, in white matter the measured field map is not only bulk magnetization, but also microstructural orientation dependent. A multiple orientation method based on COSMOS, which takes the Lorentzian correction into account was proposed. The interpretation of the results for the three different contrasts R_2^* , R_2 and QSM on the microstructure level is not straight forward. Therefore the measurement of ex-vivo tissue samples and its histological evaluation could enable deeper insights into the origin of the measured components for different white matter fibres.

Furthermore, the measurement of a broader range of fibre angles in respect to the magnetic field would allow the calculation of the full angle distribution from 0 to $\pi/2$ and would hence give a robust assessment of the orientation dependence of R_2^* and R_2 .

Standardization

Nowadays many methods are available for each processing step of the

QSM calculation: the phase unwrapping, background removal and QSM reconstruction. Each of the different methods has its advantages and disadvantages and the implementation depends on the availability of these methods and the facility infrastructure. Also different vendors and sequence parameters are used for data acquisition.

In order to rely on the quantitative nature of QSM, the influence of this huge initial variability needs to be systematically evaluated and each variability needs to be assessed: inter- and intrasubject, intra- and interfacility, and different processing methods. After the evaluation of the variability and the differences a standard QSM calculation method could be postulated.

Applications of QSM

In order to use QSM as a clinical application, QSM needs to be evaluated in respect to disease diagnosis or even prognosis. The correlations found should be, if possible, analysed in correlation with its histology to proof the evidence.

When studying the human cortex with the aid of a motion correction protocol, ultra-high resolution of isotropic 0.3 mm was achieved for the R_1 maps, enabling the delineation of smaller Brodmann regions. Besides, more points can be achieved when analysing the transition of the different contrasts from the inner to the outer layer.

Bibliography

- [1] J. J. Thomson. XXIV. On the structure of the atom: an investigation of the stability and periods of oscillation of a number of corpuscles arranged at equal intervals around the circumference of a circle; with application of the results to the theory of atomic structure. *Philosophical Magazine Series 6*, 7(39):237–265, March 1904. 2
- [2] Professor E. Rutherford. LXXIX. The scattering of α and β particles by matter and the structure of the atom. *Philosophical Magazine Series 6*, 21(125):669–688, May 1911. 2
- [3] N. Dr Bohr. I. On the constitution of atoms and molecules. *Philosophical Magazine Series 6*, 26(151):1–25, July 1913. 2
- [4] W. Gerlach and O. Stern. Der experimentelle Nachweis des magnetischen Moments des Silberatoms. *Zeitschrift für Physik*, 8(1):110–111, December 1922. 2
- [5] G. E. Uhlenbeck and S. Goudsmit. Ersetzung der Hypothese vom unmechanischen Zwang durch eine Forderung bezüglich des inneren Verhaltens jedes einzelnen Elektrons. *Die Naturwissenschaften*, 13(47):953–954, November 1925. 2
- [6] W. Pauli. Zur Frage der theoretischen Deutung der Satelliten einiger Spektrallinien und ihrer Beeinflussung durch magnetische Felder. *Naturwissenschaften*, 12(37):741–743, September 1924. 2
- [7] I. I. Rabi. On the Process of Space Quantization. *Physical Review*, 49(4):324–328, February 1936. 2
- [8] I. I. Rabi. Space Quantization in a Gyration Magnetic Field. *Physical Review*, 51(8):652–654, April 1937. 2
- [9] F. Bloch. Nuclear Induction. *Physical Review*, 70(7-8):460–474, October 1946. 3

- [10] E. M. Purcell, H. C. Torrey, and R. V. Pound. Resonance Absorption by Nuclear Magnetic Moments in a Solid. *Physical Review*, 69(1-2): 37–38, January 1946. 3
- [11] Raymond Damadian. Tumor Detection by Nuclear Magnetic Resonance. *Science*, 171(3976):1151–1153, March 1971. 3
- [12] P. C. Lauterbur. Image Formation by Induced Local Interactions: Examples Employing Nuclear Magnetic Resonance. *Nature*, 242(5394): 190–191, March 1973. 3
- [13] P. C. Lauterbur. Magnetic resonance zeugmatography. *Pure and Applied Chemistry*, 40(1-2):149–157, 1974. 3
- [14] Richard R Ernst, Anil Kumar, and Dieter Welti. NMR Fourier zeugmatography. *Journal of Magnetic Resonance (1969)*, 18(1):69–83, April 1975. 3
- [15] P. Mansfield and P. K. Grannell. NMR 'diffraction' in solids? *Journal of Physics C: Solid State Physics*, 6(22):L422, 1973. 4
- [16] A. N. Garroway, P. K. Grannell, and P. Mansfield. Image formation in NMR by a selective irradiative process. *Journal of Physics C: Solid State Physics*, 7(24):L457, 1974. 4
- [17] P. Mansfield. Multi-planar image formation using NMR spin echoes. *Journal of Physics C: Solid State Physics*, 10(3):L55, 1977. 4
- [18] NIST. CODATA Values of the Fundamental Constants, 2015. 10
- [19] A. Hendrix. Magnets, Spins, and Resonances: An introduction to the basics of Magnetic Resonance. 2003. 13, 14, 15, 19, 22, 24, 26, 28, 29, 32, 33, 35, 37, 38
- [20] T. R. Brown, B. M. Kincaid, and K. Ugurbil. NMR chemical shift imaging in three dimensions. *Proceedings of the National Academy of Sciences*, 79(11):3523–3526, January 1982. 25
- [21] Stig Ljunggren. A simple graphical representation of fourier-based imaging methods. *Journal of Magnetic Resonance (1969)*, 54(2):338–343, September 1983. 25
- [22] Donald B. Twieg. The k-trajectory formulation of the NMR imaging process with applications in analysis and synthesis of imaging methods. *Med Phys*, 10:610–621, 1983. 25

- [23] Mark A. Griswold, Peter M. Jakob, Robin M. Heidemann, Mathias Nitka, Vladimir Jellus, Jianmin Wang, Berthold Kiefer, and Axel Haase. Generalized autocalibrating partially parallel acquisitions (GRAPPA). *Magnetic Resonance in Medicine*, 47(6):1202–1210, June 2002. 29, 38
- [24] Klaas P. Pruessmann, Markus Weiger, Markus B. Scheidegger, and Peter Boesiger. SENSE: Sensitivity encoding for fast MRI. *Magnetic Resonance in Medicine*, 42(5):952–962, November 1999. 30
- [25] R. R. Ernst and W. A. Anderson. Application of Fourier Transform Spectroscopy to Magnetic Resonance. *Review of Scientific Instruments*, 37(1):93–102, January 1966. 34
- [26] Chunlei Liu, Wei Li, Karen A. Tong, Kristen W. Yeom, and Samuel Kuzminski. Susceptibility-Weighted Imaging and Quantitative Susceptibility Mapping in the Brain. *Journal of magnetic resonance imaging : JMRI*, 42(1):23–41, July 2015. 36, 44, 51, 61
- [27] Tom Hilbert, Tobias Kober, Tilman J. Sumpf, Tan Zhengguo, Jens Frahm, Pavel Falkovskiy, Heiko Meyer, Rolf Bendl, Jean-Philippe Thiran, Reto Meuli, and Gunnar Krueger. MARTINI and GRAPPA - When Speed is Taste. 2014. 38, 132, 133, 142
- [28] Tilman J. Sumpf, Martin Uecker, Susann Boretius, and Jens Frahm. Model-based nonlinear inverse reconstruction for T2 mapping using highly undersampled spin-echo MRI. *Journal of Magnetic Resonance Imaging*, 34(2):420–428, August 2011. 38, 132
- [29] Tom Hilbert and Tobias Kober. Model-based Accelerated T2 Mapping. April 2015. 39
- [30] Lauren J. O'Donnell and Carl-Fredrik Westin. An introduction to diffusion tensor image analysis. *Neurosurgery clinics of North America*, 22(2):185–viii, April 2011. 40, 41, 42, 43
- [31] Brian J. Jellison, Aaron S. Field, Joshua Medow, Mariana Lazar, M. Shariar Salamat, and Andrew L. Alexander. Diffusion Tensor Imaging of Cerebral White Matter: A Pictorial Review of Physics, Fiber Tract Anatomy, and Tumor Imaging Patterns. *American Journal of Neuroradiology*, 25(3):356–369, January 2004. 41
- [32] A. J. De Crespigny, T. P. L. Roberts, J. Kucharczyk, and M. E. Moseley. Improved sensitivity to magnetic susceptibility contrast. *Magnetic Resonance in Medicine*, 30(1):135–137, July 1993. 43

- [33] J. R. Reichenbach, R. Venkatesan, D. J. Schillinger, D. K. Kido, and E. M. Haacke. Small vessels in the human brain: MR venography with deoxyhemoglobin as an intrinsic contrast agent. *Radiology*, 204(1):272–277, July 1997. 43, 44, 53
- [34] E Mark Haacke, Yingbiao Xu, Yu-Chung N Cheng, and Jürgen R Reichenbach. Susceptibility weighted imaging (SWI). *Magnetic resonance in medicine: official journal of the Society of Magnetic Resonance in Medicine / Society of Magnetic Resonance in Medicine*, 52(3):612–618, September 2004. 43, 69
- [35] J. M. de Souza, R. C. Domingues, L. C. H. Cruz, F. S. Domingues, T. Iasbeck, and E. L. Gasparetto. Susceptibility-weighted imaging for the evaluation of patients with familial cerebral cavernous malformations: a comparison with t2-weighted fast spin-echo and gradient-echo sequences. *AJNR. American journal of neuroradiology*, 29(1):154–158, January 2008. 44
- [36] Yu-Kun Tsui, Fong Y. Tsai, Anton N. Hasso, Fred Greensite, and Binh V. Nguyen. Susceptibility-weighted imaging for differential diagnosis of cerebral vascular pathology: a pictorial review. *Journal of the Neurological Sciences*, 287(1-2):7–16, December 2009. 44
- [37] K. A. Tong, S. Ashwal, A. Obenaus, J. P. Nickerson, D. Kido, and E. M. Haacke. Susceptibility-weighted MR imaging: a review of clinical applications in children. *AJNR. American journal of neuroradiology*, 29(1):9–17, January 2008. 44
- [38] M. Hermier, N. Nighoghossian, L. Derex, Y. Berthezène, K. Blanc-Lasserre, P. Trouillas, and J. C. Froment. MRI of acute post-ischemic cerebral hemorrhage in stroke patients: diagnosis with T2*-weighted gradient-echo sequences. *Neuroradiology*, 43(10):809–815, October 2001. 44
- [39] Nathaniel D. Wycliffe, Judy Choe, Barbara Holshouser, Udo E. Oyoyo, E. Mark Haacke, and Daniel K. Kido. Reliability in detection of hemorrhage in acute stroke by a new three-dimensional gradient recalled echo susceptibility-weighted imaging technique compared to computed tomography: A retrospective study. *Journal of Magnetic Resonance Imaging*, 20(3):372–377, September 2004. 44
- [40] Miriam H. Beauchamp, Richard Beare, Michael Ditchfield, Lee Coleman, Franz E. Babl, Michael Kean, Louise Crossley, Cathy Catroppa,

- Keith O. Yeates, and Vicki Anderson. Susceptibility weighted imaging and its relationship to outcome after pediatric traumatic brain injury. *Cortex; a Journal Devoted to the Study of the Nervous System and Behavior*, 49(2):591–598, February 2013. 44
- [41] Jonathan Rosand, Alona Muzikansky, Ashok Kumar, Jonathan J. Wisco, Eric E. Smith, Rebecca A. Betensky, and Steven M. Greenberg. Spatial clustering of hemorrhages in probable cerebral amyloid angiopathy. *Annals of Neurology*, 58(3):459–462, September 2005. 44
- [42] Karen A. Tong, Stephen Ashwal, Barbara A. Holshouser, Lori A. Shutter, Gwenael Herigault, E. Mark Haacke, and Daniel K. Kido. Hemorrhagic shearing lesions in children and adolescents with posttraumatic diffuse axonal injury: improved detection and initial results. *Radiology*, 227(2):332–339, May 2003. 44
- [43] Janine M. Lupo, Suchandrima Banerjee, Kathryn E. Hammond, Douglas A. C. Kelley, Duan Xu, Susan M. Chang, Daniel B. Vigneron, Sharmila Majumdar, and Sarah J. Nelson. GRAPPA-based susceptibility-weighted imaging of normal volunteers and patients with brain tumor at 7 T. *Magnetic Resonance Imaging*, 27(4):480–488, May 2009. 44
- [44] Vivek Sehgal, Zachary Delproposto, E. Mark Haacke, Karen A. Tong, Nathaniel Wycliffe, Daniel K. Kido, Yingbiao Xu, Jaladhar Neelavalli, Djamel Haddar, and Jürgen R. Reichenbach. Clinical applications of neuroimaging with susceptibility-weighted imaging. *Journal of Magnetic Resonance Imaging*, 22(4):439–450, October 2005. 44
- [45] Vivek Sehgal, Zachary Delproposto, Djamel Haddar, E. Mark Haacke, Andrew E. Sloan, Lucia J. Zamorano, Geoffery Barger, Jiani Hu, Yingbiao Xu, Karthik Praveen Prabhakaran, Ilaya R. Elangovan, Jaladhar Neelavalli, and Jürgen R. Reichenbach. Susceptibility-weighted imaging to visualize blood products and improve tumor contrast in the study of brain masses. *Journal of Magnetic Resonance Imaging*, 24(1):41–51, July 2006. 44
- [46] Yi Wang and Tian Liu. Quantitative susceptibility mapping (QSM): Decoding MRI data for a tissue magnetic biomarker. *Magnetic Resonance in Medicine*, 73(1):82–101, January 2015. 45, 52, 53, 55, 70, 124, 125

- [47] Rares Salomir, Baudouin Denis de Senneville, and Chrit TW Moonen. A fast calculation method for magnetic field inhomogeneity due to an arbitrary distribution of bulk susceptibility. *Concepts in Magnetic Resonance Part B: Magnetic Resonance Engineering*, 19B(1):26–34, 2003. 49, 70, 78, 107, 118, 149
- [48] J. F. Schenck. The role of magnetic susceptibility in magnetic resonance imaging: MRI magnetic compatibility of the first and second kinds. *Medical Physics*, 23(6):815–850, June 1996. 53
- [49] John F. Schenck. Safety of Strong, Static Magnetic Fields. *Journal of Magnetic Resonance Imaging*, 12(1):2–19, July 2000. 53
- [50] E. Mark Haacke, Norman Y.C. Cheng, Michael J. House, Qiang Liu, Jaladhar Neelavalli, Robert J. Ogg, Asadullah Khan, Muhammad Ayaz, Wolff Kirsch, and Andre Obenaus. Imaging iron stores in the brain using magnetic resonance imaging. *Magnetic Resonance Imaging*, 23(1):1–25, January 2005. 53, 77, 106
- [51] B. Hallgren and P. Sourander. The Effect of Age on the Non-Haemin Iron in the Human Brain. *Journal of Neurochemistry*, 3(1):41–51, October 1958. 53
- [52] Berkin Bilgic, Adolf Pfefferbaum, Torsten Rohlfing, Edith V. Sullivan, and Elfar Adalsteinsson. MRI estimates of brain iron concentration in normal aging using quantitative susceptibility mapping. *NeuroImage*, 59(3):2625–2635, February 2012. 53, 54, 77, 80, 84, 107, 112
- [53] Issel Anne L. Lim, Andreia V. Faria, Xu Li, Johnny T. C. Hsu, Raag D. Airan, Susumu Mori, and Peter C. M. van Zijl. Human brain atlas for automated region of interest selection in quantitative susceptibility mapping: Application to determine iron content in deep gray matter structures. *NeuroImage*, 82:449–469, November 2013. 53, 54, 107, 112
- [54] Sam Wharton and Richard Bowtell. Whole-brain susceptibility mapping at high field: A comparison of multiple- and single-orientation methods. *NeuroImage*, 53(2):515–525, November 2010. 53, 72, 77, 107, 112
- [55] Ferdinand Schweser, Andreas Deistung, Berengar Wendel Lehr, and Jürgen Rainer Reichenbach. Quantitative imaging of intrinsic magnetic tissue properties using MRI signal phase: An approach to in vivo brain iron metabolism? *NeuroImage*, 54(4):2789–2807, February 2011. 53, 54, 69, 77, 84, 107, 112, 123

- [56] Wei Li, Bing Wu, and Chunlei Liu. Quantitative susceptibility mapping of human brain reflects spatial variation in tissue composition. *NeuroImage*, 55(4):1645–1656, April 2011. 53
- [57] Tian Liu, Jing Liu, Ludovic de Rochefort, Pascal Spincemaille, Ildar Khalidov, James Robert Ledoux, and Yi Wang. Morphology enabled dipole inversion (MEDI) from a single-angle acquisition: comparison with COSMOS in human brain imaging. *Magnetic resonance in medicine: official journal of the Society of Magnetic Resonance in Medicine / Society of Magnetic Resonance in Medicine*, 66(3):777–783, September 2011. 53, 149
- [58] L. Pauling and C. D. Coryell. The Magnetic Properties and Structure of Hemoglobin, Oxyhemoglobin and Carbonmonoxyhemoglobin. *Proceedings of the National Academy of Sciences of the United States of America*, 22(4):210–216, April 1936. 53
- [59] Donald S. Taylor and Charles D. Coryell. The Magnetic Susceptibility of the Iron in Ferrohemo-globin. *Journal of the American Chemical Society*, 60(5):1177–1181, May 1938. 53
- [60] Charles D. Coryell, Fred Stitt, and Linus Pauling. The Magnetic Properties and Structure of Ferrihemoglobin (Methemoglobin) and Some of its Compounds. *Journal of the American Chemical Society*, 59(4):633–642, April 1937. 53
- [61] Christian Langkammer, Ferdinand Schweser, Nikolaus Krebs, Andreas Deistung, Walter Goessler, Eva Scheurer, Karsten Sommer, Gernot Reishofer, Kathrin Yen, Franz Fazekas, Stefan Ropele, and Jürgen R Reichenbach. Quantitative susceptibility mapping (QSM) as a means to measure brain iron? A post mortem validation study. *NeuroImage*, 62(3):1593–1599, September 2012. 54, 77, 107, 112, 118
- [62] Andreas Schäfer, Birte U Forstmann, Jane Neumann, Sam Wharton, Alexander Mietke, Richard Bowtell, and Robert Turner. Direct visualization of the subthalamic nucleus and its iron distribution using high-resolution susceptibility mapping. *Human brain mapping*, 33(12):2831–2842, December 2012. 54
- [63] Carsten Stüber, Markus Morawski, Andreas Schäfer, Christian Labadie, Miriam Wähnert, Christoph Leuze, Markus Streicher, Nirav Barapatre, Katja Reimann, Stefan Geyer, Daniel Spemann, and Robert Turner. Myelin and iron concentration in the human brain: a

- quantitative study of MRI contrast. *NeuroImage*, 93 Pt 1:95–106, June 2014. 54, 106, 112, 118, 121
- [64] Weili Zheng, Helen Nichol, Saifeng Liu, Yu-Chung N. Cheng, and E. Mark Haacke. Measuring iron in the brain using quantitative susceptibility mapping and X-ray fluorescence imaging. *NeuroImage*, 78: 68–74, September 2013. 54, 105
- [65] Wei Li, Bing Wu, Anastasia Batrachenko, Vivian Bancroft-Wu, Rajendra A Morey, Vandana Shashi, Christian Langkammer, Michael D De Bellis, Stefan Ropele, Allen W Song, and Chunlei Liu. Differential developmental trajectories of magnetic susceptibility in human brain gray and white matter over the lifespan. *Human brain mapping*, September 2013. 54, 55
- [66] Jeff H. Duyn, Peter van Gelderen, Tie-Qiang Li, Jacco A. de Zwart, Alan P. Koretsky, and Masaki Fukunaga. High-field MRI of brain cortical substructure based on signal phase. *Proceedings of the National Academy of Sciences*, 104(28):11796–11801, October 2007. 54, 77
- [67] Masaki Fukunaga, Tie-Qiang Li, Peter van Gelderen, Jacco A. de Zwart, Karin Shmueli, Bing Yao, Jongho Lee, Dragan Maric, Maria A. Aronova, Guofeng Zhang, Richard D. Leapman, John F. Schenck, Hellmut Merkle, and Jeff H. Duyn. Layer-specific variation of iron content in cerebral cortex as a source of MRI contrast. *Proceedings of the National Academy of Sciences*, 107(8):3834–3839, February 2010. 54
- [68] Jongho Lee, Yoshiyuki Hirano, Masaki Fukunaga, Afonso C. Silva, and Jeff H. Duyn. On the contribution of deoxy-hemoglobin to MRI gray-white matter phase contrast at high field. *NeuroImage*, 49(1):193–198, January 2010. 54, 60
- [69] Chunlei Liu, Wei Li, G Allan Johnson, and Bing Wu. High-field (9.4 T) MRI of brain dysmyelination by quantitative mapping of magnetic susceptibility. *NeuroImage*, 56(3):930–938, June 2011. 54, 56, 77, 107
- [70] Gregory A. Lodygensky, José P. Marques, Rajika Maddage, Elodie Perroud, Stéphane V. Sizonenko, Petra S. Hüppi, and Rolf Gruetter. In vivo assessment of myelination by phase imaging at high magnetic field. *NeuroImage*, 59(3):1979–1987, February 2012. 54, 55, 56, 77, 107, 129
- [71] Jongho Lee, Karin Shmueli, Byeong-Teck Kang, Bing Yao, Masaki Fukunaga, Peter van Gelderen, Sara Palumbo, Francesca Bosetti,

- Afonso C. Silva, and Jeff H. Duyn. The contribution of myelin to magnetic susceptibility-weighted contrasts in high-field MRI of the brain. *NeuroImage*, 59(4):3967–3975, February 2012. 55, 56
- [72] Wei Li, Bing Wu, Alexandru V. Avram, and Chunlei Liu. Magnetic susceptibility anisotropy of human brain in vivo and its molecular underpinnings. *NeuroImage*, 59(3):2088–2097, February 2012. 55, 57, 149
- [73] Theodor Kaes. *Die Grosshirnrinde des Menschen in ihren Massen und in ihrem Fasergehalt: ein gehirnanatomischer Atlas, mit erläuterndem Text*. Fischer, 1907. 55
- [74] Kai Zhong, Thomas Ernst, Steve Buchthal, Oliver Speck, Lynn Anderson, and Linda Chang. Phase contrast imaging in neonates. *NeuroImage*, 55(3):1068–1072, April 2011. 55
- [75] Ioannis Argyridis, Wei Li, G. Allan Johnson, and Chunlei Liu. Quantitative Magnetic Susceptibility of the Developing Mouse Brain Reveals Microstructural Changes in the White Matter. *NeuroImage*, 0:134–142, November 2013. 55, 56
- [76] Dmitriy A. Yablonskiy, Jie Luo, Alexander L. Sukstanskii, Aditi Iyer, and Anne H. Cross. Biophysical mechanisms of MRI signal frequency contrast in multiple sclerosis. *Proceedings of the National Academy of Sciences*, 109(35):14212–14217, August 2012. 55, 56, 77, 98, 107
- [77] Christian Langkammer, Tian Liu, Michael Khalil, Christian Enzinger, Margit Jehna, Siegrid Fuchs, Franz Fazekas, Yi Wang, and Stefan Ropele. Quantitative susceptibility mapping in multiple sclerosis. *Radiology*, 267(2):551–559, May 2013. 55
- [78] Weiwei Chen, Susan A. Gauthier, Ajay Gupta, Joseph Comunale, Tian Liu, Shuai Wang, Mengchao Pei, David Pitt, and Yi Wang. Quantitative Susceptibility Mapping of Multiple Sclerosis Lesions at Various Ages. *Radiology*, 271(1):183–192, April 2014. 56
- [79] Wei Cao, Wei Li, Hui Han, Shonagh K. O’Leary-Moore, Kathleen K. Sulik, G. Allan Johnson, and Chunlei Liu. Prenatal alcohol exposure reduces magnetic susceptibility contrast and anisotropy in the white matter of mouse brains. *NeuroImage*, 102, Part 2:748–755, November 2014. 56

- [80] Way Cherng Chen, Sean Foxley, and Karla L. Miller. Detecting microstructural properties of white matter based on compartmentalization of magnetic susceptibility. *NeuroImage*, 70:1–9, April 2013. 56
- [81] Russell Dibb, Wei Li, Gary Cofer, and Chunlei Liu. Microstructural origins of gadolinium-enhanced susceptibility contrast and anisotropy. *Magnetic Resonance in Medicine*, 72(6):1702–1711, December 2014. 56
- [82] Peter van Gelderen, Jacco A de Zwart, Jongho Lee, Pascal Sati, Daniel S Reich, and Jeff H Duyn. Nonexponential T₂ decay in white matter. *Magnetic resonance in medicine: official journal of the Society of Magnetic Resonance in Medicine / Society of Magnetic Resonance in Medicine*, 67(1):110–117, January 2012. 56
- [83] Samuel Wharton and Richard Bowtell. Effects of white matter microstructure on phase and susceptibility maps. *Magnetic Resonance in Medicine*, 73(3):1258–1269, March 2015. 56, 63, 119, 150, 153, 157
- [84] Dmitriy A. Yablonskiy and Alexander L. Sukstanskii. Generalized Lorentzian Tensor Approach (GLTA) as a biophysical background for quantitative susceptibility mapping. *Magnetic Resonance in Medicine*, 73(2):757–764, February 2015. 56, 57, 62, 63, 149, 150, 153
- [85] Dmitriy A. Yablonskiy and E. Mark Haacke. Theory of NMR signal behavior in magnetically inhomogeneous tissues: The static dephasing regime. *Magnetic Resonance in Medicine*, 32(6):749–763, December 1994. 56
- [86] Xiang He and Dmitriy A. Yablonskiy. Biophysical mechanisms of phase contrast in gradient echo MRI. *Proceedings of the National Academy of Sciences*, 106(32):13558–13563, November 2009. 56, 59, 62, 77, 107, 119, 149, 157
- [87] Jongho Lee, Karin Shmueli, Masaki Fukunaga, Peter van Gelderen, Hellmut Merkle, Afonso C. Silva, and Jeff H. Duyn. Sensitivity of MRI resonance frequency to the orientation of brain tissue microstructure. *Proceedings of the National Academy of Sciences*, March 2010. 56, 130, 149
- [88] Chunlei Liu. Susceptibility Tensor Imaging. *Magnetic resonance in medicine : official journal of the Society of Magnetic Resonance in Medicine / Society of Magnetic Resonance in Medicine*, 63(6):1471–1477, June 2010. 56, 60, 119, 149

- [89] Pascal Sati, Peter van Gelderen, Afonso C. Silva, Daniel S. Reich, Hellmut Merkle, Jacco A. de Zwart, and Jeff H. Duyn. Micro-compartment specific T2? relaxation in the brain. *NeuroImage*, 77:268–278, August 2013. 56, 62, 129
- [90] Alexander L Sukstanskii and Dmitriy A Yablonskiy. On the role of neuronal magnetic susceptibility and structure symmetry on gradient echo MR signal formation. *Magnetic resonance in medicine: official journal of the Society of Magnetic Resonance in Medicine / Society of Magnetic Resonance in Medicine*, February 2013. 56, 62
- [91] Samuel Wharton and Richard Bowtell. Fiber orientation-dependent white matter contrast in gradient echo MRI. *Proceedings of the National Academy of Sciences of the United States of America*, 109(45):18559–18564, November 2012. 56, 62, 129, 142, 150
- [92] Ferdinand Schweser, Andreas Deistung, Berengar W Lehr, and Jürgen R Reichenbach. Differentiation between diamagnetic and paramagnetic cerebral lesions based on magnetic susceptibility mapping. *Medical physics*, 37(10):5165–5178, October 2010. 57
- [93] Andreas Deistung, Ferdinand Schweser, Benedikt Wiestler, Mario Abello, Matthias Roethke, Felix Sahm, Wolfgang Wick, Armin Michael Nagel, Sabine Heiland, Heinz-Peter Schlemmer, Martin Bendszus, Jürgen Rainer Reichenbach, and Alexander Radbruch. Quantitative susceptibility mapping differentiates between blood depositions and calcifications in patients with glioblastoma. *PloS one*, 8(3):e57924, 2013. 57
- [94] Dominik Fritsch, Martin Reiss-Zimmermann, Robert Trampel, Robert Turner, Karl-Titus Hoffmann, and Andreas Schäfer. Seven-tesla magnetic resonance imaging in Wilson disease using quantitative susceptibility mapping for measurement of copper accumulation. *Investigative Radiology*, 49(5):299–306, May 2014. 57
- [95] Jie Luo, Xiang He, D. Andre' d'Avignon, Joseph J. H. Ackerman, and Dmitriy A. Yablonskiy. Protein-Induced Water 1h MR Frequency Shifts: Contributions from Magnetic Susceptibility and Exchange. *Journal of magnetic resonance (San Diego, Calif. : 1997)*, 202(1):102, January 2010. 57, 77
- [96] Karin Shmueli, Stephen J. Dodd, Tie-Qiang Li, and Jeff H. Duyn. The Contribution of Chemical Exchange to MRI Frequency Shifts in Brain

- Tissue. *Magnetic resonance in medicine : official journal of the Society of Magnetic Resonance in Medicine / Society of Magnetic Resonance in Medicine*, 65(1):35–43, January 2011. 57, 77
- [97] Kai Zhong, Jochen Leupold, Dominik von Elverfeldt, and Oliver Speck. The molecular basis for gray and white matter contrast in phase imaging. *NeuroImage*, 40(4):1561–1566, May 2008. 57, 77
- [98] D. Qiu, G. C.-F. Chan, J. Chu, Q. Chan, S.-Y. Ha, M. E. Moseley, and P.-L. Khong. MR quantitative susceptibility imaging for the evaluation of iron loading in the brains of patients with β -thalassemia major. *AJNR. American journal of neuroradiology*, 35(6):1085–1090, June 2014. 57
- [99] Ashley K. Lotfipour, Samuel Wharton, Stefan T. Schwarz, V. Gontu, Andreas Schäfer, Andrew M. Peters, Richard W. Bowtell, Dorothee P. Auer, Penny A. Gowland, and Nin P.S. Bajaj. High resolution magnetic susceptibility mapping of the substantia nigra in Parkinson’s disease. *Journal of Magnetic Resonance Imaging*, 35(1):48–55, 2012. 58
- [100] Dmitriy A. Yablonskiy, Xiang He, Jie Luo, and Alexander L. Sukstanskii. Lorentz sphere versus generalized Lorentzian approach: What would lorentz say about it? *Magnetic Resonance in Medicine*, 72(1):4–7, July 2014. 59
- [101] Xu Li, Deepti S. Vikram, Issel Anne L. Lim, Craig K. Jones, Jonathan A.D. Farrell, and Peter C.M. van Zijl. Mapping magnetic susceptibility anisotropies of white matter in vivo in the human brain at 7 T. *NeuroImage*, 62(1):314–330, August 2012. 60
- [102] Cynthia Wisnieff, Tian Liu, Pascal Spincemaille, Shuai Wang, Dong Zhou, and Yi Wang. Magnetic susceptibility anisotropy: Cylindrical symmetry from macroscopically ordered anisotropic molecules and accuracy of MRI measurements using few orientations. *NeuroImage*, 70:363–376, April 2013. 60
- [103] Xu Li and Peter C. M. van Zijl. Mean magnetic susceptibility regularized susceptibility tensor imaging (MMSR-STI) for estimating orientations of white matter fibers in human brain. *Magnetic Resonance in Medicine*, 72(3):610–619, September 2014. 60
- [104] Chunlei Liu, Wei Li, Bing Wu, Yi Jiang, and G Allan Johnson. 3d fiber tractography with susceptibility tensor imaging. *NeuroImage*, 59(2):1290–1298, January 2012. 60, 119, 149

- [105] Luke Xie, Russell Dibb, Gary P. Cofer, Wei Li, Peter J. Nicholls, G. Allan Johnson, and Chunlei Liu. Susceptibility tensor imaging of the kidney and its microstructural underpinnings. *Magnetic Resonance in Medicine*, 73(3):1270–1281, March 2015. 61
- [106] J. Luo, X. He, and D. A. Yablonskiy. Magnetic susceptibility induced white matter MR signal frequency shifts-experimental comparison between Lorentzian sphere and generalized Lorentzian approaches. *Magnetic Resonance in Medicine*, 71(3):1251–1263, March 2014. 63, 107, 119
- [107] Matt A. Bernstein, Mladen Grgic, Thomas J. Brosnan, and Norbert J. Pelc. Reconstructions of phase contrast, phased array multicoil data. *Magnetic Resonance in Medicine*, 32(3):330–334, September 1994. 66
- [108] Kun Lu, Thomas T. Liu, and Mark Bydder. Optimal phase difference reconstruction: comparison of two methods. *Magnetic Resonance Imaging*, 26(1):142–145, January 2008. 66
- [109] Jie Luo, Bharathi D. Jagadeesan, Anne H. Cross, and Dmitriy A. Yablonskiy. Gradient Echo Plural Contrast Imaging - Signal model and derived contrasts: T2*, T1, Phase, SWI, T1f, FST2*and T2*-SWI. *NeuroImage*, 60(2):1073–1082, April 2012. 66
- [110] M. Bydder, D.j. Larkman, and J.v. Hajnal. Combination of signals from array coils using image-based estimation of coil sensitivity profiles. *Magnetic Resonance in Medicine*, 47(3):539–548, March 2002. 67
- [111] Diana Khabipova, Yves Wiaux, Rolf Gruetter, and José P. Marques. A modulated closed form solution for quantitative susceptibility mapping - A thorough evaluation and comparison to iterative methods based on edge prior knowledge. *NeuroImage*, 107:163–174, February 2015. 67, 74, 107, 109, 122, 132, 142, 143, 149, 151, 153
- [112] Mark Bydder, Gavin Hamilton, Takeshi Yokoo, and Claude B. Sirlin. Optimal phased-array combination for spectroscopy. *Magnetic Resonance Imaging*, 26(6):847–850, July 2008. 67
- [113] R Gruetter. Automatic, localized in vivo adjustment of all first- and second-order shim coils. *Magnetic resonance in medicine: official journal of the Society of Magnetic Resonance in Medicine / Society of Magnetic Resonance in Medicine*, 29(6):804–811, June 1993. 67, 83, 98

- [114] Simon Robinson, Günther Grabner, Stephan Witoszynskyj, and Siegfried Trattnig. Combining phase images from multi-channel RF coils using 3d phase offset maps derived from a dual-echo scan. *Magnetic Resonance in Medicine*, 65(6):1638–1648, June 2011. 68
- [115] Joseph Dagher and Kambiz Nael. MAGPI: A framework for maximum likelihood MR phase imaging using multiple receive coils. *Magnetic Resonance in Medicine*, pages n/a–n/a, May 2015. 68
- [116] Simon Robinson, Kristian Bredies, Diana Khabipova, and Ferdinand Schweser. An illustrated comparison of processing methods for phase MRI and QSM: Combining array coil signals and phase unwrapping. 2016. 69
- [117] Hussein S. Abdul-Rahman, Munther A. Gdeisat, David R. Burton, Michael J. Lalor, Francis Lilley, and Christopher J. Moore. Fast and robust three-dimensional best path phase unwrapping algorithm. *Applied Optics*, 46(26):6623–6635, September 2007. 69, 83
- [118] Stephan Witoszynskyj, Alexander Rauscher, Jürgen R. Reichenbach, and Markus Barth. Phase unwrapping of MR images using Phi UN—a fast and robust region growing algorithm. *Medical Image Analysis*, 13(2):257–268, April 2009. 69
- [119] Mark Jenkinson. Fast, automated, N-dimensional phase-unwrapping algorithm. *Magnetic Resonance in Medicine*, 49(1):193–197, January 2003. 69
- [120] Dennis C. Ghiglia and Louis A. Romero. Robust two-dimensional weighted and unweighted phase unwrapping that uses fast transforms and iterative methods. *Journal of the Optical Society of America A*, 11(1):107, January 1994. 69
- [121] Wei Feng, Jaladhar Neelavalli, and E. Mark Haacke. Catalytic multi-echo phase unwrapping scheme (CAMPUS) in multiecho gradient echo imaging: removing phase wraps on a voxel-by-voxel basis. *Magnetic Resonance in Medicine*, 70(1):117–126, July 2013. 69
- [122] Bing Wu, Wei Li, Arnaud Guidon, and Chunlei Liu. Whole brain susceptibility mapping using compressed sensing. *Magnetic Resonance in Medicine*, 67(1):137–147, 2012. 69, 73, 78, 87, 107
- [123] Hongfu Sun and Alan H. Wilman. Background field removal using spherical mean value filtering and Tikhonov regularization. *Magnetic*

- Resonance in Medicine*, 71(3):1151–1157, March 2014. 69, 107, 110, 123, 125
- [124] Tian Liu, Ildar Khalidov, Ludovic de Rochefort, Pascal Spincemaille, Jing Liu, A. John Tsiouris, and Yi Wang. A novel background field removal method for MRI using projection onto dipole fields (PDF). *NMR in Biomedicine*, 24(9):1129–1136, 2011. 69, 107, 110, 123, 125
- [125] Ludovico De Rochefort, Hongchen Wand, Paulo Loureiro de Sousa, and Jean-Paul Armspach. Efficient and Automatic Harmonic Field Pre-Filtering for Brain Quantitative Susceptibility Mapping. In *ISMRM*, volume 21st, page 170, Salt Lake City, Utah, USA, 2013. 70, 83, 109, 110, 122, 125, 153
- [126] Dong Zhou, Tian Liu, Pascal Spincemaille, and Yi Wang. Background field removal by solving the Laplacian boundary value problem. *NMR in Biomedicine*, 27(3):312–319, March 2014. 70, 125
- [127] J.P. Marques and R. Bowtell. Application of a fourier-based method for rapid calculation of field inhomogeneity due to spatial variation of magnetic susceptibility. *Concepts in Magnetic Resonance Part B: Magnetic Resonance Engineering*, 25(1):65–78, 2005. 70, 77, 78, 79, 107, 118, 149
- [128] Tian Liu, Pascal Spincemaille, Ludovic de Rochefort, Bryan Kressler, and Yi Wang. Calculation of susceptibility through multiple orientation sampling (COSMOS): a method for conditioning the inverse problem from measured magnetic field map to susceptibility source image in MRI. *Magnetic resonance in medicine: official journal of the Society of Magnetic Resonance in Medicine / Society of Magnetic Resonance in Medicine*, 61(1):196–204, January 2009. 72, 77, 78, 79, 107, 110, 149, 153
- [129] Andreas Schäfer, Sam Wharton, Penny Gowland, and Richard Bowtell. Using magnetic field simulation to study susceptibility-related phase contrast in gradient echo MRI. *NeuroImage*, 48(1):126–137, October 2009. 72, 78
- [130] Ferdinand Schweser, Andreas Deistung, Karsten Sommer, and Jürgen Rainer Reichenbach. Toward online reconstruction of quantitative susceptibility maps: superfast dipole inversion. *Magnetic resonance in medicine: official journal of the Society of Magnetic Resonance in Medicine / Society of Magnetic Resonance in Medicine*, 69(6):1582–1594, June 2013. 72, 78, 87, 107

- [131] Karin Shmueli, Jacco A. de Zwart, Peter van Gelderen, Tie-Qiang Li, Stephen J. Dodd, and Jeff H. Duyn. Magnetic susceptibility mapping of brain tissue in vivo using MRI phase data. *Magnetic Resonance in Medicine*, 62(6):1510–1522, 2009. 72, 78, 107, 149
- [132] Sam Wharton, Andreas Schäfer, and Richard Bowtell. Susceptibility mapping in the human brain using threshold-based k-space division. *Magnetic Resonance in Medicine*, 63(5):1292–1304, 2010. 72, 78, 107
- [133] J. Tang, S. Liu, J. Neelavalli, Y. C. N. Cheng, S. Buch, and E. M. Haacke. Improving susceptibility mapping using a threshold-based K-space/image domain iterative reconstruction approach. *Magnetic Resonance in Medicine*, 69(5):1396–1407, 2013. 72
- [134] Ferdinand Schweser, Karsten Sommer, Andreas Deistung, and Jürgen Rainer Reichenbach. Quantitative susceptibility mapping for investigating subtle susceptibility variations in the human brain. *NeuroImage*, 62(3):2083–2100, September 2012. 73, 78, 80, 84, 87, 107
- [135] Ludovic de Rochefort, Tian Liu, Bryan Kressler, Jing Liu, Pascal Spincemaille, Vincent Lebon, Jianlin Wu, and Yi Wang. Quantitative susceptibility map reconstruction from MR phase data using bayesian regularization: Validation and application to brain imaging. *Magnetic Resonance in Medicine*, 63(1):194–206, 2010. 74, 78, 80, 82, 107, 110, 123, 149
- [136] Bryan Kressler, Ludovic de Rochefort, Tian Liu, Pascal Spincemaille, Quan Jiang, and Yi Wang. Nonlinear regularization for per voxel estimation of magnetic susceptibility distributions from MRI field maps. *IEEE transactions on medical imaging*, 29(2):273–281, February 2010. 74, 78, 80, 107
- [137] Jing Liu, Tian Liu, Ludovic de Rochefort, James Ledoux, Ildar Khali-dov, Weiwei Chen, A John Tsiouris, Cynthia Wisnieff, Pascal Spincemaille, Martin R Prince, and Yi Wang. Morphology enabled dipole inversion for quantitative susceptibility mapping using structural consistency between the magnitude image and the susceptibility map. *NeuroImage*, 59(3):2560–2568, February 2012. 74, 78, 80, 107
- [138] Tian Liu, Cynthia Wisnieff, Min Lou, Weiwei Chen, Pascal Spincemaille, and Yi Wang. Nonlinear formulation of the magnetic field to source relationship for robust quantitative susceptibility mapping. *Magnetic Resonance in Medicine*, 69(2):467–476, 2013. 74

- [139] Berkin Bilgic, Itthi Chatnuntawech, Audrey P. Fan, Kawin Setsompop, Stephen F. Cauley, Lawrence L. Wald, and Elfar Adalsteinsson. Fast image reconstruction with L2-regularization. *Journal of Magnetic Resonance Imaging*, pages n/a–n/a, 2013. 74, 78, 81, 87, 107, 149
- [140] Berkin Bilgic, Audrey P. Fan, Jonathan R. Polimeni, Stephen F. Cauley, Marta Bianciardi, Elfar Adalsteinsson, Lawrence L. Wald, and Kawin Setsompop. Fast quantitative susceptibility mapping with L1-regularization and automatic parameter selection. *Magnetic Resonance in Medicine*, pages n/a–n/a, 2013. 74
- [141] Alexander Rauscher, Jan Sedlacik, Markus Barth, Hans-Joachim Mentzel, and Jürgen R Reichenbach. Magnetic susceptibility-weighted MR phase imaging of the human brain. *AJNR. American journal of neuroradiology*, 26(4):736–742, April 2005. 77
- [142] Jie Luo, Dmitriy A Yablonskiy, Charles F Hildebolt, Samantha Lancia, and Anne H Cross. Gradient echo magnetic resonance imaging correlates with clinical measures and allows visualization of veins within multiple sclerosis lesions. *Multiple sclerosis (Houndmills, Basingstoke, England)*, July 2013. 77, 96
- [143] Samuel Wharton and Richard Bowtell. Gradient echo based fiber orientation mapping using R2* and frequency difference measurements. *NeuroImage*, 83:1011–1023, December 2013. 77, 107, 129, 130, 131
- [144] Michael Lustig, David Donoho, and John M. Pauly. Sparse MRI: The application of compressed sensing for rapid MR imaging. *Magnetic Resonance in Medicine*, 58(6):1182–1195, December 2007. 80
- [145] G. Puy, J.P. Marques, R. Gruetter, J. Thiran, D. Van De Ville, P. Vanderghenst, and Y. Wiaux. Spread Spectrum Magnetic Resonance Imaging. *IEEE Transactions on Medical Imaging*, 31(3):586–598, March 2012. 80
- [146] Tian Liu, Weiyu Xu, Pascal Spincemaille, A. Salman Avestimehr, and Yi Wang. Accuracy of the Morphology Enabled Dipole Inversion (MEDI) Algorithm for Quantitative Susceptibility Mapping in MRI. *IEEE transactions on medical imaging*, 31(3):816–824, March 2012. 80
- [147] A. Beck and M. Teboulle. Fast Gradient-Based Algorithms for Constrained Total Variation Image Denoising and Deblurring Problems. *IEEE Transactions on Image Processing*, 18(11):2419–2434, 2009. 80

- [148] J.P. Marques, T. Kober, G. Krueger, W. van der Zwaag, P.-F. Van de Moortele, and R. Gruetter. MP2rage, a self bias-field corrected sequence for improved segmentation and T1-mapping at high field. *NeuroImage*, 49(2):1271–1281, 2010. 82, 108, 131, 150
- [149] P. C. Hansen. The L-Curve and its Use in the Numerical Treatment of Inverse Problems. In *in Computational Inverse Problems in Electrocardiology*, ed. P. Johnston, *Advances in Computational Bioengineering*, pages 119–142. WIT Press, 2000. 84
- [150] Andreas Deistung, Andreas Schäfer, Ferdinand Schweser, Uta Biedermann, Robert Turner, and Jürgen R Reichenbach. Toward in vivo histology: a comparison of quantitative susceptibility mapping (QSM) with magnitude-, phase-, and R2*-imaging at ultra-high magnetic field strength. *NeuroImage*, 65:299–314, January 2013. 87, 91, 95, 96, 113
- [151] Jinyuan Zhou, Xavier Golay, Peter C.M. van Zijl, M. Johanna Silvennoinen, Risto Kauppinen, James Pekar, and Michael Kraut. Inverse T2 contrast at 1.5 Tesla between gray matter and white matter in the occipital lobe of normal adult human brain. *Magnetic Resonance in Medicine*, 46(2):401–406, August 2001. 87
- [152] Tobias Kober, Cristina Granziera, Delphine Ribes, Patrick Browaeys, Myriam Schlupe, Reto Meuli, Richard Frackowiak, Rolf Gruetter, and Gunnar Krueger. MP2rage Multiple Sclerosis Magnetic Resonance Imaging at 3 T:. *Investigative Radiology*, 47(6):346–352, June 2012. 98
- [153] K. Brodmann. *Vergleichende Lokalisationslehre der Grosshirnrinde in ihren Prinzipien dargestellt auf Grund des Zellenbaues*. Leipzig, 1909. 105
- [154] Constantin von Economo and Georg N. Koskinas. *Die Cytoarchitektonik der Hirnrinde des erwachsenen Menschen*. Springer, Wien, 1925. 105
- [155] S. A. Sarkissov, I. N Filimonoff, E.P. Kononowa, I.S. Preobraschenskaja, and L.A. Kukuiew. *Atlas of the cytoarchitectonics of the human cerebral cortex*. Medgiz, Moscow, 1955. 105
- [156] Cécile Vogt and Oskar Vogt. Allgemeinere Ergebnisse unserer Hirnforschung. *J. Psychol. Neurol.*, 25:292–398, 1919. 105

- [157] Adolf Hopf and Helge Gräfin Vitzthum. Über die Verteilung myeloarchitektonischer Merkmale in der Scheitellappenrinde beim Menschen - HopfAdolf2.pdf. 3, 1957. 105
- [158] Arthur W. Toga, Paul M. Thompson, Susumu Mori, Katrin Amunts, and Karl Zilles. Towards multimodal atlases of the human brain. *Nature reviews. Neuroscience*, 7(12):952–966, December 2006. 105
- [159] K. Zilles, N. Palomero-Gallagher, C. Grefkes, F. Scheperjans, C. Boy, K. Amunts, and A. Schleicher. Architectonics of the human cerebral cortex and transmitter receptor fingerprints: reconciling functional neuroanatomy and neurochemistry. *European Neuropsychopharmacology*, 12(6):587–599, December 2002. 105
- [160] Karl Zilles and Katrin Amunts. Receptor mapping: architecture of the human cerebral cortex:. *Current Opinion in Neurology*, 22(4):331–339, August 2009. 105
- [161] Karla Hopp, Bogdan F.Gh. Popescu, Richard P.E. McCrea, Sheri L. Harder, Christopher A. Robinson, Mark E. Haacke, Ali H. Rajput, Alex Rajput, and Helen Nichol. Brain iron detected by SWI high pass filtered phase calibrated with synchrotron X-ray fluorescence. *Journal of Magnetic Resonance Imaging*, 31(6):1346–1354, June 2010. 105
- [162] Christian Langkammer, Ferdinand Schweser, Nikolaus Krebs, Andreas Deistung, Walter Goessler, Eva Scheurer, Karsten Sommer, Gernot Reishofer, Kathrin Yen, Franz Fazekas, Stefan Ropele, and Jürgen R. Reichenbach. Quantitative susceptibility mapping (QSM) as a means to measure brain iron? A post mortem validation study. *NeuroImage*, 62(3):1593–1599, September 2012. 105
- [163] Reagan McRae, Pritha Bagchi, S. Sumalekshmy, and Christoph J. Fahrni. In Situ Imaging of Metals in Cells and Tissues. *Chemical Reviews*, 109(10):4780–4827, October 2009. 105
- [164] M. Morawski, Ch. Meinecke, T. Reinert, A. C. Dörffel, P. Riederer, T. Arendt, and T. Butz. Determination of trace elements in the human substantia nigra. *Nuclear Instruments and Methods in Physics Research Section B: Beam Interactions with Materials and Atoms*, 231(1-4):224–228, April 2005. 105
- [165] Steven C. Cramer, Mriganka Sur, Bruce H. Dobkin, Charles O’Brien, Terence D. Sanger, John Q. Trojanowski, Judith M. Rumsey, Ramona Hicks, Judy Cameron, Daofen Chen, Wen G. Chen, Leonardo G.

- Cohen, Christopher deCharms, Charles J. Duffy, Guinevere F. Eden, Eberhard E. Fetz, Rosemarie Filart, Michelle Freund, Steven J. Grant, Suzanne Haber, Peter W. Kalivas, Bryan Kolb, Arthur F. Kramer, Minda Lynch, Helen S. Mayberg, Patrick S. McQuillen, Ralph Nitkin, Alvaro Pascual-Leone, Patricia Reuter-Lorenz, Nicholas Schiff, Anu Sharma, Lana Shekim, Michael Stryker, Edith V. Sullivan, and Sophia Vinogradov. Harnessing neuroplasticity for clinical applications. *Brain*, 134(6):1591–1609, June 2011. 105
- [166] Karl Zilles and Katrin Amunts. Centenary of Brodmann’s map - conception and fate. *Nature Reviews Neuroscience*, 11(2):139–145, February 2010. 105
- [167] K. Kleist. Bericht über die Gehirnpathologie in ihrer Bedeutung für Neurologie und Psychiatrie. *Zeitschrift für die gesamte Neurologie und Psychiatrie*, 158(1):159–193, December 1937. 105
- [168] Stephen M. Smith, Paul M. Matthews, and Peter Jezzard. *Functional MRI: an introduction to methods*. Oxford University Press, 2001. 105
- [169] Jeff H. Duyn, Peter van Gelderen, Tie-Qiang Li, Jacco A. de Zwart, Alan P. Koretsky, and Masaki Fukunaga. High-field MRI of brain cortical substructure based on signal phase. *Proceedings of the National Academy of Sciences of the United States of America*, 104(28):11796–11801, July 2007. 106
- [170] Bruce Fischl, David H. Salat, Evelina Busa, Marilyn Albert, Megan Dieterich, Christian Haselgrove, Andre van der Kouwe, Ron Killiany, David Kennedy, Shuna Klaveness, Albert Montillo, Nikos Makris, Bruce Rosen, and Anders M. Dale. Whole Brain Segmentation: Automated Labeling of Neuroanatomical Structures in the Human Brain. *Neuron*, 33(3):341–355, January 2002. 106
- [171] Bruce Fischl, David H. Salat, André J. W. van der Kouwe, Nikos Makris, Florent Ségonne, Brian T. Quinn, and Anders M. Dale. Sequence-independent segmentation of magnetic resonance images. *NeuroImage*, 23, Supplement 1:S69–S84, 2004. 106
- [172] Matthew F. Glasser and David C. Van Essen. Mapping Human Cortical Areas In Vivo Based on Myelin Content as Revealed by T1- and T2-Weighted MRI. *The Journal of Neuroscience*, 31(32):11597–11616, October 2011. 106

- [173] Joseph C. J. Bot, Erwin L. A. Blezer, Wouter Kamphorst, Geert J. Lycklama à Nijeholt, Herman J. Ader, Jonas A. Castelijns, Klaas Nicolay Ig, Elisabeth Bergers, Rivka Ravid, Chris Polman, and Frederik Barkhof. The Spinal Cord in Multiple Sclerosis: Relationship of High-Spatial-Resolution Quantitative MR Imaging Findings to Histopathologic Results. *Radiology*, 233(2):531–540, November 2004. 106
- [174] J. P. Mottershead, K. Schmierer, M. Clemence, J. S. Thornton, F. Scaravilli, G. J. Barker, P. S. Tofts, J. Newcombe, M. L. Cuzner, R. J. Ordidge, W. I. McDonald, and Prof D. H. Miller. High field MRI correlates of myelin content and axonal density in multiple sclerosis. *Journal of Neurology*, 250(11):1293–1301, November 2003. 106
- [175] Klaus Schmierer, Francesco Scaravilli, Daniel R. Altmann, Gareth J. Barker, and David H. Miller. Magnetization transfer ratio and myelin in postmortem multiple sclerosis brain. *Annals of Neurology*, 56(3):407–415, September 2004. 106
- [176] N.A. Bock, A. Kocharyan, J.V. Liu, and A.C. Silva. Visualizing the entire cortical myelination pattern in marmosets with magnetic resonance imaging. *Journal of Neuroscience Methods*, 185(1):15–22, 2009. 106
- [177] Stefan Geyer, Marcel Weiss, Katja Reimann, Gabriele Lohmann, and Robert Turner. Microstructural parcellation of the human cerebral cortex - from Brodmann’s post-mortem map to in vivo mapping with high-field magnetic resonance imaging. *Frontiers in Human Neuroscience*, 5:19, 2011. 106
- [178] Irina S. Sigalovsky, Bruce Fischl, and Jennifer R. Melcher. Mapping an intrinsic MR property of gray matter in auditory cortex of living humans: A possible marker for primary cortex and hemispheric differences. *NeuroImage*, 32(4):1524–1537, October 2006. 106
- [179] William D. Rooney, Glyn Johnson, Xin Li, Eric R. Cohen, Seong-Gi Kim, Kamil Ugurbil, and Charles S. Springer. Magnetic field and tissue dependencies of human brain longitudinal 1h2o relaxation in vivo. *Magnetic Resonance in Medicine*, 57(2):308–318, February 2007. 106
- [180] J. Cohen-Adad, J. R. Polimeni, K. G. Helmer, T. Benner, J. A. McNab, L. L. Wald, B. R. Rosen, and C. Mainero. T2* mapping and B0 orientation-dependence at 7 T reveal cyto- and myeloarchitecture

- organization of the human cortex. *NeuroImage*, 60(2):1006–1014, April 2012. 106
- [181] Martin I. Sereno, Antoine Lutti, Nikolaus Weiskopf, and Frederic Dick. Mapping the Human Cortical Surface by Combining Quantitative T1 with Retinotopy. *Cerebral Cortex*, 23(9):2261–2268, January 2013. 106, 118, 122, 123
- [182] Frederic Dick, Adam Taylor Tierney, Antoine Lutti, Oliver Josephs, Martin I. Sereno, and Nikolaus Weiskopf. In Vivo Functional and Myeloarchitectonic Mapping of Human Primary Auditory Areas. *The Journal of Neuroscience*, 32(46):16095–16105, November 2012. 106
- [183] Ferdinand Schweser, Karsten Sommer, M Atterbury, Andreas Deistung, Berengar Wendel Lehr, and Jürgen Rainer Reichenbach. On the impact of regularization and kernel type on SHARP-corrected GRE phase images. In *Proceedings of the 19th Annual Meeting of ISMRM*, page 2667, Montreal, 2011. 107
- [184] F. Eggenschwiler, T. Kober, A.W. Magill, R. Gruetter, and J.P. Marques. SA2rage: A new sequence for fast B1 +-mapping. *Magnetic Resonance in Medicine*, 67(6):1609–1619, 2012. 108
- [185] J.P. Marques and R. Gruetter. New Developments and Applications of the MP2rage Sequence - Focusing the Contrast and High Spatial Resolution R1 Mapping. *PLoS ONE*, 8(7), 2013. 108, 109
- [186] Michiel Kleinnijenhuis, Tim van Mourik, David G. Norris, Dirk J. Ruiter, Anne-Marie van Cappellen van Walsum, and Markus Barth. Diffusion tensor characteristics of gyrencephaly using high resolution diffusion MRI in vivo at 7t. *NeuroImage*, 109:378–387, April 2015. 110
- [187] David C. Van Essen. A Population-Average, Landmark- and Surface-based (PALS) atlas of human cerebral cortex. *NeuroImage*, 28(3):635–662, November 2005. 111, 120
- [188] Christian Langkammer, Nikolaus Krebs, Walter Goessler, Eva Scheurer, Franz Ebner, Kathrin Yen, Franz Fazekas, and Stefan Ropele. Quantitative MR Imaging of Brain Iron: A Postmortem Validation Study. *Radiology*, 257(2):455–462, November 2010. 112, 118
- [189] J. Cohen Adad, J.R. Polimeni, K.G. Helmer, T. Benner, J.A. McNab, L.L. Wald, B.R. Rosen, and C. Mainero. T2* mapping and B0

- orientation-dependence at 7 T reveal cyto- and myeloarchitecture organization of the human cortex. *NeuroImage*, 60(2):1006–1014, April 2012. 118, 119, 122, 123
- [190] Peter van Gelderen, Hendrik Mandelkow, Jacco A. de Zwart, and Jeff H. Duyn. A torque balance measurement of anisotropy of the magnetic susceptibility in white matter. *Magnetic Resonance in Medicine*, 74(5):1388–1396, November 2015. 119, 130, 149
- [191] Rudolf Nieuwenhuys. The myeloarchitectonic studies on the human cerebral cortex of the Vogt-Vogt school, and their significance for the interpretation of functional neuroimaging data. *Brain Structure and Function*, 218(2):303–352, March 2013. 120
- [192] Rudolf Nieuwenhuys, Cees A. J. Broere, and Leonardo Cerliani. A new myeloarchitectonic map of the human neocortex based on data from the Vogt-Vogt school. *Brain Structure and Function*, 220(5):2551–2573, June 2014. 120
- [193] N. Honnorat, H. Eavani, T. D. Satterthwaite, R. E. Gur, R. C. Gur, and C. Davatzikos. GraSP: Geodesic Graph-based Segmentation with Shape Priors for the functional parcellation of the cortex. *NeuroImage*, 106:207–221, February 2015. 120
- [194] J. Dinse, N. Härtwich, M. D. Waehnert, C. L. Tardif, A. Schäfer, S. Geyer, B. Preim, R. Turner, and P. L. Bazin. A cytoarchitecture-driven myelin model reveals area-specific signatures in human primary and secondary areas using ultra-high resolution in-vivo brain MRI. *NeuroImage*, 114:71–87, July 2015. 120
- [195] Christoph Birkel, Christian Langkammer, Johannes Haybaeck, Christina Ernst, Rudolf Stollberger, Franz Fazekas, and Stefan Ropele. Temperature-induced changes of magnetic resonance relaxation times in the human brain: a postmortem study. *Magnetic Resonance in Medicine*, 71(4):1575–1580, April 2014. 121
- [196] Andreas Deistung, Andreas Schäfer, Ferdinand Schweser, and Jürgen R Reichenbach. Cortical Mapping of Magnetic Susceptibility and R2* reveals Insights into Tissue Composition. 2015. 122, 123
- [197] Martina F. Callaghan, Patrick Freund, Bogdan Draganski, Elaine Anderson, Marinella Cappelletti, Rumana Chowdhury, Joern Diedrichsen, Thomas H. B. FitzGerald, Peter Smittenaar, Gunther Helms, Antoine

- Lutti, and Nikolaus Weiskopf. Widespread age-related differences in the human brain microstructure revealed by quantitative magnetic resonance imaging. *Neurobiology of Aging*, 35(8):1862–1872, August 2014. 129
- [198] George Bartzokis. Alzheimer’s disease as homeostatic responses to age-related myelin breakdown. *Neurobiology of Aging*, 32(8):1341–1371, August 2011. 129
- [199] George Bartzokis, Po H. Lu, Panthea Heydari, Alexander Couvrette, Grace J. Lee, Greta Kalashyan, Frank Freeman, John W. Grinstead, Pablo Villablanca, J. Paul Finn, Jim Mintz, Jeffrey R. Alger, and Lori L. Altshuler. Multimodal Magnetic Resonance Imaging Assessment of White Matter Aging Trajectories Over the Lifespan of Healthy Individuals. *Biological Psychiatry*, 72(12):1026–1034, December 2012. 129
- [200] Frederik Barkhof, Peter A. Calabresi, David H. Miller, and Stephen C. Reingold. Imaging outcomes for neuroprotection and repair in multiple sclerosis trials. *Nature Reviews Neurology*, 5(5):256–266, May 2009. 129
- [201] Jason D. Yeatman, Brian A. Wandell, and Aviv A. Mezer. Lifespan maturation and degeneration of human brain white matter. *Nature Communications*, 5:4932, September 2014. 129
- [202] Wei Li, Bing Wu, Anastasia Batrachenko, Vivian Bancroft-Wu, Rajendra A. Morey, Vandana Shashi, Christian Langkammer, Michael D. De Bellis, Stefan Ropele, Allen W. Song, and Chunlei Liu. Differential developmental trajectories of magnetic susceptibility in human brain gray and white matter over the lifespan. *Human Brain Mapping*, 35(6):2698–2713, June 2014. 129, 157
- [203] P. J. Basser, S. Pajevic, C. Pierpaoli, J. Duda, and A. Aldroubi. In vivo fiber tractography using DT-MRI data. *Magnetic Resonance in Medicine*, 44(4):625–632, October 2000. 129
- [204] Derek K. Jones, Thomas R. Knösche, and Robert Turner. White matter integrity, fiber count, and other fallacies: The do’s and don’ts of diffusion MRI. *NeuroImage*, 73:239–254, June 2013. 129
- [205] Hui Zhang, Torben Schneider, Claudia A. Wheeler-Kingshott, and Daniel C. Alexander. NODDI: practical in vivo neurite orientation dispersion and density imaging of the human brain. *NeuroImage*, 61(4):1000–1016, July 2012. 129

- [206] Yaniv Assaf and Peter J. Basser. Composite hindered and restricted model of diffusion (CHARMED) MR imaging of the human brain. *NeuroImage*, 27(1):48–58, August 2005. 129
- [207] Nicolas Kunz, Hui Zhang, Lana Vasung, Kieran R. O’Brien, Yaniv Assaf, François Lazeyras, Daniel C. Alexander, and Petra S. Hüppi. Assessing white matter microstructure of the newborn with multi-shell diffusion MRI and biophysical compartment models. *NeuroImage*, 96: 288–299, August 2014. 129
- [208] Jongho Lee, Peter van Gelderen, Li-Wei Kuo, Hellmut Merkle, Afonso C. Silva, and Jeff H. Duyn. T2*-based fiber orientation mapping. *NeuroImage*, 57(1):225–234, July 2011. 129, 130, 142
- [209] Se-Hong Oh, Young-Bo Kim, Zang-Hee Cho, and Jongho Lee. Origin of B0 orientation dependent R2? (= 1/T2?) in white matter. *NeuroImage*, 73:71–79, June 2013. 129, 139, 141
- [210] J.P. Marques, W. Van Der Zwaag, C. Granziera, G. Krueger, and R. Gruetter. Cerebellar cortical layers: In vivo visualization with structural high-field-strength MR imaging. *Radiology*, 254(3):942–948, 2010. 131
- [211] E Visser, S Qin, and Marcel P. Zwiers. EPI distortion correction by constrained nonlinear coregistration improves group fMRI. Stockholm, Sweden, 2010. 134, 151
- [212] Nikola Stikov, Jennifer S. W. Campbell, Thomas Stroh, Mariette Lavelée, Stephen Frey, Jennifer Novek, Stephen Nuara, Ming-Kai Ho, Barry J. Bedell, Robert F. Dougherty, Ilana R. Leppert, Mathieu Boudreau, Sridar Narayanan, Tanguy Duval, Julien Cohen-Adad, Paul-Alexandre Picard, Alicja Gasecka, Daniel Côté, and G. Bruce Pike. In vivo histology of the myelin g-ratio with magnetic resonance imaging. *NeuroImage*, 118:397–405, September 2015. 139, 141, 143
- [213] Michael J. Knight, Bryony Wood, Elizabeth Couthard, and Risto Kauppinen. Anisotropy of spin-echo T 2 relaxation by magnetic resonance imaging in the human brain in vivo. *Biomedical Spectroscopy and Imaging*, 4(3):299–310, June 2015. 139, 142
- [214] Sina Aslan, Hao Huang, Jinsoo Uh, Virendra Mishra, Guanghua Xiao, Matthias J. P. van Osch, and Hanzhang Lu. White matter cerebral

- blood flow is inversely correlated with structural and functional connectivity in the human brain. *NeuroImage*, 56(3):1145–1153, June 2011. 141, 143
- [215] Andrea Cherubini, Patrice Péran, Gisela Elisabeth Hagberg, Ambra Erika Varsi, Giacomo Luccichenti, Carlo Caltagirone, Umberto Sabatini, and Gianfranco Spalletta. Characterization of white matter fiber bundles with T₂* relaxometry and diffusion tensor imaging. *Magnetic Resonance in Medicine*, 61(5):1066–1072, May 2009. 142
- [216] Tie-Qiang Li, Bing Yao, Peter van Gelderen, Hellmut Merkle, Stephen Dodd, Lalith Talagala, Alan P. Koretsky, and Jeff Duyn. Characterization of T₂* heterogeneity in human brain white matter. *Magnetic Resonance in Medicine*, 62(6):1652–1657, December 2009. 142
- [217] José P. Marques and R. W. Bowtell. Using forward calculations of the magnetic field perturbation due to a realistic vascular model to explore the BOLD effect. *NMR in biomedicine*, 21(6):553–565, July 2008. 142
- [218] R. C. Carpenter Truex. Human neuroanatomy. September 1969. 143
- [219] Julian Maclaren, Michael Herbst, Oliver Speck, and Maxim Zaitsev. Prospective motion correction in brain imaging: A review. *Magnetic Resonance in Medicine*, 69(3):621–636, March 2013. 144
- [220] Daniel Gallichan, José P. Marques, and Rolf Gruetter. Retrospective correction of involuntary microscopic head movement using highly accelerated fat image navigators (3d FatNavs) at 7t. *Magnetic Resonance in Medicine*, pages n/a–n/a, April 2015. 144
- [221] Dmitriy A. Yablonskiy, Alexander L. Sukstanskii, Jie Luo, and Xiaoqi Wang. Voxel spread function method for correction of magnetic field inhomogeneity effects in quantitative gradient-echo-based MRI. *Magnetic Resonance in Medicine*, 70(5):1283–1292, November 2013. 144
- [222] Andrew M. Peters, Matthew J. Brookes, Frank G. Hoogenraad, Penny A. Gowland, Susan T. Francis, Peter G. Morris, and Richard Bowtell. T₂* measurements in human brain at 1.5, 3 and 7 T. *Magnetic Resonance Imaging*, 25(6):748–753, July 2007. 144
- [223] P. van Gelderen, J.a. de Zwart, P. Starewicz, R.s. Hinks, and J.h. Duyn. Real-time shimming to compensate for respiration-induced B₀ fluctuations. *Magnetic Resonance in Medicine*, 57(2):362–368, February 2007. 144

- [224] Jie Wen, Anne H. Cross, and Dmitriy A. Yablonskiy. On the role of physiological fluctuations in quantitative gradient echo MRI: implications for GEPCI, QSM, and SWI. *Magnetic Resonance in Medicine*, 73(1):195–203, January 2015. 144
- [225] John G. Sled and G. Bruce Pike. Correction for B1 and B0 variations in quantitative T2 measurements using MRI. *Magnetic Resonance in Medicine*, 43(4):589–593, April 2000. 144
- [226] S. N. Sotiropoulos, S. Moeller, S. Jbabdi, J. Xu, J. L. Andersson, E. J. Auerbach, E. Yacoub, D. Feinberg, K. Setsompop, L.L. Wald, T.E.J. Behrens, K. Ugurbil, and C. Lenglet. Effects of Image Reconstruction on Fibre Orientation Mapping from Multi-channel Diffusion MRI: Reducing the Noise Floor Using SENSE. *Magnetic resonance in medicine : official journal of the Society of Magnetic Resonance in Medicine / Society of Magnetic Resonance in Medicine*, 70(6), December 2013. 150
- [227] Marcel P. Zwiers. Patching cardiac and head motion artefacts in diffusion-weighted images. *NeuroImage*, 53(2):565–575, November 2010. 151
- [228] Alessandro Daducci, Erick Jorge Canales-Rodriguez, Maxime Descoteaux, Eleftherios Garyfallidis, Yaniv Gur, Ying-Chia Lin, Merry Mani, Sylvain Merlet, Michael Paquette, Alonso Ramirez-Manzanares, Marco Reisert, Paulo Reis Rodrigues, Farshid Seppehrband, Emmanuel Caruyer, Jeiran Choupan, Rachid Deriche, Mathews Jacob, Gloria Menegaz, Vesna Prckovska, Mariano Rivera, Yves Wiaux, and Jean-Philippe Thiran. Quantitative Comparison of Reconstruction Methods for Intra-Voxel Fiber Recovery From Diffusion MRI. *IEEE Transactions on Medical Imaging*, 33(2):384–399, February 2014. 158
- [229] Berkin Bilgic, Borjan A. Gagoski, Stephen F. Cauley, Audrey P. Fan, Jonathan R. Polimeni, P. Ellen Grant, Lawrence L. Wald, and Kawin Setsompop. Wave-CAIPI for highly accelerated 3d imaging. *Magnetic Resonance in Medicine*, 73(6):2152–2162, June 2015. 158

publications and conferences

D.Khabipova, R.Gil, M.Zwiers, R.Gruetter and J.P.Marques *Quantitative susceptibility mapping including a white matter Lorenzian correction* (in preparation)

R.Gil and **D.Khabipova**, M.Zwiers, T.Hilbert, T.Kober, J.P.Marques *An in vivo study of the transverse relaxation rate orientation (in)dependence in white matter* (in preparation)

D.Khabipova, R.Gruetter and J.P.Marques *Studying cyto and myeloarchitecture of the human cortex at ultra-high field with quantitative imaging: R_1 , R_2^* and susceptibility* (in preparation)

D.Khabipova, R.Gil, M.Zwiers, J.P.Marques *Mapping orientation dependent and independent components of R_2^* in the human white matter - an in vivo study* 23th Annual Meeting of the International Society for Magnetic Resonance in Medicine (ISMRM), 2016, Singapore **oral communication**

D.Khabipova, R.Gil, M.Zwiers, J.P.Marques *Quantitative susceptibility mapping including a white matter Lorenzian correction* 23th Annual Meeting of the International Society for Magnetic Resonance in Medicine (ISMRM), 2016, Singapore **electronic poster**

R.Gil, and **D.Khabipova**, M.Zwiers, T.Hilbert, T.Kober, J.P.Marques *Assessing the (an)isotropic component of R_2 as a mean to study White Matter properties* 23th Annual Meeting of the International Society for Magnetic Resonance in Medicine (ISMRM), 2016, Singapore **power pitch presentation**

S.Robinson, K.Bredies, **D.Khabipova**, W.Li, F.Schweser *An illustrated comparison of processing methods for phase MRI and QSM: Combining array coil signals and phase unwrapping.*, 2015, NMR in Biomedicine (submitted)

D.Khabipova, R.Gruetter, J.P.Marques *Human cortical surface maps of three quantitative imaging parameters: R_1 , R_2^* and Magnetic Susceptibility* 22th Annual Meeting of the International Society for Magnetic Resonance in Medicine (ISMRM), 2015, Toronto, Canada, **oral communication and summa cum laude**

D.Khabipova, R.Gruetter, J.P.Marques *The impact of background removal techniques on the quantification of magnetic susceptibility in the human cortex* 22th Annual Meeting of the International Society for Magnetic Resonance in Medicine (ISMRM), 2015, Toronto, Canada, **electronic poster presentation**

D.Khabipova, R.Gruetter and J.P.Marques *Human cortical surface maps of three quantitative imaging parameters: R_1 , R_2^* and Magnetic Susceptibility* 7th Annual Meeting of the ISMRM Benelux Chapter, 2015, Ghent, Belgium,

oral communication

D.Khabipova, R.Gruetter and J.P.Marques *Human Cortical Surface for three different contrasts: R_1 , R_2^* and Susceptibility* 2nd International Workshop in Quantitative Susceptibility Mapping, 2014, Durham, North Carolina, USA, **poster presentation and honorable mention**

D.Khabipova, Y.Wiaux, R.Gruetter and J.P.Marques *A Modulated Closed Form solution for Quantitative Susceptibility Mapping - a thorough evaluation and comparison to iterative methods based on edge prior knowledge*, 2014, Neuroimage (published)

D.Khabipova, R.Gruetter and J.P.Marques *Modulated closed form solution for quantitative susceptibility mapping* 22th Annual Meeting of the International Society for Magnetic Resonance in Medicine (ISMRM), 2014, Mailand, Italien, **oral communication and summa cum laude**

R. Maddage, J.P. Marques, **D. Khabipova**, R. Gruetter *Towards in vivo manganese quantification at 14.1T using Susceptibility Mapping* 2nd International Workshop in Quantitative Susceptibility Mapping, 2013, Ithaka, New York, USA, **poster presentation**

D.Khabipova, Y.Wiaux, R.Gruetter and J.P.Marques *The importance of priors for l_2 and l_1 total variation methods in quantitative susceptibility mapping* 2nd international biomedical and astronomical signal processing (BASP) Frontiers workshop, 2013, Villars-sur-Ollon, Schweiz, **poster presentation and best poster award**

D.Khabipova, Y.Wiaux, R.Gruetter and J.P.Marques *Relevance of morphological information for l_2 and l_1 total variation methods in quantitative susceptibility mapping and reconstruction quality assessment without presence of the ground truth* 21th Annual Meeting of the International Society for Magnetic Resonance in Medicine (ISMRM), 2013, Salt Lake City, Utah, USA, **poster presentation**

D.Khabipova, J.P.Marques, G.Puy, R.Gruetter and Y.Wiaux *The importance of priors for l_2 and l_1 total variation methods in quantitative susceptibility mapping* 29th Annual Meeting of the European Society for Magnetic Resonance in Medicine and Biology (ESMRM), 2012, Lisabon, Portugal, **oral communication**

R.Maddage, J.P.Marques, **D.Khabipova**, and R.Gruetter *Phase based manganese quantification in MEMRI at 14* 29th Annual Meeting of the European Society for Magnetic Resonance in Medicine and Biology (ESMRM), 2012, Lisabon, Portugal, **oral communication**

Curriculum vitae

Diana Khabipova

Education

- 08/2011-now **PhD in Physics**, *Ecole Polytechnique Fédérale de Lausanne (EPFL)*, Switzerland, Lausanne.
"Quantitative susceptibility mapping in the human brain at 7T"
- 01/2014- **SNF Doc.Mobility grant**, *Donders Institute for Brain, Cognition and Behaviour*,
01/2015 Nijmegen, Netherlands.
"Mapping the white matter (in)dependent components of quantitative MRI"
- 10/2005- **Dipl. Physik, M.Sc equivalent**, *Technische Universität*, Deutschland, Berlin.
07/2011
- 09/2000- **Allgemeine Hochschulreife, (academic high school diploma)**, *Gymnasium*
07/2005 *Martino-Katharineum*, Deutschland, Braunschweig.

Experience

- 2014 **Teaching Assistant**, *Teaching Support Centre, EPFL*, Lausanne.
"Teaching Toolkit", Pedagogical Skills Development Workshops for PhD students
- 03/2013- **Teaching Assistant**, *School of Basic Sciences, Physics, EPFL*, Lausanne.
02/2014 Lectures in physics for Life Science
- 09/2012- **Teaching Assistant**, *School of Basic Sciences, Physics, EPFL*, Lausanne.
02/2013 Supervision of Experiments for Bachelor students in their 3rd year
- 03/2012- **Teaching Assistant**, *School of Basic Sciences, Physics, EPFL*, Lausanne.
08/2012 Supervision of Experiments for Bachelor students in their 2nd year
- 04/2008- **Teaching Assistant**, *Institut für Optik und Atomare Physik, Technische Universität*
07/2011 *Berlin*, Berlin.
Lectures in physics for engineers
- 08/2009- **Internship**, *HELIOS medical hospital Emil-von-Behring*, Berlin.
09/2009 working with MRI, CT, US in the Department of Diagnostic and Interventional Radiology
- 05/2005- **Internship**, *PTB, National Metrology Institute of Germany*, Braunschweig.
07/2005 measurements in the Division of Ionizing Radiation
wafer manufacturing in clean room environment

Awards and recognition

- 2015 **summa cum laude (top 5%) und travel award**, *ISMRM 2015*, Toronto, Kanada.
- 2014 **honorable mention (contribution was rated with “excellent”, 9/10 points) and travel award**, *3rd International Workshop on MRI Phase Contrast and Quantitative Susceptibility Mapping*, Durham,NC, USA.
- 2014 **summa cum laude (top 5%) and travel award**, *Joint Annual Meeting ISMRM-ESMRMB 2014*, Mailand, Italien.
- 2013 **best poster award**, *international biomedical and astronomical signal processing (BASP)Frontiers workshop*, Villars-sur-Ollon, Schweiz.

Activities and Interests

- 2016 **member of a jury**, *Youth Research Competition*, Braunschweig.
ranking of projects in the field of physics
- 2011-2013 **StartigDoc mentee**, *female PhD students program*, Switzerland.
- 2007-2011 **member of a jury**, *Youth Research Competition*, Braunschweig.
ranking of projects in the field of physics
- hobbies Tango Argentino, Sailing, Wind- and Kitesurfing, Capoeira

Special Skills and Abilities

- Office \LaTeX , MS Office Suite (Word, Excel, Powerpoint)
- programming Matlab, Python, C/C++, bash
- MRI data analysis software FreeSurfer, FSL, SPM
- others Mathematica, Origin, LabView, gnuplot
- Languages russian, native language
german, mother tongue
english, advanced
french, beginner-intermediate